M. Ali Hooshyar
Irwin Reichstein
F. Bary Malik

NUCLEAR FISSION AND CLUSTER RADIOACTIVITY

AN ENERGY-DENSITY FUNCTIONAL APPROACH

Springer

Nuclear Fission and Cluster Radioactivity

M. A. Hooshyar · I. Reichstein · F. B. Malik

Nuclear Fission and Cluster Radioactivity

An Energy-Density Functional Approach

With 82 Figures

Springer

Authors

Professor M. Ali Hooshyar

University of Texas at Dallas
Department of Mathematical Sciences
P.O. Box 830688, EC 35
Richardson, TX 75083-0688
USA
Email: ali.hooshyar@utdallas.edu

Professor Irwin Reichstein

Carleton University
School of Computer Science
Herzberg Building
1125 Colonel By Drive
Ottawa, Ontario K1S 5B6
Canada
Email: reichstein@scs.carleton.ca

Professor F. Bary Malik

Southern Illinois University at Carbondale
Department of Physics
Neckers 483A
Carbondale, IL 62901-4401
USA
Email: fbmalik@physics.siu.edu

Library of Congress Control Number: 2005929609

ISBN-10 3-540-23302-4 Springer Berlin Heidelberg New York
ISBN-13 978-3-540-23302-2 Springer Berlin Heidelberg New York

Springer is a part of Springer Science+Business Media
springeronline.com

Printed in The Netherlands

Typesetting: by the authors and TechBooks using a Springer LaTeX macro package

Cover design: Cover design: E. Kirchner, Springer Heidelberg

Printed on acid-free paper SPIN: 10017708 56/TechBooks 5 4 3 2 1 0

This book is dedicated to
Dina and Nahid Hooshyar and Akemi Oikawa Malik
for their encouragement and support and to the memories of
Balgice and Masharief Hooshyar
and Rebecca and Solomon Reichstein

Preface

There are a number of excellent treaties on fission in the market and a reader may wonder about the reason for us to write another book. All of the existing books, however, deal with the phenomena associated with fission from the vantage point of the liquid-drop model of nuclei. In this monograph, we depart from that and investigate a number of fission related properties from a simple energy-density functional point of view taking into consideration the actual density-distribution function of nuclei i.e., we investigate the effect of a nuclear surface of 2 to 3 fm in width on the potential energy surface of a separating daughter pair. This influences the structure of the potential energy surface significantly. The referee of the article titled "Potential Energy Surfaces and Lifetimes for Spontaneous Fission of Heavy and Superheavy Elements from a Variable Density Mass Formula" published in Annals of Physics, Volume 98, 1976, stated "The work reported in this paper is important and significant for fission theory." We, therefore, wish to bring to the scientific community a comprehensive study of the fission phenomenon done so far from the energy-density functional approach. An overview of this monograph is presented in Sect. 1.10 of Chap. 1 under the title pre-amble.

Some of the successes of the approach are the following:

In 1972, using a simple version of the theory, it was correctly predicted that half-lives of superheavy elements should be very short. So far, experiments support this.

In 1972, the mass distribution in the fission of isomer state of ^{236}U was predicted. The measurements done eight years later in 1980 confirmed this prediction.

The theory can calculate the most probable kinetic energies associated with the emission of a daughter pair in spontaneous and induced fission within a few MeV.

The theory, independent of observation done, predicted simultaneously that the mass-spectrum in the spontaneous fission of ^{258}Fm should be symmetric.

The theory can account for nuclear masses and observed density distribution functions to within 1.5%.

The theory predicted the existence of cold fission, well before it was found experimentally.

Aside from describing many phenomena related to fission, this theoretical approach can be extended to the study of cluster and alpha-radioactivities, which are discussed in Chap. 9. Thus, the theory provides a uniform approach to the emission of alpha, light clusters, and heavy nuclei from meta-stable parent nuclei.

This latter problem, on the other hand, is clearly a complex many-body one and as such, the theory presented herein is likely to be improved over time with the advancement in many-body and reaction theory. We just hope that this little book will serve as a foundation for more sophisticated work in the future.

In essence, the theory is a refinement of the pioneering work of Professors Neils Bohr and John A. Wheeler. In 1939, when their work was published, very little knowledge of actual nuclear density distribution functions was available. That work may be viewed as an energy-density approach to nuclear fission for a uniform density-distribution function. We have benefited much from the underlying physics of this monumental publication. One of us, (FBM) is very thankful to Professor John Wheeler for exposing him to many nuances of that work and teaching him much of physics in other areas.

Many persons deserve many thanks for discussion and encouragement in early parts of this investigation. Obviously, much of the subject matter noted in the monograph is based on the excellent doctorial dissertation of Dr. Behrooz Compani-Tabrizi. We are much indebted to him. We remember fondly the spirited correspondences with Professor G.E. Brown, the then editor of Physics Letters B, where some of the key papers were published. Discussion with Professors John Clark, (late) Herman Feshbach, (late) Emil Konopinski, Don Lichtenberg and Pierre Sabatier, and Dr. Barry Block are much appreciated.

For the preparation of the manuscript, we are very much thankful to Professor Arun K. Basak, Mr. Shahjahan Ali, Ms. Sylvia Shaw, Ms. Angela Lingle, and Ms. Carol Booker. We are appreciative of the helpful assistance of the staff and editors of Springer Verlag associated with the publication of this monograph. Lastly, the support of our many friends and relatives played an important role in getting this book done. We thank them collectively.

January 2005

Ali Hooshyar, Richardson, Texas
Irwin Reichstein, Ottawa, Ontario
Bary Malik, Carbondale, Illinois

Contents

1 A Summary of Observed Data and Pre-Amble

1.1 Introduction

The discovery of nuclear fission has been a key factor in establishing a major role for physics in human society in the post World War II era. It had, however, an inconspicuous beginning in the laboratories of Paris and Rome. In 1934, F. Joliot and I. Curie [1.1, 1.2] reported on a new type of radioactivity induced by alpha particles incident on nuclei. Immediately thereafter, Fermi and his collaborators reported neutron induced radioactivity on a series of targets [1.3–1.5]. It was difficult to separate clearly the resultant elements. In their zeal to discover elements heavier than uranium, the possibility of nuclear fission was overlooked [1.6, 1.7], despite the fact that Noddack [1.8], in her article, raised the possibility of nuclear fission in experiments carried out in Rome [1.5–1.7]. Ultimately, Hahn and Strassmann [1.9] concluded reluctantly that uranium irradiated by neutrons bursts into fragments and the phenomenon of particle induced fission of nuclei was established. This conclusion was immediately confirmed by Meitner and Frisch [1.10] and nuclear fission was established as an important phenomenon in the study of physical properties of nuclei.

The importance of nuclear fission for the production of energy is obvious. About 180 MeV of energy is produced in the fission of an actinide to one of its most probable daughter pairs. This means that 1 kg of uranium is capable of producing about 2×10^7 Kilowatt hours of energy, enough to keep a 100 Watt bulb burning continuously for about 25,000 years. From the theoretical standpoint, the implication of the exothermal process involved in their decay is that actinide nuclei must be in a meta-stable state, very much like alpha emitters and the then nuclear physics community started exploring the intriguing question of whether or not fission could occur spontaneously in the same fashion as the emission of alpha particles from alpha emitters. Libby searched in vain for the spontaneous fission of uranium, however, it was finally Petrzhak and Flerov [1.11] who discovered that uranium fissions spontaneously. Since then, extensive efforts have been carried out at various laboratories to determine physical properties associated with spontaneous fission as reported by Segré [1.12].

Spontaneous fission refers to the physical phenomenon where a parent nucleus decays spontaneously to daughter pairs, each member of which is

much heavier than an alpha particle. Simultaneous emission of three particles also occurs but the process is a few orders of magnitude less likely. In induced fission a target nucleus, upon bombardment by an incident projectile, decays into a series of pairs of daughter nuclei, each member of the pair being much heavier than an alpha particle. Unlike the case of alpha-particle emission, the particles in the fission processes are emitted primarily in excited states. Obviously, both of these processes involve a very complex transmutation of the parent nuclei, the understanding of which requires measurements of many associated phenomena. Extensive experimental studies of physical properties associated with fission phenomena have been carried out and are documented in many excellent treaties [1.13–1.15, 1.34]. In the next section we summarize some of the key physical properties relevant to the dynamical aspect of the fission process.

In 1984, Rose and Jones [1.17] reported the observation of the emission of ^{14}C spontaneously from ^{223}Ra which was immediately confirmed in a number of research centers around the world [1.18–1.21]. In fact, many of these laboratories observed the emission of clusters ranging from ^{14}C to ^{34}Si from parent nuclei radium to uranium. Their half-lives range from 10^{11} to 10^{25} seconds. The main observed characteristic features associated with cluster emission are also noted in Sect. 1.9.

1.2 Half-Lives and Spontaneous Decay

The half-lives associated with spontaneous decay of nuclei by fission range from greater than 10^{18} years for ^{230}Th to 10^{-3} s for ^{258}Fm i.e., a range of over 10^{28} years. These vary considerably for different isotopes of a given element, e.g., the half-lives of spontaneous decay of californium vary from 12 min ($\sim 2.3 \times 10^{-5}$ years) for the isotope ^{256}Cf to 10^{3} years for the isotope ^{246}Cf. An updated tabulation of spontaneous fission half-lives is given in Table 1.1 and a selected number of them are plotted in Figs. 1.1–1.3. A close examination of Table 1.1 reveals that odd-isotopes of a given element have consistently longer half-lives by a few orders of magnitude than those of their even-even neighbors. Similarly, odd-odd isotopes of a given element have longer half-lives compared to their adjacent odd-even ones.

The spontaneous decay is, moreover, predominately binary. Only one in every few hundred decays may be ternary. Recently, quaternary fission has also been observed, [1.22] occurring at the rate of about 5×10^{-8} per fission. For binary fission, there is a mass and charge distribution associated with the fission of a parent nucleus. A daughter pair usually has a mean or average kinetic energy called total kinetic energy (TKE) associated with it, and there is a distribution of the TKE with the fragment mass numbers, as shown in Fig. 1.4.

Table 1.1. Recommended spontaneous fission half-lives of elements from ^{230}Th to ^{259}Fm [1.81]. The number for each element refers to average values recommended in [1.81]

Element	$T_{1/2}$(Years) Unless Noted	Element	$T_{1/2}$(Years) Unless Noted
^{230}Th	$>2. \times 10^{18}$	^{246}Cm	$1.81 \pm 0.02 \times 10^{7}$
^{232}Th	$>1. \times 10^{21}$	^{248}Cm	$4.15 \pm 0.03 \times 10^{6}$
^{231}Pa	$>1. \times 10^{17}$	^{250}Cm	$1.13 \pm 0.05 \times 10^{4}$
^{230}U	$>4. \times 10^{10}$	^{249}Bk	$1.9 \pm 0.1 \times 10^{9}$
^{232}U	$8. \pm 6. \times 10^{13}$	^{246}Cf	$2.0 \pm 0.2 \times 10^{3}$
^{233}U	$>2.7 \times 10^{17}$	^{248}Cf	$3.2 \pm 0.3 \times 10^{4}$
^{234}U	$1.5 \pm 0.2 \times 10^{16}$	^{249}Cf	$8. \pm 1. \times 10^{4}$
^{235}U	$1.0 \pm 0.3 \times 10^{19}$	^{250}Cf	$1.7 \pm 0.1 \times 10^{4}$
^{236}U	$2.5 \pm 0.1 \times 10^{16}$	^{252}Cf	$85. \pm 1$
^{238}U	$8.2 \pm 0.1 \times 10^{15}$	^{254}Cf	60.7 ± 0.2 d
^{237}Np	$>1. \times 10^{18}$	^{256}Cf	$12. \pm 1.$ min
^{236}Pu	$2.1 \pm 0.1 \times 10^{9}$	^{253}Es	$6.4 \pm 0.2 \times 10^{5}$
^{238}Pu	$4.75 \pm 0.09 \times 10^{10}$	^{254}Es	$>2.5 \times 10^{7}$
^{239}Pu	$8. \pm 2. \times 10^{15}$	^{255}Es	$2.44 \pm 0.14 \times 10^{3}$
^{240}Pu	$1.16 \pm 0.02 \times 10^{11}$	^{242}Fm	$0.8 \pm 0.2 \times 10^{-3}$ s
^{241}Pu	$6. \times 10^{16}$	^{244}Fm	$3.3 \pm 0.5 \times 10^{-3}$ s
^{242}Pu	$6.77 \pm 0.07 \times 10^{10}$	^{246}Fm	$15. \pm 5.$
^{244}Pu	$6.6 \pm 0.2 \times 10^{10}$	^{248}Fm	$10. \pm 5$ hr
^{241}Am	$1.0 \pm 0.4 \times 10^{14}$	^{250}Fm	0.83 ± 0.15
^{242}Am	$>3. \times 10^{12}$	^{252}Fm	$126. \pm 11.$
^{243}Am	$2.0 \pm 0.5 \times 10^{14}$	^{254}Fm	$228 \pm 1.$ d
^{240}Cm	$1.9 \pm 6. \times 10^{6}$	^{255}Fm	$\approx 1. \times 10^{4}$
^{242}Cm	$7.0 \pm 0.2 \times 10^{6}$	^{256}Fm	2.86 ± 0.02 hr
^{243}Cm	$5.5 \pm 0.9 \times 10^{11}$	^{257}Fm	$131. \pm 3$
^{244}Cm	$1.32 \pm 0.02 \times 10^{7}$	^{258}Fm	$0.37 \pm 0.02 \times 10^{-3}$ s
^{245}Cm	$1.4 \pm 0.2 \times 10^{12}$	^{259}Fm	1.5 ± 0.02

A very important characteristic of the binary fission process is that the observed TKE associated with a decay mode is typically 10 to 30 MeV lower than the Q-value of the reaction. A typical case is shown in Fig. 1.4. Daughter pairs are emitted in predominantly excited states and cool off by emitting primarily neutrons and γ-rays. Some important characteristic behaviors of these emitted neutrons are discussed in Sects. 1.4 and 1.5.

1.3 Induced Fission

Induced fission was discovered before spontaneous fission. Experiments in Rome [1.3–1.5] and Berlin [1.9] primarily used neutrons to induce fission, although the initial experiments in France were done using alpha particles

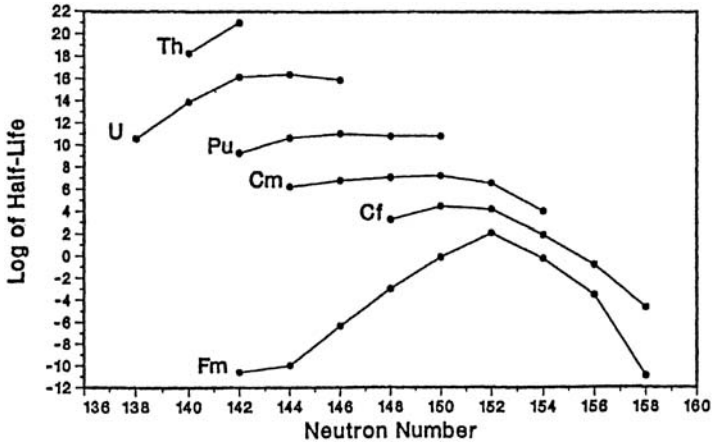

Fig. 1.1. Logarithm of spontaneous fission half-lives in years are plotted as a function of neutron number for some even-even isotopes of Th, U, Pu, Cm, Cf and Fm [1.81]

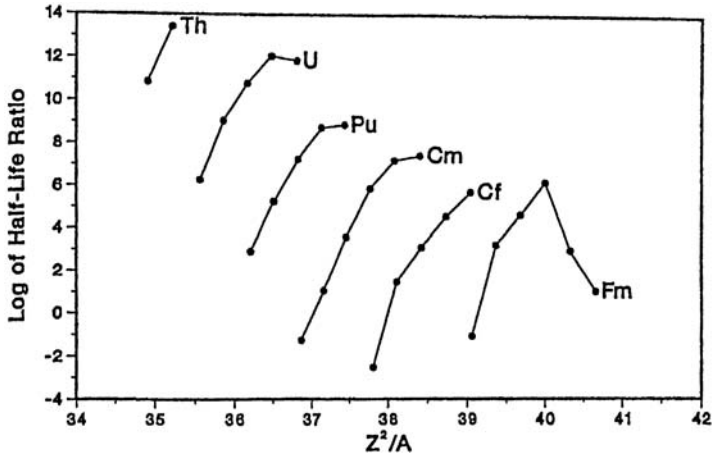

Fig. 1.2. Logarithm of spontaneous fission half life/alpha half life of even-even nuclei are plotted as a function of the square of atomic number, Z over mass number A known as the fissibility parameter [1.81]

[1.1, 1.2]. Induced fission can be initiated both by particles and by radiation and like spontaneous fission, is predominantly a binary process.

Following the discovery of the fission process, Hahn and Strassmann [1.9] in Berlin and Anderson, Fermi and Grosse in New York [1.23] established the mass distribution in the fission process. Hahn and Strassmann [1.9], Frisch [1.24], Jentschke and Prankl [1.25] and Joliot [1.26] demonstrated that a large amount of kinetic energy was associated with the fission fragments but the

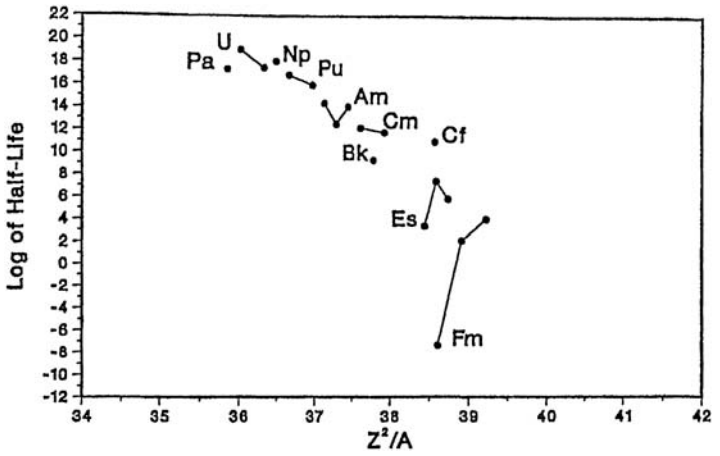

Fig. 1.3. Logarithm of spontaneous fission half-lives in years of some non-even-even isotopes are plotted as a function of the square of atomic number, Z over mass number A [1.81], i.e., the fissibility parameter

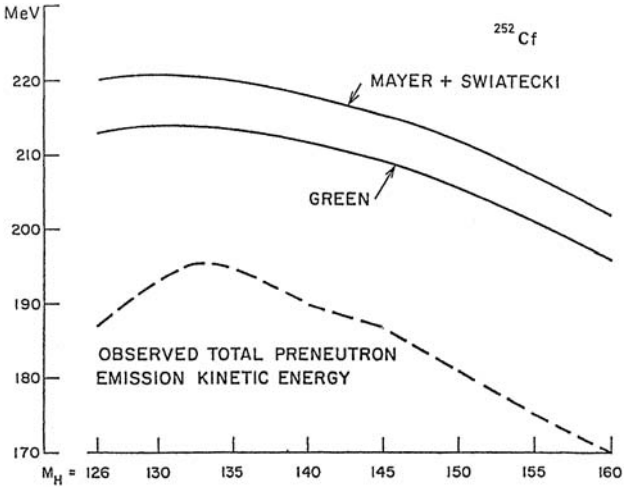

Fig. 1.4. Observed pre-neutron emission total kinetic energies shown as a *dashed* line [1.84] in the spontaneous fission of ^{252}Cf are compared to the Q-value calculated from Myers-Swiatecki's [1.88] and Green's [1.89] mass formulae for various daughter pairs. m_H is the mass of the heavier fragment

systematic measurement of the TKE spectra began after the second world war at various laboratories [1.27–1.29]. Simultaneous measurements of both the mass and TKE spectra in the same experiment were developed at a later date and are very important to our understanding of the process. Way, Wigner and Present [1.30, 1.31] in the late nineteen-forties raised the possibility of a

charge distribution associated with fission products and these distributions were established by Glendenin and others noted in review articles by Wahl [1.33, 1.34].

The projectile in induced fission is not restricted to neutrons only. Extensive studies of the fission process have been done with incident γ-rays, protons, deuterons, alpha particles, μ-mesons and other light as well as heavy nuclei [1.15] with a wide range of incident energies. Fission yields, mass, charge and TKE distributions are strongly affected by the energy of incident projectiles.

The fission cross section induced by thermal neutrons is very large, exceeding a few thousand barns and falls off inversely with neutron velocity but shows sharp narrow resonances illustrated in Fig. 1.5 for energy up to 10 keV. Figure 1.6 presents the variation of cross section with energy up to 5 eV. It exhibits sharp and well-separated resonances both in the total neutron capture, absorption and fission cross sections.

Fission cross-sections at higher incident energy vary rather smoothly with energy except for a few steps and are only a few barns.

Extensive data on angular distributions are available. Their pattern depends on incident energies.

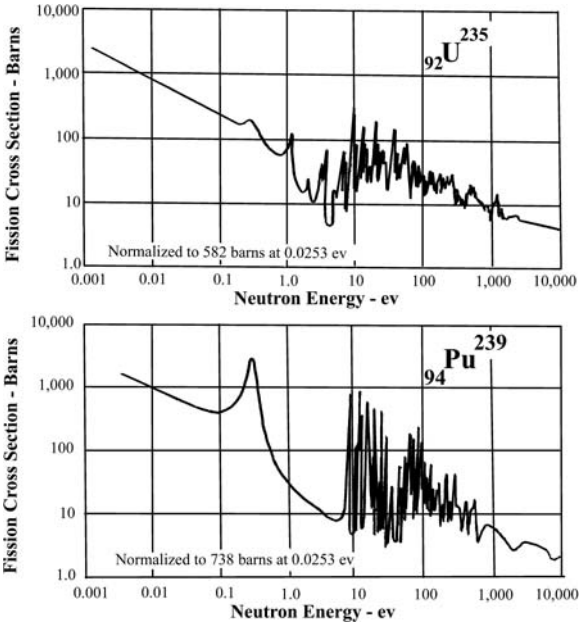

Fig. 1.5. Observed fission cross section is plotted as a function of incident neutron energy for ^{235}U and ^{239}Pu [1.82]

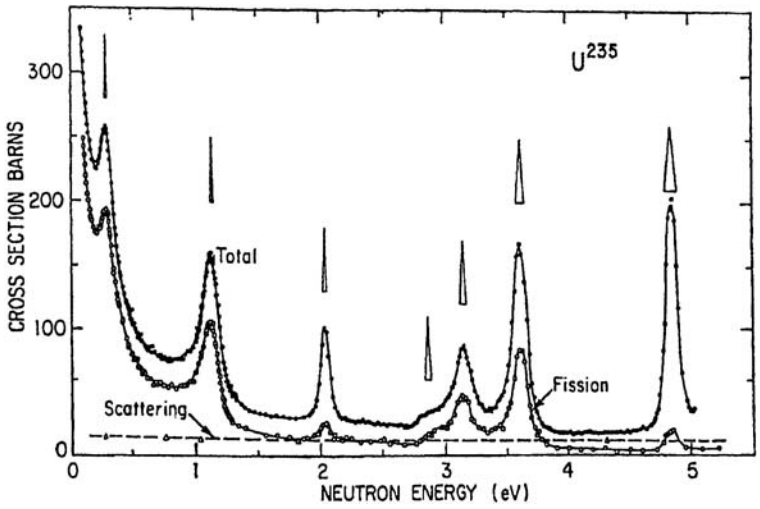

Fig. 1.6. Typical resonances observed in the interaction of neutrons with ^{235}U in the energy range of 0.1 to 5 eV. The observed total, fission and scattering cross sections are noted, respectively, as *solid* and *open* circles and *open* triangles [1.94]. Resonances observed in (n, γ) are marked with *open* spikes

1.4 Mass, Charge and Average Total Kinetic Energy Distribution

It is important to note that the decay mode in fission is neither asymmetric nor symmetric i.e., fission does not take place to a daughter pair having one partner twice as heavy as the other or to a pair each having equal mass. *Both spontaneous and induced fission leads to a distribution of emitted nuclei*, which is strongly dependent on mass number, A. The actual mass distribution in spontaneous fission depends on the mass number of the parent and in thermal neutron induced fission depends on the compound nucleus formed. For example, the locations of the peak and the valley in the mass distribution in thermally induced fission of ^{233}U and ^{239}Pu are different as shown in Fig. 1.7.

For most of the lighter actinides, mass distributions or spectra as a function of mass number A, in spontaneous fission and in thermal neutron induced fission having the same compound nucleus are nearly identical but they start to differ significantly with increasing mass number of parent nuclei. The difference becomes striking for the isotope ^{256}Fm. The mass distribution of the daughter products in the spontaneous fission of ^{256}Fm peaks towards a maximum of about A = 144 and 112 [1.35], i.e., asymmetric, whereas in the thermal neutron induced fission of ^{255}Fm, it peaks towards A = 128, i.e., symmetric [1.95]. This is indeed remarkable, since the parent compound nucleus in the induced fission has only about 6 MeV additional excitation energy.

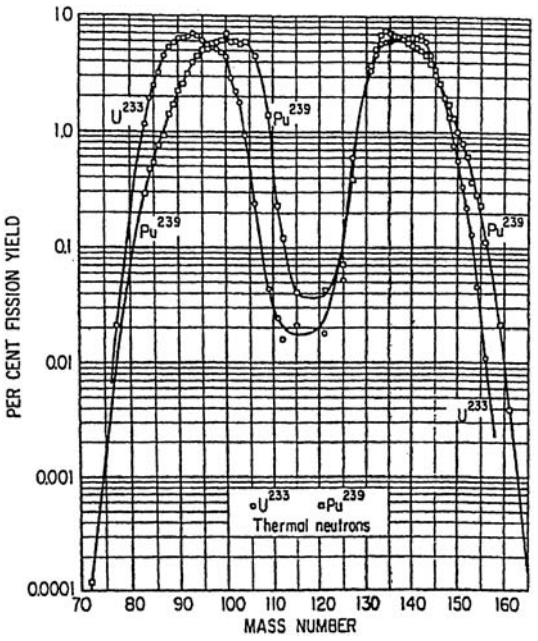

Fig. 1.7. Observed percentage mass yields for thermal neutron induced fission of ^{233}U and ^{239}Pu are plotted as a function of atomic number of daughter nuclei [1.83]

The mass distribution in particle and γ-ray induced fission changes dramatically with increase in incident energy. Figure 1.8 presents a comparison of the mass distributions in the induced fission of ^{235}U by both thermal and 14 MeV incident neutrons. In the latter case, the decay probabilities to symmetric modes increase significantly for the 14 MeV case and are comparable to those to asymmetric modes.

By far the largest part of the energy released in fission goes into the kinetic energies of daughter pairs. The average value of the released kinetic energy, however, is a few tens of MeV lower than the Q-value as shown in Fig. 1.4. The released average kinetic energy (TKE) has a significant mass dependence. A typical case is shown in Fig. 1.9 which clearly establishes that different daughter pairs are emitted with different average kinetic energies. In fact, TKE associated with a particular daughter pair has usually a significant root mean squared spread.

Aside from mass distribution, there is a charge distribution associated with fission fragments, an example of which is presented in Fig. 1.10 for the case of thermal neutron induced fission of ^{235}U. Figure 1.11 presents a collection of data indicating a typical charge distribution around Z_p, the most probable charge for a primary fission product of mass number A. Mass distribution as well as TKE spectra depends strongly on the excitation energy of fissile nuclei. This is discussed in details in Chap. 6.

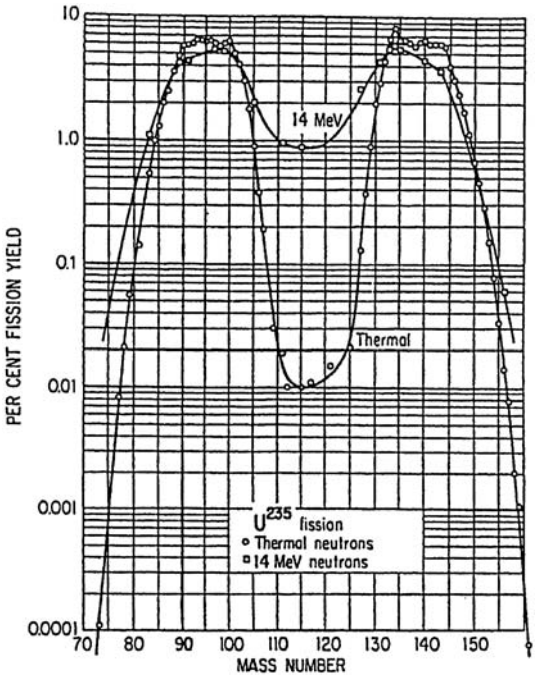

Fig. 1.8. Observed percentage mass yields for the thermal and 14 MeV neutron induced fission of ^{235}U are shown as a function of daughter masses [1.83]

1.5 Cooling of Daughter Pairs

The daughter pairs are usually in excited states and cool off primarily by emitting γ-rays and neutrons in spontaneous fission as well as induced fission by light projectiles (i.e., projectiles not heavier than ^{4}He) of energies up to a few tens of MeV. However, the measurement of significant root mean squared deviation of TKE associated with a particular decay mode characterized by a particular mass number may be indicative of the fact that the decay may take place to a particular daughter pair having various degrees of excitation, and different isotopes having the same mass number.

The average energy loss by gamma ray emission is about 6 to 8 MeV per fission fragment and constitutes 15 to 30 percent of the total excitation. The actual number of γ-rays emitted has a strong dependence on the mass numbers of the members of the daughter pair and hence, on the detailed nuclear structure of the pair, irrespective of parent nuclei as shown in Figs. 1.12, 1.13.

Early studies of induced fission already indicated that neutron emission accompanies the fission process [1.36–1.39]. In fact, Hagiwara [1.36] established that the average number of neutrons emitted per fission, ν, is about 2.5. These neutrons are actually emitted by daughter pairs and within about 4×10^{-14} sec of the scission [1.40]. The average number of neutrons emitted

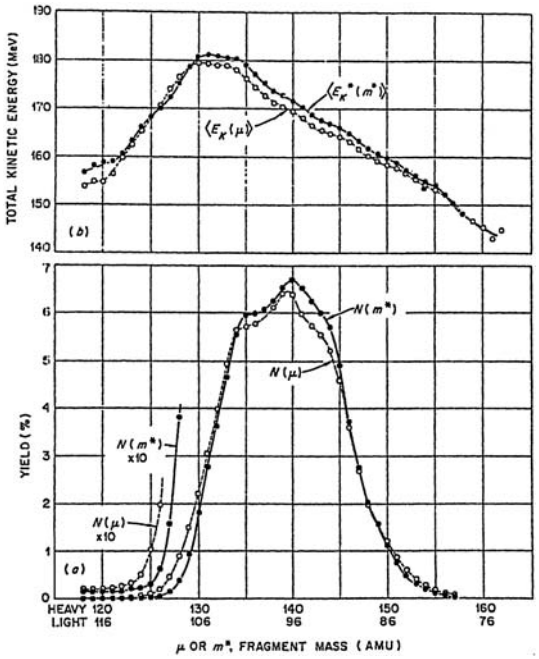

Fig. 1.9. The insert (**a**) indicates post and pre-neutron emission mass distribution $N(\mu)$ and $N(m*)$, respectively. The insert (**b**) indicates the corresponding average total kinetic energy $E_k(\mu)$ and $E_k(m*)$ distributions [1.84]. Both inserts are for thermal induced fission of ^{235}U

increases with the mass number of the parent [1.41] as shown in Fig. 1.14. Systematic studies [1.40, 1.42–1.47] have revealed that the number of emitted neutrons depends strongly on the mass numbers of the members of the daughter pair, irrespective of the mass of the associated parent nuclei emitting them. This is shown in Fig. 1.15. It seems that the nuclear structure of daughter pairs plays an important role in neutron emission. In fact, the number of neutrons emitted by closed shell nuclei is much smaller than those emitted from non-closed shell nuclei. This is similar to the situation for the number of γ-rays emitted by fission fragments. Thus, it seems that the number of neutrons emitted is dependant on the excitation energies and shell structures of the daughters.

The kinetic energy spectrum of emitted neutrons ranges from thermal to over 10 MeV. A typical case is shown in Fig. 1.16, where the probability of emission of a fission neutron with energy E, N (E), is plotted as a function of E [1.48, 1.49]. The observed spectrum in the figure is well represented by an analytic function.

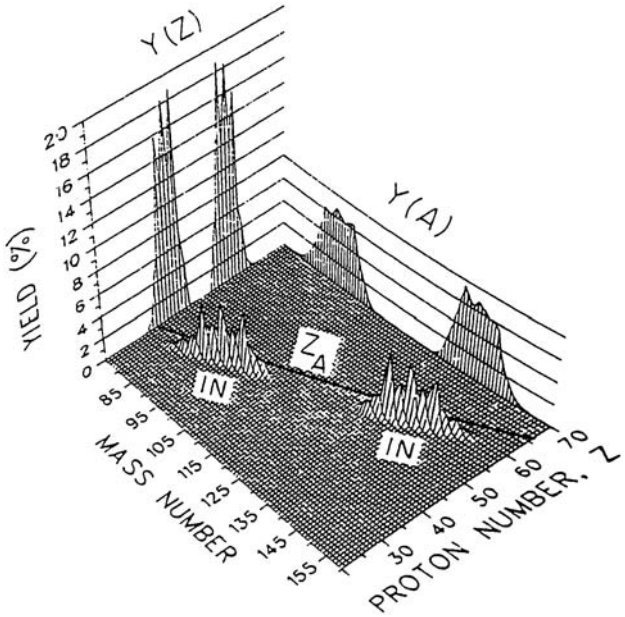

Fig. 1.10. Independent yields, noted as IN, obtained in thermal neutron induced fission of ^{235}U. Projections show mass, Y(A) and charge, Y(Z). Yields, Z_A indicate approximate location of the most stable nuclei. [1.33, 1.34]

1.6 Ternary and Quaternary Fission

In one out of a few hundred fissions, energetic alpha-particles are emitted at about right angles to the fission fragments [1.50] and hence, are not likely to be evaporated from these fragments. These alpha particles are emitted either during the breaking up of a parent nucleus simultaneously into three particles or produced at a time scale considerably shorter than the evaporation time for particle emission from daughter nuclei i.e., much less than 10^{-14} sec. These alpha particles have an energy distribution peaked around 15 MeV [1.13, 1.15]. Schmitt, Neiler, Walter and Chetham-Strode [1.51] found that the mass distribution of the daughters in thermal neutron induced fission of ^{235}U may be slightly different for the cases accompanied by alpha-emission compared to those in normal fission.

Aside from alpha particles, light charged particles such as isotopes of H and He [1.13, 1.15, 1.52] as well as heavy-ions B, C, N and O [1.53] have been detected in particle induced fission, although it has not yet been established that various charged particles are actually emitted in coincidence with fission, i.e., in actual three-body break up. As noted earlier, Gönnenwein et al. [1.22] have observed quaternary fission.

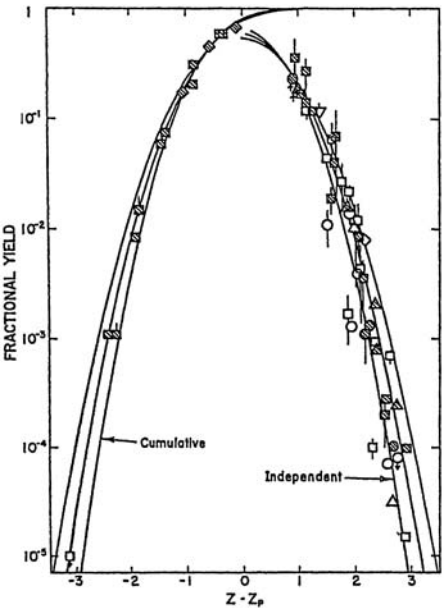

Fig. 1.11. Observed charge distribution in thermal neutron induced fission of ^{233}U, ^{235}U and ^{239}Pu shown, respectively, as squares, circles and triangles and in the spontaneous fission of ^{242}Cm and ^{252}Cf shown, respectively, as inverted triangles and diamonds are compared to the theoretical function $P(z) = (1/7, \sqrt{\pi c})\ \exp[-(Z - Z_p)^2/c]$ with $c = 0.94$. Z_p refers to the most probable charge [1.90, 1.91]

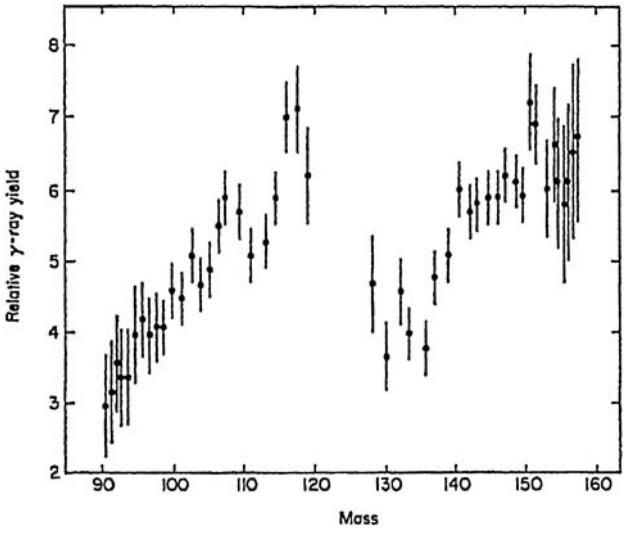

Fig. 1.12. Observed relative gamma-ray yields are shown as a function of fragment mass in the spontaneous fission of ^{252}Cf [1.85]

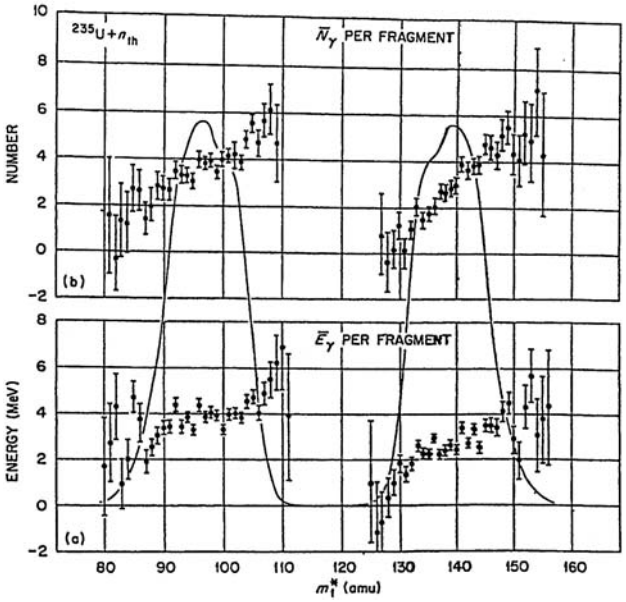

Fig. 1.13. Average number of gamma-rays emitted, Nγ and their total energy observed, $\overline{E}\gamma$ is plotted as a function of fragment atomic mass in the thermal neutron induced fission of ^{235}U [1.86]. The *solid* curve refers to observed mass spectrum

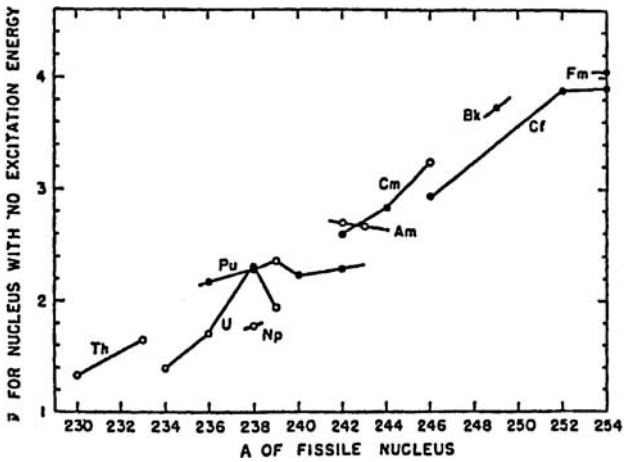

Fig. 1.14. Average number of prompt neutrons emitted is plotted as the mass number of parent nuclei [1.41]. *Solid* and *open* circles refer, respectively, to those observed in spontaneous and thermal neutron induced fission corrected for zero excitation

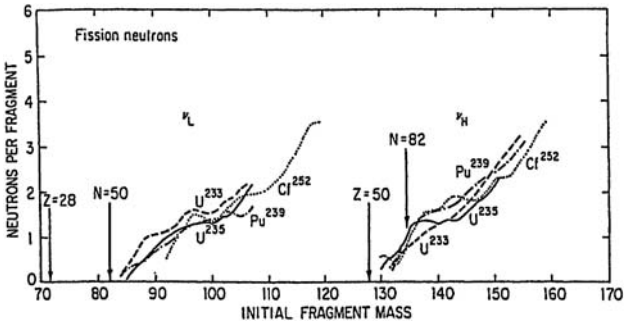

Fig. 1.15. Average numbers of neutrons emitted in the spontaneous fission of ^{252}Cf and thermal neutron induced fission of ^{233}U, ^{235}U and ^{239}Pu is plotted as a function of fragment mass number [1.47]

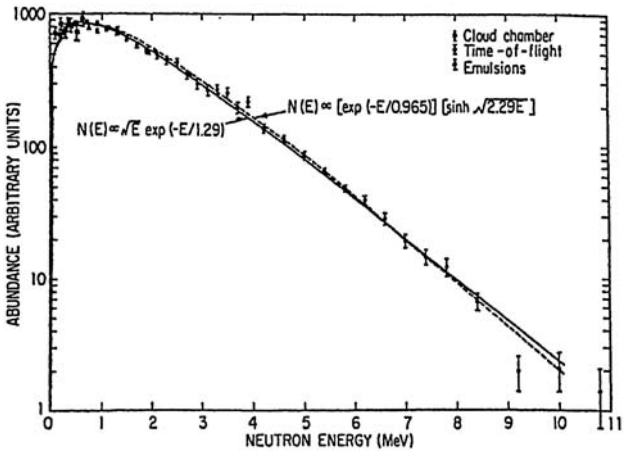

Fig. 1.16. Observed energy spectrum of emitted neutrons is compared to two theoretical functions [1.87]

1.7 Fission Isomers

In 1962 Polikanov et al. [1.54] in induced fission observed spontaneously fissioning nuclei with a very short partial half-life with a long partial gamma decay half-life. Since then, this phenomenon has been observed in many cases of induced fission and a list of such cases along with observed half-lives are presented in Table 1.2. The fissioning state lies usually a few MeV above the ground state. These have been interpreted as isomeric states lodged in the humps of the potential surface between the ground state and saddle point and referred to as shape isomers. Strutinsky's [1.55] investigation indicates that the shell structure of parent nuclei is responsible for producing these humps

Table 1.2. Half-lives of fission isomers from the compilation in [1.13]. Items marked $*$ are not well determined

Element	$T_{1/2}$(sec)	Element	$T_{1/2}$(sec)	Element	$T_{1/2}$(sec)
^{234}U	$*$			^{241}Cm	$(15 \pm 1) \times 10^{-9}$
^{235}U	$*$			^{242}Cm	180×10^{-9}
^{236}U	$(105 \pm 20) \times 10^{-9}$	^{237}Am	5×10^{-9}	^{243}Cm	$(42 \pm 5) \times 10^{-9}$
^{238}U	$(195 \pm 30) \times 10^{-9}$	^{238}Am	35×10^{-6}	^{244}Cm	$\geq 50 \times 10^{-9}$
		^{239}Am	$(160 \pm 40) \times 10^{-9}$	^{245}Cm	$(13 \pm 2) \times 10^{-9}$
^{235}Pu	$(30 \pm 5) \times 10^{-9}$	^{240}Am	$(0.91 \pm 0.07) \times 10^{-3}$		
^{236}Pu	$(34 \pm 8) \times 10^{-9}$	^{241}Am	$(1.5 \pm 0.6) \times 10^{-6}$	^{242}Bk	$(9.5 \pm 2.0) \times 10^{-9}$
					$(600 \pm 100) \times 10^{-9}$
^{237}Pu	$(82 \pm 8) \times 10^{-9}$	^{242}Am	$(14.0 \pm 0.4) \times 10^{-3}$	^{244}Bk	$(820 \pm 60) \times 10^{-9}$
	$(1120 \pm 80) \times 10^{-9}$				
^{238}Pu	$(6.5 \pm 1) \times 10^{-9}$			^{245}Bk	2×10^{-9}
	0.5×10^{-9}				
^{239}Pu	$(8 \pm 1) \times 10^{-6}$	^{243}Am	$(6 \pm 1) \times 10^{-6}$		
^{240}Pu	$(3.8 \pm 0.3) \times 10^{-9}$	^{244}Am	$(1.1 \pm 0.2) \times 10^{-3}$		
^{241}Pu	$(23 \pm 1) \times 10^{-9}$	^{245}Am	$(640 \pm 60) \times 10^{-9}$		
^{242}Pu	28×10^{-9}	^{246}Am	$(73 \pm 10) \times 10^{-6}$		
^{243}Pu	33×10^{-9}				

or pockets in the potential surface between the ground state configuration of a parent nucleus and the saddle point.

Extensive investigations of properties of these isomers have been made and reviewed in a number of articles [1.13, 1.56, 1.57]. The determination of exact excitation energies of these isomers is difficult and model-dependent but lies between 2 to 3 MeV for Pu, Am and Cm and there may be excited rotational states based on them [1.58].

The mass distribution and average kinetic energy associated with the fission of ^{236}U and its isomer have been found to be similar to those associated with the fission of the ground state by Fontenla and Fontenla [1.59] which was predicted by Hooshyar and Malik [1.60] about eight years earlier. Indication is that this may be the situation in other cases.

1.8 Cold Fission

In 1976, Hooshyar, Compani-Tabrizi and Malik's [1.61, 1.62] investigation raised the possibility of emission of unexcited and nearly unexcited daughter pairs in a fission process. Signarbieux et al. in 1981 [1.63] reported measuring daughter pairs with very little excitation energy. In fact, these pairs do not emit any neutrons because of insufficient available energy [1.63–1.66]. These processes, which are quite rare, are usually called cold fission or fragmentation.

These investigations have established the emission of cold fragments to be not a rare phenomenon but the yields of these fragments are less probable compared to the corresponding daughter pairs being emitted in excited states. The mass distribution of cold fragments covers the same mass range of daughters as that seen in normal fission. This is shown in Fig. 1.17. Measured excitation energies of these fragments range from nearly zero to 8 MeV in thermal neutron induced fission of ^{235}U. Similarly, there is also a charge distribution associated with the emission of cold fragments.

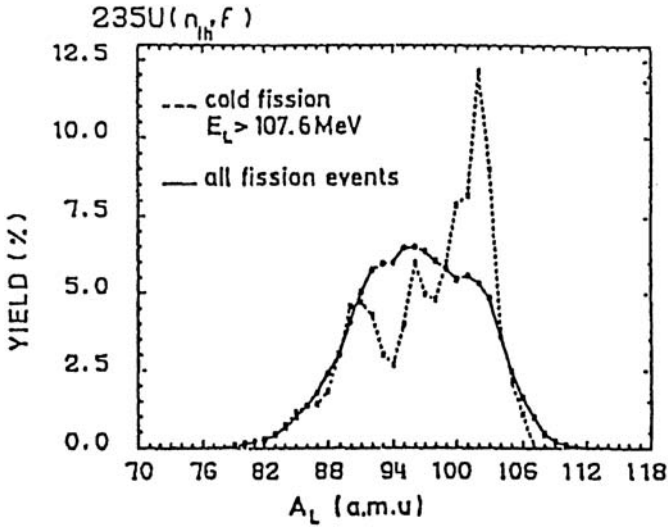

Fig. 1.17. Fragment mass distribution seen in cold fission product, noted as *dotted* line, is compared to those observed in normal fission product in thermal neutron induced fission of ^{235}U [1.93]

1.9 Cluster Radioactivity

In 1984, Rose and Jones [1.17] observed the emission of ^{14}C from ^{223}Ra. The emission of such clusters from other actinides was quickly confirmed in other laboratories [1.18–1.21]. The half-lives associated with this process are very long, ranging from 10^{11} to 10^{25} sec. The kinetic energies associated with the process are significantly lower than the corresponding Q-values which is also characteristic of spontaneous and induced fission. In Table 1.3, we present the emission of such clusters by parent nuclei from francium to curium, their observed kinetic energies, Q-values and half-lives. The understanding of cluster radioactivity in the context of the energy-density functional theory is discussed in Chap. 9.

Table 1.3. Columns 1 to 5 refer, respectively, to the cluster decay mode, the measured kinetic energy, the corresponding Q-values calculated from [1.78], logarithm of measured half-lives and references

Decay Mode	E_k(MeV)	Q-value (MeV)	Measured log T (sec)	Ref.
^{221}Fr → ^{14}C	29.28	31.28	>15.77	[1.21, 1.68]
^{221}Ra → ^{14}C	30.34	32.39	>14.35	[1.21, 1.68]
^{222}Ra → ^{14}C	30.97	33.05	11.0 ± 0.06	[1.21, 1.67]
^{223}Ra → ^{14}C	29.35	31.85	15.2 ± 0.05	[1.17–1.21]
^{224}Ra → ^{14}C	28.63	30.53	15.9 ± 0.12	[1.21]
^{225}Ac → ^{14}C	28.57	30.47	>18.64	[1.68]
^{226}Ra → ^{14}C	26.46	28.79	21.3 ± 0.2	[1.67, 1.68]
^{231}Pa → ^{23}F	46.68	51.84	>25.4	[1.69]
^{230}Th → ^{24}Ne	51.75	57.78	24.6 ± 0.07	[1.69]
^{232}Th → ^{26}Ne	49.70	55.98	>27.9	[1.70]
^{231}Pa → ^{24}Ne	54.14	60.42	23.4 ± 0.08	[1.69]
^{232}U → ^{24}Ne	55.86	62.31	20.5 ± 0.03	[1.71]
^{233}U → ^{24}Ne	54.27	60.50	24.8 ± 0.06	[1.72, 1.73]
^{233}U →^{25}Ne	54.32	60.84		[1.72, 1.73]
^{234}U → ^{24}Ne	52.81	58.84	25.9 ± 0.2	[1.74]
^{234}U →^{26}Ne	52.87	59.48		[1.74]
^{235}U → ^{24}Ne	51.50	57.36	>27.4	[1.78]
^{235}U →^{25}Ne	51.68	57.82		[1.78]
^{233}U → ^{28}Mg	65.32	74.24	>27.8	[1.78]
^{234}U → ^{28}Mg	65.26	74.13	25.7 ± 0.2	[1.74]
^{237}Np → ^{30}Mg	65.52	75.02	>27.4	[1.69]
^{236}Pu → ^{28}Mg	70.22	79.67	21.7 ± 0.3	[1.79]
^{238}Pu → ^{30}Mg	67.00	77.03	25.7 ± 0.25	[1.75]
^{238}Pu →^{28}Mg	67.32	75.93		[1.75]
^{238}Pu → ^{32}Si	78.95	91.21	25.3 ± 0.16	[1.75]
^{241}Am → ^{34}Si	80.60	93.84	>25.3	[1.69, 1.76, 1.77]
^{242}Cm → ^{34}Si	82.88	96.43	>21.5	[1.78, 1.79]

1.10 Pre-Amble

In the above sections, we have presented an overview of selected experimental data, among others, on spontaneous and particle-induced fission and cluster emission. This monograph deals with the theoretical understandings of a significant fraction of these data from the energy-density functional treatment of the fission and cluster emission dynamics. This theoretical approach allows one to investigate the nature of the potential energy surface caused by the reorganization of density distribution as well as the change in geometrical shape as a parent nucleus splits into a daughter pair. The exposition in Chap. 2 serves as a prelude to that goal by calculating nuclear masses with variable density distribution functions determined from experiments. This also implies that the nuclear masses have been determined with proper root mean

squared radii. The treatment in Chap. 3 to determine the potential energy surface in the fission process due to the change in geometry as well as the reorganization of density distributions is essentially an ab-initio calculation of the potential energy surface from a realistic two nucleon interaction in the local density approximation. The latter approximation allows one to determine energy per nucleon from a two nucleon potential at various densities of nuclear matter. The incorporation of variation of densities in the fission process changes the nature of the barrier between the saddle and scission points substantially from the one expected from models based on the liquid droplet approach.

An important aspect of the theories presented here is the emphasis on the use of observed kinetic energy in computing various observables, particularly half-lives in spontaneous fission, and the charge and mass distributions of emitted particles. The reason for this emphasis is dictated by the theorem, derived in Appendix A, relating kinetic energy and the general nature of the potential energy surface involved in defining the decay from a metastable state. The barriers computed in Chap. 3 and empirically proposed in Chap. 5 are compatible with this theorem and the analysis of the decay process compatible with observed kinetic energy presented in Appendix B.

The predictions of half-lives and mass distributions of daughter pairs in the spontaneous fission of ^{258}Fm and selected superheavy elements using the methodology of Chap. 3 are presented in Chap. 4. The predictions for superheavy elements, done almost three decades ago, are in line with experimental data so far.

In Chap. 6, the change in mass distribution and kinetic energy spectra with the variation of projectile energy in induced fission is investigated within the context of the empirical barrier of Chap. 5 using a statistical approach which is different from the one used by Fong [1.16]. The investigation leads to the understanding of the physical mechanism relating the distribution of available energy in the emission of a daughter pair between its kinetic and excitation energies. The theory enables one to determine quantitatively the most probable kinetic energy associated with the emission of a particular daughter pair. It allows a daughter pair to be emitted in all possible excited states including their ground states. This is, therefore, a pre-cursor of cold fission which has since been discovered and is discussed in detail in Chap. 7. The presentation in Chap. 7 also discusses a new phenomenon termed hot fission pointing out that the structure of the barrier, derived in Chap. 3 and proposed in Chap. 4, puts a limit on the distribution of available energy towards the excitation energies of a daughter pair which can not be emitted with zero kinetic energy.

The theorem derived in Appendix A presents a serious challenge to account for the half-lives observed in isomer fission with the appropriate kinetic energies. A coupled channel approach, presented in Chap. 8, to describe the fission process, which is an extension of the reaction theory presented in

Chap. 3, allows one to solve the difficulty. The mass distribution in isomer fission calculated using this theory has been confirmed by the measurement done eight years later. The diagonalization of the set of coupled channel equations under the conditions pertinent to the fission process is presented in Appendix C.

Cluster as well as alpha radioactivity fit into the general scheme of the theory presented herein, as discussed in Chap. 9. The barrier calculated for the emission of ^{14}C from ^{226}Ra within the context of the theory presented in Chap. 3 and the associated half-life with observed kinetic energy are presented in that chapter. The half-lives of the emission of a number of other clusters, calculated with the observed kinetic energy and not Q-values, within the context of an empirical barrier that is constructed to exhibit the salient features for the barrier obtained for ^{14}C emission from ^{226}Ra, agree well with the data. Similar calculations for alpha decays have also been presented and compared to the data. Thus, the phenomena of fission, alpha and cluster radioactivities are reasonably described by a unified approach.

References

1. F. Joliot and I. Curie. Compt. Rend. Acad. Sci. **198**, 254 (1934) and Nature, **133**, 201 (1934).
2. F. Joliot and I. Curie. Compt. Rend. Acad. Sci. **198**, 559 (1934).
3. E. Fermi. Ric. Scient. **5**, 283, 330 (1934).
4. E. Amaldi, O. D' Agostino, E. Fermi, F. Rassetti and E. Segré. Ric. Scient. **5**, 452 (1934).
5. E. Fermi, E. Amaldi, O. D'Agostino, F. Rassetti and E. Segré. Proc. Roy. Soc. (Lond.) **A 146**, 483 (1934).
6. E. Fermi. Nature, **133**, 898 (1934).
7. E. Fermi, F. Rasseti and O. D' Agostino. Ric. Scient. **5**, 533 (1934).
8. I. Noddack, Angew. Chem. **47**, 653 (1934).
9. O. Hahn, and F. Strassmann. Naturwiss., **27**, 11 (1939).
10. L. Meitner and O.R. Frisch. Nature **143**, 239 (1939).
11. K.A. Petrzhak and G.N. Flerov. Compt. Rend. Acad. Sci. (USSR) **28**, 500 (1940); Zh. Expt. Teo. Fiz. **3**, 275 (1940).
12. E. Segré, Phys. Rev. **86**, 21 (1952).
13. R. Vandenbosch and J.R. Huizenga. *Nuclear Fission* (Academic Press, New York, 1975).
14. E.K. Hyde, I. Perlman and G.T. Seaborg. *The Nuclear Properties of Heavy Elements* Vol. I and II (Prentice-Hall, 1964).
15. E.K. Hyde. *The Nuclear Properties of Heavy Elements.* Vol. 3 (Prentice Hall, 1964).
16. P. Fong, *Statistical Theory of Nuclear Fission* (Gordon and Breach, New York, 1969).
17. H.J. Rose and G.A. Jones. Nature **307**, 245 (1984).
18. S. Gales, E. Hourani, M. Hussonnois, H.P. Shapira and M. Vergnes. Phys. Rev. Lett. **53**, 759 (1984).

19. D.V. Alexandrov, A.F. Belyatsky, Yu.A. Glukov, F.Yu. Nikolsky, B.G. Novatsky, A.A. Oglobin and D.M. Stephanov. Pis'ma JETP **40**, 152 (1984).
20. W. Kutschera, I. Ahmad, S.G. Armato III, A.M. Friedman, J.E. Gindler, J.E. Henig, T. Issit, P. Paul and K.E. Rehm. Phys. Rev. C **32**, 2036 (1985).
21. P.B. Price, J.D. Stevenson, S.W. Barwick and H.L. Ravn. Phys. Rev. Lett. **54**, 297 (1985).
22. F. Gönnenwein, P. Jesinger, M. Mutterer, A.M. Gagarski, G.A. Petrov, W.H. Trzaska, V. Nesvishevsky and O. Zimmer. *Fission Dynamics of Clusters and Nuclei*, eds. J. da Providencia, D.M. Brink, F. Karpechine and F.B. Malik (World Scientific, 2001) p. 232.
23. H.L. Anderson, E. Fermi and A.V. Grosse. Phys. Rev. **59**, 52 (1941).
24. O.R. Frisch. Nature **143**, 276 (1939).
25. W. Jentschke and F. Prankl. Naturewissenschaften **27**, 134 (1939).
26. F. Joliot. Comp. Rend. **208**, 341, 647 (1939).
27. S. Katcoff, J.A. Miskel and C.W. Stanley. Phys. Rev. **74**, 631 (1948).
28. D.C. Brunton and G.C. Hanna. Cand. J. Res. **28A**, 190 (1950).
29. D.C. Brunton and W.B. Thompson. C and. J. Res. **28A**, 698 (1950).
30. K. Way and E.P. Wigner. Chicago Rep. cc-3032 (1945); Phys. Rev. **73**, 1318 (1948).
31. R.D. Present. Phys. Rev. **72**, 7 (1947).
32. L.E. Glendenin. M.I.T. Tech. Rep. No.35 (1949).
33. A.C. Wahl. *Atomic Data and Nuclear Data Tables*. **39**, 1 (1988).
34. A.C. Wahl. *50 Years with Nuclear Fission* eds. J.W. Behrens and A.D. Carlson (American Nuclear Society, U.S.A., 1989) p. 525.
35. K.F. Flynn, E.P. Horwitz, C.A.A. Bloomquist, R.F. Barnes, R.K. Sjoblom, P.R. Fields and L.E. Glendenin. Phys. Rev. C **5**, 1725 (1972).
36. T. Hagiwara. The Review of Physical Chemistry of Japan **13**, 145 (1939).
37. H.L. Anderson, E. Fermi and H.B. Hanstein. Phys. Rev. **55**, 797 (1939).
38. L. Szilard and W.H. Zinn. Phys. Rev. **55**, 799 (1939).
39. H.L. Anderson, E. Fermi and L. Szilard. Phys. Rev. **56**, 284 (1939).
40. J.S. Fraser. Phys. Rev. **88**, 536 (1952).
41. J.R. Huizenga and R. Vandenbosch. *Nuclear Reactions* Vol. II eds. P. M. Endt and P.B. Smith (North-Holland Publ. Amsterdam, 1962).
42. F. Reines, C.L. Cowan Jr., F.B. Harrison and R.E. Carter. Rev. Sci. Instr. **25**, 1061 (1954).
43. J.S. Fraser and J.C.D. Milton. Phys. Rev. **93**, 818 (1954).
44. J. Terrell. *Proc. IAEA Symp. Phys. Chem. Fission. Salzburg* (IAEA Publication, 1965) Vol. 2, p. 3.
45. B.C. Diven, D.S. Martin Jr., R.F. Taschek and J. Terrell. Phys. Rev. **101**, 1012 (1956).
46. S.L. Whetstone. Phys. Rev. **114**, 581 (1959).
47. J. Terrell. Phys. Rev. **127**, 880 (1962).
48. R.B. Leachman. Proc. Int. Conf. Peaceful Uses At. Energy (U.N. Publ.) **2**, 193 (1956).
49. B.E. Watt. Phys. Rev. **87**, 1037 (1952).
50. S.T. Tsien, Zah-wei Ho, R. Chastel and L. Vigneron. Comp. Rend. **223**, 1119 (1946), **224**, 272 (1947); Phys. Rev. **71**, 382 (1947).
51. H.W. Schmitt, J.H. Neiler, F.J. Walter and A. Chetham-Strode. Phys. Rev. Lett. **9**, 427 (1962).

52. S.L. Whetstone Jr. and T.D. Thomas. Phys. Rev. **154**, 1174 (1967).
53. G.M. Raisbeck and T.D. Thomas. Phys. Rev. **172**, 1272 (1968).
54. S.M. Polikanov, V.A. Druin, V.A. Karnaukov, V.L. Mikheev, A.A. Pleve, N.K. Skobelev, V.G. Subbotin, G.M. Ter-Akopyan and V.A. Fomichev. Soviet Physics, JETP **15**, 1016 (1962).
55. V.M. Strutinsky. Soviet J. Nucl. Phys. **3**, 449 (1966); Nucl. Phys. **A95**, 420 (1967) and **A122**, 1 (1968).
56. R. Vandenbosch. Ann. Rev. Nucl. Sci. **27**, 1 (1977) and *50 Years with Nuclear Fission*, eds. J.W. Behrens and A.D. Carlson (American Nuclear Society, La Grange Park, IL 60526, 1989) 161.
57. S. Bjornholm and J.E. Lynn. Rev. Mod. Phys. **52**, 725 (1980).
58. H. Weigmann. *50 Years with Nuclear Fission*, eds. J.W. Behrens and A.D. Carlson (American Nuclear Society, La Grange Park, IL 60526, 1989) 168.
59. C.A. Fontenla and D.P. Fontenla. Phys. Rev. Lett. **44**, 1200 (1980).
60. M.A. Hooshyar and F.B. Malik. Phys. Lett. B **38**, 495 (1972).
61. M.A. Hooshyar, B. Compani-Tabrizi and F.B. Malik. Proc. Int. Conf. Interaction Between Nucleons and Nuclei ed. E. Sheldon (U.S. Department of Commerce, Publ. CONF-760715-P1, 1976) 725.
62. B. Compani-Tabrizi. Ph.D. dissertation, Indiana University (1976).
63. C. Signarbieux, M. Montoya, N. Ribrag, C. Mazur, C. Guet, P. Perrin and M. Maurel. J. de Physique Lett. **42**, L437 (1981).
64. H.G. Clerc, W. Lang, M. Mutterer, C. Smith, J.P. Theobald, U. Quade, K. Rudolph, P. Armbruster, F. Gönnenwein, J. Schrader and D. Engelhart. Nucl. Phys. **A452**, 277 (1986).
65. M. Montoya. Zeit. Physik A **319**, 219 (1984).
66. F. Gönnenwein. *Frontier Topics in Nuclear Physics*, eds. W. Scheid and A. Sandulescu, (Plenum Press, 1994) p.113
67. E. Hourani, M Hussonnois, L. Stab, L. Brillard, S. Gales and J.P. Schapira. Phys Lett. B **160**, 375 (1985).
68. S.W. Barwick, P.B. Price, H.L. Ravn, E. Hourani and M. Hussonnois. Phys. Rev. C **34**, 362 (1986).
69. S.P. Tretyakova, A. Sandulescu, V.L. Micheev, D. Hasegan, I.A. Lebedev, Yu.S. Zamyatin, Yu.S. Korotkin and B.F. Myasoedov. JINR **13**, 34 (1985).
70. P.B. Price and S.W. Barwick, *Particle Emission from Nuclei* eds. D.N. Poenaru and M. Ivascu. Vol. II, (CRC Press (1988)).
71. S.W. Barwick, P.B. Price and J.D. Stevenson. Phys. Rev. C **31**, 1984 (1985).
72. S.P. Tretyakova, A. Sandulescu, V.L. Micheev, D. Hasegan, I.A. Lebedev, Yu.S. Zamyatin, Yu.S. Korotkin and B.F. Myasoedov. JINR Report **7**, 23 (1985).
73. S.W. Barwick. PhD Thesis, Univ. Calif., Berkley (1986).
74. S. Wang, P.B. Price, S.W. Barwick, K.J. Moody and E.K. Hulet. Phys Rev C **36**, 2717 (1987).
75. S. Wang, D. Snowden-Ifft, P.B. Price, K.J. Moody and E.K. Hulet. Phys Rev. C **39**, 1647 (1989).
76. K.J. Moody, E.K. Hulet, S. Wang, P.B. Price and S.W. Barwick. Phys Rev. C **36**, 2710 (1987).
77. M. Paul, I. Ahmad and W. Kutschera. Phys Rev. C **34**, 1980 (1986).
78. P.B. Price. *Clustering Phenomena in Atoms and Nuclei*, eds. M. Brenner, T. Lönnroth and F.B. Malik (Springer Verlag, 1993) p. 273.

79. M. Hussonnois, J.F. Le-Du, D. Trubert, R. Bonetti, A. Guglielmetti, S.P. Tretyakova, V.L. Micheev, A.N. Golovchenko, and V.A. Ponomarenko. *Pis'ma Zh. Eksp. Teor. Fiz.* **62**, 685 (1995).
80. A.A Oglobin, R. Bonetti, V.A. Denisov, A. Guglielmetti, M.G. Itkis, C. Mazzocchi, V.L. Micheev, Y.T. Oganessian, G.A. Pik-Pichak, G. Poli, S.M. Pirozhkov, V.M. Semochkin, V.A. Shigin, I.K. Shvetsov, S.P. Tretyakova. Phys. Rev. C **61**, 034301 (2000).
81. N.E. Holden, *50 Years with Nuclear Fission* eds. J. W. Behrens, and A.D. Carlson (American Nuclear Society, La Grange Park, IL 60525, 1989) 465.
82. D.J. Hughes and R.B. Schwartz. *Neutron Cross Sections*, Supp. No. 1, (Argon National Laboratory, Upton, New York, 1957).
83. S. Katcoff. Nucleonics **18**, 201 (1960).
84. H. W. Schmitt, J.H. Neiler and F.J. Walter. Phys. Rev. **141**, 1146 (1966).
85. S.A.E. Johansson. Nucl. Phys. **60**, 387 (1964).
86. F. Pleasonton, R.L. Ferguson and H.W. Schmitt. Phys. Rev. C **6**, 1023 (1972).
87. G. Frye, J.H. Gamel and L. Rosen. Los Alamos Report LA-1670 (1954) and L. Cranberg and N. Nereson, Los Alamos Report, LA-1916 (1955).
88. W.D. Myers and W.J. Swiatecki. Nucl. Phys. **81**, 1 (1966).
89. A.E.S. Green. Phys. Rev. **95**, 1006 (1954).
90. A.C. Wahl. J. Inorganic Nucl. Chem. **6**, 262 (1953).
91. A.C. Wahl, R.L. Ferguson, D.R. Nethaway, D.E. Troutner and K. Wolfsberg. Phys. Rev. **126**, 1112 (1962).
92. A.W. Wapstra and G. Audi. Nucl. Phys. A **432**, 1 (1985).
93. J. Throchon, G. Simon and C. Signarbieux. *50 Years with Nuclear Fission* eds. J. W. Behrens, and A.D. Carlson (American Nuclear Society, La Grange Park, IL 60525, 1989) p. 313
94. F.J. Shore and V.L. Sailor. Phys. Rev. **112**, 119 (1958).
95. K.E. Flynn, J.E. Gindler, R.K. Sjoblom, and L.E. Glendenin, Phys. Rev. C, **11**, 1676 (1975)

2 Energy-Density Functional Formalism and Nuclear Masses

2.1 Introduction

Nuclear masses are usually described by refined versions of Weisäcker's mass formula [2.1, 2.2], the latest version of which is described in [2.3]. The basic premise of this mass formula and its modern version is that the nuclear density distribution function is constant over its radial dimension, dropping abruptly to zero i.e. as in a liquid droplet. The liquid drop model of a nucleus has its root in the paper of Bohr and Kalcker [2.4] who postulated it to provide physical understanding of the occurrence of sharp resonances in thermal neutron scattering. Since the end of the Second World War, it has been reasonably established that the nuclear surface is not membrane-like which is characteristic of a liquid droplet, but that the central density of a nucleus, after remaining constant for a few femtometres, drops gradually to zero over a distance of about 2 to 3.0 fm [2.5,2.6]. One may estimate the fraction of nuclear matter located at the nuclear surface by approximating the observed density distribution by a trapezoidal function. This is a reasonable approximation to the observed density distribution function for medium and heavy nuclei and allows one to evaluate the integrals involved in determining the fraction of nuclear matter in different regions of a nucleus, analytically.

The trapezoidal density-distribution function shown in Fig. 2.1 may be represented by

$$\begin{array}{ll} \rho = \rho_0 & \text{for } r < c \\ \rho = \rho_0(d-r)/(d-c) & \text{for } c \le r \le d \\ \rho = 0 & \text{for } r > d \end{array} \tag{2.1}$$

The total number of nucleons in a nucleus, N(A), the number of nucleons in the constant density zone, N(o), and in the surface zone, N(s), are, respectively, given by the following expression

$$\mathrm{N(A)} = (\pi\rho_0/3)(c+d)(c^2+d^2) \tag{2.2a}$$

$$\mathrm{N(o)} = 4(\pi\rho_0/3)c^3 \tag{2.2b}$$

$$\mathrm{N(s)} = (\pi\rho_0/3)[(c+d)(c^2+d^2) - 4c^3]\ . \tag{2.2c}$$

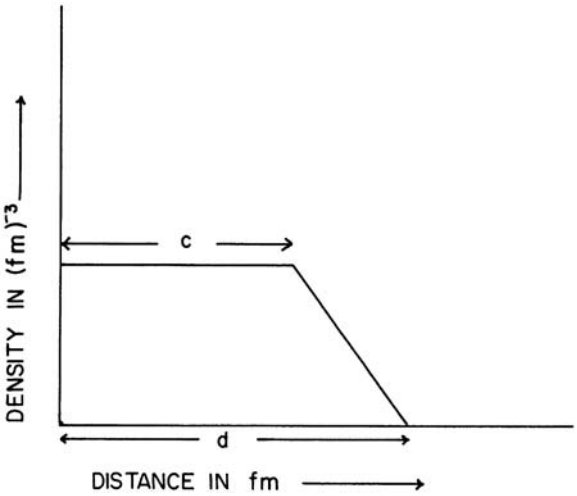

Fig. 2.1. A typical trapezoidal distribution for nuclear density given by (2.2a, 2.2b, 2.2c)

In Table 2.1, N(A), N(o), and N(s) are given in units of $(\pi\rho_0/3)$ for $c = 1.1A^{1/3}$ fm and $(d - c) = 2.5$ and 3 fm. which are typical values for realistic density distributions. Typically, approximately 40 to 50% of the nuclear mass resides in the surface zone i.e., at a density lower than the saturation density, a point already noted in [2.8, 2.9].

Table 2.1. Total number of nucleons, N(A), number of nucleons in the constant density interior, N(o) and number of nucleons in the surface region, N(s) in arbitrary units, for mass numbers A = 125 and 238. These are defined in (2.2a), (2.2b) and (2.2c). (d − c) is the surface region defined by (2.1)

A = Mass No.	(d − c) = 2.5 fm			(d − c) = 3.0 fm		
	N(A)	N(o)	N(s)	N(A)	N(o)	N(s)
125	1272	665	607	1435	666	769
238	2150	1267	883	2376	1267	1109

The ramification of a large fraction of nuclear matter residing in the nuclear surface region is that the formation of a low-density nuclear matter neck on the way to fission is very likely. Simple estimates done in [2.7] indicate that this low-density neck may affect the potential surface involved in fission significantly. Hence, its effect on the potential surface must be examined carefully. A first step towards that goal is to find an appropriate variation of the energy per nucleon with density of nuclear matter. This information may be obtained by developing a theory that accounts for observed nuclear masses

using experimentally determined density distributions because this requires the use of energy-densities at densities other than the saturation density. This is done in the next section within the framework of an energy-density functional approach.

2.2 The Energy-Density Functional for Nuclei

The energy-density functional formalism in nuclear physics has its roots in the Thomas-Fermi statistical approach to account for nuclear masses [2.10–2.13]. Hohenberg and Kohn's [2.14] observation that the total energy, $E[\rho]$, of the ground state of a Fermion system can always be expressed as a functional of its density, allows one to write the functional as follows:

$$E[\rho] = \int \varepsilon(\rho)\rho(\vec{r})d^3\vec{r} \tag{2.3}$$

where $\varepsilon(\rho)$ is the energy-density, i.e., energy per unit volume. If one writes ρ(r) in terms of wave functions, (2.3) may be considered equivalent to

$$\begin{aligned} E\left[\rho\right] &= \int d\vec{r}_1 \ldots . d\vec{r}_n \psi^*(\vec{r}_1, \vec{r}_2 \ldots \vec{r}_n)[\Sigma_i T(\vec{r}_i) \\ &\quad + \frac{1}{2}\Sigma_{i\neq j} v(\left|\vec{r}_i - \vec{r}_j\right|)]\psi(\vec{r}_1, \vec{r}_2 \ldots \vec{r}_n) \\ &\equiv \int d^3\vec{r}\psi^*(\vec{r})\left[T(r) + V(r)\right]\psi(\vec{r}) \end{aligned} \tag{2.4}$$

where $T(\vec{r})$ and $v(|\vec{r}_i - \vec{r}_j|)$ are, respectively, the single- nucleon kinetic energy operator and the two-nucleon potential. To seek an equivalent average energy per nucleon, $\varepsilon(\rho)$, one may resort to a statistical approach.

The first term on the right hand side of (2.4) is the total kinetic energy of the fermion system. One may calculate its contribution to the energy density $\varepsilon(\rho)$ for nuclear matter defined as a system of equal numbers of protons and neutrons having a density ρ which remains constant with the increase of both nucleon number, A and volume Ω. Because of the Pauli principle, only four nucleons, two protons and two neutrons having opposite spin may be put into a volume h^3. Hence the total number of nucleons, A, is given by

$$A = \int_0^{p_f} (4\Omega/h^3)4\pi p^2 dp = (16\pi\Omega/h^3)p_f^3/3\ . \tag{2.5}$$

In (2.5), Ω and p_f are, respectively the volume containing the nucleons and the highest available momentum called the Fermi-momentum. From (2.5) one obtains the relation between the density, ρ, of the system and the Fermi momentum:

$$p_f = \hbar k_f = h(3\rho/16\pi)^{1/3} \tag{2.6}$$

since ρ, the density is defined as

$$\rho = A/\Omega \, . \tag{2.7}$$

The maximum kinetic energy, E_f, called the Fermi energy is given by

$$E_f = p_f^2/2M = (h^2/2M)(3/16\pi)^{2/3}\rho^{2/3} \tag{2.8}$$

where M is the mass of a nucleon. The total kinetic energy of the system $\langle T \rangle$, is given by

$$\langle T \rangle = \int_0^{p_f} (4\Omega/h^3)(p^2/2M)4\pi p^2 dp = (3/5)E_f A \, . \tag{2.9}$$

Hence the kinetic energy per nucleon contributing to $\varepsilon(\rho)$ is

$$\langle T \rangle / A = (3/5)E_f = (3h^2/10M)(3/16\pi)^{2/3}\rho^{2/3} \, . \tag{2.10}$$

Thus, the contribution to the kinetic energy from the nucleons is proportional to $\rho^{2/3}$. Brueckner, Coon and Dabrowski [2.15] have extended this treatment to nucleonic matter having unequal numbers of protons and neutrons confined in a large volume and obtained the following density dependence of $T(\rho)$.

$$T(\rho) = C_1(\alpha)\rho^{2/3} \tag{2.11}$$

with

$$C_1(\alpha) = (3/5)(h^2/2M)(3\pi^2/2)^{2/3}(1/2)[(1-\alpha)^{5/3} + (1+\alpha)^{5/3}] \tag{2.12}$$

where $\alpha = (N - Z)/A$, is the neutron excess.

The second term of the right hand side of (2.4) represents the contribution of the interaction between nucleons to the energy-density $\varepsilon(\rho)$. $V(r)$ in (2.4) is the average self-consistent potential or mean field, generated by the mutual interaction among nucleons and in which each nucleon moves. For a smooth two-nucleon potential, the most important contribution may be computed in the Hartree-Fock approximation. The two-nucleon potential is, however, not smooth but has strong short range repulsion and may be evaluated from the K-matrices following the prescription of Brueckner and Levinson [2.16, 2.17]. The non-Coulomb part of the neutron and proton potential $V_n(\vec{k})$ and $V_p(\vec{k})$ acting on state k, are given by

$$\begin{aligned} V_n(\vec{k}) = &\sum\nolimits_{q<k_{nf}} [(\vec{k}\vec{q}|K_{nn}\,|\,\vec{k}\vec{q}) - \text{Exchange}] \\ &+ \sum\nolimits_{q<k_{pf}} (\vec{k}\vec{q}|K_{np}|\,\vec{k}\vec{q}) \end{aligned} \tag{2.13}$$

$$\begin{aligned} V_p(\vec{k}) = &\sum\nolimits_{q<k_{pf}} [(\vec{k}\vec{q}|K_{pp}|\,\vec{k}\vec{q}) - \text{Exchange}] \\ &+ \sum\nolimits_{q<k_{nf}} (\vec{k}\vec{q}|K_{np}|\,\vec{k}\vec{q}) \, . \end{aligned} \tag{2.14}$$

In the above, k_{nf} and k_{pf} are, respectively, neutron and proton Fermi momenta which are related to the nuclear matter Fermi momentum k_f by

$$k_{nf} = (1+\alpha)^{1/3} k_f \quad \text{and} \quad k_{pf} = (1-\alpha)^{1/3} k_f \ . \tag{2.15}$$

Brueckner, Coon and Dabrowski [2.15] have evaluated the average nuclear potential per nucleon, $V_{\rm nucl}(\rho)$ using the above procedure and the realistic two nucleon potential of Brueckner and Gammel [2.18]. The dependence of $V_{\rm nucl}(\rho)$ on α and ρ is shown in Fig. 2.2 and may be represented by the following function

$$V_{\rm nucl}(\rho) = b_1(1+a_1\alpha^2)\rho + b_2(1+a_2\alpha^2)\rho^{4/3} + b_3(1+a_3\alpha^2)\rho^{5/3} \tag{2.16}$$

where a_i and b_i (i = 1, 2, and 3) are appropriate constants, the values of which are noted later.

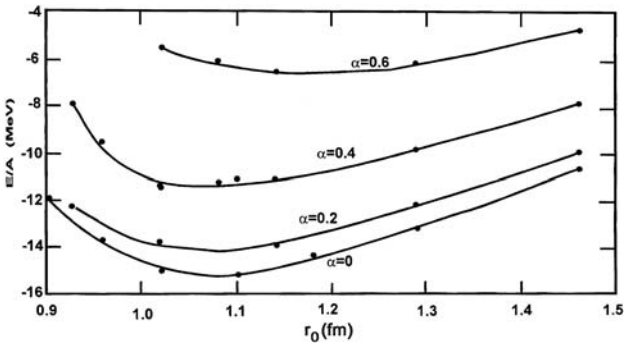

Fig. 2.2. Calculated energy per nucleon from [2.15] as a function of $r_0 = [(4/3)\pi\rho]^{-1/3}$ where ρ is the density for various values of the neutron excess parameter $\alpha = (N-Z)/A$. N, Z and A are the neutron, proton and atomic mass numbers, respectively. Dots are calculated points

In addition to the nuclear part of the potential, protons interact via the Coulomb potential. The Coulomb potential φ_c acting on a single proton from a charge distribution ρ_p is given by the following expression from classical electrodynamics:

$$\varphi_c = \frac{e}{2} \int d\vec{r}\,' \rho_p(r') / \left|\vec{r} - \vec{r}\,'\right| \tag{2.17}$$

The correction to (2.17) due to the Pauli principle among protons is approximately given by [2.19], namely $(-0.738 e^2 \rho_{\rm p}^{1/3})$.

The expressions (2.11) and (2.16) have been derived for a system of particles at a particular constant density distribution known as the local-density approximation. For a system having a variable density, $T(\rho)$ in the lowest

approximation, should include a term $(\nabla\rho)^2/\rho^2$ [2.1, 2.20]. The investigation of Brueckner, Buchler, Jorna and Lombard [2.21] indicates that a corrective term of the type $(\nabla\rho)^2/\rho$ is also necessary to approximately account for the correlation effect not included in $V_{\rm nucl}(\rho)$. Because of the many approximations involved in deducing both of these expressions, one may include in the energy-density only one of these two gradient terms with a multiplicative constant η in fm^3 to be determined from observed nuclear masses. Thus, the energy-density function $\varepsilon(\rho)$ is given by

$$\varepsilon(\rho) = C_1(\alpha)\rho^{2/3} + V_{\rm nucl}(\rho) + (1-\alpha)(e/2)\varphi_c \\ -(3/4)(3/\pi)^{1/3}e^2((1-\alpha)/2)\rho_p^{1/3} + \eta(\hbar^2/8M)(\nabla\rho)^2/\rho\,. \quad (2.18)$$

Brueckner, Buchler, Jorna and Lombard [2.21] have derived the appropriate coupled set of differential equations for the density by minimizing the total energy using (2.18) and solving it for ^{40}Ca. They found that a Fermi-like density distribution resulted for values of η from 5 to 15 fm^3 and obtained a binding energy of 364.3 MeV for $\eta = 6$ compared with the experimental value of 342.1 MeV.

Instead of solving the coupled differential equations, one may adopt an anzatz for the density function and determine its parameters by a variational method [2.21, 2.22]. The calculated binding energies, obtained using this procedure are noted in Table 2.2, and are in good agreement with the observed ones. They compare very well with those obtained from the standard mass formula based on the liquid drop model [2.23] which assumes a constant density distribution. However, the root mean squared radii as well as the surface thickness could not be reproduced with sufficient accuracy.

Table 2.2. Calculated binding energies in MeV using the energy-density functional method with an appropriate ansatz for the density function from [2.21]. Those marked B.E. (Thy.) obtained in [2.21] are compared to experimental data [2.24] shown in column 2 as B.E. (expt.) and also compared to those obtained from the Myers-Swiatecki liquid drop formula [2.23] without shell correction shown as B.E. (L. Drop) in the fourth column

Element	B.E. (expt) in MeV	B.E. (Thy) in MeV	B.E. (L. Drop) in MeV
^{16}O	128	121	120
^{40}Ca	342	339	339
^{48}Ca	416	414	415
^{116}Sn	989	987	994
^{140}Ce	1173	1168	1175
^{208}Pb	1637	1622	1620
^{246}Pu	1847	1845	1833

In an alternative approach, Reichstein and Malik [2.9] and their collaborators [2.24] have used the energy-density (2.18) along with the observed density distribution function using a fixed value of η determined from the best fit to the observed binding energies. Parameters a_i ($i = 1,\ 2,\ 3$) and b_i ($i = 1, 2, 3$) are obtained by fitting the calculated binding energy per nucleon of [2.15] and are given by

$$a_1 = -0.200, \quad a_2 = 0.316 \quad \text{and} \quad a_3 = 1.646 \tag{2.19a}$$

$$b_1 = -741.28, \quad b_2 = 1179.89 \quad \text{and} \quad b_3 = -467.54\ . \tag{2.19b}$$

In Table 2.3, calculated binding energies using $\eta = 8$ and observed density distribution functions [2.26] noted in column 2 are shown and are compared to the experimental binding energies given in column 5. The agreement is very good. Indeed, binding energy calculations were performed on 95 nuclei with parameters for the two parameter Fermi distribution, 24 nuclei with parameters for the three parameter Fermi distribution and 36 nuclei with parameters for the three parameter Gauss distribution. All parameters were taken from [2.26] and the results compared with the experimental values of [2.25]. The results for the 155 nuclei yielded an average difference of 1.5 percent per nucleus from the experimental values.

For many nuclei, the trapezoidal function is a very good approximation to the actual density distribution. The parameter d of this function determining the surface thickness and c, the range of the constant density zone are related to the half-density radius C and the surface thickness parameter t of the Fermi distribution by the relations

$$d = C + (5/8)t \quad \text{and} \quad c = C - (5/8)t\ . \tag{2.20}$$

The value of C_0, related to C by $C = C_0 A^{1/3}$, A being the mass number and the value of t that are compatible with electron scattering and μ-mesic atomic data are $C_0 = 1.07$ fm and $t = 2.4$ fm. In Table 2.3, we have also noted in column 4 the binding energies calculated using this trapezoidal distribution adjusting the values of a_i ($i = 1,\ 2,\ 3$) slightly i.e., taking $a_1 = -0.1933$, $a_2 = 0.3128$ and $a_3 = 1.715$ and for $\eta = 10.3$. This slight adjustment of a_i does not change in any significant way the calculated energy per nucleon versus density curve of [2.15]. The agreement with the data remains very good.

2.3 Conclusion

The importance of this analysis is that the energy-density (2.18) can account for the observed binding energies of nuclei with the observed density distribution function, a fact that cannot be achieved with mass formulae based on the

Table 2.3. Calculated binding energies using observed density distribution functions taken from [2.25]. Column 2 indicates whether the 2 parameter (2pf) or 3 parameter (3pf) Fermi function of [2.25] is used for Column 3 which shows calculated values of binding energies using the energy density function of (2.18) with $\eta = 8$. Column 4 shows calculated binding energies using a trapezoidal density distribution with $\eta = 10.3$. Experimental binding energies in Column 5 are from [2.24]

Element	Density Function	B.E. (Thy) MeV	B.E. (Thy. tr) MeV	B.E. (expt) MeV
^{12}C	2pf	92.5		92.2
^{16}O	3pf	125.2	123.3	127.6
^{19}F	2pf	149.2		147.8
^{24}Mg	3pf	194.5		198.3
^{32}S			270.1	271.8
^{28}Si	2pf	234.3		236.5
^{31}P	3pf	266.7		262.9
^{36}Ar	2pf	311.2		306.7
^{40}Ca	3pf	340.8	342.0	342.1
^{48}Ca			416.2	416.0
^{50}Cr	2pf	439.9		435.0
^{55}Mn	2pf	490.5		482.1
^{60}Ni			532.1	526.9
^{62}Ni	2pf	550.4		545.3
^{65}Cu	2pf	570.2		569.2
^{68}Zn	2pf	601.7		595.4
^{70}Ge	2pf	609.1		610.5
^{90}Zr			793.4	783.9
^{93}Nb	2pf	814.5		805.8
^{110}Pd	2pf	937.4		940.2
^{114}Cd	2pf	984.1		972.6
^{120}Sn	2pf	1033.2		1020.6
^{140}Ce			1181.8	1172.7
^{142}Nd	3pf	1188.5		1185.2
^{142}Ba			1185.7	1180.3
^{148}Sm	2pf	1229.6		1225.4
^{152}Sm	2pf	1268.4		1253.1
^{165}Ho			1356.1	1344.8
^{176}Yb	2pf	1450.9		1419.3
^{184}W	2pf	1470.3		1473.0
^{197}Au	2pf	1592.8		1559.4
^{206}Pb	2pf	1630.1		1622.3
^{208}Pb			1628.8	1636.5
^{238}U	2pf	1808.6	1811.0	1801.7

liquid drop model which assumes a constant density distribution for nuclei. Since a substantial fraction of nuclear matter resides at the nuclear surface where the density is lower than the saturation or central density, the ability to reproduce nuclear binding energies with observed density distribution functions implies that the energy-density functional approach can account for the energy per nucleon from the saturation to very low densities of nuclear matter reasonably. This, therefore, enables one to calculate binding energies of nuclear matter at densities different from the saturation density, involved in various configurations as a nucleus undergoes fission which is discussed in the next chapter.

The corrections to binding energies due to shell structure has also been considered within the framework of the energy-density functional [2.27], and are important only near zero separation and not for configurations close to the separation of the fission fragments shown by configuration E of Fig. 3.2.

References

1. C.F. von Weisäcker, Zeit. Physik **96**, 431 (1935); Naturwiss **27**, 133 (1939).
2. H.A. Bethe and R.F. Bacher, Rev. Mod. Phys. **8**, 193 (1936).
3. P. Möller, J.R. Nix, W.D. Myers and W.J. Swiatecki, At. Data Nucl. Data **59**, 185 (1995); *ibid.* **66**, 131 (1997).
4. N. Bohr and F. Kalcker, Kgl. Danske Videnskab. Selskab. Mat-Fys. Medd. **14**, No. 10 (1937).
5. R. Hofstader, Ann. Rev. Nucl. Sci. **7**, 231 (1957).
6. L.R.B. Elton, *Nuclear Sizes.* (Oxford University Press, 1961).
7. B. Block, J.W. Clark, M.D. High, R. Malmin and F.B. Malik, *Ann. Phys.* (N. Y.) **62**, 464 (1971).
8. F.B. Malik and I. Reichstein, *Clustering Phenomena in Atoms and Nuclei,* eds. Brenner, Lönnroth and Malik (Springer-Verlag, 1992) p. 126.
9. I. Reichstein and F.B. Malik, *Condensed Matter Theories* **8**, 243 (1993).
10. P. Gombas, *Ann. Physik* **10**, 253 (1952).
11. T.H.R. Skyrme, *Phil. Mag.* **1**, 1093 (1956).
12. L. Wilets, *Phys. Rev.* **101**, 201 (1956) and Rev. Mod. Phys. **30**, 542 (1958).
13. H. Bethe, *Phys. Rev.* **167**, 879 (1968).
14. P. Hohenberg and W. Kohn, *Phys. Rev.* **136**, B864 (1964).
15. K.A. Brueckner, S.A. Coon and J. Dabrowski, *Phys. Rev.* **168**, 1184 (1968).
16. K.A. Brueckner and C.A. Levinson, *Phys. Rev.* **97**, 1344 (1955).
17. K.A. Brueckner, *Phys. Rev.* **97**, 1353 (1955).
18. K.A. Brueckner and J.L. Gammel, Phys. Rev. **109**, 1023 (1958).
19. D.C. Peaslee, *Phys. Rev.* **95**, 717 (1959).
20. A.S. Kompaneets and E.S. Pavlovskii, *Zh. Eksperim. i Teor. Fiz.* **31**, 427 (1956) [Eng. transl. *Soviet Phys. JETP* **34**, 104 (1958)].
21. K.A. Brueckner, J.R. Buchler, S. Jorna and R.J. Lombard, *Phys. Rev.* **171**, 1188 (1968).
22. K.A. Brueckner, J.R. Buchler, R.C. Clarke and R.J. Lombard, *Phys. Rev.* **181**, 1543 (1969).

23. W.D. Myers and W.J. Swiatecki, *Nucl. Phys.* **81**, 1 (1966) and *Arkiv. Fysik* **36**, 343 (1947).
24. A.V. Pozdnyakov, I. Reichstein, Z.F. Shehadeh and F.B. Malik, *Condensed Matter Theories* **10**, 365(1995); I. Reichstein and F.B. Malik, Condense Matter Theories **15**, 283 (2000).
25. A.H. Wapstra and G. Audi, *Nucl. Phys.* **A 432**, 1 (1985).
26. H. de Vries, C.W. de Jager and C. de Vries, *Atomic Data and Nucl. Data,* **36**, 495 (1987).
27. R.J. Lombard, *Ann. Phys.* (N.Y.) **77**, 380 (1973).

3 The Decay Process, Fission Barrier, Half-Lives, and Mass Distributions in the Energy-Density-Functional Approach

3.1 Introduction

A typical density distribution function of a nucleus shown in Fig. 3.1 indicates that C, the half-density radius which is equal to about 1.07 $A^{1/3}$, A being the mass number, is about 6.6 fm for a nucleus near Uranium and t, the surface thickness parameter is between 2.4 to 3 fm. Thus, the surface of a typical nucleus is not that of a membrane as idealized in the usual liquid drop approach but extends to about 30% of the total radial dimension. Nucleons in the surface region, from 2.4 to 3.0 fm in extent, where the density drops from 90% to 10% of the central density, perceive a significantly different potential compared to those in the zone of central density. For a parent nucleus, in the process of undergoing fission to a daughter pair, this surface region prior to the scission point would allow the formation of a neck with nuclear matter of low density compared to that in the center of the nucleus. Potential energy surfaces for fission calculated using methods based on a liquid drop model of the nucleus assuming a constant density distribution [3.1, 3.2] do not usually allow for the formation of such necks of low nuclear matter. Aside from the formation of this neck of low density, the density distribution function of the parent nucleus undergoes substantial reorganization during the fission process since (a) the central density of the parent nucleus and daughter pairs are about the same and (b) the surface thickness of each nucleus is nearly the same. Taking this into consideration, the fission process is schematically depicted in Fig. 3.2. The situation A in Fig. 3.2 represents a parent nucleus, usually deformed, having nearly constant density marked by the solid central region that drops to zero over a range of 2.4 to 3.0 fm. This drop is represented by broken contour lines. The starting point of the substantial density reorganization is represented by the situation B which is probably near the saddle point. In order to arrive at the final state of the density distribution of the daughter pair, each member of which has a central and surface density similar to that of the parent, intermediate stages such as C and D are likely to emerge.

Subsequently, prior to scission, a configuration like E having a neck containing nuclear matter of density much lower than that of central density of a typical nucleus is likely to occur. The liquid-drop approach with its underlying assumption of a constant density distribution function cannot account

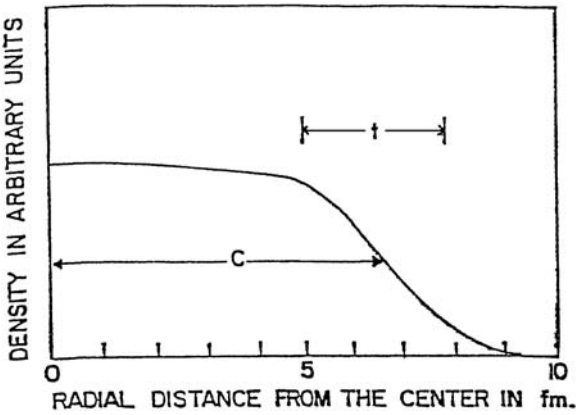

Fig. 3.1. A typical density distribution of a nucleus in the actinide region for $C = 1.07\ A^{1/3} (\cong 6$ fm for U) and $t \cong 3$ fm

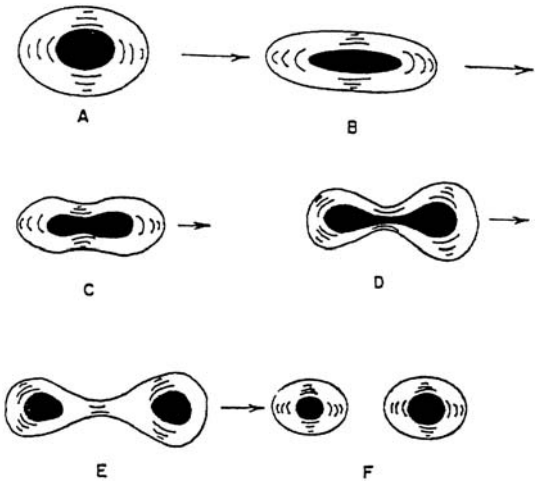

Fig. 3.2. Schematic description of the density reorganization taking place, as a nucleus fissions spontaneously into two fragments. The *black* central part represents the nearly constant high density region in the interior of a nucleus. The successively weaker contour lines show the density gradually dropping to zero. Configuration A represents the density distribution contours of a typical parent nucleus and F, that of a daughter pair. Configurations B, C, D, and E represent schematically the process of density reorganization on the way to fission

for the dynamics associated with configurations C to E. Thus, the Bohr and Wheeler theory [3.1, 3.2] of nuclear fission should be refined to incorporate present day knowledge of the nuclear density distribution function [3.3], out of which, configurations like C to E could occur.

In this chapter, energies of configurations A to E to the scission point will be calculated within the context of the energy-density functional theory using superposition of (a) two spherical and (b) two spheroidal geometries and using an appropriate density distribution function for a parent nucleus that undergoes changes to generate stages A through F. The potential energy surface for each of these configurations is calculated within the context of the energy-density functional theory formulated by Brueckner et al. [3.4, 3.5] but using the adiabatic approximation of Reichstein and Malik [3.6] suitably modified for the fission cases [3.7, 3.8].

That the use of a variable Fermi-like density distribution function, as opposed to a constant density distribution function assumed in the liquid drop model, might significantly affect the potential energy surface between the saddle and scission points is evident from the initial estimation done by Block et al. [3.9]. Their investigation indicates that the use of Fermi-like density distribution functions is likely to result in an additional external barrier between the saddle and scission points and change the potential energy surface by a few tens of MeV. This initial estimation, however, used a simple model and did not consider the Coulomb potential. But the later, more detailed investigations incorporating the Coulomb potential within the context of the energy-density functional theory, where the change in half-density and surface thickness parameters c and t, as a parent nucleus undergoes fission, are determined using a variational method, confirm the existence of such a barrier [3.7, 3.8].

Apart from including the appropriate density distribution function in calculating the potential energy surface, this treatment of the fission process is based on the observation that the masses of the daughter pairs associated with the decay of a parent nucleus are neither symmetric nor asymmetric but exhibit a mass distribution. In other words, nuclei of various types commensurate with mass, charge and energy conservation are emitted in a fission process. In the spontaneous fission of the actinides, this mass distribution is peaked toward a mass splitting of (1/3) to (2/3) of the mass numbers of the parent. This is known as asymmetric fission. In the fission of many of the Fermium isotopes, however, this mass distribution peaks towards symmetric fission i.e. near one half of the mass number of the parent nucleus. Apart from the mass distribution, one has, in many cases, information on the average kinetic energy, TKE, associated with a particular decay mode. Typically, these are about 10–25 MeV less than the related Q-value implying that daughter pairs are predominantly emitted in excited states and not in ground states. Moreover, the positive nature of the Q-values indicate that parent nuclei exist in metastable states, which, at a given time, could be generated by superposing wave functions of various daughter pairs. The overlap of the wave function of a particular daughter pair with that of the parent's, therefore, is a determining factor in deciding the decay probability of the parent nucleus to a particular decay mode. The total decay probability to that particular

daughter pair further depends on the penetration probability through the barrier relevant for that pair. The latter part has as antecedents the resonating group model [3.10], the unified reaction theory of Feshbach [3.11] and the reaction theory developed in [3.12–3.14]. In the next sections, we first present the theoretical premise of the theory, followed by sections dealing with quantitative estimation of the pre-formation probabilities of a daughter pair, computation of the barrier using the energy-density functional approach, actual calculations of mass-distribution, and half-lives of some actinides.

3.2 Theory

3.2.1 Expression for the Fission Decay Probability

As noted in [3.9], fission is viewed as a two-step process. The first is the reorganization of the nucleons of a parent nucleus into states relevant to various decay modes characterized by the asymptotic masses and excitation energies of the final daughter pairs. The second is the tunneling of these final daughter pairs through a barrier determined by their mutual interaction. The latter is determined using the energy-density functional approach.

The wave function $\Theta_m(1,\ 2 \ldots A-1,\ A)$ of the meta-stable parent nucleus in state m containing A nucleons whose coordinates are denoted by $(1,\ 2 \ldots A-1,\ A)$ may be expanded in a complete orthonormal set Ψ_n,

$$\Theta_m(1, 2 \ldots A-1, A) = \Sigma_n A_{mn} \Psi_n(1, 2 \ldots A-1, A)\ . \tag{3.1}$$

The expansion coefficient A_{mn} is then given by:

$$A_{mn} = (\Theta_m, \Psi_n)\ . \tag{3.2}$$

The integration in (3.2) is over all coordinates $(1,\ 2 \ldots A-1,\ A)$.

In the expansion (3.1), the wave functions Θ_m and Ψ_n are defined by two different Hamiltonians. Θ_m, the wave function of the parent nucleus A in the state m, is defined by the total Hamiltonian describing A, whereas Ψ_n represents the eigenstate n of the sum of the two Hamiltonians each representing intrinsic states of each member of a daughter pair. Thus, the latter does not include interaction between each member of a daughter pair. The coefficient A_{mn} is the probability amplitude of finding a given configuration, n, of a daughter pair in a well-defined configuration, m, of the parent nucleus. In the strictest sense, since the parent nucleus is in a meta-stable state, A_{mn} is a function of time, t. However, spontaneous fission, being a slow process in the time scale, A_{mn} may be considered to be time independent.

The coordinate arguments of both wave functions in (3.1) are supposed to be defined with respect to the same frame of reference. In reality however, the properties of a daughter pair are most conveniently described in terms of their intrinsic wave function defined with their respective centers of mass

in conjunction with a wave function having R, the relative location of their respective centers of mass, as a variable.

To achieve this, one may expand Ψ_n in terms of an orthonormal set consisting of a function $f_{n\alpha}(\mathbf{R})$ involving the relative coordinate and $\Phi_{n\alpha}$ involving intrinsic coordinates$(1', 2' \ldots (A-1)', A')$ measured with respect to the center of mass of each member of a daughter pair. Thus,

$$\Psi_n = \sum_{\alpha} f_{n\alpha}(\mathbf{R})\Phi_{n\alpha}(1', 2' \ldots (A-1)', A') \; . \tag{3.3}$$

The total Hamiltonian, H, may now be expressed in terms of R and the intrinsic coordinates

$$H = -\big(\hbar^2/2m\big)\nabla_R{}^2 + H_0(1', 2' \ldots (A-1)', A') + H_{\text{int}}(\mathbf{R}, 1', 2' \ldots (A-1)', A') \tag{3.4}$$

$\Phi_{n\alpha}$ is the eigenfunction of H_0, which is taken to be the sum of the following two intrinsic Hamiltonians of a daughter pair

$$H_0(1', 2' \ldots i') + H_0((i+1)' \ldots (A-1)', A') \; . \tag{3.5}$$

Using the resonating group procedure [3.10, 3.15, 3.16], one may now obtain the following set of coupled integro-differential equations for $\Phi_{n\alpha}$ $(\mathbf{R})$:

$$\begin{aligned}[-(\hbar^2/2m)\nabla_R^2 + k_{n\alpha}^2 + V_{n\alpha\alpha}(\mathbf{R}) + K_{n\alpha\alpha}(\mathbf{R})]f_{n\alpha}(\mathbf{R}) \\ = \Sigma_{\beta\alpha}[V_{n\alpha\beta}(\mathbf{R})f_{n\beta}(\mathbf{R}) + K_{n\alpha\beta}(\mathbf{R})f_{n\beta}(\mathbf{R})] \; .\end{aligned} \tag{3.6}$$

In (3.6) $V_{n\alpha\beta}(\mathbf{R})$ is the following scalar product:

$$(\Phi_{n\alpha}(1', 2' \ldots (A-1)', A'), H_{\text{int}}\Phi_{n\beta}(1', 2' \ldots (A-1)', A')) \; ,$$

$k_{n\alpha}$ is the wave number associated with a given channel $(n\alpha)$ and is equal to $(2m/\hbar^2)(E_n - E_{n\alpha})$, where E_n and $E_{n\alpha}$ are energy-eigenvalues of (3.4) and (3.5), respectively. $K_{n\alpha\beta}$ is a non-local potential such that $K_{n\alpha\beta}$ $(\mathbf{R})$ $f_{n\beta}$ $(\mathbf{R}) = \int d\ \mathbf{R}' K_{n\alpha\beta}$ $(\mathbf{R},\ \mathbf{R}')$ $f_{n\beta}$ $(\mathbf{R}')$, originating from the Pauli exclusion principal between nucleons of the same type in two members of a daughter pair.

The solution of (3.6) pertinent to fission in channel $(n\alpha)$ corresponds to finding a solution with the following asymptotic condition:

$$\lim_{|R|\to\infty} f_{n\alpha}(\mathbf{R}) = f_{n\alpha}(\theta, \varphi) \exp(ik_{n\alpha}R - i\eta \log 2k_{n\alpha}R)/R \; . \tag{3.7}$$

In denoting the boundary condition (3.7), due consideration has been given to the fact that the two members of a daughter pair interact asymptotically with a Coulomb potential given by $Z_1 Z_2 e^2/\hbar v \equiv \eta$ where Z_1 and Z_2 are the atomic numbers of each member of a daughter pair and v, their relative velocity. The fission amplitude $f_{n\alpha}(\theta, \varphi)$ is given by the following expression [3.16]:

$$f_{n\alpha}(\theta,\varphi) = -(1/4\pi)\int d\,\mathbf{R}' \exp(-ik_{n\alpha}\,\hat{e}\cdot\mathbf{R}' - i\eta\log 2k_{n\alpha}(\hat{e}\cdot\mathbf{R}')] \times \left[\sum_{\alpha\beta} {V^N}_{n\alpha\beta} + {K^N}_{n\alpha\beta}\right] f_{n\alpha}(\mathbf{R}')\ , \tag{3.8}$$

$\hat{e}$ in (3.8) is a unit vector in the direction (θ,φ) and ${V^N}_{n\alpha\beta}$ and ${K^N}_{n\alpha\beta}$ refer to the non-Coulombic part of the interaction in (3.6), i.e. it includes only the nuclear part of the matrix elements of the potential.

The equation (3.6) is also valid for $F_{mn\alpha} = A_{mn} f_{n\alpha}\ (\mathbf{R})$. Requiring a solution for $F_{mn\alpha}$ with the following asymptotic form:

$$\lim_{|R|\to\infty} F_{mn\alpha} = F_{mn\alpha}(\theta,\varphi)\exp(ik_{n\alpha}R - i\eta\log 2k_{n\alpha}R)/R\ , \tag{3.9}$$

one obtains the following expression for fission amplitude:

$$F_{m\alpha}(\theta,\varphi) = \Sigma_n A_{mn}\, f_{n\alpha}(\theta,\varphi)\ . \tag{3.10}$$

The fission differential cross section for a parent nucleus in state, m, to a daughter pair in state, n, with asymptotic kinetic energy $k^2_{n\alpha}$ is given by

$$\left|\sum_n A_{mn} f_{n\alpha}(\theta,\varphi)\right|^2\ . \tag{3.11}$$

In case, there is only one single dominant channel n, one may consider only one term in the summation and hence, the fission probability from a parent in state m to a daughter pair in state, n, is given by

$$|A_{mn} f_{n\alpha}(\theta,\varphi)|^2\ . \tag{3.12}$$

In (3.12), $|A_{mn}|^2$ represents the probability of the overlap of the wave function of a particular daughter pair in the wave function of the parent, henceforth denoted as the pre-formation probability. The determination of the pre-formation probability is discussed in the next section. $f_{n\alpha}(\theta,\varphi)$ is the fission amplitude which can be calculated once the potential between a daughter pair is known. This potential energy surface has been calculated subsequently in section 3, using energy-density-functional theory and exhibits a non-monotonic barrier. Thus, $|f_{n\alpha}(\theta,\varphi)|^2$ is the barrier penetration probability. Hence, (3.12) may be written as:

$$\begin{aligned}&\text{(fission probability)} = \text{(pre-formation probability)}\\ &\times\text{(penetration probability through the potential between a daughter pair)}\end{aligned} \tag{3.13}$$

The barrier pertinent to the penetration, in this approximation, is given by $V_{n\alpha\alpha}\ (\mathbf{R}) + K_{n\alpha}(\mathbf{R})$ which will be calculated using the energy-density functional approach. The determination of pre-formation probability is discussed in the next section.

3.2.2 Determination of the Pre-Formation Probability

The determination of the preformation probability requires knowledge of the wave functions of both the parent and the daughter pair. The daughter pairs are usually in excited states capable of emitting neutrons and gamma rays. Whereas, the detailed description of such excited states is complex the basic premise that nucleons in their nuclei move in a shell model type of potential holds. In the first approximation, the same holds for nucleons in the ground state of a parent nucleus. To the extent that only an approximate knowledge of the preformation probability is sufficient in determining the half-lives within a factor of two or three, it is sufficient to estimate it using the elementary shell model, particularly for the decay of an even-even nucleus to even-even daughter pairs where, as discussed below, the consideration of the residual interaction among the nucleons is unlikely to alter this substantially. On the other hand, for the decay of an odd-even or even-odd nucleus, the residual interaction may affect the computation of the pre-formation probability by a couple of orders of magnitudes. For the estimation of the preformation probability in the decay of an even-even nucleus to an even-even daughter pair both the parent configuration and the daughter wave function are in the first approximation considered to be a simple product of harmonic oscillator wave functions $\varphi_i(\mathbf{r}_i)$ but each with a different oscillator frequency v and v' since the latter, as is well known, depends on mass numbers. Thus,

$$\Psi_m \cong \prod_{i=1}^{A} \varphi_i(\mathbf{r}_i) = \prod_{i=1}^{A} \frac{R_{n_i l_i}(vr_i)}{r_i} Y_{l_i m_i}(\theta_i \varphi_i) x_{s_i}(\sigma_i) \ . \tag{3.14}$$

$R_{n_i l_i}(vr_i)/r_i$, $Y_{l_i m_i}(\theta_i \varphi_i)$ and $x_{s_i}(\sigma_i)$ are, respectively, the radial, normalized spherical harmonic and spin function of the orbital $\varphi_i(\mathrm{r}_i)$ For an isotropic harmonic oscillator, r times the radial wave function is given by,

$$R_{nl}(vr) = \sqrt{\frac{2(2v)^{l+3/2}(n-1)!}{[\Gamma(n+l+\frac{1}{2})]^3}} r^{l+1} e^{-vr^2} L_{n+l-\frac{1}{2}}^{l+\frac{1}{2}}(2vr^2) \ , \tag{3.15}$$

L_k^m in (3.15) is an associated Laguerre polynomial.

The wave function of a daughter pair is also a product of harmonic oscillator functions but v is replaced by v'.

$$\Phi_n = \prod_{i=1}^{A} (R_{n_i l_i}(v' r_i)/r_i) Y_{l_i m_i}(\theta_i, \varphi_i) x_{s_i}(\sigma_i) \ . \tag{3.16}$$

The overlap integral between (3.14) and (3.16) is non-zero only for the cases where spin and spherical harmonic functions are identical. To compute the overlap of the radial wave functions, we first examine the typical configurations involved, e.g., in the fission of a typical actinide ^{234}U. The proton and neutron configurations in ^{234}U are the following:

$$\text{Proton Configuration} : (1s_{1/2})^2\ (1p_{3/2})^4\ (1p_{1/2})^2\ (1d_{5/2})^6\ (2s_{1/2})^2\ (1d_{3/2})^4 \times(1f_{7/2})^8\ (2p_{3/2})^4\ (2p_{1/2})^2\ (1f_{5/2})^6\ (1g_{9/2})^{10}\ (2d_{5/2})^6\ (1g_{7/2})^8\ (3s_{1/2})^2 \times(2d_{3/2})^4\ (1h_{11/2})^{12}\ (2f_{1/2})^8\ (1h_{9/2})^2 \tag{3.17}$$

Neutron configuration: proton configuration plus

$$(1h_{9/2})^8(3p_{3/2})^4(2f_{5/2})^6(3p_{1/2})^2(1i_{13/2})^{14}(2g_{9/2})^{10}(1i_{11/2})^6\ . \tag{3.18}$$

Noting that the main radial quantum number, n, in (3.17) and (3.18) is 1, 2, and 3, the overlap factor, A_{mn}, may be calculated from the following results, where $m = v/v'$ [3.9]

$$I_{11} = \int_0^\infty R_{1l}(vr)R_{1l}(v'r)dr = [2\sqrt{m}/(1+m)]^{l+3/2} \tag{3.19}$$

$$I_{22} = \int_0^\infty R_{2l}(vr)R_{2l}(v'r)dr = I_{11}\left[\frac{2m}{(1+m)^2}(2l+5) - \frac{2l+3}{2}\right], \tag{3.20}$$

$$\begin{aligned} I_{33} &= \int_0^\infty R_{3l}(vr)R_{3l}(v'r)dr \\ &= I_{11}\left[(2l+5)(2l+3)\left\{-\frac{3}{8} + \frac{1}{2}\frac{1+m^2+4m(2l+5)/(2l+3)}{(1+m)^2}\right.\right. \\ &\quad \left.\left. - \frac{2(2l+5)(2l+7)m}{(1+m)^2} + \frac{2(2l+7)(2l+9)m^2}{(1+m)^4}\right\}\right]\ . \end{aligned} \tag{3.21}$$

One may note that for $m = 1$, $I_{11} = I_{22} = \mathrm{I}_{33} = 1$, as it should be.

Frequencies v and v' can be computed from the knowledge of nucleon separation energy using [3.17].

The observed nucleon-separation energy, S_n, in ^{234}U is 6.8 MeV [3.17]. This leads to $\hbar v = 6.255$ MeV. The nucleon-separation energy $S_n{}'$ in a daughter pair is likely to lie between 1 and 6 MeV for neutron rich isotopes. However, noting that the daughter pair, immediate after scission should be excited enough to emit neutrons, $S_n{}'$ must be low and is taken to be about 2 MeV. This yields $\hbar v' \cong 7.30$ MeV. Using v and v' from these, one obtains $A_{mn} \cong 4 \times 10^{-3}$. Hence,

$$\text{Pre-formation probability} \cong 1.6 \times 10^{-5}\ . \tag{3.22}$$

This pre-formation probability is not expected to change substantially in the spontaneous fission of the neighboring even-even nuclei since the addition or subtraction of a few orbitals to (3.17) and (3.18) does not affect the calculation in a significant way. This holds also for the decay of odd-nuclei.

One may easily estimate the range of values allowed for A_{mn}. Obviously, the maximum is one when $v = v'$. However, noting that similar calculations for alpha-decay has led to a value of about 10^{-2} [3.18, 3.19], the realistic maximum is 10^{-2}. The minimum value corresponds to zero separation energy in a daughter pair i.e. $S_n{}' = 0$. The corresponding A_{mn} is about 0.4×10^{-3}. Thus, the lowest limit of the pre-formation probability is 0.16×10^{-6}.

3.2.3 The Influence of the Residual Interaction on the Pre-Formation Probability

An appropriate way to investigate the influence of incorporating the residual interaction among nucleons on the calculation of A_{mn} is to consider the pairing model [3.20–3.22] of nuclei where the nucleons, aside from moving in a harmonic oscillator potential, interact with a pairing potential. Actual calculations indicate that the inclusion of a pairing interaction does not significantly change the value of the overlap integral, which is essentially A_{mn}, for even-even nuclei. Thus, the value of A_{mn} calculated in the proceeding section, is not likely to change substantially for the decay of even-even nuclei to even-even daughter pairs.

However, the spontaneous decay half-lives of odd-even nuclei differ from their neighboring even-even nuclei by a factor of about 10^3. This is similar to the situation in alpha-decay where the difference is about 10^2. In the case of alpha-decay, this difference is attributed to the difference in the wave-function due to residual interaction of a pairing type [3.18, 3.19]. Similar reasoning is applicable to the fission case [3.9].

In terms of the elementary shell model, one does not expect any significant difference between the wave functions of an even (refers to neutron)-even (refers to proton) parent nucleus and to the even-even core of the neighboring odd-even isotopes. However, the inclusion of the pairing interaction [3.20,3.21] could significantly alter the even-even core wave function of the odd-even isotope from its neighboring even-even nuclei. This is illustrated in Fig. 3.3, the upper part of which represents the configuration of odd-numbers of neutrons in an odd-even parent nucleus. In case, the pairing interaction among the neutrons occupying all but the last orbital is turned on, the new core wave function involves summation over all unoccupied states, which now is to exclude the last occupied orbital. This would not have been the case for an even-even neighbor. This effect, known as the blocking effect, significantly alters the wave function of the even-even core of an odd-even nucleus from the wave functions of its neighboring even-even nuclei.

Neutron configurations of a daughter pair emanating from the odd-even parent nucleus shown in the upper insert, are represented by (a), (b), (c), and (d) configurations in the lower insert of Fig. 3.3. The most unfavored of these configurations is (d) because (i) it costs about 1 to 2 MeV to break a pair and (ii) the neutron configurations of both partners being odd, result in a double-blocking effect. Thus, the pair breaking configuration (d) has a

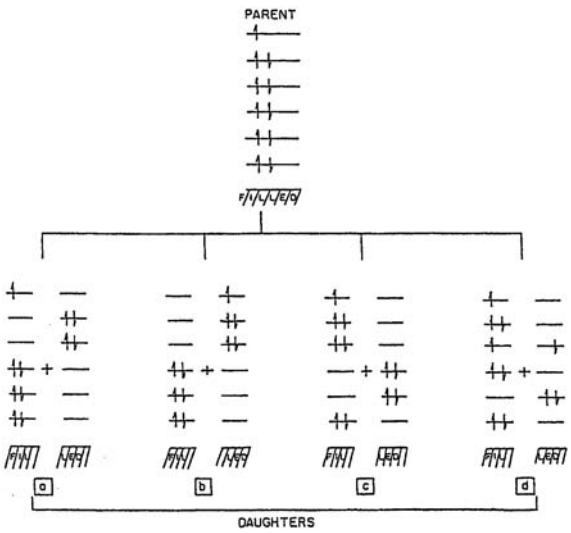

Fig. 3.3. Schematic representation of different decay configurations of an odd-N-even-Z nucleus. Only odd neutrons are considered. But for the last odd neutron, other neutrons are paired off in the parent and in (**a**), (**b**), and (**c**) types of daughter configurations. In (**d**) type, there are three unpaired neutrons. In the parent nucleus the core wave function is now influenced by the blocking effect because of the close proximity of the blocked level of the unpaired nucleon, and may, therefore, be somewhat different from its two even-even neighbors. (**a**), (**b**), (**c**), and (**d**) are typical configurations of various daughter modes. (**d**) types of configurations are unfavored because of the pair breaking and of the double blocking effect. The blocking effect in (**a**), (**b**), and (**d**) types of configuration is expected to be less pronounced than in the case of the parent configuration

considerably different overlap with the wave function of the parent and is unfavored.

The blocking effect in configurations (a), (b) and (c) is considerably less than that in the parent since, in the case of (a), the blocked state is energetically much higher, and in the case of (b) and (c), the even-even particles could scatter into unoccupied holes or particle states. As a result, the overlap integral of the daughter states with that of the odd-even parent differs significantly from the decay of a neighboring even-even isotope to an even-even daughter pair. In the case of alpha-decay this difference is about 10^2 and hence, it is reasonable to expect at least a factor of 10^2 difference in the pre-formation calculation in the fission of an odd-even and its neighboring even-even isotopes. The pre-formation probability, $|A_{mn}|^2$ in the fission of an odd-even nucleus is at least smaller than that of its even-even neighbor by about two orders of magnitude. Because of this difference in the pre-formation probability, the half-lives for the spontaneous fission of odd-parent nuclei is

always expected to be two to three orders of magnitude longer than those in the neighboring nuclei. Experimentally this is the case [see Table 1.1].

The blocking effect is expected to influence the calculation of the pre-formation probability in the spontaneous fission of odd-odd nuclei from those of their even-even and odd-even neighbors in a systematic way. However, the understanding of low-lying spectra of these odd-even nuclei indicates that the residual interaction between the valence odd neutron and proton plays an important role. This makes it more difficult to do a qualitative argument in determining the difference in the pre-formation probability in spontaneous decay of odd-odd nuclei from those of their even-even or even-odd neighbors.

3.3 Calculation of the Potential Energy Surface and Half-Lives

In determining the potential energy surface through which a particular daughter pair is to penetrate after being preformed, we follow closely the theory discussed in [3.7,3.8]. A parent nucleus, in the process of fissioning, is expected to pass through various configurations depicted in Fig. 3.2. In the usual theory of Bohr and Wheeler [3.1,3.2] and its various versions based on the basic premises of Bohr and Wheeler's theory [3.24,3.25], the key assumption is that the nuclear density distribution function is basically constant as a function of nuclear radius, dropping sharply to zero at the surface. Strutinsky's attempt to incorporate the effect of shell correction [3.26] does not change this basic premise of the Bohr-Wheeler theory. For a constant density distribution, computation of energies of various configurations involves basically a change of the shape of a parent nucleus resulting in a competition between the change of Coulomb and surface energies due to the change in geometry only. However, the actual nuclear density distribution function is closer to a two or three point Fermi function [3.26,3.30,3.31] shown schematically in Fig. 3.1. Typically, the half-density radius $c = 1.1\mathrm{A}^{1/3}$ fm, A being the mass number and t, the distance over which the density drops from 90% to 10% of its value at $r = 0$, is between 2.4 to 3.0 fm. Thus, for a typical fissile nucleus, ^{234}U, the region of constant density is about 5.4 fm, whereas the surface thickness as given by t is about 2.4 fm. The nuclear surface is, therefore, not like a membrane of a liquid droplet but extends about 30% of the total radial dimension of the nucleus.

Apart from that, the density distribution functions of all medium, light and heavy nuclei, are typically, described by a 2 parameter Fermi function with $c = 1.1A^{1/3}$ fm and t being between 2.4 and 3.0 fm. This necessarily means that a substantial density reorganization, apart from the change in geometry, must take place as a nucleus passes through different configurations on the way to fission into a daughter pair. In particular, the theory relevant to fission must be in a position to describe the energy of a configuration like E in Fig. 3.2 which cannot be described within the context of a mass formula based

on a liquid-droplet, since its constants are empirically determined from the masses of configuration A. Actual calculations have clearly indicated that key coefficients of liquid droplet based mass formulas, e.g. coefficient of energy per nucleon, change substantially with the density of nuclear matter [3.4,3.5,3.27] as shown in Fig 3.2. The actual value of the energy per nucleon i.e., the coefficient of A in a mass formula based on the liquid droplet concept differs markedly at low density from its value at saturation density.

In Chap. 2, we have already used the energy-density-functional method to determine nuclear masses using observed density distributions. These calculated total energies are in excellent agreement with the experimental ones, implying that the energy per nucleon versus density curve used in this calculation is reasonably accurate. This, then, allows us to calculate total energies of various configurations depicted in Fig. 3.2. We, therefore, modify the theory of Bohr and Wheeler to incorporate the role of the variable density distribution as well as deformation, during the fission process using the energy-density-functional approach.

The total energy E of any one of the configurations depicted in Fig. 3.2 is given by

$$E(\rho) = \int E[\rho(\mathbf{r})] d^3r \ . \tag{3.23}$$

Following the work of Brueckner et al. [3.4,3.5,3.28] we may use the following expression for the energy density $E(\rho)$.

$$\begin{aligned} E(\rho) = {} & (3/5)(\hbar^2/2M)(3\pi^2/2)^{2/3}(1/2)[(1-\alpha)^{5/3} + (1+\alpha)^{5/3}]\rho^{5/3} + \rho V(\rho,\alpha) \\ & + (e/2)\Phi_c\rho_p - 0.739e^2{\rho_p}^{4/3} + (\hbar^2/8M)\eta(\nabla\rho)^2 \ . \end{aligned} \tag{3.24}$$

Where α is the neutron excess, M is the mass of a nucleon, ρ is the local density of nuclear matter, ρ_p is the charge density and η is the strength of the gradient term in the density. V (ρ, α) is the density-dependent mean potential calculated from a realistic two-nucleon interaction using the Hartree-Fock-Brueckner approach and is given by

$$V(\rho,\alpha) = b_1(1 + a_1\alpha^2)\rho + b_2(1 + a_2\alpha^2)\rho^{4/3} + b_3(1 + a_3\alpha^2)\rho^{5/3} \tag{3.25}$$

and Φ_c, the Coulomb potential, is given by:

$$e \int d^3r' \frac{\rho_p(r')}{|r - r'|} \ . \tag{3.26}$$

This is the same functional used in Chap. 2 to calculate the nuclear masses very successfully using experimentally determined density distributions and hence, has been tested to account for the appropriate energy per nucleon for the range of very small densities to the saturation density.

The potential energy surface, $V(R)$, R being the separation distance between two members of a daughter pair, is calculated following the basic

premise of Bohr-Wheeler theory that $V(R)$ between the two daughter nuclei is given by the London-Heitler approximation, namely by the energy difference between total energy of the two configurations.

$$V(R) = E(\rho_1[R], \rho_2[R]) - E(\rho_1[\infty]) - E(\rho_2[\infty]) \equiv E(R) - E(\infty)\ . \quad (3.27)$$

$E(\rho_1[R], \rho_2[R])$ in (3.27) is the energy of the composite systems such as A to E in Fig. 3.2 generated by *not* superimposing the density distribution functions of each member of a daughter pair but by modifying them according to the adiabatic model described below, where the density at no point of the composite system can exceed the central density of the parent nucleus. $E(\rho_1[\infty])$ and $E(\rho_2[\infty])$ are the energies of each member of a daughter pair when they are far apart.

It is to be emphasized that $E(R)$ cannot be calculated by simply superimposing the density of two daughter nuclei but the density of the composite system has been determined with due consideration of the conditions that (a) the central density of the parent and the daughter pair is about the same, (b) the density of the composite system at no point exceeds the saturation density of [3.28] which is 0.182 fm^{-3} and (c) the surface thickness of the density functions of a daughter pair is established as they emerge. Thus, the parameter characterizing the densities in $E[\rho_1(R), \rho_2(R)]$ vary continuously as a function of R in a manner described below.

In addition to that, we consider here two separate geometries, one in which the two members of a daughter pair are emitted, each with spherical shape, called the sphere-sphere case or model and the second of which, each member of the daughter pair emerges in spheroidal shape but both having the same eccentricity called the spheroid-spheroid case or model.

Although the actual density distribution should be a Fermi function shown in Fig. 3.1, calculations presented here are done using a simple trapezoidal approximation to that function. However, actual calculations using a Fermi function in a few test cases have shown no significant difference in calculating half-lives or mass distribution functions. On the other hand, the use of a trapezoidal density distribution simplifies the computational task significantly. The trapezoidal distribution used has the following functional form that is schematically shown in Fig. 3.4.

$$\begin{aligned} \rho(r) &= \rho_0 && 0 \le r \le r_0 \\ &= \rho_0(b-r)/(b-r_0) && r_0 \le r \le b \\ &= 0 && b \le r \le \infty \end{aligned} \quad (3.28)$$

(3.28) represents a distribution function with a central region of radius r_0 in which the density is constant and equal to ρ_0 and a surface region in which the density falls off linearly to zero at a distance, b, from the center.

Instead of b and r_0, it is more convenient to use half-density radius C and the surface thickness parameter, t which are related by the following equations

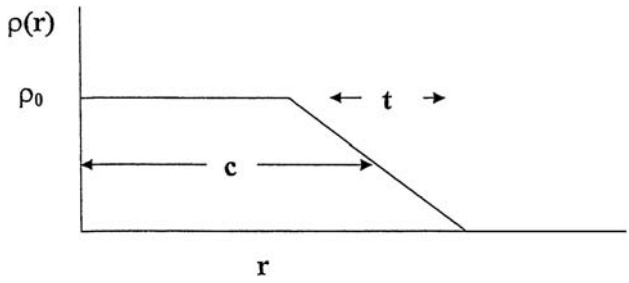

Fig. 3.4. An example of the trapezoidal approximation to the density distribution function shown in Fig. 3.1. ρ_0 is the central density

$$b = C + (5/8)t$$
$$r_0 = C - (5/8)t \; . \tag{3.29}$$

The relation between the mass number and density, given below, determines the central density ρ_0:

$$A = \int \rho(\mathbf{r}) d^3 r \; . \tag{3.30}$$

The half-density radius C is related to mass number, A by:

$$C = C_0 A^{1/3} \; . \tag{3.31}$$

The values of C_0 and t used in the calculations [3.27–3.29] are the following:

$$C_0 = 1.07\,\mathrm{fm} \tag{3.32a}$$
$$t = 2.4\,\mathrm{fm} \; . \tag{3.32b}$$

The parameters a_1, a_2, a_3, b_1, b_2, b_3 and η in (3.25) have originally been determined by Brueckner et al. [3.5] by fitting the energy per nucleon versus density graph determined in the Brueckner-Hartree-Fock approximation using a realistic two nucleon potential [3.28]. In determining these parameters, Brueckner et al., used the nuclear compressibility, K and the momentum k, corresponding to the saturation density as a guide and calculated energy per nucleon $E/A \, . \, \eta$ was determined to reproduce the observed masses of a few nuclei using observed density distribution functions. Since the trapezoidal distribution differs from the observed distribution, we have changed these parameters slightly to reproduce the observed root mean squared radii of a reasonable number of nuclei [3.29]. The value of these parameters are $a_1 = -0.1933$, $a_2 = 0.3128$, $a_3 = 1.715$, $b_1 = -741.28$, $b_2 = 1179.89$, $b_3 = -467.54$ and $\eta = 10.8$. These correspond to $K = 184.7$, $\kappa_\mathrm{f} = 1.447\,\mathrm{fm}^{-1}$ and $E/A = -16.59$ which are close to their expected values. In order to

check the adequacy of using the trapezoidal distribution function, the ground state energies of a number of nuclei have been calculated. These, shown in Table 3.1, are within 1% of the experimentally determined values [3.17] and hence, the use of the trapezoidal distribution function is sufficient for the purpose of the calculations. The value of C_0 and t are in conformity of their accepted numbers [3.30, 3.32].

Table 3.1. Experimental [3.17] and theoretical binding energies in MeV for selected nuclei. The theoretical binding energies are calculated using a trapezoidal distribution that reproduces the observed root mean squared radius

Nucleus	Exp. (MeV)	Theory (MeV)
^{16}O	127.6	123.3
^{32}S	271.8	270.1
^{40}Ca	416.0	416.0
^{56}Fe	492.3	496.7
^{60}Ni	526.9	532.1
^{140}Ce	1172.7	1181.8
^{142}Ba	1180.3	1185.7
^{165}Ho	1344.8	1356.1
^{208}Pb	1636.5	1628.8
^{236}U	1776.0	1778.0
^{238}U	1801.7	1798.5
^{240}Pu	1813.4	1811.0

The values of C_0 and t are suitable for the ground state of stable nuclei. To reflect the enormous reorganization of the density distribution function during the fission process, these two parameters characterizing the density distribution should be dependent on R. At $R = 0$, the density distributions $\rho_1[0] + \rho_2[0]$ must be chosen so that their sum adds up to the central density of the parent nucleus and on the other hand, as $R \to \infty$ the density distributions $\rho_1[\infty]$ and $\rho_2[\infty]$ must be those of the excited states of the daughter pair.

To ensure these boundary conditions of the density distribution function at $R = 0$ and $R = \infty$, we use the special adiabatic approximation for the variation of C and t with R proposed in [3.6]. The density distribution function ρ, in this approximation, is generated in such a way that, at no point of the composite system, does the density exceed that of the average central density of a nucleus and at $R = 0$ and $R = \infty$ the density distribution functions are, respectively, given by the appropriate ones for the parent and for the associated daughter pair. The ansatz for the variation of C and t with R is as follows:

$$\begin{aligned} C_d(R) &= C_p \exp[\ln(C_d(\infty)/C_p)(R/R_{\rm cut})^n] \qquad \text{for} \quad R \le R_{\rm cut} \\ &= \mathrm{C_d}(\infty) \qquad\qquad\qquad\qquad\qquad\quad R \ge R_{\rm cut}\ . \end{aligned} \tag{3.33}$$

In (3.33) C_d and C_p are, respectively, the C-parameter of the density distribution function for the daughter and the parent. Similarly, the variation of t with R is given by the ansatz:

$$\begin{aligned} t_d(R) &= t_p \exp[\ln(t_d(\infty)/t_p)(R/R_{\rm cut})^n] \qquad \text{for} \quad R \le R_{\rm cut} \\ &= t_d(\infty) \qquad\qquad\qquad\qquad\quad \text{for} \quad R > R_{\rm cut}\ . \end{aligned} \tag{3.34}$$

In (3.34) the subscripts d and p stand, respectively, for daughter and parent.

The quantity $R_{\rm cut}$ in (3.33) and (3.34) has the role of a scaling parameter determining the separation distance at which the densities of the daughter pair reach their final value. At $R \ge R_{\rm cut}$, the density distributions of the daughter pair remains unchanged as the fragments separate. At $R = R_{\rm cut}$, the daughter pair essentially establishes their identity. It is easy to establish the upper and the lower limits of $R_{\rm cut}$. $R_{\rm cut}$ must be greater than $C_1 + C_2$, otherwise it is possible to have densities in excess of the central density of a nucleus but it must also be less than the scission radius; otherwise it is difficult for the daughter pair to develop a proper density distribution near their surface region. In our calculation $R_{\rm cut}$ is taken to be one half of the scission radius which is justified by the result of the point by point variation of the fractional parameter $p(R)$ defined in (3.35). In terms of the schematic configurations shown in Fig. 3.2, $R \ge R_{\rm cut}$ falls somewhere between configuration D and E. Finally, the parameter n in (3.33) and (3.34) determines how quickly the daughter fragments establish their own identity by acquiring final values of their respective density distribution.

At each separation point R, we generate the appropriate values of C_d and t_d and hence, obtain $\rho_1(R)$ and $\rho_2(R)$ needed to calculate $E(R)$ in (3.27). Furthermore, the use of (3.30) insures that for each R, the nucleon number is conserved. The condition (3.30) replaces the Bohr-Wheeler auxiliary condition of volume conservation which is valid only for a constant density distribution but not for a Fermi or trapezoidal distribution.

Another measure for the variation of C and t with R is to define a fractional parameter $p(R)$ for both C and t as follows:

$$p(R) = \frac{C_d(R) - C_d(\infty)}{Cp - C_d(\infty)} \tag{3.35}$$

with a similar expression for fractional parameter t. In (3.35), C_p is the half-density radius of the parent nucleus.

This parameter is a measure of the progress made by the parameters denoting the density distribution function towards their final values in terms of the difference of these parameters between a parent and a daughter nucleus. For $R \ge R_{\rm cut}$, the potential energy surface does not depend on n, and is basically determined by the overlap of densities of a daughter pair. For example,

the use of ansatz (3.33) and (3.34) leads to $p(0) = 1$ and $p(R_{\text{cut}}) = 0$. In between $p(R)$ is completely determined by (3.35).

It is possible to determine $C_d(R)$ and $t_d(R)$ by a point by point variation of $p(R)$ as a function of R and minimizing it with respect to n. R_{cut} is then determined by that R where $p(R)$ is zero. In all cases computed so far, such a minimum has always been found to exist for every R. The interpretation of this corresponds to the physical situation of allowing the formation of the smallest cluster or condensation for a given R. Finally, one must determine the scission radius, R_{sc}. Since the daughter pair is usually in an excited state, R_{sc} cannot be $C_0(A_1^{1/3} + A_2^{1/3}) + (5/8)(t_1 + t_2)$ but should be somewhat larger. Particularly, for the sphere-sphere case where the density distribution function is calculated by superposing two spherical configurations, one expects the two nuclei of a daughter pair to emerge in spherical shape. For the spheroid-spheroid case, they emerge in spheroidal shapes. Within the context of classical physics, the asymptotic kinetic energy of a daughter pair is equal to its Coulomb energy at the scission point. Unfortunately, experimentally determined asymptotic kinetic energies have usually an uncertainty of a few MeV. To accommodate that and possible energy loss due to oscillation prior to scission, we determine the scission radius from:

$$Z_1 Z_2 e^2 / R_{\text{sc}} = E_{\text{kin}} + f(A_{\text{p}}) \tag{3.36}$$

$f(A_{\text{p}})$ in (3.36) is chosen to be linear in A_{p} for simplicity and is determined from the fastest decay mode in the spontaneous fission of ^{240}Pu to be

$$f(A_p) = -0.883 A_p + 215.9 \, . \tag{3.37}$$

Thus, $f(A_p)$ is a small correction to the observed kinetic energy and usually lies within the observed experimental uncertainties. As noted in [3.8], for the spheroid-spheroid case where the density distribution function for each R is determined by superimposing spheroidal geometry, one must also specify the eccentricity, ε, of each member of the daughter pair. Unfortunately ε is not well known experimentally. To determine this in a systematic way, we have imposed the auxiliary condition that the dimension of the surface to the total dimension is constant and equal to the one obtained in the spherical case, i.e.

$$\eta = (b(\theta) - a(\theta))/b(\theta) = \text{constant} = 0.78 \, . \tag{3.38}$$

Where $b(\theta)$ and $a(\theta)$ are, respectively, the outer boundary of the constant density zone in a nucleus. $f(A_p)$, for this case called $f_1(A_p)$ is again determined from one of the fastest decaying modes of ^{240}Pu and given by

$$f_1(A_{\text{p}}) = -0.983 A_p + 220.39 \, . \tag{3.39}$$

The calculated potential energy surfaces for different decay modes for a particular parent nucleus differ from each other since $C_d(R)$, $C_d(\infty)$ and R_{sc} depends on the mass numbers of each member of a daughter pair. The

difference in their potential energy surface along with the difference in the average kinetic energy associated with different decay modes ensures a mass and a charge distribution in the decay of a particular parent.

As noted earlier, the central density of a nucleus in these calculations is taken to be $0.182\,\mathrm{fm}^{-3}$. For the calculation of half-lives, we have used a pre-formation probability of 10^{-5} determined in [3.9] since we present here the results for spontaneous decay of even-even nuclei to even-even daughter pairs. The barrier penetration probability is calculated using expression (28) of [3.33]. As noted in [3.33], the use of the more accurate expression (27) therein would have affected the results at the most by one order of magnitude. It is to be emphasized that the kinetic energy of a daughter pair in this theory plays an important role. The theory emphasizes that the calculated half-lives and kinetic energy used in the calculations are to be in accord with the data.

3.4 Results and Discussion

3.4.1 The Potential Energy Surface

In case one assumes the density distribution function of the parent and the daughter pairs to be constant, dropping sharply to zero at the surface, one obtains potential energy surfaces similar to those obtained in Bohr-Wheeler type of theories. There would be no external barrier in that case. Our approach, however, not only considers the change in energy due to the change in geometrical shape as a nucleus undergoes fission, which is the key feature in the Bohr-Wheeler type of theories, but it incorporates also the dramatic change in the density distribution function as a parent nucleus undergoes fission to daughter pairs. This latter feature of the theory allows for the formation of a neck of low density nuclear matter prior to scission to a given daughter pair. The formation of this neck generates an external barrier in the potential energy surface. The liquid drop model with its premise of a constant density distribution cannot simulate that. The incorporation of a folded surface either of Gaussian or of Yukawa type around a geometrical shape [3.34] calculated from a constant density distribution and mass formulae whose constants are determined from ground state energies based on a liquid droplet, may not exhibit this dip in the potential energy surface simply because these constants of those mass formulas are invalid at densities other than the average saturation density of a nucleus in its ground state geometry.

Instead of presenting the potential energy surfaces for each case considered herein, we present only some sample cases. In Fig. 3.5, we present the contribution to the potential energy surface due to the change in Coulomb energy in the decay of ^{234}U to ^{142}Xe + ^{92}Sr using the ansatz $n = 2$ and $n = 3$ in (3.33) and (3.34) for the sphere-sphere case. In the same figure, we have plotted by dashed line, the result obtained by varying (3.35) at every separation distance (i.e. by a point by point variation) with respect to n and

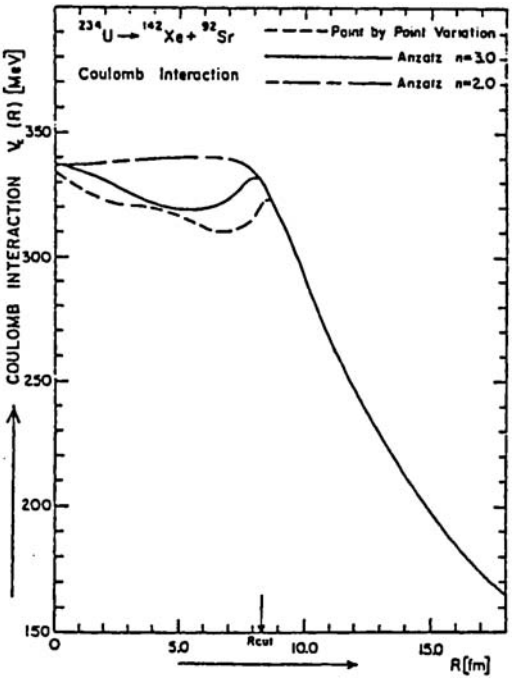

Fig. 3.5. Computed Coulomb interaction for the decay $^{234}\mathrm{U} \rightarrow {}^{92}\mathrm{Sr} + {}^{142}\mathrm{Xe}$ for $n = 2,\ 3$ in (3.33) and (3.34) and point by point variation of $p(R)$ given by (3.35)

determining n from the minimum in $\rho(R)$. The three calculations differ in the region R less than R_{cut} *but yield about the same results in the region* R *greater than* R_{cut}. We also note that the case $n = 2$ produces a surface close to the one expected from the liquid droplet. Since the region external to R_{cut}, where all three calculations yield about the same results, is a prime contributor to the half-lives and the point by point calculations are very time consuming, we present in the subsequent section results for $n = 2$. A few sample calculations using $n = 2$ or point by point variation did not indicate any significant change in potential energy surface in the region greater than R_{cut}, which is the determining factor governing the calculations of half-lives.

In Fig. 3.6, we exhibit a sample case of the potential energy surface in the decay of $^{234}\mathrm{U} \rightarrow {}^{142}\mathrm{Xe} + {}^{92}\mathrm{Sr}$ for the case of $n = 2$ using the sphere-sphere model. The interior part of the surface is similar to the one expected from the Bohr-Wheeler case but the potential surface exhibits an external barrier prior to scission which is around 16 fm. The occurrence of this external barrier is a direct consequence of the existence of a neck of low density nuclear matter prior to scission shown in configuration E in Fig. 3.2. It is instructive to illustrate the change of C and t as $^{234}\mathrm{U}$ fissions to $^{142}\mathrm{Xe} + {}^{92}\mathrm{Sr}$. This is shown in Fig. 3.7 for the point by point case in the sphere-sphere model.

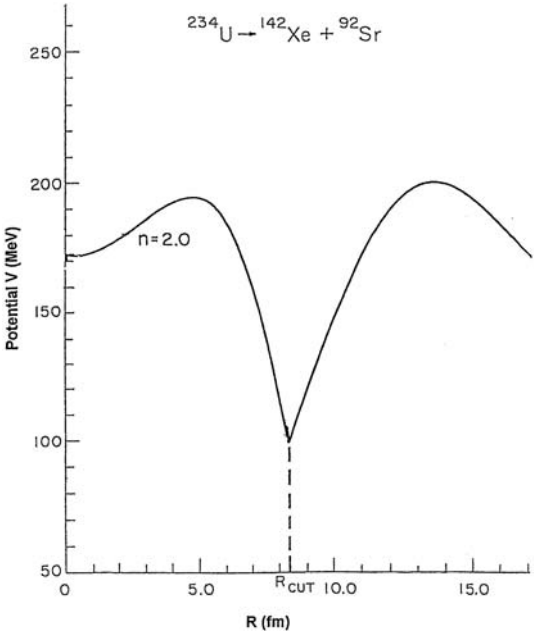

Fig. 3.6. The potential energy surface for the spontaneous fission of ^{234}U to ^{92}Sr and ^{142}Xe using $n = 2$ in the ansatz (3.33) and (3.34)

Indeed, the variation is substantial. The corresponding change in density contours is shown in Fig. 3.8 and 3.9 using the point by point variation for the sphere-sphere model and for the spheroid-spheroid, respectively. In the latter case, the scission point is extended further outwards and the height of the external barrier in the spheroid-spheroid case is lower than that in the sphere-sphere case. An example of the difference in the external barriers for the two cases is shown in the lower parts of Fig. 3.10. In both cases the area of the potential energy surface above the asymptotic kinetic energy for this decay mode is about the same resulting in similar half-lives as noted in Table 3.3.

In Fig. 3.11 we exhibit the evolution of the density contour for $n = 2$ in the decay of ^{240}Pu to ^{122}Cd and ^{118}Pd in the sphere-sphere model. The formation of a low density neck is very prominent. This is one of the least likely decay modes i.e. one of the symmetric modes.

In the upper half of Fig. 3.10 the external potential energy surface for this decay mode is compared to that of the decay to ^{142}Ba and ^{98}Sr, one of the fastest modes, for the spheroid-spheroid case. The latter barrier is lower than the former. This, along with the fact, that the kinetic energy associated with the decay to ^{142}Ba and ^{98}Sr is about 7 MeV higher than that for the decay to ^{122}Cd and ^{118}Pd is responsible for five orders of magnitude difference in their half-lives as shown in Table 3.2.

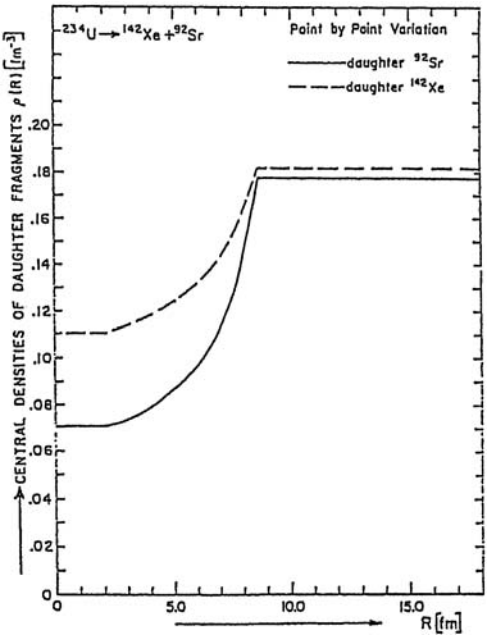

Fig. 3.7. The partition of the central saturation density of the parent ^{234}U into those of the daughter pair ^{142}Xe and ^{92}Sr as a function of R obtained from a point by point variation of $p(R)$, for the sphere-sphere model

Table 3.2. Calculated spontaneous fission half-lives of ^{240}Pu to a number of decay modes in the spheroid-spheroid model are noted in column 5 and in the sphere-sphere model, noted in column 6. ε is the eccentricity used in the spheroid-spheroid model. $E_{\rm kin}$ is the observed kinetic energy and the logarithm of experimental half-lives is shown in the last column from [3.35]. The experimental half-lives are for all daughter pairs having the same mass number and do not specify atomic number

Parent	Daughters	$E_{\rm kin}$ (MeV)	ε	$\log_{10}\ t_{1/2}$ (years)(spheroid)	$\log_{10} t_{1/2}$ (years)(sphere)	$\log_{10} t_{1/2}$ (exp) (years)
$^{240}Pu_{94}$	$^{86}Se_{34} + ^{154}Nd_{60}$	161.5	0.62	10.7	10.7	-
	$^{92}Kr_{36} + ^{148}Ce_{58}$	167.9	0.58	11.2	11.0	11.5
	$^{98}Sr_{38} + ^{142}Ba_{56}$	175.0	0.53	11.1	11.1	11.1
	$^{100}Zr_{40} + ^{140}Xe_{54}$	177.6	0.53	11.8	11.6	11.1
	$^{106}Mo_{42} + ^{134}Te_{52}$	185.4	0.44	10.8	11.1	11.0
	$^{108}Ru_{44} + ^{132}Sn_{50}$	185.5	0.47	11.4	11.5	11.2
	$^{118}Pd_{46} + ^{122}Cd_{48}$	167.9	0.67	16.8	16.1	14.0

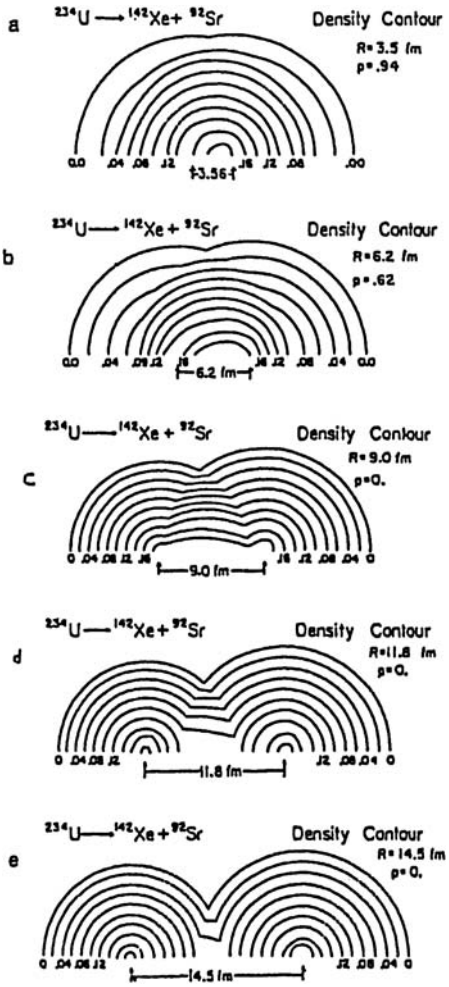

Fig. 3.8. The evolution of the density contour for the decay of $^{234}\mathrm{U} \rightarrow ^{92}\mathrm{Sr} + ^{142}\mathrm{Xe}$ as a function of R for the case of a point by point variation of $p(R)$, for the sphere-sphere model. The contour lines are represented by matter per $(\mathrm{fm})^3$

3.4.2 Half-Lives

Apart from the nature of the potential energy surface, the asymptotic kinetic energy plays a crucial role in any decay process and also in fission as discussed in Appendices A and B. Thus, in order to calculate half-lives, knowledge of the latter is necessary. In many cases this is available. As noted in these appendices, in the presence of an external barrier such as the one shown in Fig. 3.6, half-lives are primarily determined by the area bounded by the kinetic energy and potential energy surface of the external barrier above the

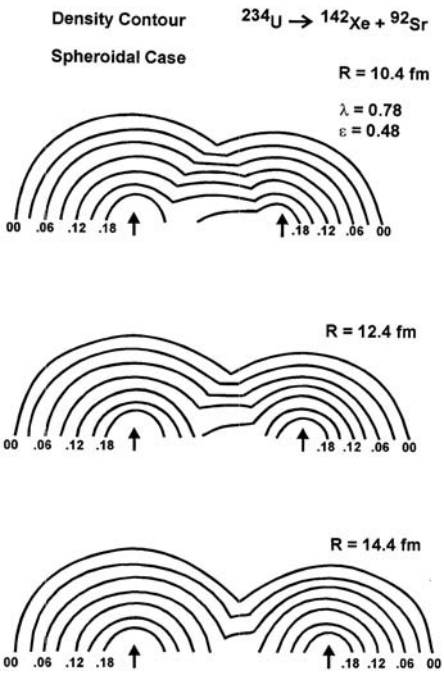

Fig. 3.9. The evolution of the density contour, represented by nuclear matter per fm^3 between 10.4 and 14.4 fm separation calculated in the spheroid-spheroid model for the decay of ^{234}U to ^{142}Xe and ^{92}Sr. Since this is the region of the external barrier, $n = 2$ and the point by point variation yield the same result

kinetic energy. The internal barrier has no discernible effect on half-lives. Since the nature of the external barrier and the magnitude of the kinetic energy are different for different decay modes of a parent nucleus, one expects a mass distribution in the fission of any nucleus. In Table 3.2 we present an example of this mass distribution calculated for the spontaneous decay of ^{240}Pu in terms of half-lives along with the data. The agreement is reasonable. The potential energy surface of all decay modes shown in Table 3.2 has been calculated using the energy density functional theory and the corresponding half-lives have been computed using the observed kinetic energy and a preformation probability of 10^{-5}. The differences in the potential energy surface at the external barrier, an example of which is shown in Fig. 3.10, and of the kinetic energy associated with different decay modes are the underlying cause of the observed mass spectrum in spontaneous fission not only of ^{240}Pu, but in the spontaneous fission of other nuclei. The interrelated role of these two factors is responsible for the dominance of the decay to an asymmetric mode mass distribution over the symmetric ones in the decay of Ra to Cf isotopes. Once the balance of these two interrelated factors changes, decay to

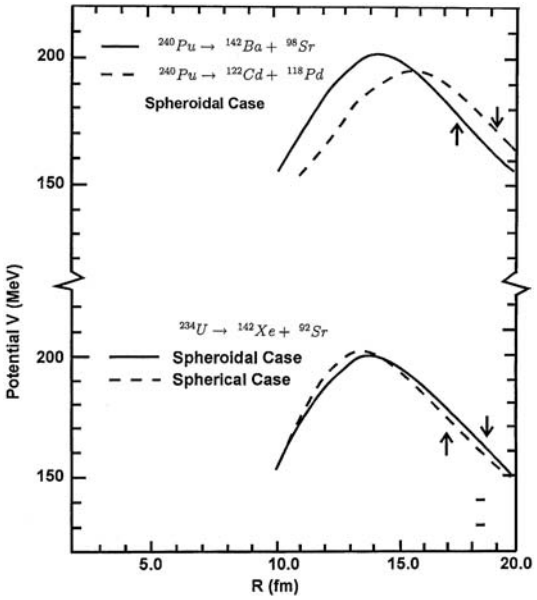

Fig. 3.10. The upper half exhibits the potential energy surface in the region of the external barrier in the spheroid-spheroid model for the decay of ^{240}Pu to one of the fasted decay modes, ^{142}Ba and ^{98}Sr and to one of the slowest decay modes, ^{122}Cd and ^{118}Pd. The lower half compares the potential energy surface near the external barrier in the sphere-sphere and the spheroid-spheroid case for the decay of ^{234}U to ^{142}Xe and ^{92}Sr

symmetric modes could become dominant as in the case of ^{258} fm discussed in the next chapter.

Clearly, calculations of total half-lives are extremely time-consuming because one must calculate partial half-lives for the decay to all possible daughter pairs characterized by mass and charge numbers. However, since the half-lives to the fastest decay modes differ quite often by one or a few orders of magnitude, it is sufficient to calculate only the decay rates to a few fastest decay modes. We have tested this by actual calculations. In fact, only a few fastest decay modes determine the total fission half-life of a parent nucleus, since these decay modes are the dominant contributors to half-lives. In Table 3.3 calculated half-lives of even-even parent nuclei ^{226}Ra, ^{234}U, ^{236}U, ^{240}Pu, ^{244}Cm, ^{248}Cf and ^{252}Cf to one of their fastest decay modes for the sphere-sphere (i.e. $\varepsilon = 0$) and the spheroid-spheroid cases using observed TKE are compared to the observed ones. The TKE for the decay of Ra is unknown experimentally. Similarly, its spontaneous fission half-life is unknown but determined to be greater than 10^{14} years by Segré [3.38] and greater than 6.6×10^{17} years by Tretyakova [3.39]. The value used for TKE in the calculation is calculated using the theory outlined in Sect. 3.2 of Chap. 4. As

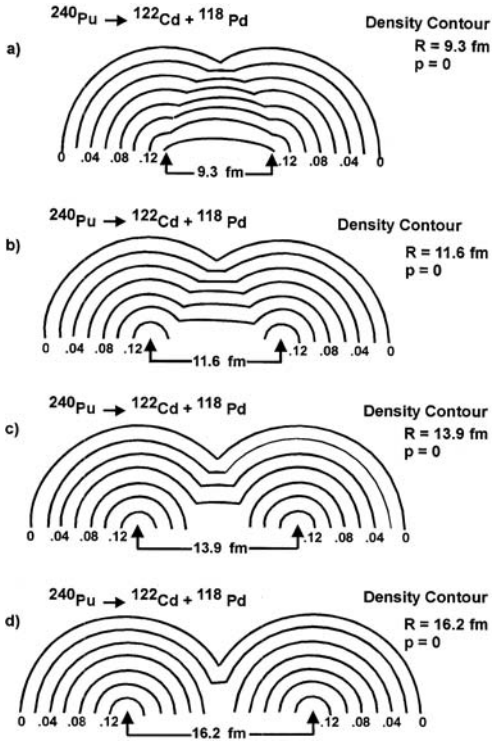

Fig. 3.11. The evolution of the density contour, represented by nuclear matter per fm^3 just before the scission calculated using the sphere-sphere model for the decay of ^{240}Pu to ^{122}Cd and ^{118}Pd. In this region $n = 2$ and point by point variation yield the same result

noted earlier, the typical uncertainties in the theoretical calculation is about an order of magnitude originating from the use of the approximate formula for barrier penetrations and for pre-formation probabilities. Within these uncertainties both sets of theoretical calculations explain the observed half-lives calculated with observed TKE sufficiently well.

Since the external barrier, critical for the determination of half-lives, is relatively thin, the half-lives are somewhat sensitive to TKE used in the calculation. For example, in the fission of ^{244}Cm to ^{144}Ba and ^{100}Zr, the use of 183, 185, 197 MeV for E_{kin}, all of them being within the error bars results in half-lives of 8.8, 8.4 and 8.1 years, respectively, in the sphere-sphere case. Using the same approximation, calculated half-lives for the fission of ^{248}Cf to ^{152}Sm and ^{96}Kr are 2.7, 3.0 and 3.3 years for $E_{\mathrm{kin}} = 190$, 188 and 186 MeV, respectively.

Table 3.3. Columns 1 to 7 represents, respectively, the parent nucleus, one of the fastest decay modes, observed kinetic energies from [3.35–3.37] which are also used in theoretical calculations, logarithm of half-lives in the sphere-sphere model in years, the eccentricity used in the spheroid-spheroid model, logarithm of half-lives in years in the spheroid-spheroid model and observed half-lives [3.36]. Typical experimental uncertainties in kinetic energy is about 2 MeV, except for ^{244}Cm where it is ±5 MeV

Parent	Daughter	K.E. (exp) MeV	log $t_{1/2}$(th) years (sphere)	ε	log $t_{1/2}$(th) years (spheroid)	log $t_{1/2}$(exp) years
^{226}Ra	^{132}Sn + ^{94}Sr	156.0	—	0.17	20.5	>17.8
^{234}U	^{142}Xe + ^{92}Sr	168.5	16.2	0.48	16.4	16.2
^{236}U	^{140}Xe + ^{96}Sr	171.3	13.7	0.44	13.4	16.3
^{240}Pu	^{142}Ba + ^{98}Sr	175.0	11.1	0.53	11.1	11.1
^{244}Cm	^{144}Ba + ^{100}Zr	185.5	8.4	0.55	8.4	7.1
^{248}Cf	^{152}Sm + ^{96}Kr	188.7	3.1	0.54	2.2	3.8
^{252}Cf	^{144}Xe + ^{108}Ru	187.0	3.3	0.69	1.9	1.9

3.5 Conclusion

The main feature of the potential-energy surface calculated using the energy-density functional theory is the occurrence of an additional barrier between the saddle and scission points originating from the formation of a neck of low-density nuclear matter prior to the scission. Unpublished calculations indicate that such a barrier exists even for unrealistic geometries such as half-cone attached to a half sphere. As noted in Appendix A, only the existence of such a barrier allows the potential to drop below the asymptotic kinetic energy, which is a necessary condition for the existence of a meta-stable state. It is also established that the observed half-lives can be accounted for using observed TKE. The preference for parent nuclei, considered herein, to decay primarily to asymptotic modes is also accounted for.

References

1. N. Bohr and J.A. Wheeler, Phys. Rev. **56**, 426 (1939).
2. D.L. Hill and J.A. Wheeler, Phys. Rev. **89**, 1102 (1953).
3. See e.g. H. de Vries, C.W. de Jager and C. de Vries, Atomic Data and Nuclear Data Tables **36**, 496 (1987).
4. K.A. Brueckner, J.R. Buchler, S. Jorna and R.J. Lombard, Phys. Rev. **171**, 1188 (1968).
5. K.A. Brueckner, J.R. Buchler, R.C Clark, and R.J. Lombard, Phys. Rev **181**, 1543 (1968).
6. I. Reichstein and F.B. Malik, Phys. Lett. **37B**, 344 (1971).
7. I. Reichstein and F.B. Malik, Ann. Phys. (N.Y.) **98**, 322 (1976).

8. F.B. Malik and I. Reichstein, *Superheavy Elements*, ed M.A.K. Lodhi (Gordon and Breach 1978).
9. B. Block, J.W. Clark, M.D. High, R. Malmin and F.B.Malik, Ann. Phys. (N.Y.)**62**, 464 (1971).
10. J.A. Wheeler, Phys. Rev. **52**, 1123 (1937).
11. H. Feshbach, Ann. Phys. (N.Y.) **5**, 237 (1958); **19**, 287 (1962).
12. M.G. Mustafa and F.B. Malik, Ann. Phys. (N.Y.) **83**, 340 (1974).
13. Q. Haider and F.B. Malik, Phys. Rev. C **28**, 2328 (1983).
14. F.B. Malik, Condensed Matter Theories **7**, 11 (1992).
15. A. Herzenberg and A.S. Roberts, Nucl. Phys. **3**, 314 (1957).
16. N.F. Mott and H.S.W. Massey, The Theory of Atomic Collisions (Clarendon Press, Oxford, 1965).
17. A.H. Wapstra and G. Audi, Nucl. Phys. A **432**, 1 (1985).
18. H.J. Mang, Z. Physik **148**, 582 (1957): Phys. Rev. **119**, 1069 (1960).
19. H.J. Mang and J.O. Rasmussen, Kgl. Dan. Vidensk. Selsk. Mat. Fys. Skr. **2**, 3 (1961).
20. S.T. Belyaev, Kgl. Dan. Vidensk. Selsk. Mat. Fys. Medd. **31**, 11 (1959).
21. S.G. Nilsson and 0. Prior, Kgl. Dan. Vidensk. Selsk. Mat. Fys. Medd. **32**, 16 (1961).
22. L.S. Kisslinger and R.A. Sorensen, Rev. Mod. Phys. **35**, 853 (1963).
23. W. Scholz and F.B. Malik, Phys. Rev. **176**, 1355 (1968).
24. L. Wilets, *Theories of Nuclear Fission* (Clarendon Press, Oxford 1964).
25. M. Brack, J. Damgaard, A.S. Jensen, H.C Pauli, V.M. Strutinsky and C.Y. Wong, Rev. Mod. Phys. **44**, 320 (1972).
26. V.M. Strutinsky, Nucl. Phys. **A 95**, 420 (1967); ibid **122**, 1 (1968).
27. H. de Vries, C.W. de Jager and C. de Vries, At. Data Nucl. Data Tables **36**, (1987).
28. K.A. Brueckner, S.A. Coon, and J.Dabrowski, Phys. Rev. **168**, 1184 (1968).
29. I. Reichstein and F.B. Malik, Condensed Matter Theories **1**, 291 (1985).
30. H.L. Acker, G. Backentoss, C. Daum, J.C. Sens and S.A. Dewitt, Nucl. Phys **87**, 1 (1966).
31. L.R.B. EIton, *Nuclear Sizes* (Clarendon Press, Oxford, 1961).
32. Y.N. Kim, *Mesic Atoms and Nuclear Structures* (North-Holland, Amsterdam 1971).
33. F.B. Malik and P.C. Sabatier, Helv. Phys. Acta **46**, 303 (1973).
34. H.J. Krappe and J.R. Nix, Proc. Int'l. Conf On Physics and Chemistry of Fission held at Rochester, N.Y. (IAEA Publication 1974).
35. J.H. Neiler, E.J. Walter and H.W. Schmitt, Phys. Rev. **149**, 894 (1966).
36. E.K. Hyde, *The Nuclear Properties of Heavy Elements* vol. 3, (Prentice Hall Englewood Cliff, N.J.).
37. F. Pleasonton, Phys. Rev. **174**, 1500 (1968).
38. E. Segré, Phys. Rev. **86**, 21 (1952).
39. S. Tretyakova, Private Communication (2000).

4 Spontaneous Fission Half-Lives of Fermium and Super-Heavy Elements

4.1 Introduction

In 1967, Strutinsky [4.1] proposed a method to incorporate the correction due to shell closure of parent nuclei to the potential energy surfaces calculated by models based on liquid drop type of approaches. The method is discussed in further detail in Chap. 8. The incorporation of this correction in the calculations of the potential energy surface within the context of the liquid drop model enhances the stability of closed shell nuclei against spontaneous fission. At about the same time a number of calculations [4.2–4.6] indicated that additional proton and neutron shell closures might occur at atomic number $N = 184$. The additional few MeV associated with such a shell closure raises the computed potential energy surface, by a few MeV, within the context of models based on the liquid drop approach, thus making these elements more stable against spontaneous fission in comparison with their neighboring isotopes. In fact, Nilsson et al. [4.7, 4.8] predicted spontaneous fission half-lives of $10^2, 10^{16}, 10^{15}$ and 10^{14} years for the isotopes of 294, 298, 300 and 302 of the element 114. This was confirmed in [4.9] and the investigation in [4.10] raised the possibility of even longer half-lives for $^{298}(114)$, stating "when these same general methods are applied to superheavy nuclei, we find that the fission barrier of nuclei near $^{298}(114)$ is even higher than previously supposed". Such long spontaneous fission half-lives implied that these elements should exist in nature. Despite much effort, no evidence of the existence of any superheavy element has been found in nature to date.

The underlying premise of the above calculations is embedded in the fundamental assumption of the constant distribution of nuclear density inherent in the liquid drop approach, which does not allow for the formation of a neck of low-density nuclear matter, depicted in the configuration E of Fig. 3.2. Furthermore, the calculations of barrier penetration probabilities in the above models were done in the JWKB approximation using the Q-values for the ground state to the ground state transitions of a particular daughter pair, which implies the daughter pair to be emitted in unexcited states. This is contrary to the spontaneous fission process involving actinides where the daughter pairs are predominantly emitted in excited states.

The energy-density functional discussed in Chap. 3 allows one to alleviate these difficulties. In particular, the potential energy surface associated with

the configuration E in Fig. 3.2 can be calculated in a suitable approximation. This leads to an external barrier prior to scission. The lowest points of this external barrier lie below the pre-neutron emission kinetic energy allowing a parent nucleus to decay in excited states of daughter pairs, as discussed in [4.11] and noted in Appendices A and B. In fact, using an empirical external barrier that explains the observed half-lives, mass and charge distributions of some actinides [4.12, 4.13] discussed in detail in Chap. 5, it was concluded in 1972 [4.13] that "The realistic upper limits of fission-decay and alpha-decay half-lives are less than a year. This means that elements 112 and 114, if produced in the laboratory, have a lower limit of half-life *that is long enough to measure*. However, these half-lives are too short for the element to occur naturally on the earth and it is fruitless to search for them." Subsequent detailed calculations [4.14,4.15] using the energy-density functional approach, discussed in the next section, confirms this conclusion. Recent experiments also support this conclusion [see e.g. [4.16]]. All data point to the fact that elements up to 116 produced in the laboratory have spontaneous fission as well as alpha decay half-lives significantly shorter than a year (production of elements heavier than 116, although reported in [4.16, 4.17] is yet to be confirmed).

As noted in [4.18], the total half-lives of heavy elements depend on beta-decay, K-capture rate, alpha decay and spontaneous fission processes. The beta decay and K-capture half-lives of super-heavy elements are about 10^4 sec. [4.13, 4.19] or less. Calculations of alpha decay half-lives depend critically on Q-values, determinations of which using the usual mass-formulae, have typical uncertainties of about 0.5 MeV. Actual theoretical computation of alpha-decay half-lives of a number of isotopes of superheavy elements yield results that are typically less than a year [4.7, 4.20] but long enough for the production of these elements in laboratories. Hence, the ability to produce these elements in laboratories depends critically on whether or not their spontaneous fission half-lives are long, short, or nearly zero. Calculations based on the energy-density functional theory, reported in the next section, indicate these half-lives to be short or in some cases, zero. As noted in Appendices A and B, the asymptotic kinetic energy plays a vital role in determining half-lives. Unfortunately, these are unknown for superheavy elements. We, therefore, first discuss the method used in determining asymptotic kinetic energy in Sect. 4.1.

However, before computing the spontaneous fission half-lives of superheavy elements, one needs to account for the very interesting change in the mass distribution spectrum occurring in the spontaneous decay of fermium isotopes starting from ^{258}Fm. The dominant decay modes in the fission of ^{258}Fm are no longer asymmetric but symmetric [4.21]. Calculations done using the energy-density functional approach to investigate the spontaneous fission of superheavy elements supports this experimental fact. Hence, we, in Sect. 4.3, present the results for the fission of ^{258}Fm followed by calculations of half-lives of a number of superheavy elements.

4.2 Determination of Asymptotic Kinetic Energy

Spontaneous fission half-lives are determined by two critical factors, namely, the potential-energy surface and the asymptotic kinetic energies. The latter quantities are experimentally unknown for superheavy elements and poorly determined for ^{258}Fm and hence, are to be determined theoretically. For this purpose, we follow the prescription of Terrell [4.25], which has been successful in accounting for the asymptotic kinetic energies in the fission of the actinides. The asymptotic kinetic energy, $E_{\rm kin}$, associated with the spontaneous fission of a parent nucleus to a particular daughter pair is related to the Q-value and excitation energy, $E(exc)$ as follows:

$$E_{\rm kin} = Q - E(exc)\ . \tag{4.1}$$

Q-values can be evaluated from some standard liquid-drop based mass formulae like that of Møeller et al. [4.26], Myers and Swiatecki [4.27] or Green [4.28]. $E(exc)$, the average excitation energy of a daughter pair is given by:

$$E(exc) = \sum_{n(i),i=1,2} B(i,n(i)) - \sum_{i=1,2} (v(i)\eta(i) + \gamma(i))\ . \tag{4.2}$$

In (4.2) $B(i,\ n\ (i))$ is the binding energy of the $(n(i))$th neutron emitted from the i-th fragment $(i = 1,\ 2)$ and can again be obtained from a mass formula or, in some cases, from experimental information on neutron separation energy. $\gamma(i)$, the energy of prompt gamma rays emitted from the i-th fragment, is estimated by Terrell to be $(1/2)\ B\ (i,\ n\ (i))\,.\,\nu(i)$ and $\eta(i)$ are, respectively, the number of emitted neutrons and the average center of mass kinetic energy of emitted neutrons from the i-th fragment. As noted in [4.25],

$$\begin{aligned} &\eta(i) \cong 1.4 \text{ MeV and} \\ &\nu(i) \cong 0.08\ (A(i) - 82) \quad \text{if} \quad 82 \le A \le 126 \\ &\qquad \cong 0.1\ (A(i) - 126) \quad \text{if} \quad A > 126 \end{aligned} \tag{4.3}$$

From Fig. 1.15 reproduced from [4.25] $\nu(i)$, in the first approximation, does not depend on the mass number of the parent nucleus but on the mass number of the individual daughter fragments. Knowing the mass number of the individual daughter pair, $\nu(i)$ can easily be obtained from Fig. 1.15. The calculated $E_{\rm kin}$ associated with the decay of $^{296}(112)$, $^{298}(114)$, $^{293}(118)$ and $^{310}(126)$ to respective daughter pairs $^{148}(56) + ^{148}(56)$, $^{148}(58) + ^{150}(56)$, $^{147}(59) + ^{146}(59)$ and $^{156}(64) + ^{154}(62)$ are, respectively, 262, 270, 323 and 352 MeV [4.14, 4.15, 4.30]. These are the fastest decay modes in the spontaneous fission of elements 112, 114, 118, and 126.

The determination of kinetic energy using Terrell's method has a typical uncertainty of about 5 MeV. An alternative method is to determine the kinetic energy from a knowledge of the scission radius and identifying the

Coulomb energy at the scission point with asymptotic kinetic energy. However, it is difficult to determine the scission radius and the latter procedure in determining the asymptotic kinetic energy leads also to an uncertainty of a few MeV, as noted in Sect. 4.3.

Experimental determination of kinetic energy associated with the spontaneous fission of ^{258}Fm to its fastest decay mode has large uncertainty but lies in the range of 202 to 220 MeV [4.21,4.22,4.29]. The kinetic energy calculated using Terrell's method for this decay is about (210 ± 5) MeV.

4.3 Spontaneous Fission of ^{258}Fm

Simultaneously, with the discovery that the primary decay modes in the spontaneous fission of ^{258}Fm and ^{259}Fm are symmetric [4.21], it was established that the spontaneous fission half-life of ^{258}Fm is very short $(3.8 \pm 0.6)\ 10^{-4}$ sec. [4.22]. As discussed in Chap. 5, Hooshyar and Malik [4.23] were able to account for the short half-life of ^{258}Fm as well as the fact that its dominant decay mode is symmetric using an empirical barrier and a kinetic energy of about 205 MeV. Subsequent calculations based on the energy-density functional theory [4.29] confirmed the earlier theoretical results. In particular, the calculation established that the fastest decay modes are symmetric and that one of the fastest modes is the decay to ^{130}Sn and ^{128}Sn. Since protons in tin form a closed shell, this daughter pair is likely to be spherical or has a small deformation. Hence, we present in Fig. 4.1, the external part of the potential

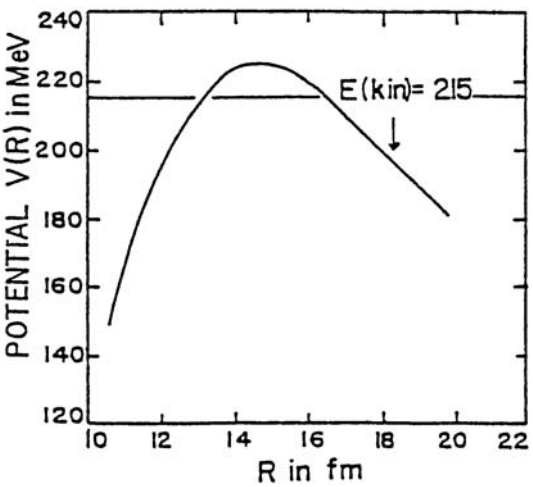

Fig. 4.1. The external part of the potential energy surface for the decay of ^{258}Fm to ^{128}Sn and ^{130}Sn in the sphere-sphere model. Asymptotic kinetic energy E(kin) refers to $E_{\rm kin}$ and is marked by a straight line and calculated using 4.2. The arrow indicates the scission point

energy surface calculated using the sphere-sphere model. Since the actual density distribution of ^{258}Fm is unknown, the potential energy surface has been calculated using a trapezoidal function. The scission radius, marked by an arrow, is at about 18.5fm. The half-life associated with this decay mode is calculated using a kinetic energy of 215 MeV, which is consistent with the one reported in [4.24] and shown in Fig. 4.1. The calculated half-life of 1.4×10^{-11} years [4.29] is in agreement with the observed value of 1.2×10^{-11} years [4.22]. The theoretical calculation, however, depends critically on the kinetic energy used. For example, the use of a smaller kinetic energy of 210 MeV would increase the half-life by an order of magnitude. Nevertheless, the theory does account for the very short half-life, and the fact that the dominant decay modes in the spontaneous fission of ^{258}Fm are symmetric.

4.4 The Potential-Energy Surface and Half-Lives of Superheavy Elements

The aim of this chapter is to determine the upper limit of spontaneous fission half-lives of a number of superheavy elements. To this end, it is necessary to calculate the half-lives of the decay to the fastest modes. The calculations indicate that in each of the cases considered here, the dominant decay modes are the symmetric ones [4.14, 4.15, 4.30]. As a result, we focus on these decay modes. It is likely that daughter pairs associated with these decay modes would be spheroidal. Nevertheless, we report here results of calculating potential-energy surfaces that are generated by superimposing both two spheres and two spheroids with a variable density distribution function of trapezoidal type. The details of the calculations are given in Chap. 3. The key assumptions related to these calculations are the following:

(a) The density distributions of the parent and daughter pairs are represented by a trapezoidal distribution schematically shown in Fig. 3.4. The central density of each member of a daughter pair, even though it is an excited state, is the same as that in its ground state.
(b) The eccentricity of each member of a daughter pair is the same, for the spheroid-spheroid model and zero for the sphere-sphere model.
(c) The parameters, c and t, are given by the ansatz described in equations 3.33 and 3.34 as a function of the separation distance for a particular daughter pair.
(d) The ratio of the surface to central region in the daughter ellipsoids remains the same as a function of angle. In other words, the density contours follow the shape of a particular ellipsoid.
(e) The penetration time is calculated using the expression (B.24) rather than the more accurate expression (B.23) which has an accuracy of about 10^{-22}.

As noted in Chap. 3, the Coulomb energy, $Z_1 Z_2 e^2/R_{\rm sc}$, at the scission radius, may not be equal to the kinetic energy, $E_{\rm kin}$. The energy balance equation at the scission point may, then, be written as:

$$E_{\rm kin} = Z_1 Z_2 e^2/R_{\rm sc} - f(A_p)\ . \tag{4.4}$$

Where A_p in (4.4) is the mass number of the parent nucleus. From the analysis of the observed kinetic energy spectra in the fission of the actinides, the empirically determined uncertainty is reflected by the function $f(A_p)$. The empirically determined function $f(A_p)$, for the sphere-sphere case is given by [4.14]

$$f(A_p) = -0.883A_p + 215.9\ . \tag{4.5}$$

And for the spheroid-spheroid case is given by [4.15]

$$f(A_p) = -0.9083A_p + 220.39\ . \tag{4.6}$$

We first examine the determination of the upper limit of spontaneous fission half-lives of the elements 112, 114, 118, and 126 in the spheroid-spheroid model. In the absence of any information on their density-distribution function, we have used a trapezoidal function. In Fig. 4.2 we have plotted the

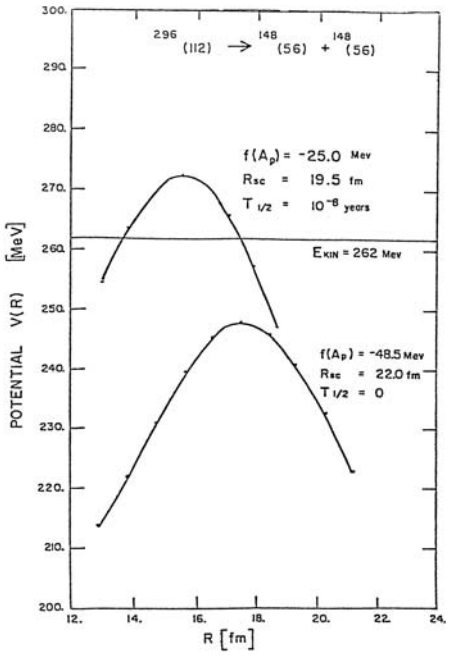

Fig. 4.2. Computed external barrier in the decay of $^{296}(112)$ to $^{148}(56)$ and $^{148}(56)$ for two different scission radii in the spheroid-spheroid model. $E_{\rm kin}$, calculated from (4.2), is shown as a straight line. $f(A_p)$ is calculated from 4.4 and 4.6 and $T_{1/2}$ is the half-life for the corresponding barrier

external barrier calculated in relation to $E_{\rm kin}$ computed in [4.15] for the decay of $^{296}(112)$ to $^{148}(56) + ^{148}(56)$ using $f(A_p)$ determined from (4.5). The scission radius, $R_{\rm sc}$, determined from (4.4) is 22.0 fm. The maximum of the barrier lies below the kinetic energy and as such the decay is instantaneous and the half-life is zero. In Table 4.1, we present an example of the sensitivity of the calculated half-life to the choice of the value of $f(A_p)$. $f(A_p)$ calculated using (4.5) for the parent nuclei $^{296}(112)$, $^{298}(114)$ and $^{310}(126)$ are, respectively, (-48.5), (-50.3) and (-61.2) MeV. Recognizing that the empirical value of $f(A_p)$ given by (4.5) was determined from the spontaneous fission of even-even actinide isotopes which primarily decay to asymmetric modes, whereas the superheavy elements decay primarily to symmetric ones, this empirical value may not be a suitable one for the decay of superheavy elements. Since the objective is to compute an upper limit of fission half-lives, this can be achieved by noticing the fact that the scission radii in the decay of these isotopes cannot be smaller than that in the decay of californium. (Since the experimentally determined kinetic energy in the decay of ^{258} Fm has large uncertainties, it is difficult to use it to determine scission radius). The scission radius in the decay of californium in its fastest decay mode is 19.5fm in the spheroid-spheroid case. Using this scission radius in (4.4) leads to a new set of $f(A_p)$ which are considerably smaller than those given by the $f(A_p)$ calculated above. As a consequence, the maxima of the external barriers exceed the asymptotic kinetic energy, an example of which is shown in Fig. 4.2. This leads to finite half-lives. The decay of $^{310}(126)$ to its fastest decay mode leads to zero half-life for a scission radius of 19.5 fm. However, a scission radius of 19.3 fm yields a finite but very small half-life, noted in Table 4.2. In Table 4.2, calculated half-lives for the fission of four superheavy

Table 4.1. Predicted spontaneous fission half-lives of superheavy elements 112, 114, and 126 to one of their fastest decay modes, in the spheroid-spheroid model. $f(A_p)$ calculated from (4.5) are noted in the second column in the first row in each case. Other values for $f(A_p)$ corresponds to the scission radii, $R_{\rm sc}$, noted in column(4). $E_{\rm kin}$ is calculated from (4.4) and (4.6). Half-lives, $t_{1/2}$ are noted in years and second in columns 5 and 6, respectively

Decay Mode	$f(A_p)$ (MeV)	$E_{\rm kin}$ (MeV)	$R_{\rm sc}$ (fm)	$t_{1/2}$ (year)	$t_{1/2}$ (sec)
$^{296}(112) \rightarrow {}^{148}(56) + {}^{148}(56)$	-48.5	262	22.0	0	0
	-25.0	262	19.5	2.2×10^{-9}	7.0×10^{-2}
$^{298}(114) \rightarrow {}^{154}(58) + {}^{144}(56)$	-50.3	270	22.2	0	0
	-25.0	270	19.5	1.5×10^{-6}	4.8×10^{1}
$^{310}(126) \rightarrow {}^{156}(64) + {}^{154}(62)$	-61.2	352	20.2	0	0
	-40.0	352	18.6	5.5×10^{-10}	1.7×10^{-2}
	-61.2	342	21.0	0	0
	-40.0	342	19.3	8.3×10^{-10}	2.6×10^{-2}

elements calculated with a scission radius of 19.5 fm for the decay of three elements and 19.3 fm for the decay of 126, in the spheroid-spheroid model are tabulated [4.30]. The calculations noted in Table 4.3 are done with a pre-formation probability of 10^{-5} for the decay of elements 112, 114, 118, and 126. As discussed in Chap. 2, the pre-formation probability for the odd-isotope $^{293}(118)$ is likely to be smaller than 10^{-5} at least by an order of magnitude, leading to a spontaneous half-life of 3.47×10^{-5} sec calculated using 10^{-6} for preformation probability, which is noted in Table 4.2.

Table 4.2. Predictions of the upper limits of spontaneous fission half-lives in years (column 6) and in seconds (column 7) for the decay of parent nuclei listed in column 1 to the daughter pair listed in column 2 in the spheroid-spheroid model. $E_{\rm kin}$, $R_{\rm sc}$ and $f(A_p)$ are, respectively, the asymptotic kinetic energy in MeV calculated using (4.1), scission radius in fm and the function defined by (4.2) and (4.6)

Parent	Daughter	$E_{\rm kin}$ MeV	$R_{\rm sc}$ (fm)	$f(A_p)$ (MeV)	$t_{1/2}$ (year)	$t_{1/2}$ (sec)
$^{296}(112)$	$^{148}(56) + ^{148}(56)$	262	19.5	−25.0	2.2×10^{-9}	6.95×10^{-2}
$^{298}(114)$	$^{148}(58) + ^{150}(56)$	270	19.5	−25.0	1.5×10^{-6}	$4.73 \times 10^{+1}$
$^{293}(118)$	$^{147}(59) + ^{146}(59)$	323	19.5	−35.0	1.1×10^{-12}	3.47×10^{-5}
$^{310}(126)$	$^{156}(64) + ^{154}(62)$	342	19.3	−40.0	8.3×10^{-10}	2.61×10^{-2}

Table 4.3. Computed half-lives $t_{1/2}$ associated with the decay of elements 112 and 114 to two of their fastest decay modes in the sphere-sphere model. The relation between $E_{\rm kin}$, the asymptotic kinetic energy, scission radius $R_{\rm sc}$ and $f(A_p)$ is given by (4.4). $f(A_p)$, calculated using (4.5) are noted in the first row of each decay mode. Other values of $f(A_p)$ are deduced from (4.4) using the corresponding $R_{\rm sc}$. Half-lives in year and second are noted in column 5 and 6, respectively

Decay Mode	$f(A_p)$ (MeV)	$E_{\rm kin}$ (MeV)	$R_{\rm sc}$ (fm)	$t_{1/2}$ (year)	$t_{1/2}$ (sec)
$^{296}(112) \rightarrow ^{148}(56) + ^{148}(56)$	−45.5	262	20.86	0	0
	−25.0	260		0	0
		262	19.1	1.0×10^{-10}	3.2×10^{-3}
		260		1.2×10^{-10}	3.8×10^{-3}
$^{298}(114) \rightarrow ^{144}(56) + ^{154}(58)$	−47.2	270	21.0	0	0
		268		0	0
$^{298}(114) \rightarrow ^{148}(56) + ^{150}(58)$	−25.0	270	19.1	1.9×10^{-8}	6.0×10^{-1}
		268		2.3×10^{-8}	7.3×10^{-1}

It is very likely that the limit of stability of superheavy elements is somewhere around element 116 or 118 since the scission radius of 19.5 fm is very conservative in determining the asymptotic kinetic energy for the decay of the element 118 to its fastest decay mode. It is safe to predict that the element 126 is unstable against spontaneous fission.

The situation is similar, if one uses the sphere-sphere model where the scission radius is usually slightly smaller compared to the one in the spheroid-spheroid case. For the decay of $^{296}(112)$ to $^{148}(56) + {}^{148}(56)$ and $^{298}(114)$ to $^{148}(56) + {}^{154}(58)$, $f(A_p)$ calculated from (4.6) are, respectively, (-45.5) and (-47.2) MeV. The computed external fission barrier for the decay of $^{296}(112)$ to $^{148}(56)$ and $^{148}(56)$, shown in Fig. 4.3 lies lower than the kinetic energy implying an instantaneous decay. However, the maximum of the barrier height is higher than $E_{\rm kin}$, if one uses a scission radius of 19.1 fm used in the decay of californium. The barrier shown using a scission radius of 18.5 fm in Fig. 4.3

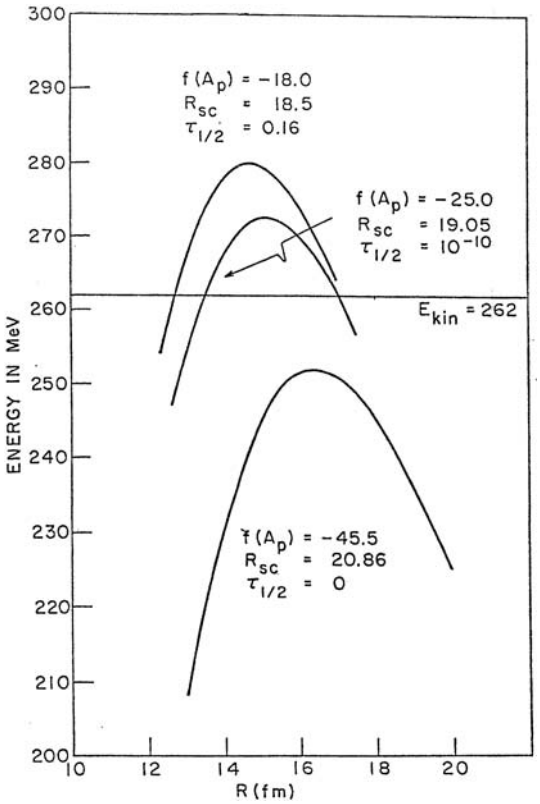

Fig. 4.3. Computed external barrier in the decay of $^{296}(112)$ to $^{148}(56)$ and $^{148}(56)$ for three different scission radii in the sphere-sphere model. $f(A_p)$ is calculated from (4.4). $T_{1/2}$ is the half-life for the corresponding barrier

is unrealistic and is included only for illustrative purposes, since this scission radius is less than the one used for fission of californium to one of its fastest decay modes.

In Table 4.3, we present the spontaneous fission half-lives of these two elements to their fastest decay modes which are symmetric in the sphere-sphere model. In the decay of $^{298}(114)$, two modes shown in the table, have essentially the same half-lives and compete with each other. In the same table, we have illustrated the dependence of half-lives on kinetic energy and scission radii in the sphere-sphere approximation. $f(A_p)$ in column two has been calculated using (4.4). A pre-formation probability of 10^{-5} has been used in each case. The spontaneous fission half-life of $^{310}(126)$ is zero, as noted in [4.13–4.15], for any realistic scission radius and is not tabulated.

Thus, both in the spheroid-spheroid and sphere-sphere model, the half-lives of the elements 112 to 118 are very short. The currently produced isotopes of these element in heavy-ion collision, reported in [4.16] differ from those used in Tables 4.1 to 4.3. However, the basic situation that the maximum barrier height is close to the expected kinetic energy does not change leading to the fact that the spontaneous half-lives of superheavy elements are short and close to a fraction of a few seconds.

4.5 Conclusion

Within the framework of the energy-density functional approach it is concluded that the spontaneous fission half-lives of super-heavy elements are much less than a year, as already noted in 1972 [4.13]. Although the calculations are presented only for a few isotopes, from the general features of these calculations, it is evident that this conclusion stands for all super-heavy elements and isotopes. It is very likely that one may have reached the limit of stability against spontaneous fission at element 118 or around that. All experimental evidence, so far, confirm this prediction.

References

1. V.M. Strutinsky, Nucl. Phys. A **95**, 420 (1967).
2. A. Sabiczewsky, F.A. Gareev and B.N. Kalinski, Phys. Lett. **22**, 500 (1966).
3. V.M. Strutinsky, and Yu. A. Muzychka, *Proc. Int'l Conf. On the Physics of Heavy-ions* (Dubna, 1966).
4. C.Y. Wong, Phys. Lett. **21**, 688 (1966).
5. M. Meldner, Ark. Fys. **36**, 593 (1967).
6. E. Rost, Phy. Lett. B **26**, 184 (1967).
7. S.G. Nilsson, J.R. Nix, A. Sobiczewski, Z. Symanski, S. Wyech, C. Gustafson and P. Møller, Nucl. Phys. A **115**, **545**(1968).
8. S.G. Nilsson, C.F. Tsang, A. Sobiczewski, Z. Symanski, S. Wyech, C. Gustafson, I.L. Lamm, P. Miller and B. Nilsson, Nucl. Phys. A **131**, 1 (1969).

9. J. Grunmann, U. Mosel, B. Fink and W. Greiner, Z. Physik **228**, 371 (1969).
10. M. Bolsterli, E.O. Fiset, J.R. Nix and J.L. Norton, Phys. Rev. C **5**, 1050 (1972).
11. F.B. Malik and P.C. Sabatier, Helv. Phys. Acta **46**, 303 (1973).
12. M.A. Hooshyar and F.B. Malik, Phys. Lett. B **38**, 495 (1972); *ibid* **55**, 144 (1975).
13. F.B. Malik, *Magic Without Magic: John Archibald Wheeler*. Ed. J.R. Klauder (W.H. Freeman, 1972) p. 47; I. Reichstein and F.B. Malik, Bull. Am. Phys. Sec. **18**, 627 (1973); M.A. Hooshyar and F.B. Malik, Bull. Am. Phys. Sec. **18**, 628 (1973).
14. I. Reichstein and F.B. Malik, Ann. Phys. (N.Y.) **98**, 322 (1976).
15. I. Reichstein and F.B. Malik, *Superheavy Element* ed. M.A.K. Lodhi (Pergamon Press, New York, 1978).
16. Yu. Ts. Oganessian, M.G. Itkis and V.K. Utyonkov, *Fission Dynamics of Atomic Clusters and Nuclei*, eds. J. daProvidencia, D.M. Brink, F. Karpechine and F.B. Malik (World Scientific, 2001) p. 275.
17. V. Ninov, K.E. Gregorich, W. Loveland, A. Ghiorso, D.C. Hoffman, D.M. Lee, H. Nitsche, W. Swiatocki, U.M. Kirbach, C.A. Laue, J.L. Adams, J.B. Patin, D.A. Shaugnessy, D.A. Strellis and P.A. Wilk (Phys. Rev. Lett. **83**, 1104 (1999).
18. F.G. Werner and J.A. Wheeler, Phys. Rev. **109**, 126 (1958).
19. N.B. Gove and M.J. Martin, Private Communication (1969).
20. M.D. High, R. Malmin, and F.B. Malik, Helv. Phys. Acta **45**, 738 (1972).
21. W. John, E.K. Hulet, J.F. Wild, R.W. Longheed and J.J. Wesloshi, Phys. Rev. Lett. **27**, 45(1971).
22. E.K. Hulet, J.F. Wild, R.W. Longheed, J.F. Evans and B.J. Qualheim, Phys. Rev. Lett. **26**, 523 (1971).
23. M.A. Hooshyar and F.B. Malik, Helv. Phys. Acta **46**, 724 (1973).
24. E.K. Hulet, *50 Years With Nuclear Fission* eds. J.W. Behrens and A.D. Carlson (American Nucelar Society, 1989) p. 533.
25. J. Terrell, Phys. Rev. **174**, 880(1962).
26. P. Møller, J.R. Nix, W.D. Myers, W.J. Swiatecki, At. Data Nucl. Data **59**, 185 (1995); *ibid* **66**, 131 (1997).
27. W.D. Myers and W.J. Swiatecki, Nucl. Phys. **81**, 1 (1966).
28. A.E.S. Green, Phys. Rev. **95**, 1006 (1954).
29. I. Reichstein and F.B. Malik, Condensed Matter Theories **8**, 243 (1993).
30. I. Reichstein and F.B. Malik, *Fission Dynamics of Atomic Clusters and Nuclei*, eds. da Providencia, Brink, Karpechine and Malik (World Scientific, 2001) p. 127.

5 Empirical Barrier and Spontaneous Fission

5.1 Introduction

In the previous chapter we have established the existence of a barrier just prior to the scission point in the potential energy surface of a daughter pair in the fission process as a result of the formation of a neck of low density nuclear matter. This barrier is the consequence of the observed fact that the nuclear density distribution function has a significant surface region of 2.2 to 3.0 fm. The liquid drop model with its underlying assumption of a constant nuclear density cannot incorporate the effect of this low density neck prior to scission in calculating the potential energy surface of a daughter pair. Hence, the energy-density functional approach has been taken to calculate the potential energy surface between two members of a daughter pair. To compute such a barrier for each daughter pair using the energy-density functional approach is very time consuming and costly in terms of computer time. Hence, we develop in this chapter an empirical potential energy surface depending analytically on mass numbers and atomic numbers of parents and daughter pairs.

Apart from the calculation of the potential energy surface done in Chap. 3 the necessity of such an external barrier can be ascertained from an analysis of observed kinetic energy, T_k, of a daughter pair. Experimentally, the observed kinetic energy lies between 20 to 40 MeV below the Q-value associated with a particular decay mode. The Q-value is positive and as such the parent nuclei are in a meta-stable state. Taking these two conditions into account, Malik and Sabatier [5.1] have proven that the barrier derived in Chap. 3 is mathematically consistent with the conditions (a) $T_k < Q$ and (b) the matastablility of parent nuclei. The details of the proof are given in Appendix A but a simplified version of the analysis is discussed in Sect. 5.2 of this chapter.

We may note that the theory discussed in Chap. 3 has basically two parts. Since in the fission process a parent nucleus decays to many daughter pairs, there is a preformation probability for each daughter pair. This is followed by a penetration through a barrier determined by the physical characteristics of a particular daughter pair, such as density distribution. The preformation probability has been calculated in Chap. 3 from the elementary shell model to be approximately 1.6×10^{-5} for a typical case [5.2]. In the calculation of half-lives done in Sect. 5.3, we have kept this constant for all decay modes.

The theory presented in Chap. 3, deals with the decay process using a set of coupled equations. In principle, the decay to various excited states of a particular daughter pair is possible and there is a coupling among various channels. Apart from the diagonal part of the matrix elements of the two-body potential in each channel, the net potential energy surface has a contribution from the terms representing the coupling of that channel with other channels. For the calculation of spontaneous fission half-lives and the associated mass, charge and kinetic energy spectra, the consideration of the channel coupling is not important but it plays an important role in our understanding of the dynamics associated with the decay of fission isomers as discussed in Chap. 8.

The details of the interior of the potential, determined from the energy-density functional theory in Chap. 3 do not influence the penetration probabilities in a significant way as discussed in Appendix A [5.1]. The critical part of the potential for half-life calculation is the external barrier just prior to scission generated by the neck of low-density nuclear matter. This observation simplifies the task of determining an empirical barrier considerably. This is done in Sect. 5.2. Calculated half-lives, mass and charge distributions in spontaneous fission and kinetic energy spectra using this barrier are presented in Sect. 5.3 for ^{234}U, ^{236}U and ^{240}Pu and compared to the corresponding data. A detailed discussion is presented in Sect. 5.4.

5.2 The Nature of the Empirical Barrier

The fission phenomenon as envisioned by the model emphasizes, or idealizes, the effects that (i) the nuclear density distribution function is not constant but varies as a function of nuclear radius and (ii) a density reorganization takes place as a daughter pair is formed out of a parent nucleus. This is necessarily so because both the daughter pair and its parent have a density distribution given by Fermi functions and their central densities are nearly equal. The calculation of the barrier in the previous chapter within the framework of the energy-density functional formalism emphasizing the effect of this density reorganization leads to an external thin barrier. It is one of the main goals of this chapter to establish that if a thin external barrier exists in a region between the saddle and scission point, the detailed behavior of the potential surface near the equilibrium position or saddle point does not have any discernible effect on half-lives. This fact which has been proven by Malik and Sabatier [5.1], indicates that one need not be concerned about the fine details of the potential surface in the interior of the fission barrier for computing half-lives and mass distributions in the fission process. This observation has also been checked by performing actual computer modeling. This important realization enables one to determine a reasonable empirical barrier that is suitable to determine half-lives, fission widths, mass, charge

and kinetic energy spectra in the spontaneous fission of a nucleus, which are in good agreement with experimental results [5.3–5.5].

In order to justify the above statements and also deduce some information about the nature of the fission barrier for the case of spontaneous and binary fission, let us consider the case of a parent nucleus of mass number A and atomic number Z decaying spontaneously to a daughter pair of mass numbers, A_1 and A_2, and charge numbers, Z_1 and Z_2. The conservation of total energy for this reaction leads to the following equation

$$M(A,Z)c^2 = M(A_1,Z_1)c^2 + M(A_2,Z_2)c^2 + Q \tag{5.1}$$

where, M is the mass of each nucleus and Q is the total amount of energy released during this decay when each member of the daughter pair is in the ground state. Q may be calculated from the observed masses from any standard mass formula such as that of Green [5.6] or Myers and Swiatecki [5.7] or Möller et al. [5.22]. The experimental fact is that both nuclei of a daughter pair are predominantly emitted in excited states and as such their kinetic energy, T_k, is less than Q. Based on experimental information on pre-gamma and pre-neutron emissions, one can conclude that T_k is 20 to 40 Mev less than the Q-value of the decay. This is a key observation based on experiment. The other key fact is that the parent nucleus is in a meta-stable state prior to fission. Since spontaneous fission involves a barrier-penetration problem, we can also conclude that the maximum of the interaction potential must be higher than the asymptotic kinetic energy T_k. Using these three basic but important observations, we would like to examine the conclusions that can be drawn about the nature of the fission barrier. In order to keep the discussion simple and present the essential points, we assume the tunneling stage of the fission can be regarded as a simple tunneling problem associated with the radial Schrödinger equation with zero angular momentum. For a more general treatment of this decay problem, the reader is referred to the appendix based on [5.1]. In this simplified model of the tunneling stage of fission, the equation of motion is given by

$$\frac{d^2u(R)}{dR^2} = q^2(R)u(R) \tag{5.2}$$

$$q^2(R) = \frac{2\mu}{\hbar^2}[V(R) - E] \,. \tag{5.3}$$

Here Φ is the reduced mass, E is the total energy, being equal to the asymptotic kinetic energy T_k, $V(R)$ is the potential and $u(R)$ is R times the radial wave function. The regular solution satisfies the following boundary conditions near the origin

$$u(0) = 0 \,. \tag{5.4}$$

We now examine the necessary condition for the existence of a meta-stable state in context with a barrier penetration problem. The potential at $R = 0$ is the Q-value of the decay process and since $Q > T_k$, which is equal to E,

therefore $q^2(R=0) = 2\mu(Q - T_k)/\hbar^2 > 0$. Hence $R = 0$ is not a turning point. Let R_0 be the largest value of R at which $q^2 = 0$. The question to be investigated is whether a meta-stable state could be formed if $q^2(R) > 0$ for all values of $R < R_0$, where R_0 is the only turning point in the region $0 < R < R_0$. Since $q^2(R) > 0$ for all values of $R < R_0$, it then follows from (5.2) and (A.8) that $d^2u/dR^2 > 0$ for all values of $R < R_0$. Making use of the relation

$$\frac{du(R)}{dR} = \int_0^R dR' \frac{d^2u(R')}{dR'^2} \tag{5.5}$$

and since $d^2u/dR^2 > 0$ in the entire domain of integration, we find

$$\frac{du(R)}{dR} > 0 \quad \text{for all} \quad R < R_0 \; . \tag{5.6}$$

The condition (5.6) means that $du(R)/dR$ can not be zero in the region $0 < R < R_0$. As a result the wave function within the barrier does not have a maximum and bend over to exhibit resonant structure, which is critical for the existence of a meta-stable state. In fact, the wave function keeps on growing and can not have any node in the region $0 < R < R_0$ which is a necessary condition for the existence of a meta-stable state. Thus, the Malik-Sabatier theorem states that the necessary condition for the existence of a meta-stable state in a barrier penetration problem is that $q^2(R) < 0$ at least at one point inside the barrier. A potential $V(R)$ consistent with this finding is shown in Fig. 5.1. Of course Fig. 5.1 is only one possible example and the main thing to be emphasized in this figure is that we must at least have one region where $V(R) < E$ which precedes the region where $V(R) > E$, i.e.

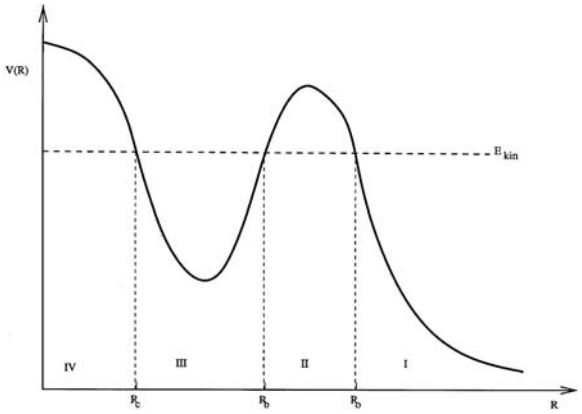

Fig. 5.1. A schematic potential barrier commensurate with the condition of meta-stability of parent nucleus and observed average kinetic energy in spontaneous fission

region III in Fig. 5.1. The existence of region III is critical for the formation of a meta-stable state if $Q > T_k$. Obviously, there could be more than one region in the domain $0 < R < R_0$, where the potential could be less than T_k, but at least one such a region needs to exist for the occurrence of a meta-stable state.

We note that the potential energy surface derived from the energy-density functional formalism is similar to the schematic potential of Fig. 5.1 and is compatible with the existence and decay of a meta-stable state.

The nature of the potential $V(R)$ can be studied further if we try to find the half-life, T, related to barrier penetration of the meta-stable state. A way to find the relation between T and $V(R)$ is to consider the energy derivative of the phase shift associated with the scattering by the potential. Following, for example Goldberger and Watson [5.8], we find that

$$T = 2\hbar \frac{d\delta}{dE} = \sqrt{2\mu/E}\, \frac{d\delta}{dk} \tag{5.7}$$

where the wave number $k = \sqrt{2\mu E/\hbar^2}$ and δ is the phase shift of the regular wave function in the asymptotic region

$$u(R) = A(k)\sin(kR - \eta \log 2kR + \delta + \sigma), \quad \text{for} \quad R \to \infty \tag{5.8}$$

with $\eta = \mu Z_1 Z_2 e^2/\hbar k$ and $\sigma = \arg\Gamma(1 + i\eta)$ being Sommerfeld's Coulomb parameter and phase-shift, respectively. Equation (5.8) can be considerably simplified [5.1] if we neglect terms of the order of k^{-1} in evaluation of the derivative of phase-shift $d\delta/dk$. Such an approximation in (5.8) results in the following relation

$$T = \sqrt{2\mu/E}(2/A^2) \int_0^{R_0} u^2(R) dR\,. \tag{5.9}$$

It should be emphasized that in deriving (5.9), no detailed information about the form of the potential $V(R)$ has been used and the formula is not based on any other aspect of the approximation except for the stated fact that it is correct to within the order of k^{-1}. Of course in order to make further use of (5.9) we need to have some general form of the potential in mind. Let us assume that $V(R)$ follows a form as given in Fig. 5.1. In that case it is evident that the wave function $u(R)$ is very small in the region $0 < R < R_c$ and therefore will not contribute significantly to the integral in (5.9). In other words integration in (5.9) can be carried out from R_c to R_0 and the detailed form of the potential in the region IV will not play any important role in determining half-lives. Using the JWKB approximation we may express the wave function in terms of $V(R)$ and make use of (5.9) to determine T in terms of the potential. We have, then, the expression [5.1, 5.9]

$$T = 2\mu \left[\int_{R_c}^{R_b} \{E - V(R)\}^{-1/2} dR\right] \exp\left[2\int_{R_b}^{R_0} \left\{\frac{2\mu}{\hbar^2}(V(R) - E)\right\}^{1/2} dR\right]\,. \tag{5.10}$$

The half-life associated with the decay does not depend on the details of the potential at every point. All potentials yielding the same value of the two integrals involved in (5.10) would give the same half-life. In other words, all potentials having the same area below E in the region $R_b \geq R \geq R_c$ and above E in the region $R_0 \geq R \geq R_b$ would give the same half-life. However, it is important that the chosen empirical potential be consistent with the three criteria stated earlier which are relevant for the existence of a meta-stable state. Clearly, there should be a region in the potential where $V(R) > E$; otherwise the nucleus would decay instantaneously. There should also be at least one region where $V(R) < E$ so that a meta-stable state can exist when the observed Q-value is greater than E.

An empirically determined potential consistent with these criteria must also reproduce observed mass and charge spectra in spontaneous fission of many elements along with the appropriate observed kinetic energy spectrum. Mass and charge dependence of such a potential must be explicit in order to achieve this goal. This difficult task becomes, however, somewhat easier from the observation that the first integral in (5.10) does not contribute significantly to half-lives and as such an approximate choice of the potential in the region $R_b \geq R \geq R_c$ is sufficient for our purpose. Furthermore, the nature of the potential in the interior region i.e. $R < R_c$ has also very little consequence in determining decay probabilities. For fission dynamics, the determining region is the potential between R_b and R_0. However, all potentials having the same area above E in this region would yield the same results. R_0 is the separation point and as such is the sum of two radii of a daughter pair of mass number A_1 and A_2 and should be $r_0({A_1}^{1/3} + {A_2}^{1/3}) + t$, with t being the sum of the surface thicknesses. From the analysis of the energy-density functional calculation of the barrier, one may determine R_c to be that point where the central part (i.e. the region of constant density part of the density distribution function) of the density of each member of a daughter pair barely touches each other. For most of the daughter pairs, this distance is about the same. (Actually, this depends on ${A_1}^{1/3} + {A_2}^{1/3}$ but the details of this part of the potential are not critical.) Based on these analyses, we have chosen the following empirical barrier $V(R)$,

$$V(R) = V_D(R) + V_C(R) \; . \tag{5.11}$$

with

$$V_D(R) = \begin{cases} V & \text{for} \quad R < R_c \\ V_0 & \text{for} \quad R_c < R < R_b \\ V_{\text{coul}} \exp[(R - R_0)/d] & \text{for} \quad R_b < R < R_0 \\ Z_1 Z_2 e^2 / R & \text{for} \quad R_0 < R \end{cases} \tag{5.12}$$

where $V = 200\,\text{Mev}$ which is about the Q-value of the reactions under consideration, $R_c = 8$ fm, $V_0 = V_{\text{coul}} - 60\,\text{Mev}$, $d = 5.0$ fm, $V_{\text{coul}} = Z_1 Z_2 e^2 / R_0$, $R_b = R_0 + d \log(V_0 / V_{\text{coul}})$ and $R_0 = r_0({A_1}^{1/3} + {A_2}^{1/3}) + t$, with $\text{r}_0 = 1.3 + 0.13\ g(A_1,$

$A_2)$, $t = 3.7$ fm and $g(A_1, A_2) = \exp(-0.036(|A_1 - A_2|)^{1.6}$. Although the effective coupling potential V_C need not be introduced if we are only interested in discussing the spontaneous fission, in order to understand the dynamical properties of isomer fission one needs to introduce this coupling potential which we have parameterized to be

$$V_C(R) = \lambda \exp\{-|(R - R_0)/c|^3\} \tag{5.13}$$

with $\lambda = 4.56 + 36.1\, g_0(A)$ MeV, $c = 4.8 - 0.6 g(A_1, A_2)$, and $g_0(A) = \exp(-|(175 - A)/75.3|^{9.5})$.

In (5.13), A, A_1, and A_2 are, respectively, mass numbers of the parent and two daughter nuclei. Except for the small correction $g(A_1, A_2)$ this is the same barrier used in [5.3–5.5]. In fact, for the fission to asymmetric decay modes $g \to 0$ and we get exactly our old barrier. This slight modification affects, however, the mass yields near the symmetric modes. Neither the spontaneous half-lives nor the mass yields spectra in spontaneous fission are influenced by this slight change because they are determined by the asymmetric decay modes accounting for most of the yields, and the percentage mass yields are very low for the spontaneous fission to symmetric modes. Quite often the experimental mass yields for symmetric modes are less than 0.1 percent, and have considerable uncertainties. However, in neutron induced fission, the percentage mass yields to symmetric modes becomes significantly large and is sensitive to the details of the barriers relevant to these yields. Thus, the information obtained in induced fission by neutrons of tens of MeV incident energy is a significant one in learning about that part of the barrier which is relevant to the decay to symmetric modes. On the other hand, data on spontaneous fission of these nuclei are not good enough to determine the details of the barrier contributing primarily to mass yields near symmetric decay modes. The value of λ used here is not significantly different from that used in [5.3–5.5]. The slight change in λ is motivated from the investigation in [5.3] indicating that λ might depend on the parent nucleus. For $A = 234$, 238 and 240, $\lambda = 37.3$, 36.1 and 32.7, respectively, which is very close to values of 37.4, 35.9 and 32.9 needed to obtain the best fit to the data in [5.3]. The value of λ used here provides equally good fit, as discussed in Sect. 5.4. The slight difference in the definition of the functional form of $g(A_1, A_2)$ actually improves the results.

The details concerning the coupling potential and the intimate relation between spontaneous and isomer fission will be discussed in Chap. 8, when we deal with the theory of isomer fission as envisioned by our model. V_c in this chapter may be viewed as a part of the empirical potential which contributes to the potential barrier for spontaneous fission. The values of the four parameters R_0, d, λ, c are determined from the observed partial half-life of the spontaneous and isomer fission of $^{240}\mathrm{Pu} \to {}^{142}\mathrm{Ba} + {}^{98}\mathrm{Sr}$. Having found the desired values of these parameters [5.3, 5.4], we have kept them fixed for all other calculations carried out for different elements. A small dependency

of these parameters on the mass of the parent nucleus has been observed for elements with masses much greater than that of ^{240}Pu and this variation has been taken into account by introducing the factors $g_0(A)$ and $g(A_1, A_2)$. As can be seen, the effect of $g(A_1, A_2)$ on the parameters is minimal. Its value is almost zero for asymmetric decay modes and it has some effect only for symmetric decay modes. It should be also made clear that values presented for these parameters are not the only ones which can produce satisfactory half-lives, mass, charge and kinetic energy spectra specially for spontaneous and thermal neutron induced fission. In fact, in our original calculations [5.3] and [5.10] the values of $d = 3.2$ fm, $t = 3.0$ fm and $g(A_1, A_2) = \exp(-0.036(|A_1 - A_2| - A + 4[A/4])^{1.6})$ have been used, where $[A/4]$ stands for rounding up $A/4$ to the nearest integer. This choice of parameters could also reasonably explain data on spontaneous and thermal neutron induced fission. However, for the analyses of data in induced fission by neutrons of higher energies using a statistical approach as presented in Chap. 6, the choice of parameters as given by (5.11) and (5.12) is better for a wide range of the incident neutron energy. Of course, for spontaneous and thermal neutron induced fission, the results for the two different set of parameters given above do not differ appreciably.

Before discussing the results of the calculations of half-lives, mass and charge distributions using the empirical barrier in Sect. 5.4, we present in Sect. 5.3, Terrell's empirical formula for determining the average kinetic energies of daughter pairs from Q-values. These have been used wherever the observed values are not available.

5.3 Empirical Formula for Kinetic Energy

Based on the analysis of data, Terrell [5.12, 5.13] has pointed out that the kinetic energy associated with the decay to a particular daughter pair may be determined from the corresponding Q-value. The relation between kinetic energy, E, Q-value and available excitation, $E(exc)$ of a daughter pair is given by

$$E = Q - E(exc) \; . \tag{5.14}$$

$E(exc)$ can be obtained from knowledge of the number of neutrons and gamma rays emitted from each fragment, as follows:

$$E(exc) = \sum_{n(i),i} [B(i, n(i)) - (v(i)n(i) + \gamma(i))] \tag{5.15}$$

where $i = 1$, 2 and B $(i, n(i))$ is the binding energy of the $n(i)$th neutron emitted from the i-th fragment with $i = 1$ and 2. The latter can be obtained either from observed data on separation energy or from a mass formula. $\gamma(i)$ is the energy of prompt gamma rays emitted from the i-th fragment and is estimated by Terrell to be approximately equal to $(1/2)(B(i, n(i))$.

$\nu(i)$ and $n(i)$ are, respectively, the number of emitted neutrons and the average center of mass kinetic energy of emitted neutrons from the i-th fragment. Terrell's analysis indicates $n(i)$ to be about 1.4 MeV and

$$v(i) \approx \begin{cases} 0.08(A(i) - 82) & \text{if} \quad 82 < A < 126 \\ 0.1(A(i) - 126) & \text{if} \quad 126 < A \,. \end{cases} \tag{5.16}$$

Instead of using (5.16) one may also get the values of $\nu(i)$ from the compilation of neutron emission data e.g. in [5.12, 5.13]. It is interesting and important to note that in the first approximation $\nu(i)$ does not depend on the parent nucleus but it depends on the individual members of a daughter pair [5.12–5.14]. Thus, the shell structure of daughter pairs play an important role in determining $\nu(i)$.

To obtain the average kinetic energy associated with a daughter pair characterized only by mass numbers A_1 and A_2, one must calculate kinetic energy for all isobars having mass numbers A_1 and A_2 and average over them.

5.4 Spontaneous Fission Half-Lives, Mass and Charge Spectra

5.4.1 Spontaneous Fission Half-Lives

Data on spontaneous fission half-lives and average kinetic energies associated with the decay process are available. Within the context of the theory described here, half-lives of spontaneous fission are a product of (preformation probabilities) and (half-lives associated with decay to various modes). Although the preformation probabilities associated with the formation of different clusters of daughter pairs depend in principle on the masses and charges of parents and of the particular daughter pair, such dependence is expected to be minute compared to the large variation of half-lives observed in spontaneous fission. We, therefore, adopt here the value of 10^{-5} for all decay processes. The barrier penetration probabilities vary sharply with mass and atomic numbers of parents and daughter pairs. However, the spontaneous half-lives are essentially determined by a few fastest decay modes. For the calculation of half-lives, it is sufficient to concentrate on these fastest modes in our calculation. Calculations of half-lives are sensitive to the kinetic energy because of the relative thinness of the outer barrier – a 2 to 5 Mev change in kinetic energies could change half-lives by a few orders of magnitude. Hence, we have presented calculated values in Table 5.1 for the range of kinetic energy consistent with the observed error bars. It is impressive to note that the theoretically calculated half-lives agree with the observed ones over 27 orders of magnitude using the range of average kinetic energy. The numerical values of half-lives are very sensitive to the choice of kinetic energy, yet the theory correctly accounts for both of them.

Table 5.1. Comparison between calculated half-lives in years y, and average kinetic energies and the observed ones. Data marked with (a), (c), (e) are from [5.17], (b) from [5.18], (d) from [5.19], (f) from [5.20], (g) from [5.21], (h) from [5.22], , (i) from [5.26], (j) from [5.23], (k) from [5.24], (l) from [5.31], (m) from [5.25], (n) from [5.27], (o) from [5.28], (p) from [5.30] and (q) from [5.29]

Parent	K.E. (exp) MeV	K.E. (th) MeV	S. F. Half-life (exp) y	S.F. Half-life (th) y
^{234}U	163 ± 2 (a)	161	1.60×10^{16} (b)	2.0×10^{17}
		163		2.0×10^{15}
		165		2.0×10^{13}
^{236}U	165 ± 2 (c)	163	2.00×10^{16} (d)	2.0×10^{15}
		165		2.0×10^{13}
		167		2.0×10^{11}
^{240}Pu	172 ± 2 (e)	170	1.34×10^{11} (f)	5.0×10^{13}
		172		6.0×10^{11}
		174		7.0×10^{9}
^{244}Cm	185.5 ± 5 (g)	183	1.34×10^{7} (h)	1.0×10^{9}
		185		2.0×10^{7}
		187		3.0×10^{5}
^{250}Cm		180.5	2.00×10^{4} (i)	2.2×10^{6}
		182.3		3.1×10^{4}
^{246}Cf	195.6 ± 2.0 (j)	196	2.00×10^{3} (k)	3.8×10^{3}
^{252}Cf	186.5 ± 1.2 (l)	186.7	85.5 (m)	86.0
^{254}Cf	186.1 ± 2.0 (n,j)	188.6	1.78×10^{-1} (i)	2.4×10^{-1}
^{258}Fm	$190 \sim 200$(p)	200.7	3.8×10^{-11} (q)	3.90×10^{-9}
		203.3		5.10×10^{-11}

The difference in half-lives among even-even, odd-even, even-odd and odd-odd nuclei has, in this theory, been attributed to the sharp difference in the preformation probabilities among these groups [5.2]. The situation is very similar to the role of preformation in alpha decay where the large difference in half-lives between neighboring odd-even and even-even isotopes is largely due to the difference in the overlap of their wave function.

5.4.2 Mass Spectra

A most striking feature of the fission process, spontaneous or induced, is the fact that a parent nucleus decays into many daughter pairs. Fission involves decay to neither symmetric nor asymmetric modes but decays to many modes and has a mass spectrum of the decay products. Usually the decay yields are measured as a function of mass number. Associated with each mass number of the decay products, there is a kinetic energy which is less than the Q-value implying that daughter pairs are emitted in excited states. Thus, associated with a mass spectrum, there is also a kinetic energy spectrum. A successful theory should not only explain half-lives with proper average kinetic energy

but must also account for the mass spectrum of daughter pairs with the appropriate kinetic energy spectrum. Calculation of yields for a given mass involves calculating decay probabilities to all isobars with the same mass and then averaging over them. It also involves calculating Q-values for all isobars and averaging over them. Similarly, measured kinetic energy for a given mass is an average of all kinetic energies of all nuclei having the same mass. Thus, we have concentrated on the data where both the mass and the kinetic energy spectrum are measured in the same experiment.

In Fig. 5.2 we have plotted the experimental data on percentage mass yields of the heavy fragment group in the spontaneous fission of ^{240}Pu, as a function of heavy fragment mass, M_H, along with the data on the average kinetic energy associated with each mass number. The data are plotted as solid lines. The percentage yields spectrum is symmetric about mass number 120 and hence, the data on the light fragments have not been shown. The theoretical calculations can reproduce the mass spectrum using a kinetic energy spectrum which at some places deviate from data by a few MeV but reproduce the general trend. The theoretical percentage mass yields curve calculated using the barrier (5.11) along with the average kinetic energies used in calculating the yields are shown as solid dots. Considering that the typical errors in experimental determination of kinetic energy are a few MeV, the agreement is very good for the set of data.

In Fig. 5.3 and Fig. 5.4, we have compared calculated percentage yields, noted as solid dots, with the observed ones, drawn as solid lines, in the

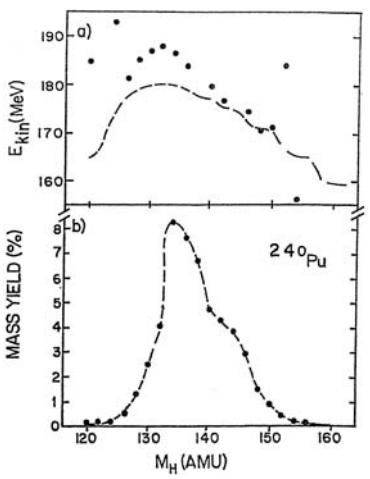

Fig. 5.2. The average kinetic energy $E_{\rm kin}$ in MeV, and percentage mass yields spectra, SFS yield (%) associated with spontaneous fission of ^{240}Pu. The data taken from [5.33] are shown in *solid* lines. The *broken* line in the upper insert is the average kinetic energy used in calculating percentage mass yields shown as *solid* dots in the lower insert

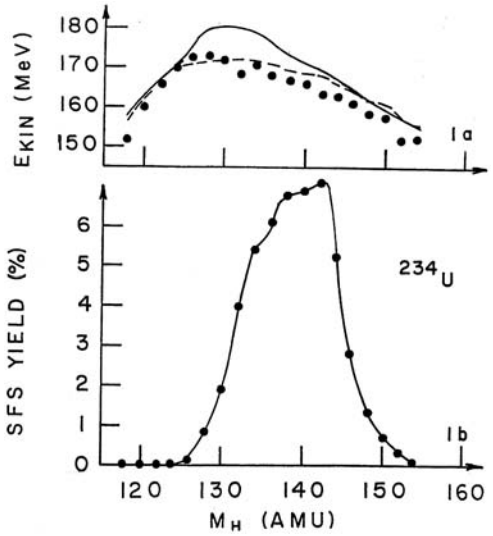

Fig. 5.3. The average kinetic energy E_{kin} in MeV, and percentage mass yields spectra, SFS yield (%) associated with spontaneous fission of ^{234}U. The data taken from [5.34] are shown as *solid* lines. The *broken* line in the upper insert is the average kinetic energy used in calculating percentage mass yields shown as *solid* dots in the lower insert

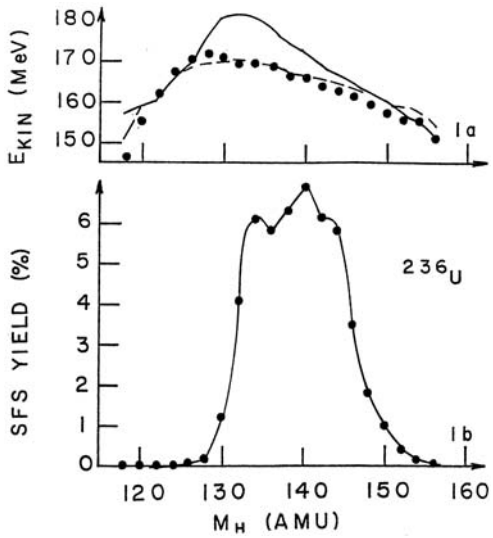

Fig. 5.4. The average kinetic energy, E_{kin} in MeV, and percentage mass yields spectra, SFS yield (%), associated with spontaneous fission of ^{236}U. The data taken from [5.34] are shown as *solid* lines. The *broken* line in the upper insert is the average kinetic energy used in calculating percentage mass yields shown as *solid* dots in the lower insert

spontaneous fission of ^{234}U and ^{236}U. (The data are actually for thermal neutron induced fission of ^{233}U and ^{234}U, but are very close to the data on spontaneous fission.) The average kinetic energies used in the calculation of percentage yields are shown as dots along with the observed ones, marked as a solid line, in the upper half of the figures. A similar comparison of the data and calculation for the spontaneous fission of ^{252}Cf is done in Fig. 5.5. In the same figure we have also plotted the calculated kinetic energy spectrum associated with the decay of ^{252}Cf obtained from Terrell's theory, i.e., the equations (5.15) and (5.16). The observed mass spectrum is well accounted for by the calculation using a kinetic energy spectrum which reproduces the shape and magnitude of the experimental spectrum very well, except in a few cases where the difference between the data and calculated kinetic energy deviates only by few MeV.

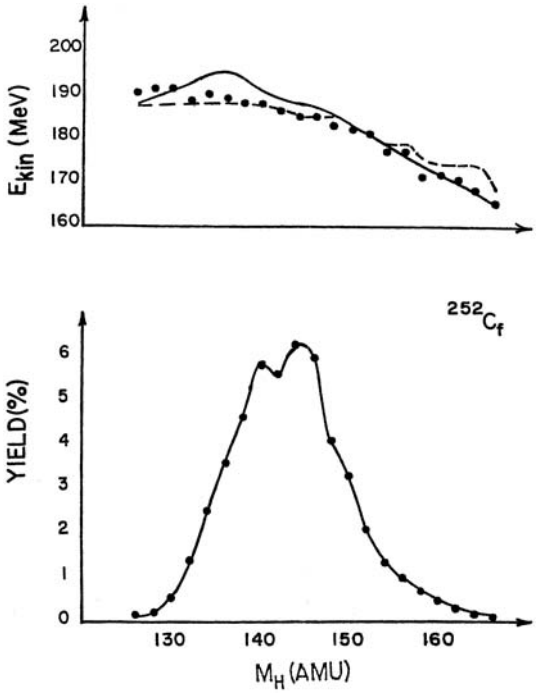

Fig. 5.5. The average kinetic energy, $E_{\rm kin}$ in MeV, and percentage mass yields spectra, SFS yield (%), associated with spontaneous fission of ^{252}Cf. The data on percentage mass yields taken from [5.34] are shown as *solid* lines. The *broken* line in the upper insert is the average kinetic energy used in calculating percentage mass yields shown as *solid* dots in the lower insert. The *solid* dots in the upper insert is the $E_{\rm kin}$ calculated from the Terrell's prescription (5.14)

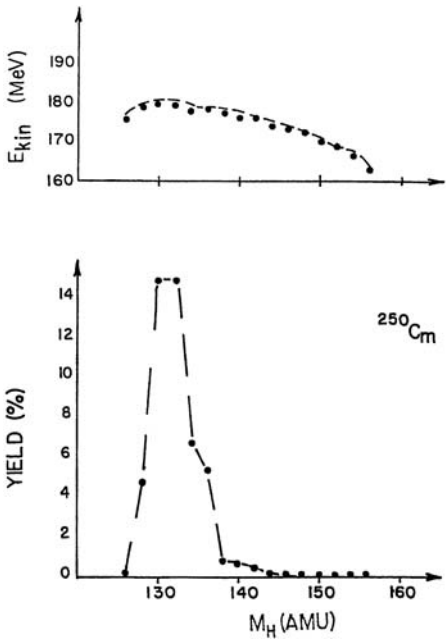

Fig. 5.6. The calculated percentage mass yields, SFS yield (%), in the spontaneous fission of ^{250}Cm taken from [5.4] are shown as the *solid* line. The *broken* line in the upper insert is the average kinetic energy, $E_{\rm kin}$ in MeV, used in calculating percentage mass yields shown as *solid* dots in the lower insert. The *solid* dot in the upper insert is the calculated $E_{\rm kin}$ using Terrell's prescription (5.14)

Data on the average kinetic energy spectrum in the spontaneous fission of ^{250}Cm, ^{254}Cf and ^{258}Fm are not available. However, this can be calculated using Terrell's prescription and are shown as solid dots in the upper half of Figs. 5.6, 5.7 and 5.8. Calculated percentage mass yields as a function of masses of heavy fragments are shown in the same figures as solid dots and dashed lines. The kinetic energies used in the calculation are noted as dashed curves in the upper half of these two figures.

Figures 5.6, 5.7 and 5.8 show that while the dominant decay modes for ^{250}Cm and ^{254}Cf are non-symmetric, ^{258}Fm prefers to decay primarily to the symmetric daughter pairs. This theoretical finding is consistent with observation [5.30]. Theoretical values of total spontaneous decay half-lives and average kinetic energy for ^{250}Cm, ^{254}Cf and ^{258}Fm are also presented in Table 5.1. The agreement with experimental results is good.

5.4.3 Charge Distribution

The underlying assumption of the theory is that a parent nucleus has a finite probability to decay to a well defined daughter pair comprising of two nuclei

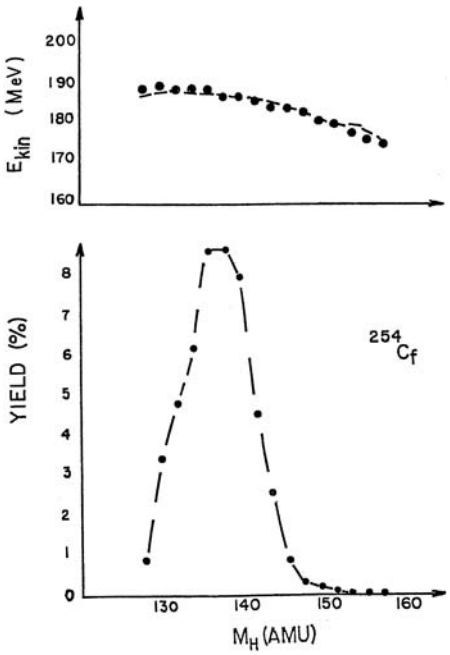

Fig. 5.7. The same as in Fig. 5.6 except for the spontaneous fission of ^{254}Cf

having well defined atomic charges and masses. The decay probabilities to two nuclei specified only by their mass number are calculated by summing over such probabilities of decay to all pairs having the same mass number but different atomic number. From such calculations one can also obtain decay probabilities to a daughter pair characterized only by their charge numbers by summing over all mass numbers having the same pair of charges. Experimental data on charge distribution have become available since the sixties. In Tables 5.2 to 5.5, we present the calculated results and compare them with the observed ones, for spontaneous fission of ^{234}U, ^{236}U, ^{240}Pu and ^{252}Cf. The data on charge distribution and associated average mass for ^{234}U, ^{236}U and ^{240}U are actually for thermal neutron induced fission of ^{233}U, ^{235}U and ^{239}Pu, respectively, but those on ^{252}Cf are for spontaneous fission. The theory can successfully account for the observed charge distribution, in all four cases, reasonably well. Theoretical estimates of percentage charge yields, and average nuclear mass, $\langle M \rangle$, associated with each charge of daughter nuclei, for ^{254}Cf, ^{254}Fm, ^{256}Fm and ^{258}Fm are presented in Table 5.6.

The success of the empirical barrier in accounting for the mass yield spectra with proper kinetic energies and the general trend of charge distribution is primarily due to the realization of the necessity of having an external barrier which follows from the necessary condition for the existence of a metastable state for parent nuclei. The same barrier has been used to analyze the

Table 5.2. Theoretical and experimental percentage charge yields, noted as % yield, and average nuclear mass, ⟨M⟩, associated with each atomic number of daughter nuclei. The theoretical calculation is for spontaneous fission of ^{234}U and the experimental results are for thermal neutron induced fission of ^{233}U [5.32]

Charge	Theory		(n, f) (exp.)	
Z	⟨M⟩	% Yield	⟨M⟩	% Yield
32	81.5	0.4	–	
34	85.3	2.0	85.7	3.55 ± 0.20
36	89.3	7.9	90.5	16.44 ± 0.80
38	94.0	20.9	95.4	17.06 ± 0.40
40	98.9	11.5	100.3	12.57 ± 0.30
42	103.2	7.0	104.9	3.02 ± 0.33
44 to 48		$\leq$0.5		$\leq$0.5
50	130.8	7.0	129.1	3.02 ± 0.33
52	135.0	11.5	133.7	12.57 ± 0.30
54	140.0	20.9	138.6	17.06 ± 0.40
56	144.7	7.9	143.5	16.44 ± 0.80
58	148.7	2.0	148.3	3.55 ± 0.20
60	152.5	0.4	153.1	0.43 ± 0.06

Table 5.3. Theoretical and experimental percentage charge yields, noted as % yield, and average nuclear mass, ⟨M⟩, associated with each charge of daughter nuclei. The calculation is for spontaneous fission of ^{236}U and the experimental results are for thermal neutron induced fission of ^{235}U [5.32]

Charge	Theory		(n, f) (exp.)	
Z	⟨M⟩	% Yield	⟨M⟩	% Yield
32	80.0	0.1	–	
34	85.0	1.6	86.2	3.17 ± 0.24
36	90.7	11.1	91.2	12.84 ± 0.48
38	96.0	19.5	96.3	16.16 ± 0.13
40	101.0	12.1	101.4	15.10 ± 0.37
42	104.7	5.6	106.1	3.34 ± 0.48
44 to 48		$\leq$0.5		$\leq$0.4
50	131.3	5.6	129.6	3.34 ± 0.48
52	135.0	12.1	134.6	15.10 ± 0.37
54	140.0	19.5	139.7	16.16 ± 0.48
56	145.3	11.1	144.8	12.48 ± 0.48
58	151.0	1.6	149.8	3.17 ± 0.24
60	156.0	0.1	154.9	0.38 ± 0.05

Table 5.4. Theoretical and experimental percentage charge yields, noted as % yield, and average nuclear mass, ⟨M⟩, associated with each charge of daughter nuclei. The theoretical calculation is for spontaneous fission of ^{240}Pu and the experimental results are for thermal neutron induced fission of ^{239}Pu [5.32]

Charge Z	Theory		(n, f) (exp.)	
	⟨M⟩	% Yield	⟨M⟩	% Yield
32	81.3	0.3	–	
34	86.6	2.0	85.2	1.20 ± 0.10
36	92.5	7.6	90.4	4.17 ± 0.25
38	97.1	9.6	95.55	11.20 ± 0.35
40	101.0	12.0	100.7	15.73 ± 0.14
42	104.9	11.7	105.7	14.64 ± 0.50
44	109.3	6.8	110.6	3.07 ± 0.33
50	130.6	6.8	129.4	3.07 ± 0.33
52	135.1	11.7	134.3	14.64 ± 0.33
54	139.0	12.0	139.3	15.73 ± 0.14
56	142.9	9.6	144.45	11.28 ± 0.35
58	147.5	7.6	149.6	4.17 ± 0.25
60	153.4	2.0	154.8	1.20 ± 0.10
62	158.7	0.3	159.7	0.20 ± 0.03

Table 5.5. Theoretical and experimental percentage charge yields, noted as % yield, and average nuclear mass, ⟨M⟩, associated with each charge of daughter nuclei in the spontaneous fission of ^{252}Cf. The experimental numbers, Exp., noted in columns 4 to 6, are from [5.15, 5.16]

Charge Z	Theory		Exp.		Exp.	
	⟨M⟩	% yield	⟨M⟩	% yield	⟨M⟩	% yield
34	86	0.1	–	–	–	–
36	93.5	1.7	–	–	–	–
38	97.5	2.3	94.6	1.97 ± 0.27	95.5	2.9 ± 0.1
40	101.9	9.5	100.8	7.38 ± 0.52	100.6	7.9 ± 0.3
42	107.5	17.9	105.0	15.36 ± 1.13	105.2	15.4 ± 0.3
44	112.7	10.4	109.8	11.86 ± 0.85	109.6	13.6 ± 0.2
46	116.5	6.1	114.1	6.83 ± 0.73	113.8	7.8 ± 0.3
48	119.5	2.2	118.9	1.66 ± 0.21	–	–
50	131	2.2	–	–	–	–
52	135	6.1	134.5	4.96 ± 0.21	133.9	7.8 ± 0.3
54	139.4	10.4	138.5	9.63 ± 0.70	138.5	13.6 ± 0.2
56	144.5	17.9	143.3	16.23 ± 1.08	143.3	15.4 ± 0.3
58	150.2	9.5	148.0	9.2 ± 0.68	147.9	7.9 ± 0.3
60	154.5	2.3	152.6	2.4 ± 0.26	152.5	2.9 ± 0.1
62	159.5	1.7	158.6	1.08 ± 0.99	156.9	1.13 ± 0.06
64	166	0.1	–	–	–	–

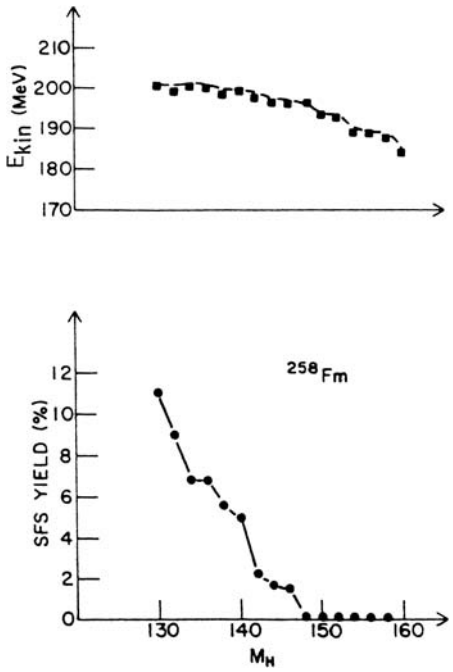

Fig. 5.8. The calculated percentage mass yields, SFS yield (%), in the spontaneous fission of ^{258}Fm taken from [5.4] are shown as the *solid* line. The *broken* line in the upper insert is the average kinetic energy, $E_{\rm kin}$ in MeV, used in calculating percentage mass yields shown as *solid* dots in the lower insert. The *solid* dot in the upper insert is the calculated $E_{\rm kin}$ using Terrell's prescription (5.14)

variation of percentage mass yields and average kinetic energy spectra with the incident neutron energy in induced fission in Chap. 6 and isomer fission in Chap. 8.

5.5 Conclusion

The empirical barrier and the mass dependence of its parameters can account for the observed half-lives with the observed kinetic energies, mass dependence of yields of elements in spontaneous fission. The mass dependence of kinetic energy needed to account for the percentage yields of masses follow closely the one calculated from Terrell's formulae.

Table 5.6. Theoretical percentage charge yields, noted as % yield, and average nuclear mass, ⟨M⟩, associated with each charge of daughter nuclei. The two theoretical results presented for ^{258}Fm are such that their average kinetic energy become identical with the ones given in Table 5.1, respectively

Charge	^{254}Cf		^{254}Fm		^{256}Fm		^{258}Fm (1)		^{258}Fm (2)	
Z	⟨M⟩	% yield	⟨M⟩	% yield	⟨M⟩	% yield	⟨M⟩	% yield	⟨M⟩	% yield
34	—	—	—	—	—	—	88.0	0.3	—	—
36	92.6	1.0	91.4	0.3	92.0	0.1	91.2	1.3	—	—
38	97.2	1.7	95.2	0.8	96.5	1.5	96.2	3.3	96.7	0.7
40	102.5	7.3	100.5	3.8	101.2	2.4	102.1	5.4	102.4	1.8
42	108.1	15.6	106.3	10.1	106.4	7.7	108.1	6.6	108.4	4.7
44	113.9	15.0	111.1	10.9	112.2	14.0	113.0	5.3	113.1	5.4
46	118.8	6.7	115.9	16.2	117.0	10.9	118.1	10.2	118.2	12.5
48	122.9	2.7	121.1	7.4	121.6	10.3	124.1	13.0	124.1	18.1
50	131.1	2.7	127.0	0.6	128.0	6.3	129.0	9.5	129.0	13.6
52	135.2	6.7	132.8	7.4	134.4	10.3	133.9	13.0	133.9	18.1
54	140.1	15.0	138.1	16.2	139.0	10.4	139.9	10.2	139.8	12.5
56	145.9	15.6	142.9	10.9	143.8	14.0	145.0	5.3	144.9	5.4
58	151.5	7.3	147.7	10.1	149.6	7.7	149.9	6.6	149.6	4.7
60	156.8	1.7	153.5	3.8	154.8	2.4	155.9	5.4	155.6	1.8
62	161.4	1.0	158.8	0.8	159.5	1.5	161.8	3.3	161.3	0.7
64	—	—	162.6	0.3	164.0	0.1	166.8	1.3	—	—
66	—	—	—	—	—	—	170.0	0.3	—	—

References

1. F.B. Malik and P.C. Sabatier, Helv. Phys. Acta **46**, 303 (1973).
2. B. Block, J.W. Clark, M.D. High, R. Malmin and F.B. Malik, Ann. Phys. (N.Y.) **62**, 464 (1971).
3. M.A. Hooshyar and F.B. Malik, Phys. Lett. **38 B**, 495 (1972).
4. M.A. Hooshyar and F.B. Malik, Helv. Phys. Acta **46**, 724 (1973).
5. M.A. Hooshyar and F.B. Malik, Phys. Lett. **55 B**, 144 (1975).
6. A.E.S. Green, Phys. Rev. **93**, 1006 (1954).
7. W.D. Myers and W.J. Swiatecki, Nucl. Phys. **81**, 1 (1966).
8. M.L. Goldberger and K.M. Watson, *Collision Theory*, (John Willey and Sons, New York, 1964).
9. M.A. Hooshyar and F.B. Malik, Helv. Phys. Acta **45**, 567 (1972).
10. M.A. Hooshyar and F.B. Malik, "A statistical model analysis for the neutron induced fission of ^{235}U, ^{235}U and ^{239}Pu." Unpublished.
11. B. Compani-Tabrizi, M.A. Hooshyar and F.B. Malik, *Proc. Int's Conference on interaction between nucleons and nuclei*, ed. E. Sheldon (ERDA: Conf. 7607115-Pl, 1976) 725.
12. J. Terrell, Phys. Rev. **113**, 527 (1959).
13. J. Terrell, Phys. Rev. **127**, 880 (1962).
14. J.S. Fraser and J.C.D. Milton, Phys. Rev. **93**, 818 (1954).

15. E. Cheifetz, J.B. Wilhelmy, R.C. Jared and S.G. Thompson, Phys. Rev. **C 4**, 1913 (1971).
16. W. Residorf, J.P. Unik, H.C. Griffin and L.C. Glendenin, quoted in ref. 15 as a private communication.
17. W.E. Stein, Phys. Rev. **108**, 94 (1957).
18. A. Ghiorso, G.H. Higgens, A.E. Larsh, G.T. Seaborg and S.G. Thompson, Phys. Rev. **87**, 163 (1952).
19. A.H. Jaffey and A. Hirsh, Unpublished data (1949).
20. D.E. Watt, F.J. Bannister, J.B. Laidler and F. Brown, Phys. Rev. **126**, 265 (1962).
21. A.B. Smith, P. Fields, A. Fiedman, S. Cox and S. Sjoblom, *Second International Conf. On the Peaceful use of Atomic Energy*, (U. N. Publ, 1959).
22. P. Möller, R.J. Nix, W.D. Myers and W.J. Swiatecki, At. Data Nucl. Data, **66**, 131 (1997).
23. A.M. Friedman, J.W. Meadows, A.B. Smith, P.R. Fields. J. Milsted and J.F. Whalen, Phys. Rev. **131**, 1203 (1963).
24. E.K. Hulet, Phys. Rev. **89**, 878 (1953).
25. E.K. Hyde, *The Nuclear Properties of Heavy Elements*, Vol. III (Prentice Hall Inc., 1964).
26. J. Huizenga and H. Diamand, Phys. Rev. **107**, 1087 (1957).
27. R. Brandt, S.G. Thompson, R.C. Gatti and L. Phillips, Phys, Rev. **131**, 1146 (1966).
28. L. Phillips, R.C. Gatti, R. Brandt and S.G. Thompson, J. Inorg Nucl. Chem. **25**, 1085 (1963).
29. E.K. Hulet, J.F. Wild, R.W. Longheed, J.E. Evans and B.J. Qualheim, Phys. Rev. Lett., **26**, 523 (1971).
30. W. John, E.K. Hulet, R.W. Longheed and J.J. Wesolowski, Phys. Rev. Lett. **27**, 45 (1971) quote 191 MeV but indicate that their result may lie about 10 MeV lower in some cases e.g., at the asymmetric end of mass distribution. Their energies are about 10MeV lower than those of J.P. Balaga, G.P. Ford, D.C. Hoffman and J.D. Knight, Phys. Rev. Lett. **26**, 145 (1971).
31. J.H. Neiler, F.J. Walter and H.W. Schmitt, Phys. Rev. **149**, 894 (1966).
32. W. Reisdorf, J.P. Unik, H.C. Griffin and L.C. Glendenin, Nucl. Phys. A **177**, 337 (1971).
33. F. Pleasonton, Phys. Rev. **174**, 1500 (1968).
34. H.W. Schmitt, J.H. Neiler and F.J. Walter, Phys. Rev. **141**, 1146 (1966).

6 Induced Fission

6.1 Introduction

As noted in Chap. 1, one of the most interesting characteristics of the induced fission process is the dramatic change in percentage mass yields spectra of daughter pairs in the final channel, with the variation of the incident kinetic energy of projectiles. For example, the spectra of percentage mass yields in the induced fission of ^{235}U and ^{239}Pu by incident thermal neutrons peak towards the asymmetric modes i.e. towards A/3 and 2A/3, (where A is the mass of the compound nucleus), whereas for 14 MeV incident neutrons on ^{235}U, the mass-yields-spectrum near symmetric modes, i.e., near (A/2), becomes comparable to those near asymmetric modes. The same phenomenon occurs for incident charged particles [6.1–6.4]. In a series of papers D'yachenko, Kuzminov and their collaborators [6.5–6.11] have reported results of the systematic studies of variation of both percentage mass yield spectra and the associated average kinetic energies, TKE, as a function of daughter masses, with incident neutron energies for ^{233}U, ^{235}U and ^{239}Pu targets. While the change in the percentage mass yield is found to be substantial in these experiments, the variation of TKE spectra was less dramatic. A similar situation had been observed for alpha-induced fission of ^{226}Ra earlier by Unik and Huizenga [6.4]. Since the yields of daughter pairs are governed by their associated kinetic energies, a theoretical understanding of induced fission must *simultaneously* account for the variation of both TKE and percentage mass yield spectra with the change in incident projectile energy. In this chapter we present a theory explaining this variation. The role of the external barrier used in connection with spontaneous fission in previous chapters is central to the understanding of these variations.

Another feature, that a theory must account for, is the shape of the spectrum of the percentage yields curve for daughter pairs characterized by their mass number as a function of their kinetic energy. Theoretical computation of such a curve involves summing over the yields to all pairs of isotopes having the same pair of mass number. In other words, the observed kinetic energy is the average of the kinetic energies associated with the emission of all daughter pairs having the same mass number but different charges. The discovery of cold fission further points to the possibility that the compound system may be decaying to different excited states of each member of a particular

daughter pair. The shape of the yields versus kinetic energy curve determines the mechanism that distributes the available energy to excitation of a daughter pair and the kinetic energy associated with that. A theoretical understanding of this experimental curve provides, therefore, the physical mechanism involved in distributing the available energy into the excitation of a daughter pair and its kinetic energy.

In the next section we present a theory that leads to the understanding of the above features. In addition, the theory is in a position to calculate TKE.

6.2 Theory

The theory assumes that the induced fission proceeds in two steps. First a projectile and target coalescence into a compound system, termed generically as the compound nucleus and then this system decays into various excited states of two nuclei with specific mass and charge numbers. The statistical theory of Weisskopf [6.12], Weisskopf and Ewing [6.13], Newton [6.14] and Ericson [6.15], is particularly suitable to describe this two step process [6.16–6.18] and calculate absolute total and differential cross sections and decay probabilities. The theory may also be adopted to calculate decay probabilities to all permitted excited states of a particular daughter pair and to all nuclei having the same pair of mass numbers. This leads to calculation of TKE which is the location of the maximum of the average kinetic energy. We discuss these cases in the following sections.

6.2.1 Cross Section and Decay Probabilities

Denoting the incident and final channels by α and β, the differential cross section is given by

$$\frac{d\sigma_{\alpha\beta}}{d\Omega} = \sum\nolimits_I \sum\nolimits_\ell (\pi/k^2)(2\ell+1)T_\ell(\alpha) \left[\frac{P_\beta(I, U_c, \varepsilon, \vec{n})}{\sum_\gamma \int d\Omega P\gamma(I, U_c, \varepsilon, \vec{n})} \right] \qquad (6.1)$$

where k, ℓ and I are, respectively, the incident channel wave number, orbital angular momentum and the total spin of the compound system. $P_\beta(I, U_\mathrm{c}, \varepsilon, \ \vec{n})$ and $P_\gamma(I, U_c, \varepsilon, \ \vec{n})$, respectively, are the decay probabilities into daughter pairs characterized by channel indices β and γ in the direction $\vec{n}$ with kinetic energy ε from a compound or composite nucleus of spin I and excitation energy U_c. The summation over γ extends to all decay modes including the channel β. $T_\ell(\alpha)$ is the transmission coefficient leading to the formation of the compound or composite system.

The total cross section for the production of a pair characterized by channel β from the initial channel α is given by

$$\sigma_{\alpha\beta} = \sum\nolimits_I \sum\nolimits_\ell (\pi/k^2)(2\ell+1)T_\ell(\alpha) \left[\frac{\int d\Omega P_\beta(I, U_c, \varepsilon, \vec{n})}{\sum_\gamma \int d\Omega P\gamma(I, U_c, \varepsilon, \vec{n})} \right] . \qquad (6.2)$$

Calculation of absolute cross section involves a model to evaluate $\sum_\ell (\pi/k^2)(2\ell+1)T_\ell(\alpha)$. For an incident proton, neutron and alpha particle one may approximate the capture probabilities by the reaction cross section and then

$$T_\ell(\alpha) = (1 - |\exp(2i\delta_\ell)|^2) \; . \tag{6.3}$$

Where δ_ℓ is the complex phase shift in the incident channel which may be evaluated from a complex potential obtained by fitting elastic scattering data for incident projectiles.

One may integrate over the angle to obtain the decay probability, P_β (I, U_c, ε) to a particular daughter pair with a kinetic energy ε

$$P_\beta(I, U_c, \varepsilon) = 2\pi \int_0^\pi P_\beta(I, U_c, \varepsilon, \vec{n}) d(\cos\theta) \; . \tag{6.4}$$

The partial decay width $\Gamma(A_1,\ A_2,\ U_c,\ \varepsilon)$ from a compound nucleus of excitation energy U_c and spin I to a particular daughter pair denoted by mass numbers A_1 and A_2 moving with kinetic energy ε is given by

$$\Gamma(A_1, A_2, I, U_c, \varepsilon) = P_\beta(I, U_c, \varepsilon) \tag{6.5}$$

and the total decay width is given by

$$\Gamma(A_1, A_2, I, U_c) = \int_0^\xi \Gamma(A_1, A_2, I, U_c, \varepsilon) d\varepsilon \; . \tag{6.6}$$

In (6.6) ξ is the maximum energy available for the intrinsic excitation of a daughter pair in accordance with energy conservation. This maximum available energy ξ is related to the masses of target, $M(T)$, projectile $M(P)$, and daughter pair, $M(A_1)$ and $M(A_2)$, and incident channel kinetic energy T by the following relation:

$$\xi = [M(T) + M(P) + T - M(A_1) - M(A_2)]c^2 \; . \tag{6.7}$$

This energy is distributed between excitation energies of a daughter pair U_1 and U_2 and their relative kinetic energy ε. Thus

$$\xi = U_1 + U_2 + \varepsilon \; . \tag{6.8}$$

Within the frame work of the statistical model, the partial decay with (6.5) may be related to the level densities, $\rho_1(U_1)$ and $\rho_2(U_2)$ of each member of a daughter pair and a transmission function $T(\varepsilon)$ through the barrier associated with the decay of the compound nucleus to a particular daughter pair [6.15, 6.19, 6.20] as follows

$$\begin{aligned} \Gamma(A_1, A_2, I, U_c, \varepsilon) &= T(\varepsilon) \int_0^{\xi-\varepsilon} \rho_1(U_1)\rho_2(U_2) dU_1 \\ &= T(\varepsilon) \int_0^{\xi-\varepsilon} \rho_1(U_1)\rho_2(\xi - \varepsilon - U_1) dU_1 \end{aligned} \tag{6.9}$$

Fong [6.21, 6.22] and Faissner and Wildermuth [6.23, 6.24] have used similar expressions to calculate decay width but set $T(\varepsilon) = 1$. This amounts to neglecting the barrier and hence, the interaction between members of a particular daughter pair has been neglected in their models which are essentially based on an evaporation model.

For the calculation of decay width one should, however, specify the interaction between two members of a daughter pair and the functional form of their level densities. The decay widths, using the theory presented herein, have been calculated using (6.9). Calculations of the transmission coefficient, $T(\varepsilon)$, have been done using the barrier adopted in Chap. 5 to calculate decay probabilities in spontaneous fission. Hence, the potential between the two emerging members of a daughter is taken to be the following

$$V_{nc}(R) = \begin{cases} V_1 & \text{for} \quad R < R_c \\ V_0 & \text{for} \quad R_c < R < R_b \\ V_{\text{coul}} \exp[(R - R_0)/d] & \text{for} \quad R_b < R < R_0 \\ Z_1 Z_2 e^2/R & \text{for} \quad R_0 < R \, . \end{cases} \tag{6.10}$$

In (6.10) $V_1 = 200\,\text{MeV}$, $V_0 = V_{\text{coul}} - 60\,\text{MeV}$, $V_{\text{coul}} = Z_1 Z_2 e^2/R_0$ with $R_0 = r_0({A_1}^{1/3} + {A_2}^{1/3}) + 3.0$ fm and $r_0 = 1.3 + 0.13\, g(A_1, A_2)$, $R_c = 8$ fm, and $R_b = R_0 + d \log(V_0/V_{\text{coul}})$ with $d = 3.2$ fm and $g(A_1, A_2) = \exp[-0.036(|A_1 - A_2|)^{1.6}]$. The barrier (6.10) is the diagonal part of the same barrier used in explaining half-lives, mass and charge yields in the spontaneous and isomer fission of ^{234}U, ^{236}U and ^{240}Pu [6.25, 6.26].

For excitation energy above 5 MeV, the level density function is taken to be the one suggested by Gadioli and Zeta [6.27].

$$\rho(I, V) = \frac{\hbar^3}{24\sqrt{2}}(2I + 1) \exp\left[-\frac{I(I+1)}{2\sigma^2}\right] \sqrt{a} G^{-3/2} \exp[2(aV)^{1/2}]/(V + 1)^2 \, . \tag{6.11}$$

In (6.11), V is the effective excitation energy related to U and energy-gap parameter Δ by [6.28].

$$V = U - \Delta + (70/A) \quad \text{in} \quad \text{MeV} \, . \tag{6.12}$$

G is the moment of inertia of the nucleus in consideration and is taken to be the following

$$\begin{aligned} G &= 0.7[\textit{rigid body moment of inertia}] \\ &= (0.7)(2/5)AR^2 \text{ with } R = 1.5A^{1/3} fm \, . \end{aligned} \tag{6.13}$$

σ is the spin cut-off parameter regulating the distribution of level spin and a is the characteristic parameter related to single particle spacing near the Fermi sea and is taken to be $= 0.127\text{A}\ (\text{MeV})^{-1}$ i.e., a_3, of Fig. 6.1 of Gadioli and Zetta.

The effective excitation energy V is related to nuclear temperature t by

$$V = at^2 - t \; . \tag{6.14}$$

For low excitation energy i.e., energy less than 5 MeV, the density of levels is usually small and $\rho(I, V)$ is taken to be a delta function

$$\rho(I, V) = \delta - function \; of \; energy \; . \tag{6.15}$$

Following Ericsson [6.15] the expression for the partial decay width may be obtained from (6.9) and (6.14)

$$\Gamma(A_1, A_2, I, U_c, \varepsilon) = \frac{\sqrt{\pi}\hbar^6}{\rho_c(I, U_c)} \times \frac{a_1 a_2}{144(2\sqrt{2})}(G_1 G_2)^{3/2} T_0^{1,2}(\varepsilon) \times \int \frac{(\sigma_1 + \sigma_2)^3 \exp[2\sqrt{a_1 V_1} + 2\sqrt{a_2 V_2}] dV_1}{({\sigma_1}^2 + {\sigma_2}^2)^{1/2}(V_1 + t_1)^2 (V_2 + t_2)^2} \; . \tag{6.16}$$

In (6.16), $\rho_c(I, U_c)$ is the level density of the compound nucleus with spin I and excitation energy U_c. The limits of integration in (6.16) are from the minimum to maximum allowed values of V_1. The available energy ξ is distributed between the excitation energy of a daughter pair and its kinetic energy. Normally, one may set the minimum and maximum value of V_1 to be zero and ξ, respectively. However, (6.16) is derived from a statistical consideration and the decay process involves a change in entropy, Δs. If the excitation energies of the compound nucleus and daughter pairs are identified as available heat energy H, the change in entropy Δs must remain zero or positive during the decay process. Hence,

$$\Delta s \geq 0 \; . \tag{6.17}$$

Neglecting the slight correction, we may set U $\approx$ V

$$\Delta s = U_1/t_1 + U_2/t_2 - U_c/t \geq 0 \; . \tag{6.18}$$

Using (6.18) and noting that $a = 0.127 \times$ mass number, one gets

$$\Delta s = 0.127(A_1(t_1 - t) + A_2(t_2 - t) - 1 \geq 0 \; . \tag{6.19}$$

The limits in (6.16) must be chosen to insure this inequality. This can be fulfilled either by taking $t_1 > t$ and $t_2 > t$ or by setting $t_2 = t$ and choosing the lowest excitation energy U_1 corresponding to the minimum temperature $t_1(\min)$ that fulfills the following condition

$$t_1(\min) - t \geq 1/(0.127 A_1) \; . \tag{6.20}$$

The lowest limit of integration is chosen to insure a condition similar to (6.20) obtained by using V. The maximum value of t_1 corresponding to the maximum excitation energy of fragment one $U_1(t_1) = \xi - \varepsilon - U_2(t)$. The limit

of integration over V_1 according to this prescription insures that $\Delta s \geq 0$ in the entire domain of integration.

In most cases considered here, A_1 lies between 80 to 150 and hence 0.127 $A_1 \approx 0.1$ or less. Hence, at the lowest limit, $t_1 \approx t$, which implies that the temperature of each member of a daughter pair is very close to that of the corresponding compound system. In fact, had one used the relation $U = \mathrm{at}^2$ instead of (6.14), $t_1 = t$ in the lowest limit would have corresponded to $\Delta s = 0$.

6.2.2 Calculation of the Most Probable Kinetic Energy, TKE

One may calculate the most probable kinetic energy by searching for that kinetic energy, ε, which maximizes expression (6.9) for the partial width $\Gamma(A_1, A_2, I, U_c, \varepsilon)$. In essence, the decay widths to A_1 and A_2 are calculated for a series of ε, allowed by energy conservation. For a given ε, U_1 and U_2, the total excitation energy of a pair is determined using (6.8). Integration over U_1 is performed over all possible excitations of A_1 allowed by the total available excitation energy. This automatically takes into account the inclusion of decay probabilities to all allowed excited states of a daughter pair. In case the daughter pairs are identified by their mass numbers only, the decay probabilities to all the pairs having the same mass number, but different atomic numbers are calculated and summed over. Thus,

$$\begin{aligned} \textit{Most Probable Kinetic Energy} &= \textit{Max of } \Gamma(A_1, A_2, I, U_c, \varepsilon) \textit{as a function of } \varepsilon \\ &= \textit{Max of } {T_0}^{1,2}(\varepsilon) \int_0^{\xi-\varepsilon} \rho_1(U_1)\rho_2(\xi - \varepsilon - U_1)dU_1 \end{aligned} \tag{6.21}$$

The maximum of (6.21) does not occur at $\varepsilon = 0$ nor at $\varepsilon = \xi$ for the level density function used here. To emphasize this point we choose a simple form for $\rho_1(U_1)$ which maintains the key feature of ε dependence of (6.11) but is analytically simple. Taking $\rho_1 = c_1 \exp\sqrt{a_1 U_1}$ and $\rho_2 = c_2 \exp\sqrt{a_2 U_2}$ which are also quite often used in nuclear physics, we get

$$\begin{aligned} \textit{Max of } \Gamma(A_1, A_2, I, U_c, \varepsilon) = \textit{Max of } {T_o}^{1,2}(\varepsilon) \int_0^{\xi-\varepsilon} c_1 c_2 \\ \times \exp[2U_1] \exp[2\sqrt{a_2 U_2}] dU_1 \,. \end{aligned} \tag{6.22}$$

The value of the integral in (6.22) is essentially determined by integration in the neighborhood of its maximum and following Fong [6.22], the approximate value of the integral is given by

$$2\pi^{1/2} c_1 c_2 \frac{\sqrt{a_1 a}_2}{(a_1 + a_2)^{5/4}} (\xi - \varepsilon)^{3/4} \exp[2(a_1 + a_2)(\xi - \varepsilon)^{1/2}] \,. \tag{6.23}$$

Hence the location of the maximum of the width is given by

$$Max\ of\ \Gamma(A_1, A_2, I, U_c, \varepsilon) = Max\ of\ (\sqrt{\varepsilon/2\mu})(\xi - \varepsilon)^{1/4}$$
$$\times \exp\left[-2\int_1^2 \sqrt{B(V-\varepsilon)}dR\right] \exp\left[2(a_1+a_2)(\xi-\varepsilon)^{1/2}\right] . \quad (6.24)$$

In (6.24) we have omitted the constants which are not relevant for determining the location of the maximum. In arriving at (6.24), the transmission coefficient in $T(\varepsilon)$ is calculated for a barrier given by potential V in the JWKB approximation. The constant B is the reduced mass divided by $\hbar^2$. The limits of integration refer to two turning points and the integration (6.21) is replaced by (6.23). The dominating terms as a function of ε are the two exponentials in (6.24), one increasing and the other decreasing with the increasing ε. The maximum is clearly neither at $\varepsilon = 0$ nor at $\varepsilon = \xi$ but occurs for an ε value in between these two extrema. The exact location is determined by the competition between these two exponentials.

In case one neglects the barrier between the two emerging final fragments ${T_0}^{1,2}(\varepsilon) = 1$ and the maximum of width as a function of ε is given by (6.23) which is located at $\varepsilon = 0$. This means that the entire available energy is transferred into internal excitation of the daughter pairs and maximum yields occur at zero kinetic energy, i.e., fragments are evaporated. For induced as well as spontaneous fission, this is clearly not the case experimentally. In fact, this observation led Facchini and Saetta-Menichela [6.20] to suggest the necessity of considering the interaction of the type shown in Fig. 6.1 between two emerging nuclei in the final channel.

In the next section we present calculations of percentage mass yield and TKE spectra. The latter is obtained by searching numerically for the maximum of $\Gamma(A_1, A_2, I, U_c, \varepsilon)$ as a function of ε for all isotopes of a given daughter pair of mass numbers A_1 and A_2, subject to the constraint $\Delta s \geq 0$.

6.3 Applications

The experimental data considered here represent percentage mass yields, i.e., the actual yields in the decay of a compound nucleus of a given energy to a particular decay daughter pair as a percentage of all decay modes. Hence, the theoretical calculations of the formation cross section of the compound nucleus are not needed. These relative yields and TKE can be calculated using (6.18) once Q-values, level density functions and the interaction in the final channel between a daughter pair are specified. In practice, however, there are a number of problems: (i) the mass formulas used to calculate Q-values have inherent uncertainties of few MeV. This is further compounded in our case because parameters of most of the mass formulas are adjusted to reproduce nuclear masses in the valley of stability, whereas, the daughter nuclei in the fission process, are neutron rich, and quite often lie away from this

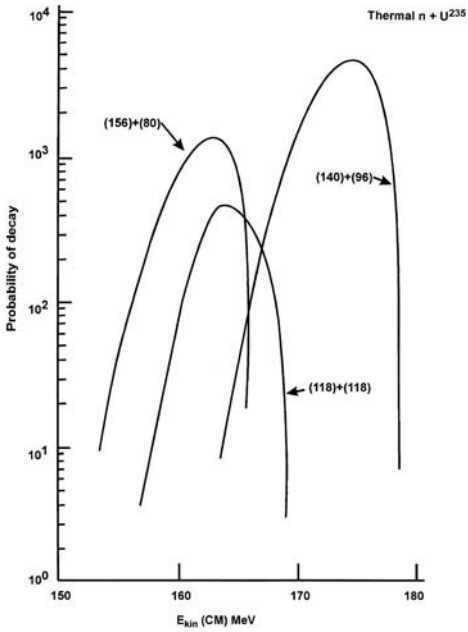

Fig. 6.1. Calculated relative probabilities, using (6.4) in arbitrary units to three sets of daughter pairs in thermal neutron induced fission of ^{235}U, are plotted as a function of kinetic energy, $E_{\rm kin}$. Atomic masses of the daughter pair are noted next to the relevant plot. The average or the most probable kinetic energy for a given pair is the location of the maximum of the plot. Total yields are calculated by summing over the yields of all isotopes

valley of stability, (ii) the experimental data on percentage yields and kinetic energy have significant uncertainties, (iii) the potential chosen here is only a good approximation to the actual one, the details of which is complicated and (iv) the details of observed level densities in individual nuclei can not be reproduced by the general function used by Gadioli and Zetta. In fact, the parameters have an inherent uncertainty of 10 to 20%. Taking these into consideration, we have adopted the following procedure to relate the calculation and the data.

The Q-values used in all calculations are first calculated from the mass formula of Myers and Swiatecki [6.30]. Since these Q-values could be uncertain by a few MeV, they were allowed to vary within a 5 MeV range of the calculated ones in order to obtain the best fit to the percentage mass yields spectrum of the spontaneous fission from the ground state of the compound nucleus formed by the coalescence of projectile and target. These Q-values have been used unchanged to calculate the percentage mass yields and TKE in the induced fission involving the same compound nucleus. The experimentally measured average kinetic energies have also inherent uncertainties of

a few MeV. We have, therefore, determined the theoretical TKE from the kinetic energy needed to fit the percentage mass yields for all isotopes of a daughter pair characterized by mass number A_1 and A_2. These are then compared with observed average kinetic energy spectra.

6.3.1 Neutron Induced Fission

We present here the analysis of some of that data where both the percentage mass yields and TKE spectra are taken in the same experiment. Such data exist for induced fission of ^{233}U by thermal, 5.5 and 15.5 MeV incident neutrons and of ^{235}U by thermal, 7.0, 15.5 and 22.0 MeV, incident neutrons, of ^{239}Pu by thermal, 5.5 and 15.5 MeV incident neutrons and of ^{229}Th by thermal neutrons. As noted earlier, the change in percentage mass yields spectra in all these cases is substantial with increasing incident neutron energy but the change in TKE spectra is less dramatic. In general, the percentage mass yields to symmetric modes relative to asymmetric modes increase significantly with increased bombarding energy. In the following sections we present also theoretically calculated TKE for each decay mode. These are obtained by calculating decay probabilities to all pairs that are characterized by the isotopes having the same mass number and then summing over them. These summed yields are then plotted as a function of kinetic energy, ε. The most probable kinetic energy or TKE is then determined from the maximum of this function. Six typical examples, one for thermal neutron induced fission of ^{235}U and another for 22 MeV neutron induced fission of ^{235}U are shown in Figs. 6.1 and 6.2. Daughter pairs considered are ($A_1 = 118$ and $A_2 = 118$), ($A_1 = 80$ and $A_2 = 156$) and ($A_1 = 96$ and $A_2 = 140$). One may note the following:

(a) These TKE curves are bell shaped which is usually the case in experimental determination of such TKE.
(b) The maximum of these curves correspond to most probable kinetic energies and are about 10 to 20 MeV below the corresponding Q-values as is the case experimentally.
(c) The additional 22 MeV imparted by the incident neutron primarily (i) broadens the widths of the bell shaped yield curves, and (ii) affects relative yields to symmetric modes relative to asymmetric modes. We discuss neutron induced fission of ^{233}U, ^{235}U, ^{239}Pu and ^{229}Th in the following sections.

6.3.1a Neutron Induced Fission of ^{233}U

We have presented the observed percentage mass yields spectrum and TKE as a function of the mass number of the heavier partner of a daughter pair for fission of ^{233}U by thermal, 5.5 and 15.5 MeV incident neutron [6.11] in Figs. 6.3 and 6.4. The percentage mass yields and TKE spectra for the lighter partner

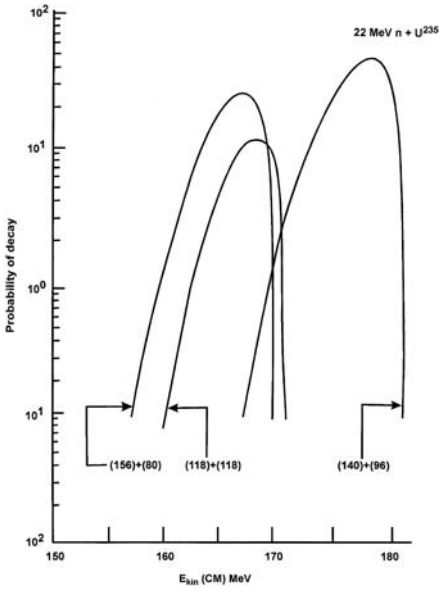

Fig. 6.2. The same as Fig. 6.1 except the incident neutron energy is 22 MeV

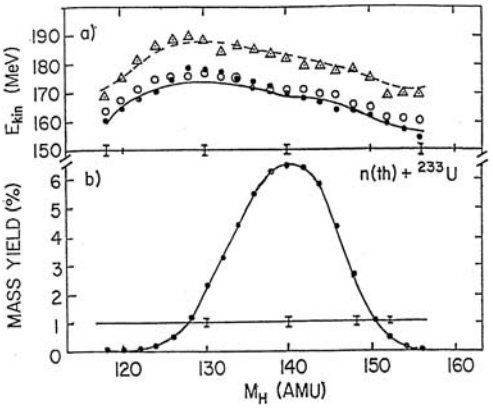

Fig. 6.3. Experimental and theoretical mass yields and average kinetic energy, $E_{\rm kin}$ are shown, respectively, by *solid* lines [6.11] and *solid* dots [6.16,6.25,6.45] in inserts (**a**) and (**b**) for thermal neutron induced fission of ^{233}U. *Open* circles in both inserts are calculated average kinetic energy given by the maxima of (6.16). *Broken* line and open triangle are, respectively, theoretical Q-values used in obtaining the fit to percentage mass yield and Q-values obtained from Myers and Swiatecki's mass formula [6.30]. M_H is the distribution of the heavy fragment of a daughter pair. Typical error bars are those shown in insert (**b**)

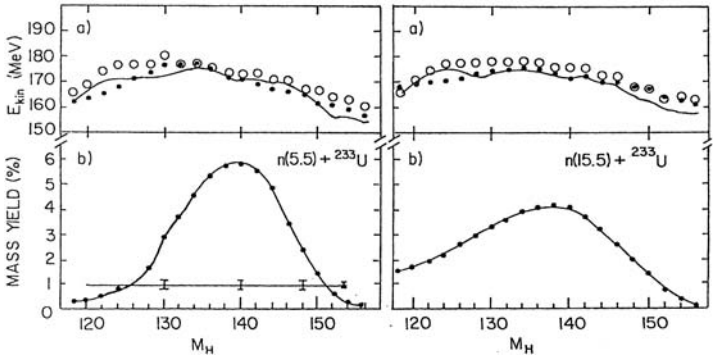

Fig. 6.4. *Solid* lines and *solid* dots are, respectively, calculated and experimental percentage mass yields in lower inserts and the most probable kinetic energies in upper inserts in 5.5 and 15.5 (*right*) MeV neutron induced fission of ^{235}U. *Open* circles in upper inserts are calculated $E_{\rm kin}$ determined from the maxima of (6.16)

of a daughter pair are basically the mirror image of plotted data in Figs. 6.3 and 6.4 and are not shown. However, the fact that the mass-yields spectra of light and heavy fragments are mirror images of each other indicates the process to be predominantly binary fragmentation and not random explosion. Two experimental percentage mass yields spectra shown in Fig. 6.3 are very instructive. At higher incident energy the yields to asymmetric modes, i.e. mass number M_H around 140 relative to those to symmetric modes decrease substantially. On the other hand the TKE spectra in both cases indicate that the change in TKE at higher incident energy over that for lower incident energy is not substantial. Nevertheless, the TKE associated with the decay to lower masses e.g. those around 120 increases somewhat at the higher incident neutron energy. This is primary responsible for the large percentage increase associated with modes that had low yields at lower incident energies. The tendency to equalize TKE for all modes results in a higher percentage increase for symmetric ones, which is likely to enhance the barrier penetration probabilities for these modes.

In the same figure, we have plotted the best fit to the percentage mass yields spectra and the TKE needed for the fit. The data and calculations are noted, respectively, as solid lines and solid dots. The Q-values used in all cases are the same ones used in describing spontaneous fission and are shown as dashed curve in Fig. 6.3 and compared to Q-values calculated using Myers and Swiatecki's mass formula [6.30] which are shown as open triangles. The observed data on TKE and percentage mass yields are well accounted for at all incident energies.

The open circles in each of these figures are theoretically calculated TKE, using the barrier (6.10) and looking for the maximum of (6.21). These are the kinetic energies where the decay probability function to all daughter pairs of

a given isotope has its maximum. Considering that the data on TKE have an uncertainty of about 5 MeV and given the approximate nature of level density functions used here, the agreement is reasonable.

6.3.1b Neutron Induced Fission of ^{235}U

A systematic study has been done at the Power Engineering Institute in Kazakstan of the variation of percentage yields spectrum along with the corresponding variation of TKE with the change in incident neutron energy for induced fission of ^{235}U [6.5–6.11]. Their measurements are for incident neutrons of thermal energy and energies of 7.0, 15.5 and 22.0 MeV. These are shown in Figs. 6.5 and 6.6 as solid dots.

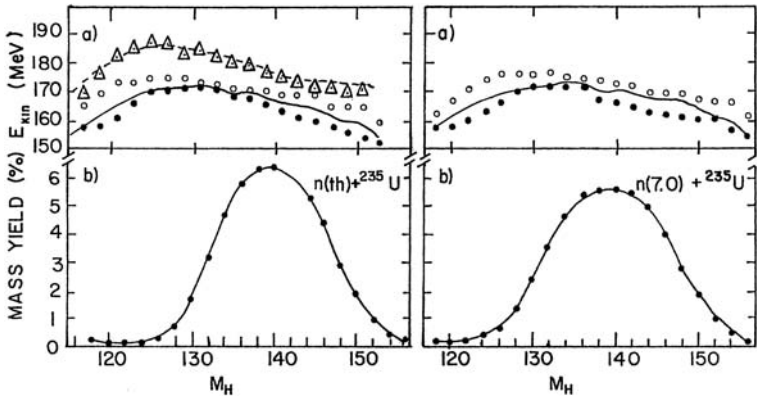

Fig. 6.5. The same as the one for Fig. 6.3 except the target is ^{235}U and incident neutron energies are thermal and 7.0 MeV. Data are taken from [6.5–6.11]

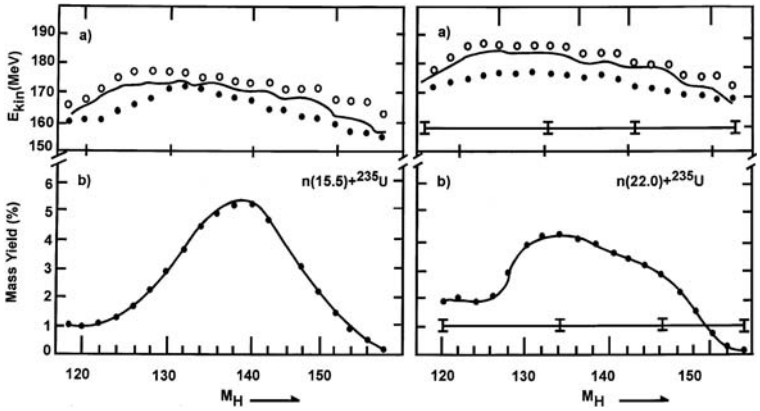

Fig. 6.6. The same as the one for Fig. 6.5 except the neutron incident energies are 15.5 and 22.0 MeV

The kinetic energy spectra necessary to fit these data along with the calculated percentage mass yields using (6.16) are shown as solid dots in these figures. The Q-values used in the calculations are the same ones used in calculation of spontaneous fission of ^{236}U and are noted as dashed lines in Fig. 6.5. The same Q-value has been used in all other cases. These Q-values are very close to the ones calculated from the liquid drop mass formula of Myers and Swiatecki [6.30] which are shown as triangles, in Fig. 6.5.

These data indicate a substantial change in the relative percentage mass yields between symmetric and asymmetric modes of decay with increasing incident energy. At thermal incident energy the percentage mass yields to the asymmetric decay modes dominate over those to symmetric ones by a few orders of magnitude, but at 22 MeV the two percentage yields are comparable, differing by a factor of about two. However, the change is gradual. The kinetic energy spectra also change with increasing neutron energy but additional energy seems to be distributed among all decay modes and hence, the change is less dramatic.

Theoretically one can account for these data and their variation with incident energy. The available increase in energy resulting from the increase in incident energy seems to be distributed in a manner that tends to equalize most probable kinetic energies associated with all decay modes.

A comparison of the decay probabilities to three particular pairs for thermal and 22 MeV incident energies shown in Figs. 6.1 and 6.2 reveals that the additional 22 MeV of energy affects the widths of the bell shaped curves. They become wider with increase in available energy. The difference in yields at maxima to the three decay modes is reduced significantly with increase of incident energy.

6.3.1c Neutron Induced Fission of ^{239}Pu

The data on percentage mass yields and TKE are exhibited as solid dots in Figs. 6.7 and 6.8 as a function of mass numbers of the daughter pair in induced fission of ^{239}Pu by thermal, 5.5 and 15.5 MeV incident neutrons. They show qualitatively the same behavior as the ones seen for ^{233}U and ^{235}U targets. Theoretical calculations of percentage mass yields and the TKE needed to fit them are shown as solid lines as a function of mass number, in these figures. The agreement is reasonable. The Q-values used in these calculations are shown in Fig. 6.7 as broken lines and they are the same ones used for spontaneous fission. They are consistent with calculations using the liquid drop mass formula [6.30].

Calculated TKE are shown as open circles in each of the figures. They are within a few MeV of observed values as well as theoretical values needed to fit the percentage mass yields spectra. In Fig. 6.8 we have also denoted by crosses, TKE calculated without the requirement that the change in entropy should be zero or positive. These values are in general not as good as the ones calculated imposing the restriction $\Delta s \geq 0$.

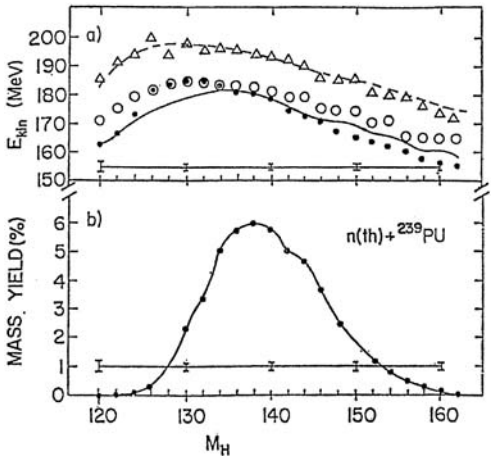

Fig. 6.7. The same as the one for Fig. 6.3 except the target is ^{239}Pu and incident neutron energy is thermal. Data are from [6.5, 6.6]

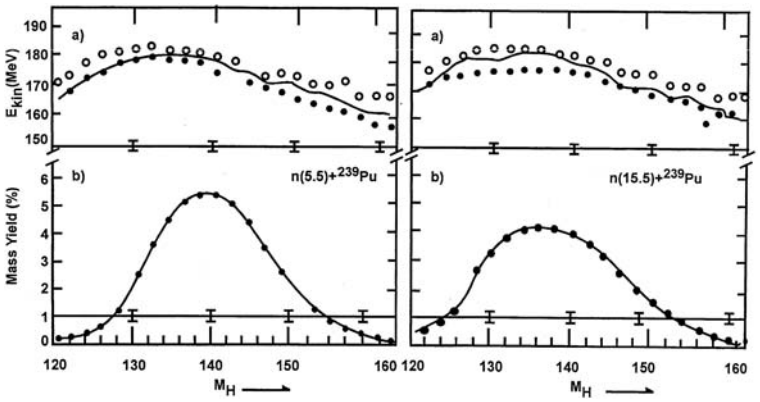

Fig. 6.8. The same as the one for Fig. 6.7 except the neutron incident energies are 5.5 and 15.5 MeV

The percentage mass yields spectra in the spontaneous fission of ^{240}Pu shown in Fig. 5.2, and thermal neutron induced fission of ^{239}Pu shown in Fig. 6.8 are not quite the same. This is, in principle, expected theoretically because in the latter case, the compound nucleus ^{240}Pu has 6.455 MeV extra excitation energy. This additional excitation energy increases somewhat the domain of integration of the phase space spanned by the product of two level density functions of emerging nuclei. The analysis of spontaneous fission done in Chap. 5 indicates that the model can also account for the observed percentage mass yields spectrum in spontaneous fission of ^{240}Pu.

6.3.1d Neutron Induced Fission of ^{229}Th

In Fig. 6.9, the observed percentage mass yields and TKE spectra in thermal neutron induced fission of ^{229}Th are plotted as solid lines as a function of the mass of the heavy fragments. The observed mass yields can easily be fitted using average kinetic energies that are very close to the observed ones. These calculations are marked in Fig. 6.9 as solid dots. One may determine average kinetic energies by locating the maximum of the decay widths. These are shown as open circles. These theoretically determined TKE are also close to the observed ones. The Q-values used in the calculations are noted as triangles. They are within 10 MeV of those expected from Myers-Swiatecki's mass formula [6.30].

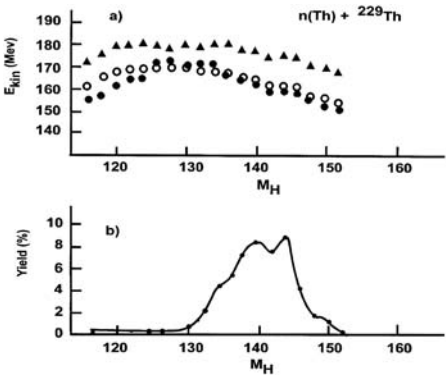

Fig. 6.9. The same as the one for Fig. 6.3 except solid, instead of open, triangles refer to Q-values used in accounting for the mass yields

6.3.1e Fission Widths

For thermal induced fission, data on fission widths may be extracted by fitting the fission cross section with a Breit-Wigner type of resonance formula and from the knowledge of neutron width. An average value of fission width is then obtained either by using an appropriate number for average level spacing or taking an appropriate average of all fission widths extracted from the fitting. Theoretically total fission widths may be calculated from (6.6), (6.15), and (6.16). Calculations have been done using Green's mass formula [6.41]. In Table 6.1 we have compared the calculated fission width for thermal neutron fission of ^{233}U, ^{235}U and ^{239}Pu with those extracted from experiment and the agreement is good for ^{233}U and ^{235}U. The extracted fission width from the experiment on ^{239}Pu has significant error bar and depends on the spin of the states and neutron widths. It also differs from earlier data. Because of relatively significant uncertainties in extracting average fission width from

Table 6.1. Comparison of calculated average fission widths (column 3) with observed ones (column 2) for thermal neutron induced fission 233U, 235U and 240Pu. Widths are in ev. a, b, c, d, are, respectively, [6.42] through [6.45]

Target	⟨Fission Width⟩ Exp	⟨Fission Width⟩ Th
^{233}U	0.34a	0.30
^{235}U	0.067b	0.06
	0.114c	
^{239}Pu	1.03d	30.0

the measurement of fission cross section, the agreement does not allow one to determine the detailed nature of the barrier.

6.3.2 Test of Compound Nucleus Formation Hypothesis

The change in percentage yields spectrum as a function of daughter masses with the change in incident kinetic energy of projectiles is not unique to incident neutrons but has also been observed for incident charged particles like protons and alpha-particles. Calculations involving percentage mass yields at a particular incident energy do not require a knowledge of formation cross sections since it involves the determination of a ratio. Only the information about the excitation energy of the compound nucleus, Q-values related to emission of daughter pairs, level density function and interaction potential between each member of a daughter pair are needed. The same holds for the calculation of TKE.

These calculations do not depend on the mechanism of the formation of the compound or composite systems but assumes their formation. A possible way to test this hypothesis is to use two different projectiles and targets, each of which could form the same compound system at about the same excitation energy and then to compare the final percentage mass yields and TKE spectra in the two cases. Such data are available for neutron induced fission of ^{235}U and alpha induced fission of ^{232}Th. The Q-values of formation of the compound system, ^{236}U in the two cases are the following:

$$n + {}^{235}\mathrm{U} \rightarrow {}^{236}\mathrm{U} + 6.47 \quad \mathrm{MeV}$$
$${}^{4}\mathrm{He} + {}^{232}\mathrm{Th} \rightarrow {}^{236}\mathrm{U} - 4.57 \quad \mathrm{MeV}\ .$$

Thus, an alpha particle having about 11.04 MeV extra-energy would form a compound system of ^{236}U having the same excitation energy as the one formed by the incident neutron. In Fig. 6.10, observed percentage mass yields spectra for an incident neutron [6.7] of 15.5 MeV and an alpha particle [6.34] of 27.5 MeV, have been plotted and they do exhibit similar mass distributions, confirming the hypothesis. The observed mass yields spectra for other cases

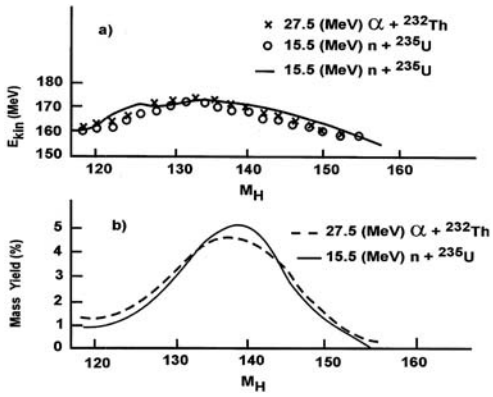

Fig. 6.10. *Open* circles and crosses in the upper insert are theoretical [6.16] average kinetic energy spectra needed to account for observed percentage mass yields for 15.5 MeV incident neutrons on ^{235}U and 27.5 MeV incident alpha particles on ^{232}Th [6.34]. The *solid* line is the observed average kinetic energy spectrum needed to fit the yield curve for the (n + ^{235}U) case. Q-values are the same ones used for thermal neutron induced fission of ^{235}U

can be fitted using (6.16) with the two TKE spectra shown in the upper insert. The two theoretical spectra are very similar and close to the observed one for the (n + ^{235}U) case, justifying the assumption of the formation of a compound system.

6.3.3 Alpha-Induced Fission

In this section, we investigate the change in percentage mass-yields and TKE with the change in alpha-induced fission of ^{226}Ra and of ^{226}Th.

6.3.4 Alpha-Particle Induced Fission of ^{226}Ra

Unik and Huizenga [6.4] have measured the TKE and percentage mass yields distribution as a function of the masses of daughter fragments for 30.8 and 38.7 MeV alpha particles incident on ^{226}Ra which are shown in Fig. 6.11. The 8 MeV of extra energy available for the 38.7 MeV case clearly influences the mass distribution, particularly near symmetric modes, whereas the change in TKE as a function of daughter the masses is less pronounced which is similar to the case of neutron induced fission.

Theoretical calculations of these observables require a knowledge of Q-values, parameters of level density functions and interaction between two members of a daughter pair. Since the compound nucleus in this case is ^{230}Th, we have taken exactly the same Q-values used in calculating the mass distribution for neutron induced fission of ^{229}Th. Calculated results are compared to the data in Fig. 6.11. Theoretically one can account for the observed mass distributions with TKE spectra close to the observed ones.

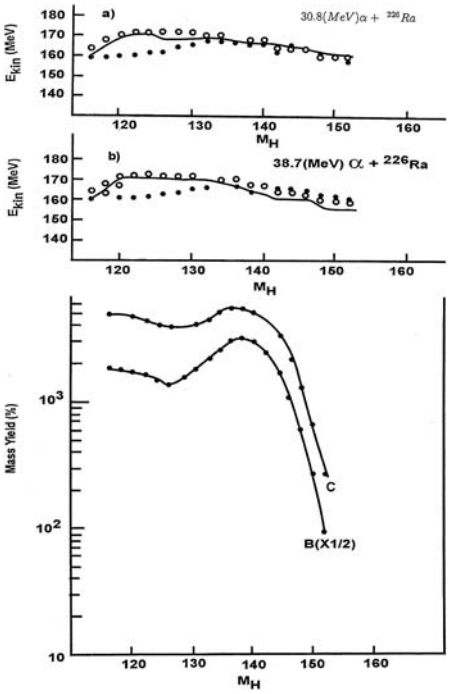

Fig. 6.11. Experimental and theoretical percentage mass yields are shown in the bottom insert as a function of masses of heavy fragments by *solid* dots and lines, respectively, for 30.8 MeV (marked B) and 38.7 MeV (marked C) alpha induced fission of ^{226}Ra. The measured and theoretical average kinetic energies needed to fit the mass yields are shown by *solid* dots and curves, respectively, in the upper insert for two cases. Open *circles* are calculated average kinetic energies obtained from maxima of (6.16). The data are from [6.35]. Calculations are from [6.16, 6.17]

One can further calculate the most probable kinetic energy for a given daughter pair by locating the maxima of the decay widths as a function of ε. Some sample calculations are shown in Fig. 6.12 for daughter pairs, ($A_1 = 140$, $A_2 = 90$), ($A_1 = 150$, $A_2 = 80$) and ($A_1 = 116$, $A_2 = 114$) for incident energies of 38.7 MeV, respectively. This situation is very similar to the neutron induced fission cases: (a) the shapes of these curves are bell shaped, (b) the maxima lies 10 to 20 MeV below the respective Q-values and (c) the additional energy broadens the widths.

Calculated TKE are shown as open circles in Fig. 6.11. They are very close to the theoretical TKE used in fitting the mass yields spectra and to the observed ones. There is, however, about 5 to 10 MeV difference between the observed and calculated TKE for the decay to symmetric modes.

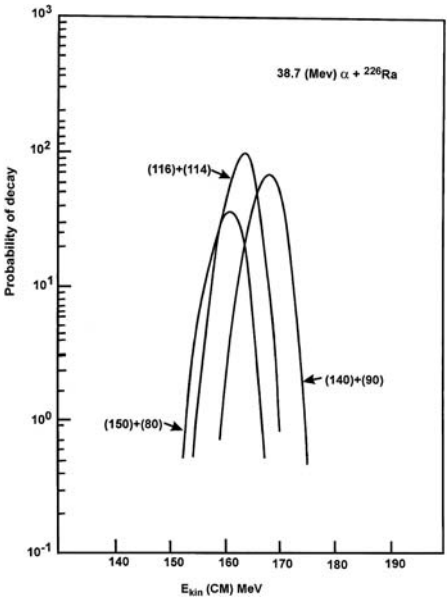

Fig. 6.12. Calculated relative decay probabilities [6.16, 6.17] to daughter pairs characterized by mass number (116, 114), (150, 80), and (140, 90) in 38.7 MeV alpha induced fission of ^{226}Ra are plotted as a function of their kinetic energies. The location of maxima are average kinetic energies and shown as open circles in Fig. 6.11

6.3.5 Alpha-Particle Induced Fission of ^{232}Th

Pavlov et al. [6.34] have made a systematic study of the variation of percentage mass yields and TKE spectra in alpha induced fission of ^{232}Th in the energy range of 24 to 35 MeV. They have observed that the yields around symmetric decay modes increase significantly relative to those around asymmetric modes with increasing incident energy which is reminiscent of the case of neutron induced fission of ^{235}U. Their data are shown as solid lines in Fig. 6.13. These have been analyzed theoretically and calculations are shown as solid dots in Fig. 6.13. The Q-values used in the calculation are the same as the ones used in the calculations of neutron induced fission of ^{235}U. Theoretical values have been calculated from the maxima of $\Gamma(A_1, A_2, I, U, \varepsilon)$ as a function of ε. These values, shown as open circles in the same figures, are very close to the values needed to fit the mass yields curve and experimental data, shown as solid circles and lines, respectively.

There is a great deal of data on the variation of percentage mass yields as a function of energy of incident charged and uncharged projectiles, particularly proton, ^{3}He, and ^{4}He as summarized in [6.1]. However, in many instances the information on TKE is absent. These data can easily be fitted using the above theory. *These fits are, however, incomplete since the observed decay*

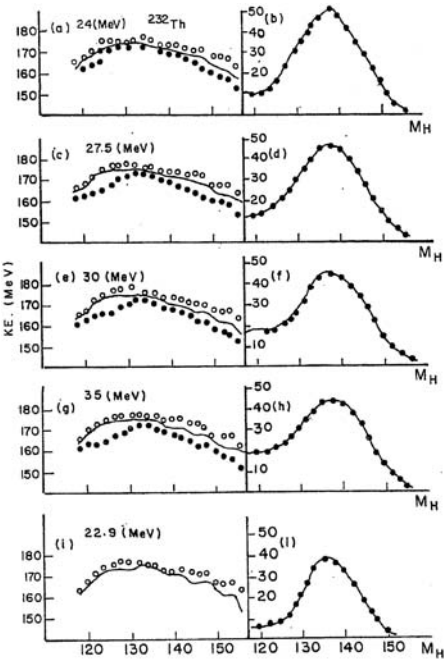

Fig. 6.13. Experimental and theoretical percentage mass yields and average kinetic energies are shown, respectively, by *solid* dots and *solid* lines in the *left* and *right* inserts. *Open* circles in the left are calculated most probable kinetic energies obtained from the maxima of (6.16). Data are from [6.34]. Incident alpha particle energies are marked in each insert on the left. Calculations are from [6.16, 6.17]

probabilities must be obtained with appropriate kinetic energy. A particular daughter pair is characterized by not only their mass and charge numbers but also by excitation energies and the associated kinetic energy. Implicit in the above theory is that (a) the decays are binary and (b) each member of a daughter pair is characterized by its charge and mass number and that decay is possible to all excited states of each pair commensurate with the total available energy. Thus, the theory also predicts charge distributions similar to those obtained in spontaneous or thermal neutron induced fission. Moreover, not only cold fission but fission to all allowed excited states of a daughter pair is permitted.

6.4 The Role of the Barrier and the Shape of the Yield-Spectrum

The importance of obtaining mass yields spectra with correct kinetic energies are exemplified in this section which presents a discussion on the relation of

this theory to the statistical theory of Fong and Wildermuth and Faessner and others. Whereas, it is possible to fit the mass yields spectra with these latter theories, the most probable decay modes in every case occur at zero kinetic energy of a daughter pair, which is in stark contrast with the data. The key difference between their theory and the one expressed here is that $T(\varepsilon)$ in their theory is taken to be one, i.e., there is no final channel interaction between an emerging daughter pair.

In this section we present an analysis of the expected kinetic energy for maximum yields if $T(\varepsilon)$ is set to one.

Fong [6.21, 6.22] Newton [6.14], Cameron [6.28, 6.35], Newson [6.36] and Faessner and Wildermuth [6.23, 6.24], have attempted to reproduce the percentage mass yields as a function of daughter masses using statistical theories that omit the final state interaction. Consequently only the integral in (6.9) is a function of kinetic energy of a daughter pair. Fong has attempted to relate this to separation radius R_{s} by assuming that the observed kinetic energies at the point of separation are converted to Coulomb potential energy between two members of a pair. He has found that R_{s}, determined from this equality, is significantly larger than the sum of two radii of the pair and attributes this to large deformation of two separating nuclei. Level density functions chosen by these authors, although different from each other, are very similar. The one used by Fong is the following:

$$\rho(U) = (2I+1)\exp\{-(I+1/2)^2/2g\sqrt{u/a}\}\rho_o(U) \tag{6.25}$$

with

$$\rho_o(U) = c\exp[2\sqrt{aU}] \quad \text{and} \quad g = (2/5)MR^2/\hbar^2 \tag{6.26}$$

with

$$c = 0.38\exp(-0.005\mathrm{A}) \quad \text{and} \quad a = 0.05A[\mathrm{MeV}^{-1}] \tag{6.27}$$

M and R are, respectively, the mass and radius of nucleus.

Fong's calculation of mass yields for thermal neutron induced fission of ^{239}U is in reasonable accord with observed data at that time. However, Perring and Story [6.41] have been unsuccessful in explaining the thermal neutron induced fission of ^{239}Pu using Fong's theory. Cameron [6.28,6.36] has pointed out that R_s need to be a function of both available energy and observed kinetic energy ε in order to understand the change in percentage mass yields from thermal to 14 MeV neutron induced fission of ^{235}U. These difficulties are a consequence of attempting to ignore the maximum of (6.9) which occurs at $\varepsilon = 0$ in Fong's theory as is evident from (6.23). Equation (6.23) corresponds to using (6.9) with level density function (6.25) and $T(\varepsilon) = 1$. The maximum of (6.23) in this case occurs at $\varepsilon = 0$. Actual calculations done using (6.16) with $T(\varepsilon) = 1$ and using level density function (6.11) confirms this. Sample calculations of decay probabilities with $T(\varepsilon) = 1$ in (6.16) are presented in Figs. 6.14–6.16 as a function of kinetic energy of a number of daughter pairs for thermal and 22 MeV induced fission of ^{235}U and 38.7 MeV alpha induced

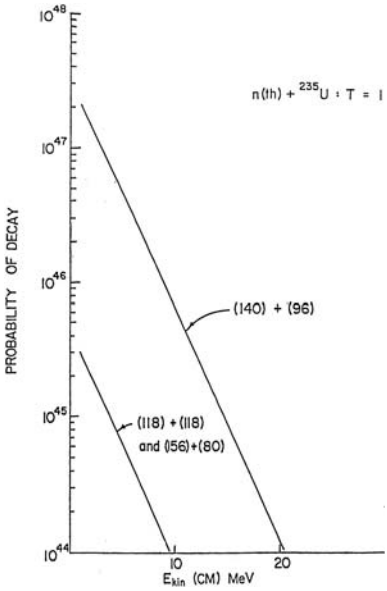

Fig. 6.14. Calculated relative decay probabilities [6.16, 6.17] to mass pairs (140, 96), (118, 118), and (156, 80) are plotted as a function of their kinetic energies, E_{kin}, for thermal induced fission of ^{235}U for the case where the transmission function $T(\varepsilon)$ in (6.16) is set to be one

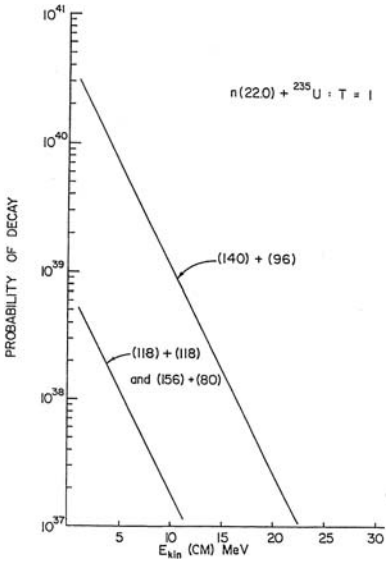

Fig. 6.15. The same as the one in Fig. 6.14 except the incident neutron energy is 22.0 MeV

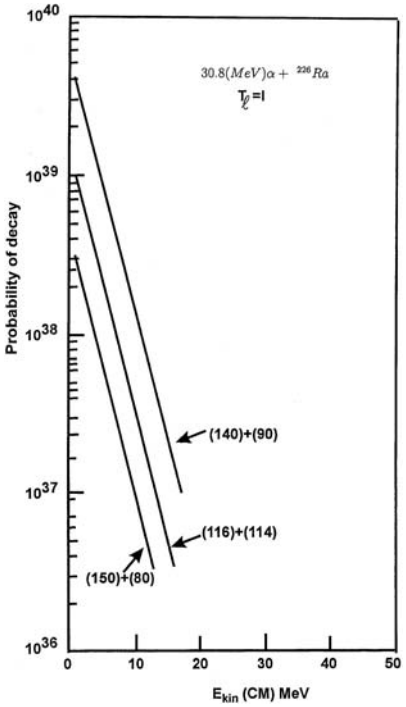

Fig. 6.16. Calculated relative decay probabilities [6.16] to mass pairs (140, 96), (118, 118), and (156, 80) in 30.8 MeV alpha induced fission of ^{226}Ra are plotted as a function of their kinetic energies for the case where the transmission in (6.16) is set to be one

fission of ^{232}Th. In all cases the most probable kinetic energy is zero, i.e., the entire available energy has been transformed to excite each member of a daughter pair which is in sharp contradiction to experimental results. In the absence of a barrier, this is the expected theoretical result.

Thus, a consistent analysis that accounts for observed mass yields along with corresponding kinetic energy requires the incorporation of a barrier in the final channel. In fact, attempts to analyze the percentage mass yields and TKE data of [6.5, 6.7, 6.39] in induced fission of ^{235}U by 6.0 and 15.5 MeV neutrons led Fachini and Saetta-Menichella to conclude the necessity of a barrier similar to the ones used here between the saddle and scission points [6.20].

6.5 Conclusion

Essentially, the same barrier which could account for the observed half-lives with appropriate kinetic energies, percentage mass yields as a function of mass

number and charge distribution, discussed in Chap. 5, can account for the change in mass distribution as a function of the change in incident energies of neutrons and alpha-particles in induced fission. Moreover, the calculated distribution of the yields as a function of the kinetic energy of a daughter pair exhibits the observed behavior. The latter point is a direct consequence of using the external barrier between the saddle and scission points. In the absence of such a barrier, the most probable kinetic energy associated with the emission of all daughter pairs is zero, which sharply contradicts the observed data.

References

1. For a summary see *Nuclear Fission* by R. Vandenbosch and J.R. Huizenga (Academic Press, New York, 1973).
2. L.J. Colby Jr., M.L. Shoaf and J.W. Cobble, Phys. Rev. **121**, 1415 (1961).
3. H.C. Britt, H.E. Wegner and J.C. Gursky, Phys. Rev. Lett. **8**, 98 (1962).
4. J.P. Unik and J.R. Huizenga, Phys. Rev. **134 B**, 90 (1964).
5. V.G. Vorob'eva, P.P. D'yachenko, B.D. Kuz'minov and M.Z. Tarasko, Sov. J. Nucl. Phys. **4**, 234 (1967).
6. P.P. D'yachenko and B.D. Kuz'minov and M.Z. Tarasko, Sov. J. Nucl. Phys. **8**, 165 (1968).
7. P.P. D'yachenko and B.D. Kuz'minov, Sov. J. Nucl. Phys. **7**, 27 (1968).
8. N.I. Akimov, V.G. Vorob'eva, V.N. Kabenin, N.P. Kolosov, B.D. Kuz'minov, A.I. Sergachev, L.D. Smirenkina and M.Z. Tarasko, Sov. J. Nucl. Phys. **13**, 272 (1971).
9. P.P. D'yachenko, B.D. Kuz'minov, L.E. Kutsaeva and V.M. Piksaikin, Sov. J. Nucl. Phys. **14**, 266 (1972).
10. A.I. Sergachev, P.P. D'yachenko, A.M. Kovalev and B.D. Kuz'minov, Sov. J. Nucl. Phys. **16**, 266 (1973).
11. V.M. Surin, A.I. Sergachev, N.I. Rezchikov and Kuz'minov, Sov. J. Nucl. Phys. **14**, 523 (1972).
12. V.F. Weisskopf, Phys. Rev. **52**, 295 (1973).
13. V.F. Weisskopf and D.H. Ewing, Phys. Rev. **57**, 472 (1940).
14. T. D. Newton, *Proc. Symp. On Physics of Fission*, Chalk River, Report, CRO-642-A and AECL-329 (1965); Cand. J. Phys. **34**, 804 (1956).
15. T. Ericson, Adv. Phys. **9**, 36 (1960).
16. B. Compani-Tabrizi, Ph.D. dissertation 1976, (Indiana University at Bloomington).
17. B. Compani-Tabrizi, M.A. Hooshyar and F.B. Malik, *Proc, Int'l Conf. on the Interaction of Neutrons with Nuclei*, ed. E. Sheldon (ERDA: Conf. 7607115-Pl, 1976) 725.
18. B. Compani-Tabrizi, M.A. Hooshyar and F.B. Malik, *50 Years with Nuclear Fission*, eds J.W. Behrens and A.D. Carlson (American Nuclear Society, 1980) p. 650.
19. E. Erba, U. Facchini and E. Saetta-Menichela, Nucl. Phys. **84**, 595 (1966).
20. U. Facchini and E. Saetta-Menichela, Acta Phys. Polonica **A84**, 537 (1970).

21. P. Fong, *Statistical Theory of Nuclear Fission* (Gordon and Breach, New York, 1969).
22. P. Fong, Phys. Rev. **102**, 434 (1956).
23. H. Faessner and K. Wildermuth, Phys. Lett. **2**, 212 (1962).
24. H. Faessner and K. Wildermuth, Nucl. Phys. **58**, 177 (1972).
25. M.A. Hooshyar and F.B. Malik, Phys. Lett. **38 B**, 495 (1972).
26. M.A. Hooshyar and F.B. Malik, Helv. Phys. Acta **45**, 567 (1972).
27. E. Gadioli and L. Zetta, Phys. Rev. **167**, 1016 (1968).
28. A.G.W. Cameron, Cand. J. Phys. **36**, 1040 (1958).
29. F.B. Malik and P.C. Sabatier, Helv. Phys. Acta **46**, 303 (1973).
30. W.D. Myers and W.J. Swiatecki, Nucl. Phys. **81**, 1 (1966).
31. V.M. Surin, A.I. Sergachev, N.I. Rezchikov and B.D. Kuz'minov, Sov. J. Nucl. Phys. **16**, 266 (1973).
32. K.F. Flynn, E.P. Horwitz, C.A.A Bloomquist, R.F. Barnes, R.K. Sjoblom, P.R. Fields and L.E. Glendenin, Phys. Rev. C **5**, 1725 (1972).
33. K.F. Flynn, J.E. Gindler, R.K. Sjoblom and L.E. Glendenin, Phys. Rev. C **11**, 1676 (1975).
34. A.F. Pavlov et al.; Publication of Nucl. Phys. Institute of Kazakh Academy of Science, Yad Fiz. **17**, 1143 (1973).
35. A.G.W. Cameron, Rev. Mod. Phys. **30**, 553 (1958).
36. H.W. Newson and N.M. Duncan, Phys. Rev. **109**, 942 (1958).
37. H.W. Newson, Phys. Rev. **122,** 1224 (1961).
38. J.K. Perring and J.S. Story, Phys. Rev. **98**, 1525 (1955).
39. H.W. Schmitt, J.H. Neiler and F.J. Walter, Phys. Rev. **141**, 1146 (1966).
40. J.P. Unik, J.E. Gindler, L.E. Glendenin, K.F. Flynn, A. Gorski and R.K. Sjoblom, Argonne National Lab. Report (1974).
41. A.E.S. Green, Phys. Rev. **93**, 1006 (1954).
42. D.W. Bergen and M.G. Silbert, Phys. Rev. **166**, 1178 (1968).
43. M. Asghar, Nucl. Phys. A **98**, 33 (1967).
44. J.D. Gramer, Nucl. Phys. A **126**, 471 (1969).
45. J.A. Farrell, Phys. Rev. **165,** 1371 (1968).

7 Hot and Cold Fission

7.1 Introduction

In the previous chapter, the most probable kinetic energy associated with the fission of a parent nucleus to a daughter pair having a particular mass division A_1 and A_2 has been calculated by (a) averaging the yields over all isobars having mass numbers A_1 and A_2, (b) averaging the yields over all excitation energies of the daughter pair characterized by mass and atomic numbers (A_1Z_1) and (A_2Z_2), and then (c) calculating the kinetic energy corresponding to the maximum yields for that particular mass split. For example, in Fig. 6.1, taken from [7.1–7.3], the most probable kinetic energy, TKE, for the thermal neutron induced fission of ^{235}U to the isobar pair $A_1 = 140$ and $A_2 = 96$ is the kinetic energy at which the yields to this particular mass splitting has its maximum. This maximum is at about 174 MeV. Thus, the most probable kinetic energy associated with the mass splitting $A_1 = 140$ and $A_2 = 96$ is 174 MeV. However, the curve denoting the probability of the decay as a function of the total kinetic energy in the center of mass system, E_{kin} (CM), is approximately bell shaped indicating a distribution of yields as a function of E_{kin} (CM). There is, therefore, a finite probability for the isobaric daughter pair, $A_1 = 140$ and $A_2 = 96$ to have a kinetic energy of about 180 MeV which is very close to the Q-value for this mass split. In other words, there is a finite probability for the pair $(140 + 96)$ to be emitted cold i.e., the pair having no or very little excitation energy. Similar results have also been obtained, theoretically, in the thermal neutron induced fission of ^{233}U and ^{239}Pu and are expected in the spontaneous fission of all fissioning nuclei within the framework of the theory expounded in Chap. 6. In 1981, Signarbieux et al. [7.4], indeed, found experimentally that, daughter pairs having no or very little excitation, called cold fragments, are emitted in the thermal neutron induced fission of ^{235}U. Subsequently, such cold fission fragments have been observed in many cases [7.5].

The theory of [7.1–7.3] has three other important predictions. *First*, there is always a finite probability of a daughter fragment being emitted with various excitation energies commensurate with the energy and angular momentum conservation. *Second*, there is an upper limit to the maximum of kinetic energy associated with the decay to a particular daughter pair. This upper limit is very close to the Q-value of the emission of that daughter pair. A

daughter pair emitted with this maximum kinetic energy has essentially no excitation and hence, is emitted cold. *Third*, there is a lower limit for the kinetic energy well above zero and hence, an upper limit of the total excitation energy of a particular daughter pair lying well below the allowed maximum available energy *for excitation*, which is the Q-value for spontaneous emission and the Q-value plus incident projectile energy in case of induced fission. This latter feature, here called hot fission, is distinct from the model used for evaporation where the most probable kinetic energy associated with the emission of a daughter pair in spontaneous fission is expected to be zero. The limits on the kinetic energies for hot and cold fission depend on the detailed structure of the external barrier. These predictions, discussed in detail in Sect. 7.3, are in accord with the observations so far. The discovery of cold fission and the validity of the other two predictions are essential consequences of the existence of a barrier close to the scission point and establish the key point of this monograph. In the next section, we present a summary of some important experimental features associated with the study of cold fission, *but also pertinent to the possibility of experimentally establishing the emission of daughter pairs in hot fission.*

7.2 Summary of Data Pointing to Hot and Cold Fission

The early experiments determining the kinetic energy spectra in spontaneous and thermal neutron induced fission using solid state detectors had provided the evidence of the occurrence of cold as well as hot fission. In Fig. 7.1, we reproduce the contour plot of pulse heights in correlated solid state detectors in the thermal neutron induced fission of ^{235}U reported by Schmitt, Neiler, and Walter [7.6]. Facchini and Saetta-Menichella [7.7] constructed from the data of Fig. 7.1, the yield versus fragment kinetic energy curve for neutron induced fission of ^{235}U to the isobaric pairs having mass number 96 and 140. This is shown in Fig. 7.2. This plot clearly indicates that the observed maximum kinetic energy is close to the Q-value and the observed minimum kinetic energy is well above zero, thereby confirming the prediction of the model. Facchini and Saetta-Menichella and High, Block, Clark, and Malik [7.8] recognized that this distribution in yields as a function of kinetic energy points to the penetration through an external barrier prior to scission. Similar contour plots have since been constructed in many experiments determining the kinetic energy spectra in spontaneous and induced fission e.g., by Pleasonton [7.9] in the thermal neutron induced fission of actinides.

In Fig. 7.2 the maximum kinetic energy at which there is some emission of the fragment pair 96 and 140 is about 190 MeV, which is very close to the maximum Q-value of the isobar pairs having these masses. Thus, the isobar pair with 190 MeV kinetic energy is essentially emitted without any excitation energy i.e., cold. As noted earlier, the evidence for cold fission was

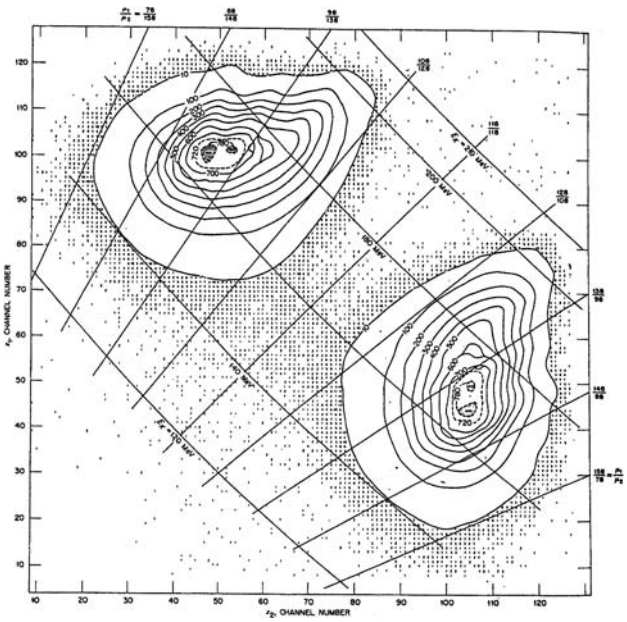

Fig. 7.1. Number of events measured in coincidence are plotted as an array (x_1, x_2) in the thermal neutron induced fission of ^{235}U. Numbers labeling the contours and those appearing outside the 10-contours indicate the number of events per channel squared. Curves of constant kinetic energy, E_{K}, and the ratio of masses μ_1 and μ_2 in amu are shown. The array contains 0.95×10^6 events (Reproduced from [7.6])

then conclusively established by Signarbieux et al. [7.4] in 1981 and further studied carefully by Montoya [7.5] in the thermal neutron induced fission of ^{233}U, ^{235}U and ^{239}Pu. In Fig. 7.3, the observed maximum Q-value is plotted as a function of the mass of the lighter member of a daughter pair in the thermal neutron induced fission of ^{235}U [7.10]. In each case, the observed kinetic energies are very close to the corresponding Q-values of the emission process implying that the daughter pairs are emitted with no or very little excitation energy. *In fact, these two energies are equal for the emission of nuclei, having mass numbers around 105.*

Figure 7.4 presents the contour plot of the observed kinetic energies of light and heavy fragments in the spontaneous fission of ^{252}Cf along with Q-values. This plot indicates that (a) there are many fragment pairs emitted with kinetic energies very close to the respective Q-values and (b) *The kinetic energy associated with the decay to a particular daughter pair has a distinct lower limit, well above zero, experimentally. This observation implies that there is an upper limit, well below the Q-value, which could be transferred to the excitation of a daughter pair.* This is the kind of hot fission expected in the theory presented in Chap. 6, which does not allow a fragment pair being

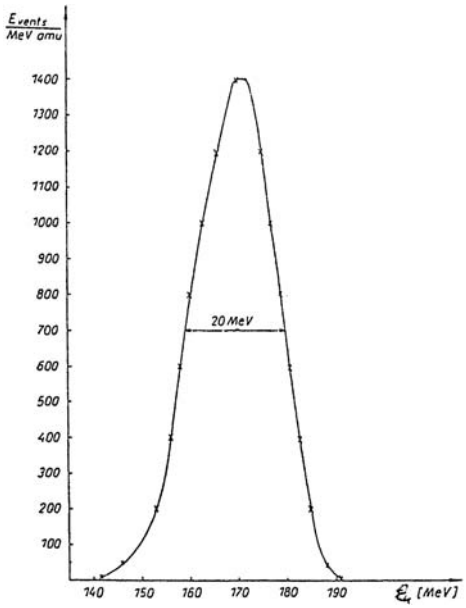

Fig. 7.2. Number of events are plotted against kinetic energy of the fission pair, $A_1 = 140$ and $A_2 = 96$ in the thermal neutron induced fission of ^{235}U (Reproduced from [7.7])

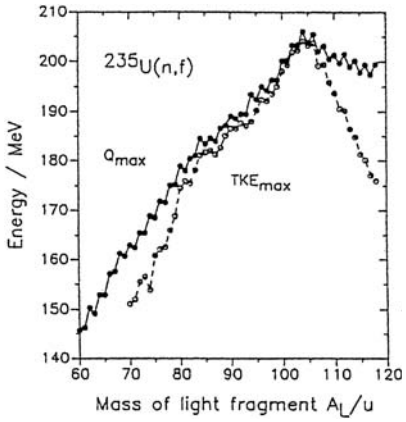

Fig. 7.3. Observed maximum kinetic energy, $\mathrm{TKE_{max}}$ shown as open circles is compared to maximum Q-values for a particular mass split, $Q_{\max}$, shown as *solid* dots. (Reproduced from [7.10]). $\mathrm{A_L}$ refers to the mass number of the lighter fragment

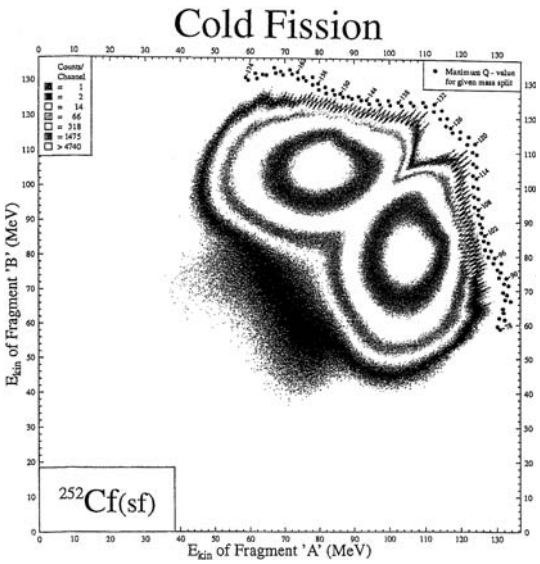

Fig. 7.4. Contour plot of the kinetic energies, E_{kin}, of two members of fissioned fragments, with the mass split with the same mass number as shown as *solid* dots (Reproduced from [7.11])

emitted with zero kinetic energy i.e., the sum of the excitation energies of both members of a fragment pair can not be as high as its allowed Q-value. Similar evidence of hot fission is present in Fig. 7.1.

There is also evidence of an odd-even effect in cold fission, i.e., the preference for emission of even-even daughter pairs, an effect already noticed in the normal fission process first by Reisdorf, Unik and Glendenin in 1973 [7.13]. This is illustrated by plotting the percentage yields in the thermal neutron induced fission of ^{233}U as a function of the mass of the light fragment for several energies in Fig. 7.5 [7.10]. The odd-even effect is most pronounced at high and low energies. At energies of 114 and 84 MeV of the light fragment, A_L, the most prominent peaks are respectively, observed at $A_L \cong 90$, 96, and 102 and $A_L \cong 90$, 94, and 98. The odd-even effect is much more pronounced when the percentage yield is plotted against the charge of the light element, Z_L, in the same experiment. This is shown in Fig. 7.6. Clearly, the emission of the light element of even number is preferred over its neighboring odd-even or even-odd element, particularly at higher energies.

7.3 Theory and Discussion

The theory of hot and cold fission essentially follows from the theory discussed in Chap. 6 dealing with induced fission. The expression for decay width is

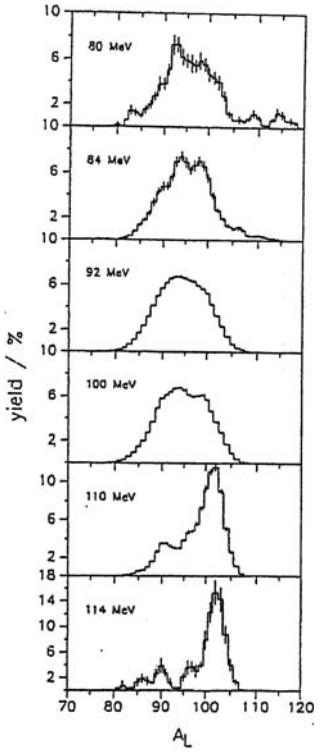

Fig. 7.5. Mass distribution of the light fission fragments in the thermal neutron induced fission of ^{235}U for a fixed kinetic energy shown in the inserts (Reproduced from [7.12])

given by (6.9). The decay probability to a daughter pair having charge and mass number (A_1, Z_1) and (A_2, Z_2) and a kinetic energy E, $P(E,\ A_1Z_1,\ A_2Z_2)$ is related to the decay width which is proportional to the right hand expression of (6.9). Thus,

$$P(\varepsilon, A_1Z_1, A_2Z_2) \sim T(\varepsilon) \int_0^{\xi-E} \rho_1(U_1)\rho_2(\xi - \varepsilon - U_1)dU_1 \qquad (7.1)$$

where U_1 and U_2 are the excitation energies of the fragments and ξ and ε are, respectively, the Q-value of the process and the kinetic energy associated with each fragment at a given excitation energy.

One may theoretically calculate the yields to an isobaric pair having mass numbers A_1, and A_2 by summing over all isotopes of an isobaric pair

$$P(\varepsilon, A_1, A_2) = \sum_{Z_1Z_2} P(\varepsilon, A_1, Z_1, A_2, Z_2)\ . \qquad (7.2)$$

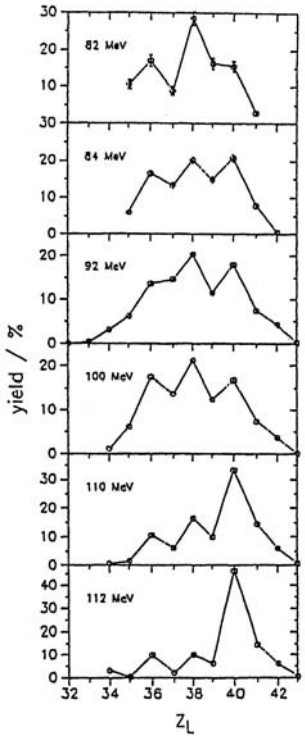

Fig. 7.6. Charge distributions of the light fission fragments in the thermal neutron induced fission of ^{235}U for fixed kinetic energies shown in the inserts (Reproduced from [7.10])

Figures 6.1 and 6.2 indicate such decay probabilities in neutron induced fission of ^{235}U for thermal and 22 MeV incident energies to daughter pairs ($A_1 = 140$, $A_2 = 96$), ($A_1 = 118$, $A_2 = 118$) and ($A_1 = 156$, $A_2 = 80$). In the case of thermal neutron induced fission of ^{235}U, the calculated decay probabilities to each of the isotopic pairs clearly indicate a finite non-zero probability for the emission of a daughter pair, each of which is emitted with a very little excitation energy. A comparison of this figure with Fig. 7.2 constructed from the experimental data for thermal neutron induced fission of ^{235}U to the daughter pair ($A_1 = 140, A_2 = 96$), indicates that the theory reproduces the general features of the yields curve shown in Fig. 7.2. The calculated maximum kinetic energy in Fig. 6.1 is about 182 MeV which is slightly less than the experimental value of about 190 MeV shown in Fig. 7.2. Considering that the typical error in measuring kinetic energy is about 2 to 3 MeV per fragment [7.6] and because of the sensitivity of the theoretically calculated yields on the choice of potential between the emitted pair, and the parameters of the level-density function as discussed below, the agreement

is reasonable. The predicted maximum kinetic energies associated with the thermal neutron induced fission of ^{235}U to the fragment pairs $(156 + 80)$ and $(118 + 118)$ are shown in Fig. 6.1, and are approximately 166 and 169 MeV, respectively, which are also close to the observed value of about 175 MeV shown in Fig. 7.3.

The calculations of decay probabilities using (7.1) are sensitive to (a) the choice of potential used in calculating $T(\varepsilon)$ and (b) the level density function and its parameters. These two factors also determine the actual shape of the curve of yields versus total kinetic energy. Level density functions are usually accurate up to about 10 to 15% at high excitation energies, but may not be very good at low excitation energies. The dependence of the decay probabilities on the shape of the external barrier may be studied by slightly changing the potential (6.10). The V_1 term of that potential i.e., the internal barrier has insignificant influence on the decay probabilities; however, the parameters characterizing the external barrier affects the decay probabilities significantly. For example, changing d to 5.0 fm (instead of 3.2), R_0 to $r_0\left({A_1}^{1/3} + {A_2}^{1/3}\right) + 3.7$ fm with the same r_0, and g to $\exp\left(-0.36|A_1 - A_2|^{1.6}\right)$ results in a shift in the width as well as the location of the maxima. The decay probabilities calculated using this new potential (set B) are shown in Figs. 7.7 and 7.8 for thermal and 22 MeV neutron induced

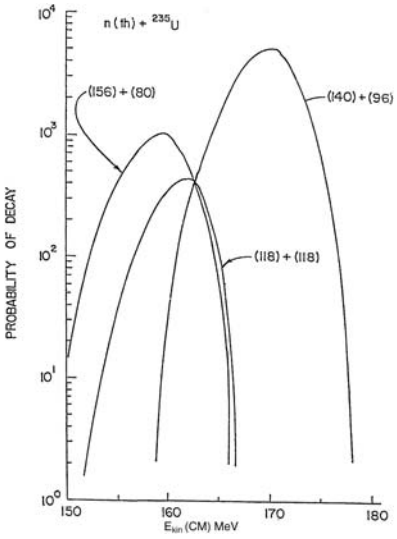

Fig. 7.7. Calculated yields in the thermal neutron induced fission of ^{235}U to daughter pairs $(140 + 96)$, $(118 + 118)$ and $(156 + 80)$ for the potential set B is plotted as a function of center of mass kinetic energy, $E_{\rm kin}$ (CM) in MeV of a daughter pair. These yields are to be compared with those in Fig. 6.1 calculated with slightly different potential (6.10). Both potentials give about the same observed half-lives and average kinetic energy in the spontaneous fission of ^{236}U

fission of ^{235}U. The minimum and maximum allowed kinetic energies which are, respectively, associated with the yields of hot and cold fission of a particular isobaric daughter pair, as well as the location of the maximum yields have changed significantly. Nevertheless, the maxima of allowed kinetic energies have remained close to respective Q-values indicating a finite possibility for the cold fission to occur in each case. The detailed experimental studies of the yields as a function of total kinetic energy of a daughter pair or isobaric pairs would certainly assist in determining the detailed nature of the external barrier.

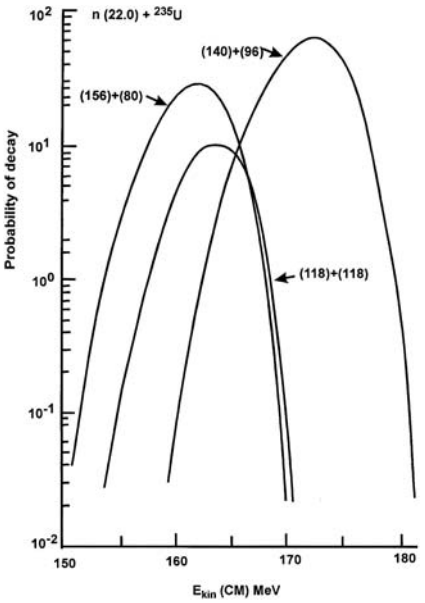

Fig. 7.8. The same as in Fig. 7.7 except for the incident neutron energy of 22 MeV. This is to be compared to Fig. 6.2

A comparison of Figs. 7.7 and 7.8 with Figs. 6.1 and 6.2 indicates that the yields of cold fission fragments increase significantly with the increase of incident neutron energy in induced fission for all three isobaric daughter pairs considered there. Thus, the study of cold fission is likely to be easier if the incident neutron has somewhat higher (e.g. 10 to 20 MeV) kinetic energies.

As noted earlier, an important ramification of the theory is that it predicts the occurrence of hot fission. The characteristic feature of hot fission discussed here, which is distinct from an evaporation process, is that the maximum allowed excitation of a particular daughter pair is significantly less than the Q-value. Thus, the entire Q-value cannot be converted into excitation energy of a daughter pair. This is due to the dissipation of energy associated with

barrier penetration. Experimentally, no fission fragments have been recorded below a certain kinetic energy in the thermal neutron induced fission of ^{235}U shown in Figs. 7.1 and 7.2 and in the spontaneous fission of ^{252}Cf indicated in Fig. 7.4, thereby giving credence to the theory.

In Fig. 7.9, we present the theoretical calculations for the decay probabilities as a function of kinetic energy for three fragment pairs in thermal neutron induced fission of ^{229}Th. Clearly cold fission to all three pairs is allowed. A characteristic feature of the theory is the approximate bell shaped nature of the yields versus kinetic energy curve associated with the emission of each pair. Whereas, the detailed shapes of these curves depend on the choice of the external barrier as well as level density functions, the characteristic bell shape of the yield curves having a minimum kinetic energy which is substantially higher than zero, is a direct consequence of the use of the external barrier (6.10) in evaluating the transmission coefficient in (7.1).

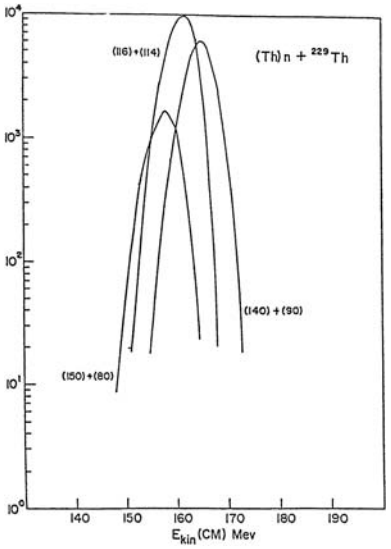

Fig. 7.9. Calculated yields of daughter pairs (140 + 90), (116 + 114) and (150 + 80) are plotted as a function of their respective center of mass kinetic energies in MeV in the thermal neutron induced fission of ^{229}Th using the potential (6.10)

In the absence of such a barrier, $T(\varepsilon) = 1$. Calculated decay probabilities in the thermal neutron induced fission of ^{229}Th to three isobaric daughter pairs *for the case* $T(\varepsilon) = 1$ *i.e., in the absence of a barrier are* plotted as a function of kinetic energy in Fig. 7.10. In each case the maximum is at zero kinetic energy and the possibility of cold fission is practically zero. Setting $T(\varepsilon) = 1$ corresponds to evaporation. It is easy to analyze the reasons for having no cold fission if the external barrier is absent. Setting $T(\varepsilon)$ in (7.1)

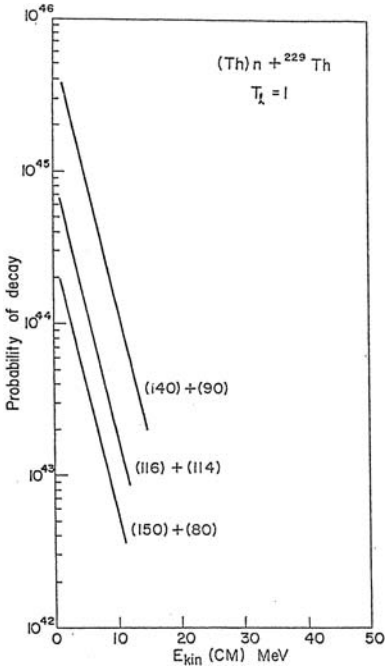

Fig. 7.10. The same as that of Fig. 7.9 except the transmission coefficient $T(\varepsilon)$ in (1) is set to one

to one and choosing the following simple but realistic level density function

$$\rho(U_1) = c_1 \exp \sqrt{a_1 U_1} \tag{7.3}$$

leads to the following expression for the probability of decay, in case the approximation (6.23), is used

$$P(\varepsilon, A_1 Z_1, A_2 Z_2) \sim 2\pi^{1/2} c_1 c_2 \frac{\sqrt{a_1 a_2}}{(a_1 + a_2)^{5/4}} (\xi - \varepsilon)^{3/4} \times \exp\left[2(a_1 + a_2)(\xi - \varepsilon)^{1/2}\right] . \tag{7.4}$$

In (7.4) A_1, A_2, c_1 and c_2 are appropriate parameters of level density functions of the daughter pair. Noting that ξ and ε in (7.4) are, respectively the Q-value and total kinetic energy, it is apparent that (a) there should be no yields when $\varepsilon = \xi$ i.e., cold fission is not allowed and (b) the maximum decay probabilities occur at $\varepsilon = 0$. Both of these conclusions contradict the observations. *It is, therefore, reasonable to infer that the observation of cold fission as well as a non-zero lower limit of the kinetic energy in the decay to all daughter pairs* is a direct manifestation of the occurrence of a barrier near the scission point.

This is further confirmed by the following model. Using a somewhat simplified version of the above theory, Florescu et al. [7.14] could parameterize the cold fission yields in terms of barrier-penetration probabilities. Noting, that in cold fission both fragments have no or little excitation, they assign both fragments a pre-determined configuration, taken to be vibration around a prolate deformation characterized by β. The decay probabilities are then, simply proportional to barrier penetration probabilities, P_s which, in the lowest JWKB approximation, is given by

$$P_s = \exp\left[-(2/\hbar) \int_{R_i}^{R_e} \sqrt{2\mu(V(r) - E)} dr \right] . \tag{7.5}$$

In (7.5) R_i and R_e, are, respectively, the internal and external turning points, μ is the reduced mass and $V(r)$ is the sum of an attractive potential and Coulomb potential given by the following expression

$$V(r) = 4\pi R b \gamma \Phi(r/b) + \frac{Z_1 Z_2 e^2}{r} F(r) . \tag{7.6}$$

In (7.6), R is the curvature of the top of the barrier, $b = 0.99\,\mathrm{fm}$, $\gamma = 0.9517\ \left(1 - 1.7826(N-Z)^2/A^2\right)\mathrm{MeV\ fm}^{-2}$, N, Z and A being the neutron, proton, and mass number of the parent, respectively. $\Phi(z)$ is the universal function of [7.15, 7.16]. $F(r)$ multiplying the Coulomb potential is a function of deformation parameters of daughter pairs which is, in this particular case, taken to be due to two coaxial ellipsoids [7.17]. Z_1 and Z_2 in (7.6) refer to the atomic number of a daughter pair. In Florescu et al.'s model [7.14], E, the asymptotic kinetic energy associated with a daughter pair is related to the observed kinetic energy, E_{cl} of cold fission by the following expression

$$E = (A/A_H) E_{cl} \tag{7.7}$$

where A and A_H are, respectively, the mass number of the parent and heavier member of a daughter pair.

The calculated yields, normalized to 100% of the experimental yields, are shown as a function of the mass number of the lighter fragment of a daughter pair in the thermal neutron induced fission of ^{235}U and ^{233}U in Figs. 7.11 and 7.12, respectively. The potential is set to be zero for $r < R_i$ and as such the barriers used in calculating half lives are located near the surface of two emerging fragments.

Unlike the theory of [7.1–7.3], this model does not predict the kinetic energy spectra and the occurrence of cold fission but assumes these to occur. In addition, (a) clearly the yields calculated using (7.5) for energies greater than E, are higher than those calculated with E and there is no apriori justification for choosing a particular energy to calculate the yields and (b) the derivation of (7.5) noted in Appendix A, requires E to be the asymptotic

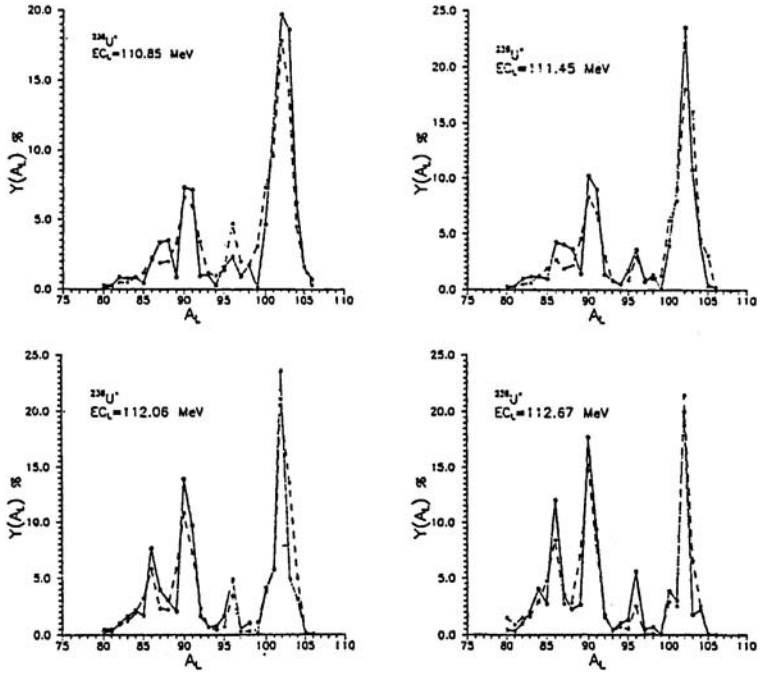

Fig. 7.11. The calculated mass yields of light fragments $Y(A_L)$ using (7.5) and (7.6) [7.14] of cold fission fragments in the thermal neutron induced fission of ^{235}U, are plotted as *open* circles connected by a *solid* line using kinetic energies of fission fragments of 110.85, 111.45, 112.06 and 112.67 MeV. These are compared to the data shown as *solid* dots and connected by a *broken* line [7.22]. The calculated yields are normalized to 100%

kinetic energy associated with the decay. E_{cl}, being different from E, cannot be identified as observed kinetic energy of a cold fission daughter pair.

Nevertheless, the basic premises of the theory, particularly, the fact that the cold fission points to an external barrier, are borne out. In studies using a semi-classical approach Stefanescu, Sandulescu and Greiner [7.18] and their collaborators [7.19, 7.20] arrived at the same conclusion. Attempts have been made to simulate the external barrier by its classical analogue of using a dissipative force [7.21].

7.4 Odd-Even Effect

The decay probabilities through the thin barrier of Chap. 5 or that given by (6.10) is sensitive to the asymptotic kinetic energy associated with a daughter pair. A one MeV change in kinetic energy affects the yields noticeably. Thus, the pairing energy of about an MeV increases ξ in (7.1) by an MeV

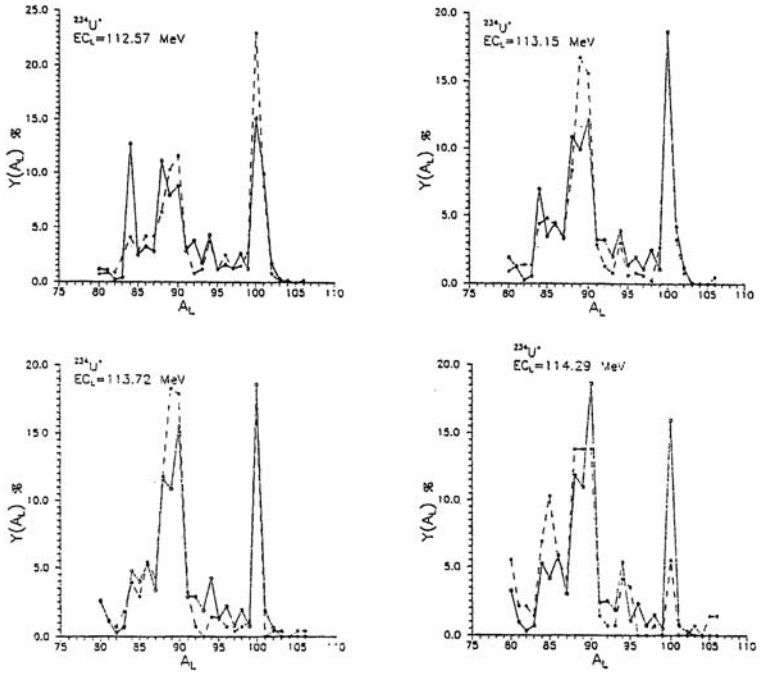

Fig. 7.12. The same as that of Fig. 7.11 except for thermal neutron induced fission of ^{233}U and kinetic energies of fission fragments of 112.57, 113.15, 113.72 and 114.29 MeV. Calculations and data are reproduced from [7.14] and [7.22], respectively

and hence, the allowed kinetic energy ε and the phase space of integration in (7.1) by an MeV or so. For a barrier like the one (6.10) this enhances the yields measurably. In general, therefore, the yield to an even-even daughter pair is preferred over the neighboring odd-even or even-odd ones *in the theory of [7.1–7.3].* For a thin barrier involved here, the effects are more pronounced for cold fission, because the asymptotic kinetic energy is larger than the one associated with the most probable decay mode and hence, the penetration occurs near the top of the barrier which is thin. Thus, the percent change in the area bounded by the potential surface and kinetic energy is larger, and the difference between the emission of an even-even isotope and its neighboring odd-even or even-odd isotopes is more pronounced. This seems to be the case in Figs. 7.5 and 7.6. The increase in the odd-even effect with the increasing kinetic energy of the light fragment is particularly evident, if one plots $\delta_p = (Y_e - Y_0)/(Y_e + Y_0)$ where Y refers to yields and the subscripts '0' and 'e' to odd and even-even isotopes, as a function of kinetic energy. This is plotted in Fig. 7.13 for the thermal neutron induced fission of ^{239}Pu.

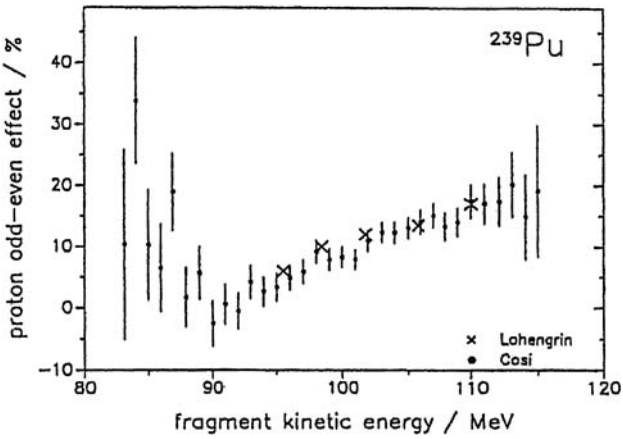

Fig. 7.13. The difference between yields of even-even pairs over odd-even or even-odd pairs, δ_ρ in percentage as a function of fragment kinetic energy in MeV in the thermal neutron induced fission of ^{239}Pu, Lohengrin and Cosi refer, respectively to the data taken at the Laue-Langevin institute using the Lohengrin [7.23] and Cosi [7.24] spectrometer (Reproduced from [7.24])

7.5 Conclusion

The theory exposed in this and Chap. 6, can account for cold fission. In addition, a salient feature of the theory is that there is a minimum kinetic energy below which no fission to a daughter pair could occur. This minimum depends on the details of the barrier and the density of states of a particular daughter. *In other words, no hot fission, where the entire available Q-value is converted to the excitation of a daughter pair, could occur.* Experimental data, so far, support this. A particular daughter pair having excitation energy between this allowed maximum and zero could be emitted in fission.

References

1. B. Compani-Tabrizi, Dissertation (Indiana University at Bloomington, 1976) Unpublished.
2. B. Compani-Tanbrizi, M.A. Hooshyar and F.B. Malik, *Proc. International Conf. on Interactions of Neutrons with Nuclei*, ed. E. Sheldon (ERDA Conf. 7607115-P1, 1976) p. 725.
3. B. Compani-Tanbrizi, M.A. Hooshyar and F.B Malik, *Proc. International conf. on Nuclear Reaction* ed. E. Gadioli (The University of Milano Press, 1988), p. 310.
4. C. Signarbieux, M. Montoya, M. Ribrag, C. Mazur, C. Guet, P. Perrin, and M. Maurel, J. de Phys. Lett. **42**, L-437 (1981).
5. M. Montoya, Zeit. Physik A., **319**, 219 (1984).

6. H.W. Schmitt, J.H. Neiler and F.J. Walter, Phys. Rev. **141**, 1146 (1966).
7. U. Facchini and E. Saetta-Menichela, Acta Phys. Polonica **A 38**, 537 (1970).
8. M. High, B. Block, J.W. Clark and F.B. Malik, Bull. Am Phys. Soc. **15**, 466 (1970).
9. F. Pleasonton, Phys. Rev. **174**, 1500 (1968).
10. F. Gönnenwein, *Frontier Topics in Nuclear Physics*, eds. W. Scheid and A. Sandulescu (Plenum Press, 1994) p. 113.
11. F. Gönnenwein (Private Communication).
12. W. Mollenkopf, J. Kaufman, F. Gőnnenwein, A. Geltenbort and P. Oed, J. Phys. G: Nucl. Part. Phys. **18**, L203 (1992).
13. W.N. Residorf, J.P. Unik and L.E. Glendenin, Nucl. Phys. **A205**, 348 (1973).
14. A. Florescu, A Sandulescu, C. Cioaca, and W. Greiner, J. Phys. G **19**, 669 (1993).
15. J. Blocki, J. Randrup, W.J. Swiatecki and C.F Tsang, Ann. Phys. (N.Y.) **105**, 427 (1977).
16. J. Blocki, and W.J. Swiatecki, Ann. Phys. (N.Y.) **132**, 53 (1981).
17. S. Cohen and W.J. Swiatecki, Ann. Phys. (N.Y.) **19**, 67 (1962).
18. E. Stefanescu, A. Sandulescu and W. Greiner, J. Phys. G **20**, 811 (1994).
19. A. Sandulescu and H. Scutaru, Ann. Phys. (N.Y.) **173**, 277 (1987).
20. E. Stefanescu, A. Sandulescu and W. Greiner, Int'l. J. Mod. Phys. E **2**, 233 (1993).
21. E. Stefanescu, W. Scheid, A. Sandulescu and W. Greiner, Phys. Rev. C **53**, 1 (1996).
22. G. Simon, These pour le grade de Docteur d' Etate, Universite' de Paris-Sud, Orsay, 1990.
23. C. Schmitt, A. Guessous, J.P. Bocquet, H.G. Clerc, R. Brissot, D. Engelhardt, H. R. Faust, F. Gőnnenwein, M. Mutterer, H. Nifenecker, J. Pannicke, Ch. Ristori, and J.P. Theobald, Nucl. Phys. A **430**, 21 (1984).
24. J. Kaufmann, W. Mollenkopf, F. Gönnenwein, P. Geltenbort and A. Oed, Zeit. Physik A **341**, 319 (1992).

8 Isomer Fission

8.1 Introduction

In the early nineteen sixties a number of Russian scientists reported finding nuclei having very short fission half-lives [8.1, 8.2] in the mass region of about 240. These nuclei with short fission half-lives were observed in nuclear reactions with light projectiles such as deuterons incident on certain actinide targets and were usually accompanied by induced fission products from the ground states of the target. Since then many other isotopes exhibiting short fission half-lives have been discovered following bombardment of actinide targets by light projectiles. They are listed in Table 1.2. The energy of these states is quite often a few MeV higher than the ground state of the corresponding compound nucleus and so far, there is no evidence of the decay of these states to the corresponding ground states of the compound nucleus; the only decay mode seems to be fission. Thus, they are a kind of isomers of the corresponding nuclei in the ground state and the fission phenomenon related to their decay is generally termed as isomer or isomeric fission. A typical ratio of mass yields in the fission of the isomeric state to that of the ground state is about 10^{-4}. For example, the isomeric state of ^{240}Am is formed at an excitation of about 3.0 MeV [8.3, 8.4] and the ratio of the yields from the fission of the isomer to that of the ground state is 5×10^{-4} [8.5]. Similarly, the isomer state of ^{240}Pu has an excitation energy of about 2.6 MeV [8.4] and the ratio of the yields is $(8.6 \pm 2.4)10^{-4}$ [8.6]. A complete list of the excitation energies of these isomer states and the ratio of the mass yields up to 1973 are noted in [8.7]. The actual determination of excitation energies of these isomeric states depends on the theoretical model used. This is usually done within the context of an evaporation model and hence, neglects the final state interaction between the members of a particular daughter pair. Thus, the determination of the excitation energies of isomeric states is, somewhat, model dependent.

Considerable insight on the probable cause leading to the formation of these states is obtained within the context of Strutinsky's idea of shape isomer [8.8–8.11]. According to this idea, there may be the formation of local minima in the potential energy surface of two members of a daughter pair between the ground state configuration of the parent and the saddle point associated with its decay, due to the change in shell structure and deformation

energy. Isomer states are states in these local minima and hence, have deformations larger than the one in ground states. Being deformed, these states are capable of exhibiting rotational spectra. Specht et al. [8.12] and Heffner et al. [8.13] have claimed to have established the occurrence of these rotational states. Although, Strutinsky's theory has been done within the framework of a liquid drop model, its basic concept may be carried over to the barrier obtained within the context of the energy-density functional method discussed in Chap. 3. In Sect. 8.2 of this chapter, we present the essential concepts of Strutinsky's model and indicate the way it could be incorporated into the barrier calculated using energy-density functional theory. A key piece of information about the dynamic associated with the fission of these states is obtained from the measurement of the average kinetic energy of the fission products from these isomer states. The investigation of Ferguson, Plasil, Alam and Schmitt [8.14] indicates that the average kinetic energy associated with the decay of the isomer state is about the same as that in the fission of the ground state. Based on this important experimental data and the fact that induced fission as well as isomer fission occurs in the same reaction, Hooshyar and Malik [8.15–8.17] have argued that the same reaction mechanism must underlie the fission of both isomeric and the corresponding ground states. They have analyzed the problem within the framework of a coupled channel decay theory and predicted the percentage mass yields and charge distribution spectra for the fission of isomer states of ^{234}U, ^{236}U and ^{240}Pu. In 1980 Fontenla and Fontenla [8.18] measured the percentage mass yields and the average kinetic energy spectra associated with the fission of the isomer state of ^{236}U and found them to be very close to the ones predicted by Hooshyar and Malik [8.16]. The theory and the comparison between the calculation and the data are discussed in Sect. 8.3.

8.2 The Shell Correction and Shape Isomers

The density distribution functions used in Chap. 3 to calculate nuclear masses are usually determined from the analyses of electron scattering data or the μ-mesic atomic level scheme. These observed data are usually not sensitive to slight fluctuations in the density distribution function and hence, the determined density distribution functions usually represent a smooth average of the actual density contour. On the other hand, one expects slight fluctuations originating from the shell structure in nuclei which usually contributes a few MeV to the total energy. Strutinsky, in a series of papers [8.8–8.11], has pointed out that the inclusion of this correction may lead to one or more local minima in the potential energy surface of a parent nucleus decaying to a given daughter pair at a deformation larger than the one associated with the ground state of the parent nucleus within the context of the liquid drop model, noted henceforth as LDM. These local minima occur before the saddle

point. The states formed in these local minima are isomeric states since they cannot readily decay to the ground state by radiative process.

Lombard [8.19] has added a term

$$-c\sum_i g_i\langle \mathbf{l}_i\cdot\mathbf{s}_i\rangle \tag{8.1}$$

to the energy-density functional of Chap. 3 to account for the shell correction to the density. c, g_i, $\mathbf{l}_i$ and $\mathbf{s}_i$ in (8.1) are, respectively, the strength of the spin-orbit interaction, the weight function of the occupation of the i-th shell, and the orbital and spin vectors of the i-th particle. His treatment is, however, restricted to spherical shapes. Strutinsky's approach, on the other hand, is based on an attempt to incorporate the shell correction to the potential energy surface calculated using the liquid drop mass formula as the reference point and to investigate the change in this energy as a function of deformation. His approach does not attempt to calculate the total energy but only the change in potential energy surface due to the shell and pairing effects. His model is summarized in the following:

The change in total energy of a nucleus as it deforms enroute to fission, ΔW, in Strutinsky's model, is given by the summation of three terms:

$$\Delta W = \Delta W(LDM) + \Delta W(shell) + \Delta W(pair) \tag{8.2}$$

where $\Delta W(LDM)$ is the change in potential energy calculated using an appropriate version of Bohr-Wheeler's theory [8.42], $\Delta W(shell)$ is the energy difference between nucleons moving in Nilsson's potential [8.21] consisting of a cylindrical symmetric anisotropic harmonic potential, a spin-orbit term and a well flattening term, $U(shell)$ and nucleons described by an appropriate function for uniform distribution, $U(unif)$ and $\Delta W(pair)$ is the difference in pairing energy for nucleonic dynamics governed by Nilsson's Hamiltonian, $P(shell)$ and nucleons described by uniform distribution, $P(unif)$. Thus,

$$\Delta W(shell) = U(shell) - U(unif) \tag{8.3a}$$

$$\Delta W(pair) = P(shell) - P(unif)\ . \tag{8.3b}$$

In [8.9], $\Delta W(LDM)$ is taken to be

$$\Delta W(LDM) = \tau A^{2/3}[0.4(1-x)\alpha^2 - 0.0381(1+2x)\alpha^3] \tag{8.4}$$

with $\tau = 16.0\,\mathrm{MeV}$, x, the fissibility parameter $= (Z^2/A)/(Z^2/A)_{\mathrm{crit}}$ where $(Z^2/A)_{\mathrm{crit}} = 45$, where A and Z refer, respectively, to the mass and atomic number of the parent nucleus. The radii of cylindrical symmetric spheroid, R_x, R_y, and R_z is related to deformation parameter α as follows:

$$R_x = R_y = R_0(1-\alpha/2), R_z = R_0(1+\alpha)\ . \tag{8.5}$$

R_0 in (8.5) is average radius of the sphere in the absence of any deformation. The expression (8.4) represents basically the change in surface and Coulomb

energy in LDM in the lowest order in α. The deformation parameter, α, is related to Bohr-Mottelson's deformation parameter β [8.42] as follows:

$$\beta = (3/2)\alpha \ . \tag{8.6}$$

$U(shell)$ in (8.3b) is given by

$$U(shell) = \sum_{\nu} 2\varepsilon_{\nu} n_{\nu}$$

where ε_{ν} are single particle energies of a nucleon described by Nilsson Hamiltonian [8.21] and n_{ν} is the occupation number of a given shell. The summation index ν is over occupied shells.

The energy for a uniform distribution of nucleons, $U(unif)$ is given by

$$U(unif) = 2 \int_{-\infty}^{\lambda} \varepsilon g(\varepsilon) d\varepsilon \tag{8.7}$$

where $g(\varepsilon)$ is the function for uniform distribution and λ is the chemical potential determined from the number of nucleon N and is given by

$$N = 2 \int_{-\infty}^{\lambda} g(\varepsilon) d\varepsilon \ . \tag{8.8}$$

The distribution function for the uniform case is taken to be

$$g(\varepsilon) = (\pi\gamma)^{-1/2} \sum_{\nu} \exp\left[\gamma^{-2}(\varepsilon - \varepsilon_{\nu})^2\right] \ . \tag{8.9}$$

The summation in (8.9) is over the number of levels in the energy interval $(\pi\gamma)^{1/2}$ which is centered around ε. The purpose is to choose γ in such a way as to smooth out the shell effect. Thus, γ is taken to be of the order of the inter-shell energy. In calculations reported here, $\gamma = 0.7\hbar\mathrm{w}_0$ where $\hbar\mathrm{w}_0$ is the oscillator quantum taken to be 7 MeV. A correction term is added to (8.9) in order to avoid the error introduced in taking a finite energy interval.

The pairing energy due to Nilsson's orbitals, $P(shell)$ is calculated using the BCS theory [8.20] and is given by

$$P = \sum_{\nu} \left[|E_{\nu}| - \frac{E_{\nu}}{E(E_{\nu}, \Delta)} - \frac{\Delta^2}{2E(E_{\nu}, \Delta)} \right] \tag{8.10}$$

where E_{ν} is related to Nilsson's energy ε_{ν} and λ, the chemical potential, both being dependent on deformation β and given by

$$E_{\nu} = \varepsilon_{\nu} - \lambda \tag{8.11}$$

and $E(E_\nu, \Delta)$ is given by

$$E(E_\nu, \Delta) = [E_\nu^2 + \Delta^2]^{1/2} \tag{8.12}$$

Δ in (8.12) is the gap parameter. It is related to G, the strength of the pairing interaction by

$$2/G = \sum_\nu{}' 1/E(E_\nu, \Delta) \; . \tag{8.13}$$

The prime over the summation in (8.10) and (8.13) indicates that the summation extends over n states equally above and below the Fermi level and n is taken to be 24.

The pairing energy for a uniform distribution is given by

$$P(unif) = n\Delta(unif) \left(t - \sqrt{1 + t^2}\right) \tag{8.14}$$

where $\Delta(unif)$ is related to G, the strength of pairing potential, by

$$(2/G) = 2g(\lambda) \ln \left(t + \sqrt{1 - t^2}\right) \; . \tag{8.15}$$

In (8.15) $g(\lambda)$ is the distribution function around Fermi energy level λ and the summation in (8.13) includes n states equally above and below λ. In most calculations of Strutinsky, $n = 24$, although in some cases n is set to be 10. The results obtained using different n were nearly the same. t in (8.15) is given by

$$t = n/2g(\lambda)\Delta(unif) \; . \tag{8.16}$$

In calculations presented in [8.9], the gap parameters are not determined by solving (8.13) and (8.15), but $\Delta(unif)$ is taken to be a parameter set equal to 0.6 MeV. Δ for $P(shell)$ is determined by equating the right hand sides of (8.13) and (8.15). ΔW and $\Delta W(LDM)$ calculated as a function of β by Strutinsky [8.9] for ^{230}Th, ^{238}U, ^{240}Pu, and ^{250}Cf are shown in Fig. 8.1 by solid and broken lines, respectively. The first minimum in these figures corresponds to the ground states of these nuclei which are known to be deformed. However, the inclusion of shell effects leads to a second (and sometime a third) minimum in the liquid drop potential surface. These minima occur at a deformation before the two members of a daughter pairs establish their identity i.e., at a separation distance of considerably less than about 8 fm. This is considerably less than the distance between the centers of mass of an emerging daughter pair where a neck of low-density nuclear matter starts to form. The actual value of ΔW is sensitive to the details of single particle states, the strength of pairing energy and the calculation of the change in Coulomb and surface energy with deformation. This can be seen by comparing Strutinsky's calculation with those done by others with somewhat different approaches e.g., with those of Tsang and Nilsson [8.22].

The magnitude and the location of these minima depend critically on the choice of parameters such as the strength of spin-orbit interaction, oscillator

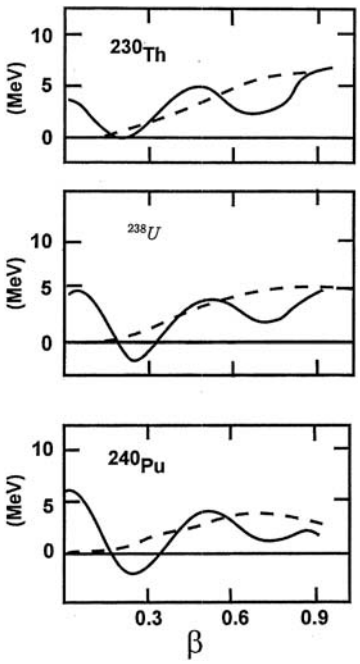

Fig. 8.1. The calculated shell corrected barrier, ΔW given by (8.2) and the standard liquid drop barrier $\Delta W(LDM)$ given by (8.4) are shown as *solid* and *broken* lines respectively, as a function of deformation β. This is taken from [8.9]

quantum etc., of Nilsson states and the pairing interaction. Depending on the choice of these parameters there may be multiple local minima. For example, a third one is also possible, as noted by Scholz and Malik [8.23] in studying the deformation dependence of potential energy surfaces of nuclei in mass region 40 to 70. There are also some uncertainties about determining $g(\varepsilon)$ for a uniform distribution of energy states for the Wood-Saxon potential [8.43].

However, Strutinsky's investigation opens up the possibility that (a) the consideration of shell structure may lead to a second local minimum or even multiple local minima in the potential energy surface at a deformation different from that of the ground state, (b) Such minima, if present, occur at a separation distance less than 8 fm and hence, do not influence the contribution to the potential energy surface from the density in the neck region, formed prior to scission and (c) the net contribution of shell effects to the potential energy surface is a few MeV compared to the effect of a few tens of MeV discussed in Chap. 3, *which is due to the formation of a neck of low-density nuclear matter prior to scission.*

The existence of multiple local minima leads to the possibility that they may be populated in a nuclear reaction. Since they occur at a larger deformation, rotational states based on this configuration should be more compressed

compared to those based on the ground state, because they would have a larger moment of inertia due to larger deformation.

The energy of a rotational band, $E(J)$, of angular momentum J, is given by

$$E_J = AJ(J+1) + BJ^2(J+1)^2 \tag{8.17}$$

where A and B are constants determined from the energy spacing. The first and second term in (8.17) represent energies due to pure rotation and its coupling to vibrational states, respectively. From the study of internal conversion electron spectroscopy, Specht et al. [8.12] have identified the rotational states based on a minimum of ^{240}Pu. This band along with the one based on the ground state of ^{240}Pu is shown in Fig. 8.2. The transition energy between two successive states of a band divided by $2(2J+1)$ is simply given by

$$(E_J - E_{J-2})/2(2J+1) = A + 2B(J^2 - J + 1) \tag{8.18}$$

The parameter A and B, then, can be determined from the data by plotting the right hand side of (8.18) as a function of $2(J^2 - J + 1)$. This is done in Fig. 8.2. The intercept and the slope of the data in that figure determine A

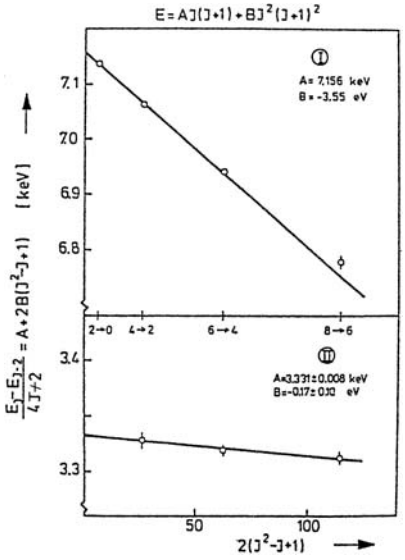

Fig. 8.2. The known rotational states of ^{240}Pu and the rotational band deduced from the measurements of the internal conversion experiment in the supposed second well by Specht et al. [8.12] are shown, respectively, in insert (**a**) and (**b**). The transition energies between adjacent states divided by $2(2J+1)$ are plotted as a function of $2(J^2 - J + 1)$, J being the spin of the state, in both cases. The intercept and the slope of the data determine parameters A and B of (8.18) which are found to be 7.156 keV and (-3.55) eV for the ground state band and (3.331 ± 0.008) keV and (0.17 ± 0.10) eV for the band based on the configuration at the second minimum

and B, respectively. The moment of inertia parameters for A, deduced from the analysis of the rotational states based on the ground states and at the excited state in the local minimum are 7.156 and 3.331 ± 0.008 keV, respectively. Since the moment of inertia parameter A in the collective model is inversely proportional to deformation, the location of this minimum in ^{240}Pu occurs at about twice the ground state deformation. The *rotational-vibrational coupling strength* parameter B for bands based on the ground and isomer state are (-3.55) and (-0.17 ± 0.1) eV, respectively.

These states in the experiments occur at a few MeV excitation energy above the corresponding ground state which is consistent with the location of isomeric states observed in [8.1–8.6]. The experiment using light projectiles populates both ground and isomeric states and fission fragments from both of these states are observed. In the next section we discuss the dynamic that couples the decay probabilities from these two states, henceforth, noted as IFS standing for isomer fissioning states and SFS, spontaneous fissioning states. This influences the mass yields and kinetic energy spectra in the emission of fission products from both of these states.

8.3 Half-Lives, Mass Yields and Kinetic Energy Spectra

As noted before, the experimental studies related to spectroscopy of isomer states associate these states with large deformations. They are formed at energies which are a few MeV higher than the energies of the ground state of the corresponding parent nuclei. They primarily decay by fission. So far, the decay probabilities of these states by emission of electro-magnetic radiation to ground or other states has not been clearly established.

The deformation parameter extracted from the observed rotational states associated with the location of IFS in a nucleus as well as Strutinsky's investigation indicates these states to be situated between the ground state and saddle point in the potential energy surface. While Strutinsky used the ground state energy determined from LDM as a reference point and calculated the variation around that value, it is perfectly reasonable to use the ground state energy calculated using the energy-density functional theory, as a reference point and calculate its change with deformation, $\Delta W(EDF)$, and add to it Strutinsky's approximate determination of $\Delta W(shell)$ and $\Delta W(pair)$. Thus, the change of potential energy in this case, $\Delta E(EDF)$, is given by

$$\Delta E(EDF) = \Delta W(EDF) + \Delta W(shell) + \Delta W(pair) \tag{8.19}$$

$\Delta W(EDF)$ in (8.19) is the change in potential energy in the energy-density functional approach as the system starts deforming as depicted in the interior region of Fig. 3.5, i.e., before the saddle point configuration is reached. Since $\Delta W(EDF)$ is a smooth function of R but $\Delta W(shell)$ *and* $\Delta W(pair)$ are not, the potential energy surface is likely to have local minima before the saddle point as indicated schematically in Fig. 8.3 in the interior part.

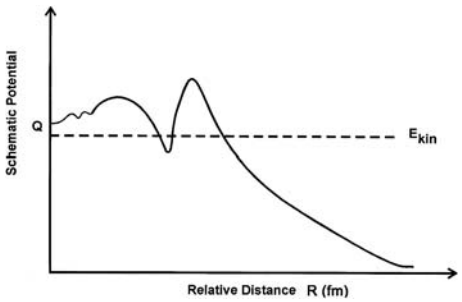

Fig. 8.3. Schematic potential energy surface in an arbitrary unit that combines the energy–density functional calculated for $n = 2$ in Chap. 3 with the shell and pairing correction of Strutinsky [8.9] between two members of an arbitrary daughter pair as a function of separation in an arbitrary unit. The dashed line represents a typical value of asymptotic kinetic energy of that daughter pair. It is typically 20–30 MeV lower than the Q-value which is the value of the potential at $R = 0$

The few MeV excitation associated to IFS, when translated into energy per nucleon, is small, being about 0.012 MeV per nucleon. This implies that there is no significant change in the density distribution function between IFS and SFS. Hence, the potential energy surface relevant to IFS is essentially the same as the one associated with the fission of the ground state except in the interior part, where it may exhibit local minima, as shown schematically in Fig. 8.3. It is expected to exhibit the thin external barrier between the saddle and scission points, as is the case for the decay of SFS. In the same figure, the location of the average kinetic energy which is about 20 MeV lower than the energy of IFS, is also shown. The situation is similar to the one associated with the decay of SFS.

The presence of this external barrier poses a serious dilemma in accounting for the short half-lives of these isomers in view of the observed fact that the average kinetic energies associated with the decay of IFS and SFS are about the same. For example, if one uses the empirical barrier of Chap. 5 in conjunction with Strutinsky's barrier, the observed half-live of about 3×10^{-9} sec of the isomer state of ^{240}Pu would require an average kinetic energy of about 205 MeV. The early experimental evidence, on the other hand, indicates that the average kinetic energy associated with the fission of the isomer state is about the same as the one associated with the fission of the ground state [8.1, 8.14] i.e., about 25 MeV less than the Q-value. Later measurements of the kinetic energy spectrum associated with the decay of the isomer state of ^{236}U by Fontenla and Fontenla [8.18] has not only confirmed the measurement of average kinetic energy of Ferguson, Plasil, Alam and Schmitt [8.14] in *the fission of the isomer state of* ^{236}U, but indicates that the kinetic energy spectrum of the fission fragments from both the IFS and the SFS of ^{236}U to be very similar, a fact that was predicted by Hooshyar and Malik [8.16] eight years earlier.

The experimental information on the kinetic energy spectrum in the decay of IFS and SFS points to the fact that the reaction mechanism underlying the fission dynamics of the two decay processes are related. This may be examined by noting that the fission process is governed by the following set of coupled equation as noted in Chap. 3:

$$\left[-\frac{\hbar^2}{2\mu}\nabla_R^2 - E_{n\alpha} + V_{n\alpha\alpha}(R)\right] f_{n\alpha}(R) = \sum_{\beta\neq\alpha} V_{n\alpha\beta}(R) f_{n\beta}(R)\ . \tag{8.20}$$

Where R is the relative location of the centers of mass of the two daughter nuclei, μ is their reduced mass, $E_{n\alpha}$ is the channel energy associated with the decay channel (n_α) and $V_{n\alpha\alpha}(R)$ and $V_{n\alpha\beta}(R)$ are diagonal and off-diagonal matrix elements of the interaction potential between two daughter nuclei. Asymptotically, $V_{n\alpha\beta}(R)$ is zero and $V_{n\alpha\alpha}(R)$ is the Coulomb potential between two nuclei and $E_{n\alpha}$ is related to the kinetic energy of the daughter pair. The off-diagonal coupling terms between infinite number of channels must have some influence on the fission process. The set of coupled equations may, however, be simplified for the physical situation pertinent to fission [8.15]. One may note that (i) the energy difference between IFS and SFS is negligible compared to the Q-value and average kinetic energies, (ii) the excitation energy of each member of a daughter pair is only about 8 to 15 MeV which is small compared to the channel kinetic energy of 150 to 180 MeV, (iii) from the analysis done in [8.15], it is evident that the diagonal part of the interaction, $V_{n\alpha\alpha}(R)$ is about the same between different excited states of a daughter pair since about 8 to 15 MeV excitation energy contributes very little to the energy per nucleon, (iv) channels which are directly coupled to the channel under consideration are important, since indirect couplings represents second or higher order processes, and (v) the level density of each member of a daughter pair, which is emitted with 8 to 15 MeV excitation energy, is very high. It is, therefore, reasonable to assume that the functional form of the coupling terms is the same for all channels coupled to the decay channel but the strength of the coupling is different. These assumptions may be summarized as follows:

$$E_n \equiv E_{nl} \approx E_{n\alpha}, \quad \alpha = 2, 3, \ldots\ldots, N \tag{8.21a}$$

$$V_{nD}(R) \equiv V_{nll}(R) \approx V_{n\alpha\alpha}(R), \quad \alpha = 2, 3 \ldots\ldots, N \tag{8.21b}$$

$$V_{n\beta 1}(R) \equiv V_{n1\beta}(R) \approx \gamma_{n\beta} V_{nc}(r) \text{ with } \beta \neq \alpha \text{ and } \beta = 2, 3, \ldots\ldots, N \tag{8.21c}$$

$$V_{n\alpha\beta}(R) = 0 \quad \text{for} \quad \alpha \neq 1 \text{ and } \beta \neq \alpha \tag{8.21d}$$

As shown in Appendix C, under these conditions, the N-coupled equation can be diagonalized exactly [8.15] which leads to the following three uncoupled equations for zero angular momentum in decay channel:

$$\left[-\frac{\hbar^2}{2\mu}\frac{d^2}{dR^2} - E_n + V_{nD}(R) + \lambda V_{nc}(R)\right] f_n(R) = 0 \tag{8.22a}$$

$$\left[-\frac{\hbar^2}{2\mu}\frac{d^2}{dR^2} - E_n + V_{nD}\right] f_n(R) = 0 \tag{8.22b}$$

$$\left[-\frac{\hbar^2}{2\mu}\frac{d^2}{dR^2} - E_n + V_{nD}(R) - \lambda V_{nc}(R)\right] f_n(R) = 0 \tag{8.22c}$$

where λ, the effective coupling strength is given by

$$\lambda = \left[\sum_{\beta=2}^{N} \gamma^2 n\beta\right]^{1/2} . \tag{8.23}$$

Some remarkable things about the set of three equations (8.22a), (8.22b), and (8.22c) are that (i) the asymptotic kinetic energy in all three cases is the same and (ii) the difference in potential in the three cases manifests itself only though the contribution of the coupling term $\lambda V_{nc}(R)$. Thus, the effective barriers in the three cases are different, but the asymptotic kinetic energy associated with the decay is the same. For positive λ, the barrier associated with (8.22a) is the highest, which is, therefore, identified as the effective barrier associated with the decay of SFS. For the coupling potential determined in Chap. 5, the effective barrier in (8.22c) lies below the asymptotic kinetic energy and hence, (8.22c) represents purely scattering phenomena by a repulsive potential, since meta-stable states cannot be formed in this potential. The barrier associated with (8.22b) is the determining factor in governing the half-lives in the decay of IFS. In Fig. 8.4, the effective potentials in (8.22a), (8.22b), and (8.22c) are plotted along with a typical kinetic energy for the parameters noted in Chap. 5. The actual potential in the interior region i.e., for $r < R_c$ should have a Strutinsky type of structure as schematically shown in Fig. 8.3, but such structure in the interior region has very little influence in determining the half-lives, as noted in Chap. 5 and Appendix A and confirmed by actual computer calculations.

IFS formed in a nuclear reaction as well as induced fission probabilities of the corresponding SFS, while attempting to decay to various excited states of a particular daughter pair results necessarily in a strong coupling among various decay channels. *The consequence of this coupling is an effective reduction and increase of the potential in the decay channel of IFS and SFS, respectively. This decrease and increase of the potential energy surface in the decay of IFS and SFS, occur between the saddle and scission points.*

The calculations of half-lives of IFS as well as SFS involves a preformation probability which is calculated to be 10^{-5} in Chap. 3 and used here. In Table 8.1, the calculated half-lives and average kinetic energies for the fission from both the SFS and the IFS of a number of even-even nuclei are presented and the overall agreement is quite reasonable. The calculations of half-lives for the SFS and the IFS are done using the same average kinetic energy for both

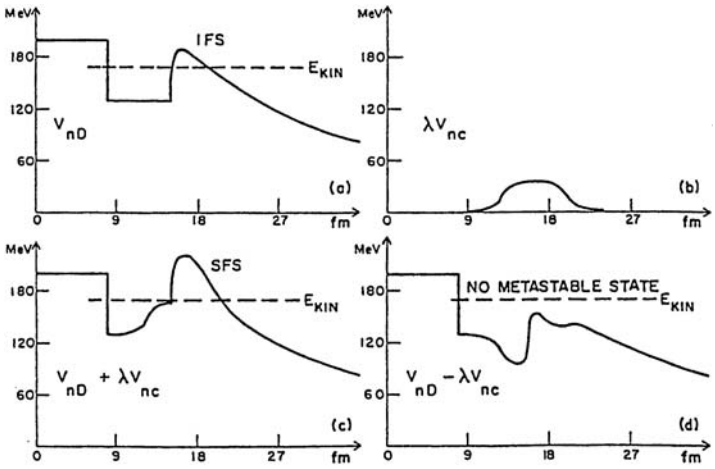

Fig. 8.4. The effective potentials for the decay of ^{240}Pu to ^{142}Ba + ^{98}Sr from the IFS and SFS are shown in inserts (**a**) and (**c**), respectively. The effective potential due to the channel coupling is shown in the insert (**b**). (**d**) is the effective potential contributing to scattering only. This is taken from [8.15]

cases, which is the case experimentally. The theoretical calculations presented in Table 8.1 are done for one of the fastest fission decay modes. The inclusion of all such decay modes does not significantly change the results as verified by actual calculations.

A more stringent test of the theory is to obtain the observed mass yields spectra along with the appropriate kinetic energy spectra. In Figs. 8.5, 8.6 and 8.7 theoretical percentage mass yields spectra for the fission of the SFS and the IFS of ^{234}U, ^{236}U, and ^{240}Pu are presented and compared to the data for the SFS decay. The average kinetic energy used for each decay mode is the same for the fission of both types of states and is shown in the upper insert in each case and is compared with the data for the fission of the SFS. The percentage mass yields spectra for the IFS in each of the three cases are predictions. In Fig. 8.8, the predicted percentage mass yields and average kinetic energy spectra in the fission of IFS of ^{236}U are compared to the data taken eight years after the predictions and the agreement is, indeed, very good.

An important consequence of the theory is that the charge distribution spectra from the fission of the SFS and the IFS of the same nucleus should be similar. So far, there has been no data available for the IFS case, but the predicted values are noted in Tables [5.2, 5.3, 5.4 and 5.5] of Chap. 5.

The calculations presented here consider the decay to one particular daughter pair. Theoretically and experimentally, there are a number of decay modes which are possible having about the same kinetic energy. Spontaneous half-lives associated with some of these decay modes are close to one another.

Table 8.1. Comparison of the computed half-lives with the observed ones for spontaneous fission and fission from the IFS. Columns three to eight are, respectively, the observed kinetic energies K.E. (exp), kinetic energy used in the calculation $E_{\rm kin}$, observed half-lives of the isomer state, calculated half-lives of the isomer state, observed spontaneous fission half-lives and calculated spontaneous fission half-lives. (a) to (k) are from [8.24] to [8.35], respectively

Parent	Daughters	K.E. (Exp)	$E_{\rm kin}$	IFS (exp) sec	IFS (th) sec	SFS (exp) y	SFS (th) y
			161		4×10^{-5}		2×10^{17}
^{234}U	^{142}Xe + ^{92}Sr	163 ± 2 (a)	163	$< 2{\times}10^{-9}$ (b)	9×10^{-7}	1.60×10^{16} (c)	2×10^{15}
			165		3×10^{-8}		2×10^{13}
			163		5×10^{-7}		2×10^{15}
^{236}U	^{142}Xe + ^{94}Sr	165 ± 2 (a)	165	1.1×10^{-7} (d)	2×10^{-8}	2×10^{16} (e)	2×10^{13}
			167		6×10^{-10}		2×10^{11}
			170		4×10^{-8}		5×10^{13}
^{240}Pu	^{142}Ba + 98$^{\rm Sr}$	172 ± 2 (a)	172	4×10^{-9} (g)	2×10^{-9}	1.34×10^{11} (f)	6×10^{11}
			174		8×10^{-11}		7×10^{9}
			183		5×10^{-11}		1×10^{9}
^{244}Cm	^{144}Ba + ^{100}Zr	185.5 ± 5 (g)	185	5×10^{-7} (h)	4×10^{-12}	1.34×10^{7} (i)	2×10^{7}
			187		3×10^{-13}		3×10^{5}
			193.6		2×10^{-13}		7×10^{4}
^{246}Cf	^{144}Ce + ^{102}Zr	195.6 ± 2 (j)	195.6	–	3×10^{-14}	2×10^{3} (k)	1×10^{3}
			197.6		5×10^{-15}		2×10^{1}

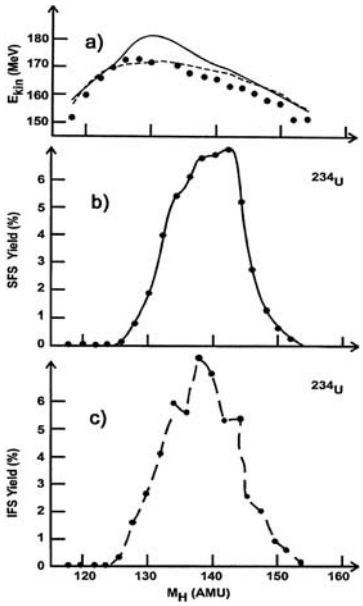

Fig. 8.5. The kinetic energy $E_{\rm kin}$, and the percentage mass yields spectra for spontaneous fission, SFS yields (%), and isomer fission states, IFS yield (%), of ^{234}U are shown at the upper, middle and lower inserts, respectively. M_H is atomic mass of the heavy fragments. *Solid* lines are experimental data of [8.36]. *Solid* dots in (**b**) and (**c**) are calculated percentage mass yields using the kinetic energy spectra shown as *broken* line in (**a**). *Solid* line in (**a**) is the observed kinetic energy and *solid* dots in (**a**) are (Q-values calculated from [8.37] −16 MeV)

Similarly, half-lives associated with the decay of the IFS of these decay modes are close to one another as evidenced by the mass yields spectrum in the decay of the IFS.

Theoretical calculations of the IFS half-lives done primarily for the decay to one of the fastest modes decrease sharply with the increase of mass number of the parent nucleus. As the half-lives associated with the decay of the IFS to the fastest mode becomes too short to measure, those associated with the decay to less dominant modes could become important and measurable. Futhermore, the calculations presented here are done by severely restricting the parameters of the potential; basically four parameters, r_0, t, λ, and d, determined from the decay of the SFS of ^{240}Pu to one of the daughter pairs, have been kept unchanged in all calculations, including the ones related to particle induced fission. This implies that we have been able to generate the mass dependence of the potential for the decay of parent nuclei from radium to fermium to a variety of decay modes associated with the decay of IFS and SFS of a parent nucleus. Clearly improved fits to the data could be obtained by relaxing this stringent requirement on the mass-dependence of

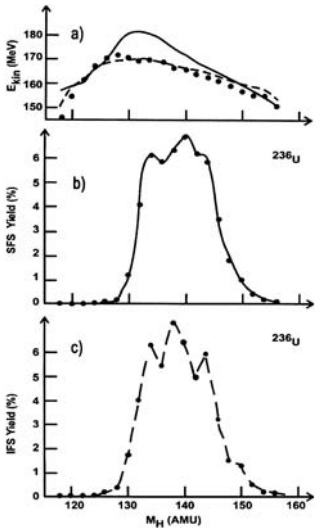

Fig. 8.6. The same as the one in Fig. 8.4, except for ^{236}U. The data on spontaneous fission are from [8.38]

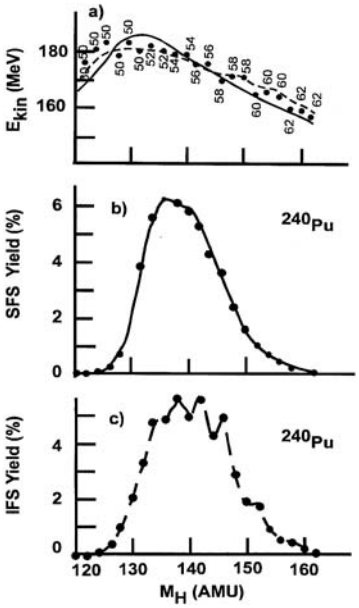

Fig. 8.7. The same as the one in Fig. 8.4 except for ^{240}Pu. The data on spontaneous fission are from [8.38] and the number next to *solid* dots in insert (**a**) refers to the atomic number

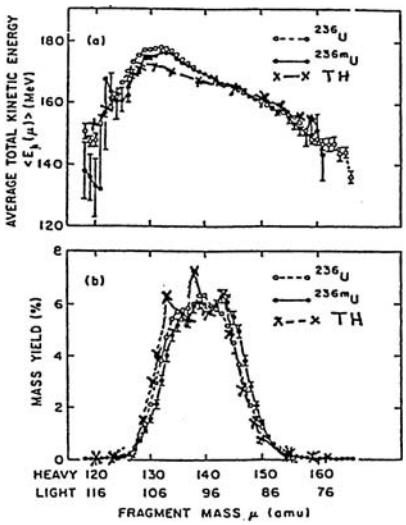

Fig. 8.8. The insert (**a**) plots the observed kinetic energy in the fission of ^{236}U from the ground state (*open circles*) and from the isomer state (*solid circles*) [8.18]. The theoretically predicted kinetic energy of [8.16] is shown as crosses in (**a**). The corresponding percentage mass yields spectra are shown in (**b**)

the barrier. For example, one could determine these parameters in different regions of the periodic table by a least squared fit. It would be extremely interesting to have experimental measurements of kinetic energy spectra for more cases and charge distributions. These will help to pin down the detailed structure of the external barrier.

8.4 Conclusion

Within the framework of the general structure of the potential-energy surface expected by incorporating Strutinsky's modification to the one generated by the energy-density functional approach, the theory is in a position to account for the observed half-lives and kinetic energy spectrum in the fission of IFS. For this, it is important to apply a coupled channel approach to the decay process. It would be very interesting to test experimentally the predictions of the theory for mass spectra associated with fission of IFS in cases other than ^{236}U and for charge distributions, in the fission yields from IFS.

References

1. G.N. Flerov, Yu. P. Ganrskii, B.N. Markov, A.A. Pleve, S.M. Polikanov and Rh. Yung-Klaussen, Dubna Preprint J1NR-P7-3067 (1960), unpublished.

2. S.M. Polikanov, V.A. Druin, V.A. Karnaukhov, V.L. Mikheev, A.A. Pleve, N.K. Skobelev, V.G. Subbotin, G.M. Ter-Akopyan and V.A. Fomichev, Soviet Phys: JETP **15**, 1016 (1962).
3. S. Bjornholm, J. Borggreen, L. Westgaard and V.A. Karnaukhov, Nucl. Phys. A **95**, 513 (1967).
4. H.C. Britt, S.C. Burnett, B.H. Erikkila, J.E. Lynn, and W.E. Stein, Phys. Rev. C **4**, 1444 (1971).
5. J. Boggreen, Yu. P. Grangrusky, G. Sletten, and S. Bjornholm, Phys. Lett. B **25**, 402 (1967).
6. R. Vandenbosch and K.L. Wolf, Proc. IAEA Second Symp. Phys. Chem. of Fission held in Vienna, 439 (1969).
7. R. Vandenbosch and J.R. Huizenga, *Nuclear Fission* (Academic Press, NewYork 1973).
8. V.M. Strutinsky, Yad. Fiz. **3**, 614 (1966).
9. V.M. Strutinsky, Nucl. Phys. A **95**, 420 (1967).
10. V.M. Strutinsky, Nucl. Phys. A **122**, 1 (1968).
11. V.M. Strutinsky, *50 Years with Nuclear Fission*, eds. J.W. Behrens and A.D. Carlson (American Nuclear Society, LaGrange Park, Illinois, 60525, U.S.A., 1989) 73.
12. H.J. Specht, J. Weber, E. Konecny, and D. Heunemann, Phys. Lett. B **41**, 43 (1972).
13. R.H. Heffner, J. Pedersen and H.H. Swanson, Private Communication reported in [8.7] (1972).
14. R.L. Ferguson, F. Plasil, G.D. Alam and H.W. Schmitt, Phys. Lett. B **31**, 526 (1970).
15. M.A. Hooshyar and F.B. Malik, Helv. Acta. Phys. **45**, 567 (1972).
16. M.A. Hooshyar and F.B. Malik, Phys. Lett. B **38**, 495 (1972).
17. M.A. Hooshyar and F.B. Malik, Phys. Lett. B **55**, 144 (1975).
18. C.A. Fontenla and D.P. Fontenla, Phys. Rev. Lett. **44**, 1200 (1980).
19. R.J. Lombard, Ann. Phys. (N.Y.) **77**, 380 (1973).
20. J. Bardeen, L.N. Cooper and J.R. Schrieffer, Phys. Rev. **108**, 1175 (1957).
21. S.G. Nilsson, Kgl. Dan. Vidskap. Selsk. Mat. Fys. Medd. **29**, No. 16 (1955).
22. C.F. Tsang and S.G. Nilsson, Nucl. Phys. A **140**, 275 (1970).
23. W. Scholz and F.B. Malik, Phys. Rev. **176**, 1345 (1968).
24. W.E. Stein, Phys. Rev. **108**, 94 (1957).
25. S. M. Polikanov and G. Sletten, Nucl. Phys. A **151**, 656 (1970).
26. A. Ghiorso, G.H. Higgens, A.E. Larsh, G.T. Seaborg and S.G. Thompson, Phys. Rev. **87**, 163 (1952).
27. N.L. Lark, G. Sletten, J. Pedersen and S. Bjornholm, Nucl. Phys. A **139**, 481 (1969).
28. A.H. Jaffey and A. Hirsh, Unpublished (1949).
29. R. Vandenbosch and K.L. Wolf, Physics and Chemistry of Fission (IAEA, Vienaa) 1969, p. 439.
30. D.E. Watt, F.J. Bannister, J.B. Laidler and F. Brown, Phys. Rev. **126**, 264 (1962).
31. A.B. Smith, P. Fields, A. Friedman, S. Cox and R. Sjoblom, Second Int'l Conf. On Peaceful Use of Atomic Energy (U.N. Publ. 1958).
32. V. Metag, R. Repnow, P. von Brentano and J.P. Fox, Physics and Chemistry of Fission (IEAE, Vienna) 1969, p. 449.

33. D. Metta, H. Diamond, R.F. Barnes, J. Milsted, J. Gray Jr., D.J. Henderson and C.M. Steven, J. Inorg. Nucl. Chem. **27**, 33 (1965).
34. A.M. Friedman, J.W. Meadows, A.B. Smith, P.R. Fields, J. Milsted and J.F. Whalen, Phys. Rev. **131**, 1203 (1963).
35. E.K. Hulet, Phys. Rev. **89**, 878 (1953).
36. F. Pleasonton, Phys. Rev. **174**, 1500 (1968).
37. W.D. Myers and W. J. Swiatecki, Nucl. Phys. **81**, 1 (1966).
38. H.W. Schmitt, J.H. Nelier and F.J. Walter, Phys. Rev. **141**, 1146 (1966).
39. J.H. Nelier, F.J. Walter and H.W. Schmitt, Phys. Rev. **149**, 894 (1966).
40. F.B. Malik, M.A. Hooshyar and B. Compani-Tabrizi, *Proc. 5^{th} Int'l Conf. On Nuclear Reaction Mechanism* ed. E. Gadioli (The Milan University Press, 1988) P. 310.
41. R.K. Sheline, I. Ragnarson and S.B. Nilsson, Phys. Lett. B.**41**, 115 (1972).
42. A. Bohr and B.M. Mottelson, Kgl. Danske Mat. Fys. Medd. Dan. Vid. Selsk, **27**, No. 16 (1953).
43. W. Lin, Phys. Rev. C **2**, 871 (1970).

9 Cluster Radioactivity

9.1 Introduction

In 1984 Rose and Jones [9.1] reported spontaneous emission of ^{14}C from the parent nucleus ^{223}Ra. Their findings were, immediately, confirmed by Gales et al. [9.2], Aleksandrov et al. [9.3], Price et al. [9.4] and Kutschera et al. [9.5]. These findings were also in accord with the earlier theoretical considerations pointing out the possibilities of such cluster emissions [9.6] in their ground states. Since then, emissions of many other clusters e.g., ^{20}O, ^{24}Ne, ^{25}Ne, ^{26}Ne, ^{28}Mg, ^{30}Mg, ^{32}Si, etc., have been observed [9.7]. The kinematics of the emitted clusters, initially, indicated that the lighter member of a daughter pair is emitted in its ground state. However, more refined measurements ultimately revealed that in one case, the lighter member of a daughter pair is emitted in an excited state e.g., ^{14}C in the spontaneous decay of ^{223}Ra [9.8]. This is reminiscent of the discovery of fine structure in alpha-decay by Rosenblum [9.9]. It has also been established that, like in alpha-decay and spontaneous fission, the cluster emission rate from odd-parent nuclei is, in many cases, hindered as compared to the ones measured for the cluster emission from the neighboring even-even isotopes [9.10]. The observed kinetic energies in cluster decay differ substantially from the corresponding Q-value implying a significant recoil effect.

In principle, a parent nucleus which exists in a meta-stable state, is capable of emitting a cluster of any size provided three conditions are satisfied, viz. (a) the Q-value is positive, (b) as noted in Chaps. 3 and 5 and in Appendix A, the minimum of the potential energy barrier must be located below the observed asymptotic kinetic energy of the cluster thereby allowing the formation of resonant meta-stable states and (c) the potential must be higher than the Q-value or asymptotic kinetic energy in the region between the minimum of the potential-energy surface and scission point, thereby preventing instantaneous decay. Aside from the three criteria, the derivation of the barrier penetration formula requires the use of asymptotic kinetic energies and not Q-values in calculating decay probabilities through barriers, as noted in Chap. 3 and the Appendices A and B.

The condition (a) in all these cases is clearly met since the Q-values for the observed cases of cluster emission are positive. A simple calculation of the estimated Coulomb barrier between the emitted cluster and its partner

given by the product of their charges divided by the sum of their radii, is usually higher than the respective Q-values, thus fulfilling, the condition (c).

Two of the models discussed in the following sections, namely the models based on Gamow-Condon-Gurney's theory of alpha-decay and the quasi-stationary state model, tacitly assume empirical potential surfaces which are compatible with the condition (b). The calculation of the potential barrier in the emission of ^{14}C from ^{226}Ra using the energy-density functional theory, similar to the one discussed in Chap. 3, indicates the formation of a neck of low-density nuclear matter between ^{14}C and ^{212}Pb prior to scission [9.11]. This results in an attraction prior to scission where the potential surface dips below the observed kinetic energy, thereby fulfilling the condition (b). The potential surfaces calculated using a hybrid model incorporating both deformation and an attractive force generated by nuclear surfaces of two members of a daughter pair, first recognized in [9.12, 9.13], and quite often termed as proximity force, does drop to the Q-values but not to the observed kinetic energy which is lower than the Q-values. Thus, these potential energy surfaces are in contradiction with criterion (b) and cannot support a resonant state prior to barrier penetration. Hence, even though, calculated half-lives, using Q-values and not observed kinetic energies, are in reasonable agreement with the observed ones [9.14, 9.15], this model is not discussed in detail any further.

In Sect. 9.2, we present the basic concept underlying the model of [9.6], which has undergone substantial refinement as discussed in [9.16]. Section 9.3 presents the basic exposition of the quasi-stationary model, which has also been refined extensively. Both of these models use empirical barriers, parameters of which are determined by fitting the data. The models also use Q-values in the computations of half-lives which implies that the recoil effect is negligible. This is in contradiction with the observed fact that the kinetic energies associated with a particular decay mode is quite often significantly less than the corresponding Q-values, as noted in Tables 9.1 and 9.2 and shown in Fig. 9.1.

In Sect. 9.4, we present the calculation of the potential-energy surface in the emission of a ^{14}C cluster from ^{226}Ra, using energy-density functional theory in the adiabatic approximation discussed in connection with fission in Chap. 3. In essence, this potential-energy surface is calculated from a realistic two-nucleon potential in a local density approximation. The calculated potential-energy surface does drop below the observed kinetic energy prior to the barrier, and hence, can support resonant states. As noted in Chap. 3, the emitted cluster starts taking on its identity in the region where the potential dips below the observed kinetic energy, i.e., just prior to the scission point because a suitable resonant state can only be supported at this location. Since the observed kinetic energy is less than the Q-value because of the significant recoil effect, this has been used in calculating penetrability.

Table 9.1. The observed kinetic energies, E_k in MeV, references of which are noted in the captions of Table 1.3, in the decay of clusters are noted in column 4 in the emission from even-even parent nuclei noted in column 1. Q-values in MeV calculated from the mass table [9.42], are listed in the last column. The light and heavy daughter partners are noted in columns 2 and 3, respectively

Parent Nuclei	Lighter Product	Heavier Product	E_k (MeV)	Q-value (cal.)
$^{222}_{88}$Ra	$^{14}_{6}$C	$^{208}_{82}$Pb	30.97	33.0531
$^{224}_{88}$Ra	$^{14}_{6}$C	$^{210}_{82}$Pb	28.63	30.5353
$^{226}_{88}$Ra	$^{14}_{6}$C	$^{212}_{82}$Pb	26.46	28.7887
$^{230}_{90}$Th	$^{24}_{10}$Ne	$^{206}_{80}$Hg	51.75	57.7767
$^{232}_{90}$Th	$^{26}_{10}$Ne	$^{206}_{80}$Hg	49.70	55.9751
$^{232}_{92}$U	$^{24}_{10}$Ne	$^{208}_{82}$Pb	55.86	62.3076
$^{234}_{92}$U	$^{24}_{10}$Ne	$^{210}_{82}$Pb	52.81	58.8432
$^{234}_{92}$U	$^{26}_{10}$Ne	$^{208}_{82}$Pb	52.87	59.4757
$^{234}_{92}$U	$^{28}_{12}$Mg	$^{206}_{80}$Hg	65.26	74.1292
$^{236}_{94}$Pu	$^{28}_{12}$Mg	$^{208}_{82}$Pb	70.22	79.6690
$^{238}_{94}$Pu	$^{28}_{12}$Mg	$^{210}_{82}$Pb	67.32	75.9305
$^{238}_{94}$Pu	$^{30}_{12}$Mg	$^{208}_{82}$Pb	67.00	77.0323
$^{238}_{94}$Pu	$^{32}_{14}$Si	$^{206}_{80}$Hg	78.95	91.2094
$^{242}_{96}$Cm	$^{34}_{14}$Si	$^{208}_{82}$Pb	82.88	96.4315

Table 9.2. The same as Table 9.1 except for parent nuclei with odd number of nucleons

Parent Nuclei	Lighter Product	Heavier Product	E_k (MeV)	Q-value (cal.)
$^{221}_{87}$Fr	$^{14}_{6}$C	$^{207}_{81}$Tl	29.28	31.2833
$^{221}_{88}$Ra	$^{14}_{6}$C	$^{207}_{82}$Pb	30.34	32.3927
$^{223}_{88}$Ra	$^{14}_{6}$C	$^{209}_{82}$Pb	29.85	31.8515
$^{225}_{89}$Ac	$^{14}_{6}$C	$^{211}_{83}$Bi	28.57	30.4673
$^{231}_{91}$Pa	$^{23}_{9}$F	$^{208}_{82}$Pb	46.68	51.8404
$^{231}_{91}$Pa	$^{24}_{10}$Ne	$^{207}_{81}$Tl	54.14	60.4195
$^{233}_{92}$U	$^{24}_{10}$Ne	$^{209}_{82}$Pb	54.27	60.5005
$^{233}_{92}$U	$^{25}_{10}$Ne	$^{208}_{82}$Pb	54.32	60.8368
$^{233}_{92}$U	$^{28}_{12}$Mg	$^{205}_{80}$Hg	65.32	74.2440
$^{235}_{92}$U	$^{24}_{10}$Ne	$^{211}_{82}$Pb	51.50	57.3579
$^{235}_{92}$U	$^{25}_{10}$Ne	$^{210}_{82}$Pb	51.68	57.8189
$^{237}_{93}$Np	$^{30}_{12}$Mg	$^{207}_{81}$Tl	65.52	75.0167
$^{241}_{95}$Am	$^{34}_{14}$Si	$^{207}_{81}$Tl	80.60	93.8382

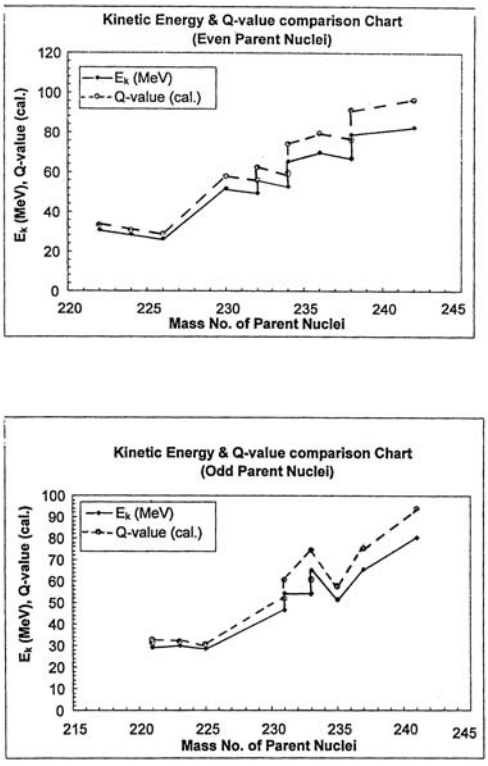

Fig. 9.1. Observed Q-values, from [9.42] and observed kinetic energies, E_k, taken from Table 1.3 for cluster emission from even-even and odd parent nuclei are shown, respectively, in the *upper* and *lower* insert, by *solid* line with *solid* dots and *light broken* line with *dots*, respectively

The key features of the calculation noted in Sect. 9.4, namely that the emitted cluster is formed just prior to scission, where the potential energy surface dips below the observed kinetic energy, thereby, being able to support a resonant state, can be produced by a model similar to the one proposed by Winslow [9.17] to describe alpha-decay. In Sect. 9.5, we present calculations of half-lives for many cases of cluster radioactivity with observed kinetic energies using this model.

9.2 Models Based on the Gamow-Condon-Gurney Approach

The theory of alpha-decay of Gamow [9.18] and Condon-Gurney [9.19] postulates the existence of an alpha-particle inside a parent nucleus which assaults against a Coulomb barrier before penetration. Inside the parent nucleus, the

alpha-particle experiences an attractive potential. The decay probability, λ (GCG), is a product of the number of assaults per second (termed also the assault frequency) ν and the barrier penetration probability, P. Thus,

$$\lambda(\mathrm{GCG}) = \nu P \; . \tag{9.1}$$

The barrier penetration probability, P, in (9.1) is calculated using the JWKB method in the lowest approximation and assuming that the asymptotic wave function of the emitted cluster is represented by an outgoing plane and not Coulomb wave having a wave number corresponding to the Q-value of the process. For zero orbital angular momentum, P, in this approximation, is given by

$$P = \exp(-(2/\hbar)) \int_1^2 [2\mu(V(r) - E_k)]^{1/2} dr \; . \tag{9.2}$$

where 1 and 2 are two turning points, $V(r)$ and μ are, respectively, the potential barrier between the emitted cluster and its partner nucleus and reduced mass, E_k is the asymptotic kinetic energy of the daughter pair in the center of the mass. Price [9.20, 9.21] used the following simple potential $V_p(r)$, to evaluate (9.2):

$$\begin{aligned} V_p(r) &= -V \qquad \text{for} \quad r \le R \\ &= Z_1 Z_2 e^2/r \qquad \text{for} \quad r > R \end{aligned} \tag{9.3}$$

where Z_1 and Z_2 are the atomic charges of the two members of the daughter pair. For the simple potential (9.3), (9.2) can be evaluated analytically leading to

$$P = \exp[-(2/\hbar)(2\mu/E)^{1/2} Z_1 Z_2 e^2 (\cos^{-1} y^{1/2} - (y - y^2)^{1/2})] \; . \tag{9.4}$$

In (9.4), $y = E_K/B$ where B is the value of the Coulomb potential at the outer turning point, R i.e. $B = Z_1 Z_2 \mathrm{e}^2/R$, R being the sum of two radii. R is given by

$$R = R_1 + R_2 = r_0[A_1^{1/3} + A_2^{1/3}] \tag{9.5}$$

In (9.5), A_1 and A_2 are the mass numbers of two members of a daughter pair. Price could fit the data reasonably well by setting E_k equal to the Q-value and choosing $r_0 = 0.928$ fm and $\nu = 4.3 \times 10^{26}$ s^{-1} for even-even parent nuclei and $\nu = 1.1 \times 10^{26}$ s^{-1} for odd-even or even-odd parent nuclei. His calculations, noted in column 5 of Table 9.3 along with calculations based on a number of different models, have been compared to the observed half-lives associated with a number of cases of cluster emission. However, the values of r_0, and ν needed in this model to account for the data are at variance with the expected values of $r_0 = 1.2$ fm and $\nu \approx 10^{22}$ s^{-1}. In addition, the use of the Q value in evaluating (9.2) implies a negligible recoil effect contradicting the data.

Table 9.3. Calculated half-lives of cluster emission in various models are compared to the data shown in column 10. The parent nuclei, along with its decay modes, are shown in column 1. The observed kinetic energy from Table 1.3 and Q-values calculated from [9.42] are shown in columns 2 and 3, respectively. Calculated half lives in seconds from [9.16], [9.20,9.21], [9.14,9.15], [9.26], [9.25], and [9.23,9.24], are shown in columns 4 to 9, respectively. They have been done using Q-values, rather than the observed kinetic energies in evaluating decay-constants. The last column represents logarithm of half-lives calculated in the surface-cluster model using the observed kinetic energies of column 2 to evaluate decay-constants as discussed in Sect. 9.5 of this chapter

Decay	E_k in MeV	Q-value (MeV)	Poe	SqW	S-S	B-M	B-W	I-S	Measured logT (sec)	Calculated logT (sec)
^{221}Fr$\rightarrow^{14}$C	29.28	31.2833	14.3	15.2	16.0	14.0	15.5	18.7	>15.77	15.82
^{221}Ra$\rightarrow^{14}$C	30.34	32.3927	14.2	14.1	14.8	>12.4	14.2	17.6	>14.35	14.38
^{222}Ra$\rightarrow^{14}$C	30.97	33.0531	11.1	11.2	11.6	11.4	11.8	10.5	11.0 ± 0.06	11.50
^{223}Ra$\rightarrow^{14}$C	29.35	31.8515	15.1	15.0	15.7	15.3	15.1	14.9	15.2 ± 0.05	15.34
^{224}Ra$\rightarrow^{14}$C	28.63	30.5353	15.9	16.0	16.8	16.1	16.2	15.3	15.9 ± 0.12	16.08
^{225}Ac$\rightarrow^{14}$C	28.57	30.4673	17.8	18.7	19.7	18.8	18.6	22.1	>18.34	19.16
^{226}Ra$\rightarrow^{14}$C	26.46	28.7887	20.9	21.0	22.2	21.0	21.1	21.7	21.3 ± 0.2	20.46
^{231}Pa$\rightarrow^{23}$F	46.68	51.8404	25.9	26.0	25.5		26.8	24.4	>25.4	25.81
^{230}Th$\rightarrow^{24}$Ne	51.75	57.7767	25.2	24.8	24.9	24.7	24.8	25.2	24.6 ± 0.07	24.94
^{232}Th$\rightarrow^{26}$Ne	49.70	55.9751	30.2	29.1	28.4	28.7	29.3	26.7	>27.9	28.40
^{231}Pa$\rightarrow^{24}$Ne	54.14	60.4195	23.3	23.7	23.5	21.6	23.4	23.9	23.4 ± 0.08	23.80
^{232}U$\rightarrow^{24}$Ne	55.86	62.3076	20.8	20.7	20.0	20.9	20.8	19.8	20.5 ± 0.03	20.27
^{233}U$\rightarrow^{24}$Ne	54.27	60.5005	25.2	24.9	24.8	23.7	25.4	24.4	24.8 ± 0.06	23.99
$\rightarrow^{25}$Ne	54.32	60.8368	25.7	25.1	24.4		26.0	24.2	24.8 ± 0.06	24.90
^{234}U$\rightarrow^{24}$Ne	52.81	58.8432	26.1	25.8	25.7	25.5	25.6	25.8	25.9 ± 0.2	25.17
$\rightarrow^{26}$Ne	52.87	59.4757	27.0	26.2	25.0	25.9	26.4	26.1	25.9 ± 0.2	26.37
^{235}U$\rightarrow^{24}$Ne	51.50	57.3579	29.9	29.7	30.1		29.9		>27.4	28.33
$\rightarrow^{25}$Ne	51.68	57.8189	30.6	29.7	29.6		28.0		>27.4	28.32
^{233}U $\rightarrow^{28}$Mg	65.32	74.2440	27.4	26.9	27.5		28.0	23.9	>27.8	27.35
^{234}U $\rightarrow^{28}$Mg	65.26	74.1292	25.9	25.4	25.7	25.4	25.4	25.7	25.7 ± 0.2	25.71
^{237}Np$\rightarrow^{30}$Mg	65.52	75.0167	28.3	28.3	27.7	>27.3	29.9	25.6	>27.4	28.62
^{236}Pu$\rightarrow^{28}$Mg	70.22	79.6690	21.1	21.2	20.5	21.5	22.0		21.7 ± 0.3	21.02
^{238}Pu$\rightarrow^{30}$Mg	67.00	77.0323	26.2	25.9	24.3	25.6	25.8	26.2	25.7 ± 0.25	25.32
$\rightarrow^{28}$Mg	67.32	75.9305	26.2	25.5		25.7	26.9	24.9	25.7 ± 0.25	25.05
^{238}Pu $\rightarrow^{32}$Si	78.95	91.2094	26.1	25.7		25.8	25.7	26.3	25.3 ± 0.16	25.41
^{241}Am$\rightarrow^{34}$Si	80.60	93.8382	25.8	26.5	26.2	25.3	28.8	23.8	>25.3	26.07
^{242}Cm$\rightarrow^{34}$Si	82.88	96.4315	23.5	23.4	22.6		24.1		>21.5	21.96

Sandelescu and his collaborators [9.6, 9.16, 9.22], and references therein could explain the data using a different potential $V_s(r)$ and defining the frequency of assaults, ν_s as follows:

$$\nu_s = (2Q/\mu)^{1/2}/R\ . \tag{9.6}$$

In (9.6), Q and μ are, respectively, the Q-value of the reaction and reduced mass and R is approximately the sum of the radii of the daughter pair

$$R = R_1 + R_2 \tag{9.7}$$

with

$$R_i = 1.128A^{1/3}(1 - 0.786A_i^{-2/3}), \qquad i = 1, 2\ . \tag{9.8}$$

The potential $V_s(r)$, used by them is the sum of nuclear and Coulomb potentials, $V_N(r)$ and $V_c(r)$, respectively.

$$V_s(r) = V_N(r) + V_c(r) \tag{9.9}$$

with

$$V_N(r) = V_0/[1 + \exp[(r - R)/a] \qquad \text{for} \quad r < R \tag{9.10}$$

$$\begin{aligned} V_c(r) &= (Z_1 Z_2 e^2/2R)(3 - r^2/R) \qquad \text{for} \quad r \le R \\ &= Z_1 Z_2 e^2/r \qquad\qquad\qquad\quad \text{for} \quad r > R \end{aligned} \tag{9.11}$$

The mass dependence of the parameters V_0 and a are set to be the following:

$$V_0 = 18\left[{A_1}^{1/3} + {A_2}^{1/3} - (A_1 + A_2)^{2/3}\right] \tag{9.12}$$

$$a = V_0(R_1 + R_2)/(16\pi R_1 R_2 \times 0.95) \tag{9.13}$$

Half-lives for a number of cases of cluster decay, calculated with this model, are noted in Table 9.3 in column 4. In evaluating (9.2) they also used Q-values of the decay and not E_k, thus overlooking significant recoil effect. The discrepancy between these calculations and the observed half-lives, is, sometimes, quantified as spectroscopic factor S, which are supposed to reflect the formation probabilities of clusters prior to their assaulting the barrier. The observed decay constant, λ(expt) is then related to the calculated decay constant of this model, λ (sand), by the following relation

$$\lambda(\text{expt}) = \text{S}\lambda\ (\text{sand}) \tag{9.14}$$

where

$$\lambda(\text{sand}) = v_s\text{P}\ (\text{sand})\ . \tag{9.15}$$

In (9.15), P (sand) is the penetrability through the barrier (9.9). Actual values of S depend on the models used in describing the nuclear structure of the parent and the daughter pairs. A number of such calculations is discussed in [9.16].

Ivascu and Silisteanu [9.23, 9.24] have investigated the cluster emission probabilities by calculating a cluster formation amplitude within the context of the Nilsson model and then, calculating the barrier penetration probabilities using a purely attractive optical model potential, with the Coulomb repulsion whose parameters are adjusted to reproduce the data. Q-values, rather than E_k have been used in evaluating (9.2). The use of a purely attractive potential implies the formation of clusters inside nuclei. Their results are also reported in Table 9.3 in the column marked as (I–S).

A different barrier, derived from the liquid drop approach but incorporating an attraction between the two emerging clusters is termed the proximity potential, and has been used in [9.14, 9.15, 9.26] to calculate half-lives using (9.2) and Q-values. This model has about the same degree of success as the model of [9.6, 9.22] and the results are noted in the column (S-S) of Table 9.3. Blendowske and Walliser [9.25] have also obtained reasonable fits to the data using a slightly different potential barrier and Q-values, as noted under the column (B-W) in the same table.

In all the models discussed in this section, the decay probabilities through the barriers have been calculated using (9.2) with the Q-values of the clusters. However, as noted in Tables 9.1 and 9.2 and Fig. 9.1, these Q-values differ significantly from observed kinetic energies. The derivation of (9.2) requires the use of the asymptotic kinetic energies which are less than the Q-values by a few to a few tens of MeV. Thus, clusters in all the models described here, are emitted with kinetic energies which are at substantial variance with the observed ones.

9.3 The Quasi-Stationary State Model

Buck and his collaborators [9.26–9.29] have applied the quasi-stationary state model whose main concept has originally been proposed by Gurwitz and Kalbermann [9.30]. In this section we shall present the results of [9.26] and discuss the key ideas of the model. Subsequent investigations basically present the refinement of [9.26]. The decay width of the cluster emission, Γ, in this model is given by

$$\Gamma = \frac{(2I_i + 1)F\hbar^2 P_B}{(2I_f + 1)(2L + 1)4\mu} \tag{9.16}$$

where I_i, I_f and L are, respectively, the initial spin of the parent nucleus, final spin of the partner nucleus of the spinless cluster and the orbital angular momentum of the daughter pair. μ is the reduced mass in the final channel, F is the normalization determined from (9.17) and P_B is the barrier penetration probability. The potential surface used in the calculation has three turning points, r, r_1, and r_2. For such a situation, F is given by

$$1/F = \int_{r_2}^{r_1} \frac{dr}{k(r)} \cos^2 \left[\int_{r_1}^{r} k(r')dr' - \pi/4 \right] . \tag{9.17}$$

In (9.17),

$$k(r) = [(2\mu/\hbar^2)(Q - V(r))]^{1/2} . \tag{9.18}$$

The penetration probability P is calculated in the lowest order JWKB approximation and is given by

$$P_B = \exp \left(-2 \int_{r_1}^{r_2} k(r)dr \right) . \tag{9.19}$$

The interaction potential $V(r)$ is the sum of nuclear, and Coulomb potentials, $V_N(r)$ and $V_c(r)$ and a centrifugal barrier in the Langer approximation.

$$V(r) = V_N(r) + V_c(r) + (\hbar^2/2\mu r^2)(L + 1/2)^2 . \tag{9.20}$$

The Coulomb part of the potential is taken to be that of an uniformly charged sphere of radius R between a daughter pair having charges of $Z_1 e$ and $Z_2 e$

$$\begin{aligned} V_c(r) &= \frac{Z_1 Z_2 e^2 (3 - (r/R)^2)}{2R} \quad \text{for} \quad r \le R \\ &= \frac{Z_1 Z_2 e^2}{r} \qquad\qquad\quad \text{for} \quad r > R . \end{aligned} \tag{9.21}$$

The form of the nuclear potential is usually taken to be

$$V_N(r) = \frac{V_0[1 + \cosh(R/a)]}{[\cosh(r/a) + \cosh(R/a)]} \tag{9.22}$$

V_0, the well-depth, is determined from the observed Q-values of the reaction using the Bohr-Sommerfeld quantization condition. a and R are essentially fixed from the observed half-lives of a few cluster emission rates particularly that of

$$^{222}\mathrm{Ra} \rightarrow \ ^{208}\mathrm{Pb} + ^{14}\mathrm{C}$$

and are found to be

$$a = 0.75\,\mathrm{fm} \text{ and } R = 1.04(A_1^{2/3} + A_2^{2/3})\,\mathrm{fm} . \tag{9.23}$$

The half-life $T_{1/2}$ is related to the width by

$$T_{1/2} = \hbar \ln 2/\Gamma \tag{9.24}$$

The calculated half-lives are shown in Table 9.3 in column 7.

Buck and his collaborators have subsequently refined the model. In particular, in the determination of Q-values, they have approximately taken into

account the correction due to electronic shielding and the recoil effect. Subsequently, potentials other than (9.22) have also been used [9.27]. The decay rates for $L \neq 0$ have also been calculated. Similar to the calculations done with the models discussed in the previous section, the computations of half-lives have been done using Q-values in calculating penetration probabilities through the barriers i.e., in evaluating (9.19). Thus, the kinetic energies of the emitted clusters in these models are the Q-values of the respective reaction which are at variance with the data on kinetic energies.

9.4 The Energy-Density Functional Approach

In Tables 9.1 and 9.2, we have presented the calculated Q-values using observed masses [9.42] for a number of emitted clusters, along with the observed kinetic energies which are, in all cases, less than the respective Q-values. This implies the presence of substantial recoil effect. In fact, a detailed measurement of the kinetic energy spectrum of ^{14}C, in the decay of ^{223}Ra, indicates that the most probable state of its partner nucleus ^{209}Pb, is not the ground state, but its first excited state [9.8]. The total decay rate is distributed among its three lowest states. The percentages of decay rates among these three states are, respectively 4, 81 and 15 leading to respective logarithm of half-lives of 16.0, 15.3, and 16.6 seconds. The decay to other excited states of ^{209}Pb has also been observed but the rates are substantially smaller [9.31]. In addition, the barriers used in all the above cases are empirical and assume the clusters in their ground states to exist inside the parent nucleus for a long time. Bethe [9.32] and Winslow [9.17] have noted in connection with alpha-decay that, within the context of many-body theories, it is difficult to visualize clusters bouncing around inside a nucleus, notwithstanding, the success of the Gamow-Condon-Gurney type of theories in explaining the data on half-lives of alpha decay. The concept of the number of assaults used in Gamow-Condon-Gurney type of theories or the cluster going around in Bohr-Sommerfeld orbits inside a nucleus, used in a quasi-stationary state model, implies that clusters exist as actual entities inside a nucleus. There is no experimental data that can substantiate this assumption; neither are there theoretical reasons to support it. On the other hand, the fission process within the context of energy-density functional theory, described in Chap. 3, does not envisage the existence of clusters inside a nucleus but they are formed just prior to scission as the neck of low-density nuclear matter begins to take shape. In fact, the investigations of Mueller and Clark [9.33], Brink and Castro [9.34], and Röpke [9.35] indicate that the formation of alpha-like clusters are more likely at low-density of nuclear matter than the formation of a pure nucleonic matter.

In the calculations of mass and charge distribution in spontaneous fission, discussed in Chaps. 3 and 5, the probabilities of the spontaneous emission

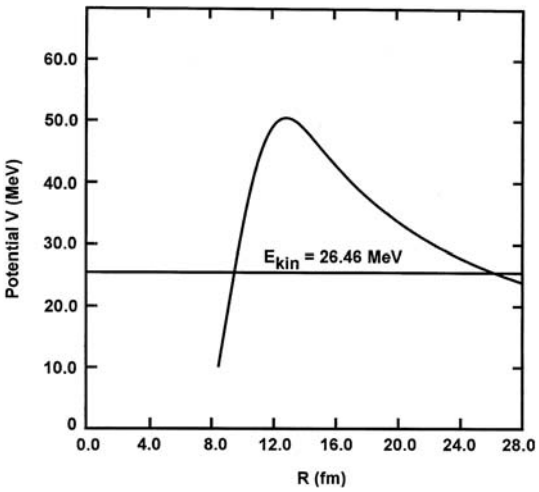

Fig. 9.2. The external part of the potential energy surface calculated using special adiabatic approximation discussed in Chap. 3 for the spontaneous emission of ^{14}C clusters from ^{226}Ra. At $r = 0$, the value of the potential is the Q-value i.e. 28.79 MeV which is larger than the observed kinetic energy, E_k. The scission point calculated using (3.31) is about 14.06 fm

of light particles, are tacitly recognized, provided the Q-values were positive. Cluster emissions are, therefore, an inherent part of these theories.

In this section, we present the potential barrier and half-life for the spontaneous emission of ^{14}C from ^{226}Ra, using the special adiabatic approximation of Chap. 3. In Fig. 9.2, we present the external part of the calculated barrier using trapezoidal density distribution functions for the parent ^{226}Ra and the daughter pair ^{212}Pb and ^{14}C. C_0 and t for the parent are taken to be 1.07 fm and 2.6 fm, which reproduce its ground state mass within a few MeV. The observed $E_{\rm kin}$ of 26.46 MeV is less than the Q-value of 28.79 MeV. The recoil energy of the daughter pair is simulated by adjusting C_0 to 0.96 fm which, in effect, smears their surface a little. $f(A_p)$ is taken to be 23.93 resulting in a scission radius $R_{\rm sc} = 14.06$ fm, calculated using (3.31). This reproduces the observed kinetic energy of 26.46 MeV. Since ^{14}C is considerably smaller than daughter pairs in nuclear fission, the pre-formation probability in its emission process is higher and taken to be 10^{-3} instead of 10^{-5}. Noting that the pre-formation probability of alpha-particles is, on the average, about 10^{-2} [9.36] and ^{14}C is slightly larger than an alpha-particle, this pre-formation probability for ^{14}C is a reasonable one. The calculated logarithm of half-life for this decay using the observed kinetic energy of 26.4 MeV is 21.4 sec. which is in accord with the observed value of 21.3 ± 0.2 sec. [9.10, 9.43].

Essentially, the same result is obtained in [9.11]. The important features of the calculated barrier are that (a) the attractive part of the potential energy surface occurs near the surface region, i.e., clusters are formed in the

low-density neck region and (b) one can get a good result using observed kinetic energy which must be the case in calculating penetrability through a barrier in the JWKB approximation, as noted in Appendices A and B.

Both of these features can be introduced in the model used by Winslow [9.17] for studying alpha-decay. Slightly modified versions of Winslow's model have also been used by Preston [9.37] and Devaney [9.38]. The model has similarity with the model of Hooshyar and Malik discussed in Chap. 5 to describe spontaneous fission.

9.5 The Surface-Cluster Model

As noted in Sect. 9.3, clusters cannot exist inside a nucleus and must be formed just prior to separation in the neck of low-density nuclear matter. In Fig. 9.2, we note that the attractive part of the potential between two members of the daughter pair occurs just prior to the scission. These two features could be simulated in the potential used by Winslow [9.17] to describe alpha-decay and Block et al. [9.39] to describe the fission process. An infinite repulsive potential of the range of R_0 which is expected to be equal to about $C_0(A_1^{1/3} + A_2^{1/3})$, C_0 being half-density radius of the trapezoidal density distribution function, would prevent the cluster from existing inside a nucleus. Since the clusters are formed prior to scission in the low-density region, the range of the attractive part is expected to be approximately one half of the surface thickness i.e., from 1.0 fm to 2.4 fm.

Thus, the potential $V(r)$ shown in Fig. 9.3 is given by

$$V(r) = \begin{array}{ll} +\infty & \text{for} \quad r < R_0 \\ -V_0 & \text{for} \quad R_0 < r < R \\ \dfrac{Z_1 Z_2 e^2}{r} & \text{for} \quad r \geq R\,. \end{array} \tag{9.25}$$

In (9.25), Z_1 and Z_2 are atomic numbers of two nuclei of a daughter pair. This potential is shown in Fig. 9.3, with R_E being the scission radius where the Coulomb potential is equal to the asymptotic kinetic energy, E_{kin}. The decay probabilities $\lambda(scm)$, in this model, is equal to the pre-formation probability, $P(scm)$, times the decay probability $\lambda(wi)$, through the barrier

$$\lambda(scm) = P(scm)\ \lambda\ (wi) \tag{9.26}$$

Instead of using the standard JWKB method, discussed in Appendices A and B, to calculate barrier penetrability, Winslow noted that a parent nucleus emitting any particle spontaneously is in a meta-stable state and as such its energy W is complex and equal to $E - (i\lambda(wi)\hbar)/2$, in region III.

$$W = E - (i\lambda(wi)\hbar/2\,. \tag{9.27}$$

The time-dependent wave function in region III, $\Phi^{III}(r,t)$ is given by

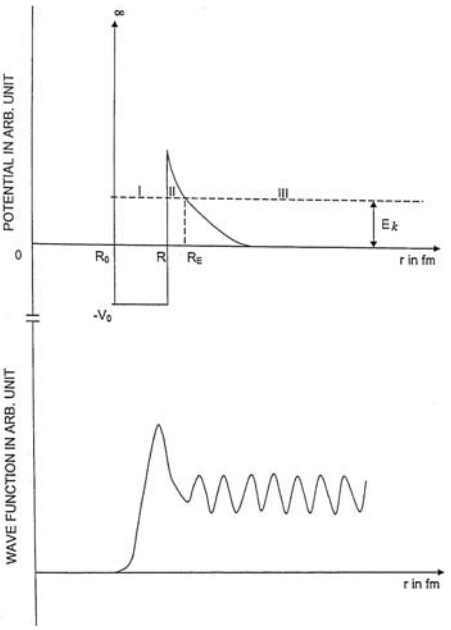

Fig. 9.3. The barrier used in the calculation of cluster emission half-lives in the surface cluster model is shown in the *upper* part. The *lower* part depicts schematically the behavior of the wave function for such a barrier. Essentially, clusters are formed near the surface, prior to penetration through the barrier

$$\Psi\left(r,t\right)=\Phi^{III}\left(r\right)\exp[iWt/\hbar]\ .$$

Noting that $|\Psi\left(r,t\right)|^2$ represents the flux in this region, $\lambda(wi)$ can be identified with the decay constant. The wave numbers k is given by

$$\hbar^2k^2/2\mu=W \tag{9.28}$$

μ in (9.8) is the reduced mass in the decay process.

The solution in region I, i.e., in the interval $R_0\leq r<R$ that vanishes at $r=R_0$, is given by

$$\begin{aligned}\Phi^I(r)=(Kr)^{1/2}[&J_{L+1/2}(Kr)J_{-(L+1/2)}(KR_0)\\&-J_{-(L+1/2)}(Kr)J_{L+1/2}(KR_0)]\end{aligned} \tag{9.29}$$

where

$$\hbar^2K^2/2\mu=W-V_0\ . \tag{9.30}$$

Thus, the energy in region I is also complex which is commensurate with the fact that the parent nucleus is in a meta-stable state. The radial part of the wave function in region II, i.e. between $R<r<R_E$, is a linear combination of regular and irregular Coulomb wave functions, F_L, and G_L

$$\Phi^{II}(r) = PG_L(r) + QF_L(r) \; . \tag{9.31}$$

Noting that asymptotically $Q = iP$, one may write

$$\Phi^{II}(r) = P(G_L(r) + iF_L(r)) \; . \tag{9.32}$$

As shown by Winslow [9.17], $G_L(r)$, and $F_L(r)$ can suitably be approximated in terms of variable $p = kr$ by the following expressions:

$$G_L(p) = |\Phi\,(p)|^{-1/4} \exp[w\,(p)] \tag{9.33}$$

$$F_L(p) = \left(1/2\right) |\Phi\,(p)|^{-1/4} \exp[-w\,(p)] \tag{9.34}$$

with

$$|\Phi\,(p)| = \eta/p + (L + 1/2)^2\,/p^2 - 1, \tag{9.35}$$

$$w(p) = \int_p^{P_E} |\Phi\,(\xi)|^{1/2} d\xi \tag{9.36}$$

and

$$\eta = (Z_1 Z_2/\hbar)\,\mu/2W \; . \tag{9.37}$$

In (9.37), Z_1 and Z_2 are the atomic numbers of each member of a daughter pair and the limit of integration P_E in (9.36) is kR_E.

This must be matched to the wave function in region III, Φ^{III}, representing the following outgoing plane wave:

$$\Phi^{III}(r) = A \exp(ip) \; . \tag{9.38}$$

Matching logarithmic derivatives at $r = R$ and $r = R_{\mathrm{E}}$ and separating real and imaginary parts, and neglecting the contributions of the imaginary part to k and K, one obtains the following expression for $\lambda(wi)$

$$\lambda\,(wi) = \frac{(2\hbar/\mu)\,k\,|\Phi|^{1/2} \exp\,(-2w)}{-\,(\hbar^2/\mu R)\,[\partial f^I/\partial W]_E + (1-\delta)\,[k\,|\Phi|^{1/2}\,(1+\delta)]} \tag{9.39}$$

where

$$\delta = (1/4)\,|\Phi|^{-3/2}\,(\partial\,|\Phi\,(\rho)|\,/\partial\rho)_{kR} \tag{9.40}$$

$$w = \int_{\rho_R}^{\rho_E} |\Phi(\xi)|^{1/2} d\xi \; . \tag{9.41}$$

In deriving (9.39), $(1-2\delta)$ has been replaced by $(1-\delta)/(1+\delta)$ since $|\delta| < 1$. $(\partial f^I/\partial W)_E$ in (9.32) is determined from the following equation

$$\begin{aligned} &-(\hbar^2/\mu R)(\partial \mathrm{f^I}/\partial \mathrm{W})_E \\ &= R[1 - [(2L+1)/(KR)](\upsilon/u) + (\upsilon/u)^2 - (2/\pi KRu)^2] \end{aligned} \tag{9.42}$$

where

$$\upsilon = J_{L+1/2}(KR)J_{-(L+1/2)}(KR_0) - J_{-(L+1/2)}(KR_0)J_{L+1/2}(KR)$$
$$u = (KR)^{-1/2}\Phi^I(R)\ .$$

We may note that the expression (9.39) for $\lambda\ (wi)$ may also be written in the following form:

$$\lambda(wi) = \frac{2\hbar}{\mu RS}k\,|\Phi|^{1/2}\exp(-2w) \tag{9.43}$$

with

$$S = 1 + (KR)^{-2}(g_L^2 + g_L - L(L+1) - (2/(\pi u)^2) + (1-\delta)/g_L \tag{9.44}$$

where

$$g_L = kR\big|\Phi\big|^{1/2}(1+\delta)\ . \tag{9.45}$$

The pre-formation probability $P(scm)$ in (9.26) has been calculated by Mang [9.36] for alpha-decay and lies between 10^{-1} and 10^{-2}. In Chap. 3, this has been evaluated for the spontaneous fission case and determined to be about 10^{-5}. Since the clusters involved are heavier than alpha-particles but lighter than the daughter nuclei in the case of fission, one expects the pre-formation probabilities for cluster emission to lie between 10^{-2} and 10^{-4}. In addition, the level density of many of the clusters are much lower than that of daughter nuclei in fission, since they have smaller masses and hence, it is likely that this number for the pre-formation probability may fluctuate substantially. In fact, as noted in [9.39], the pre-formation probabilities for cluster emission is likely to depend on the detailed structure of the energy levels of daughter and parent nuclei, because it is basically the overlap integrals of the product of the parent and daughter wave functions. A careful determination of pre-formation probabilities by fitting data is likely to provide information on nuclear structures. However, we are, at this stage, interested in describing the overall physical nature of the process and, as such, have used a single number for pre-formation probability to calculate the decay rates from even-even parent nuclei and another one for odd parent nuclei.

The extent of the infinite repulsive core, R_0, is approximately equal to $C_0\ (A_1^{1/3} + A_2^{1/3})$, i.e., the distance where the sum of the densities of the two members of a daughter pair is approximately equal to the saturation density of nuclear matter. Thus, C_0 should be between 0.9 and 1.2 fm. $\Delta R = R_1 - R_0$, is of the order of one half of the surface and should be between 1.0 to 2.4 fm. The derivation of (9.39) requires that the asymptotic kinetic energy of a daughter pair and not the Q-value, be used in calculating decay constants.

As noted in connection with the theory of fission in Chap. 3, the pre-formation probabilities in the decay of clusters from the even-even and odd-even (or even-odd) parent nuclei might differ from each other, due to the

presence of the blocking effect for parent nuclei of odd mass numbers. In Table 9.4, we present the half-lives of cluster emission from even-even parent nuclei and compare them with observed data using a pre-formation probability of 10^{-3}, $C_0 = 1.03$ fm and $\Delta R = 1.1$ fm. The scission radius, $R_{\rm sc}$ is not an arbitrary free parameter but is related to $E_{\rm kin}$ by

$$E_{\rm kin} = Z_1 Z_2 e^2 / R_{\rm sc} \tag{9.46}$$

The results are not very sensitive to the choice of V_0 which is taken to be (-50) MeV. The calculated logarithm of half-lives using $E_{\rm kin}$ are compared to the data in Table 9.4. It is remarkable that, except for three cases, namely ^{230}Th $\rightarrow^{24}$Ne, ^{236}Pu $\rightarrow^{28}$Mg and ^{238}Pu $\rightarrow^{32}$Si, the agreement between them is quite good. This is particularly satisfying, since this is achieved by using a single set of parameters, along with a simple mass number dependence.

The discrepancies in the three cases can be improved by simply changing r_0 to 1.015 fm. Calculated results [9.40] along with the data for these three cases are presented in Table 9.5. The agreement is now quite reasonable.

Table 9.4. Calculated logarithms of half-lives in seconds in the surface-cluster model, [9.40], noted in column 6 are compared to logarithm of the observed values noted in the last column taken from Table 1.3. Columns 1 to 4 are, respectively, the parent nuclei, lighter and heavier members of a daughter pair, and observed kinetic energies. The calculations are done using parameters $\Delta R = 1.1$ fm and $r_0 = 1.03$ fm defined in the text. V_0 and pre-formation probabilities are taken to be $(-50\,{\rm MeV})$ and 10^{-3} respectively. The observed kinetic energy, E_k has been used in calculating barrier penetration probabilities

Parent Nuclei	Lighter Product	Heavier Product	E_k (MeV)	Q-value (Cal.)	log (T) Cal.	log (T) Expt.
$^{222}_{88}$Ra	$^{14}_{6}$C	$^{208}_{82}$Pb	30.97	33.0531	11.504	11.0 ($\pm$ 0.06)
$^{224}_{88}$Ra	$^{14}_{6}$C	$^{210}_{82}$Pb	28.63	30.5353	16.080	15.9($\pm$ 0.12)
$^{226}_{88}$Ra	$^{14}_{6}$C	$^{212}_{82}$Pb	26.46	28.7887	20.457	21.3($\pm$ 0.2)
$^{230}_{90}$Th	$^{24}_{10}$Ne	$^{206}_{80}$Hg	51.75	57.7767	23.364	24.6($\pm$ 0.07)
$^{232}_{90}$Th	$^{26}_{10}$Ne	$^{206}_{80}$Hg	49.70	55.9751	28.424	>27.9
$^{232}_{92}$U	$^{24}_{10}$Ne	$^{208}_{82}$Pb	55.86	62.3076	20.275	20.5($\pm$ 0.03)
$^{234}_{92}$U	$^{24}_{10}$Ne	$^{210}_{82}$Pb	52.81	58.8432	25.174	25.9($\pm$ 0.2)
$^{234}_{92}$U	$^{26}_{10}$Ne	$^{208}_{82}$Pb	52.87	59.4757	26.375	25.9($\pm$ 0.2)
$^{234}_{92}$U	$^{28}_{12}$Mg	$^{206}_{80}$Hg	65.26	74.1292	25.707	25.7($\pm$ 0.2)
$^{236}_{94}$Pu	$^{28}_{12}$Mg	$^{208}_{82}$Pb	70.22	79.6690	19.863	21.7($\pm$ 0.3)
$^{238}_{94}$Pu	$^{28}_{12}$Mg	$^{210}_{82}$Pb	67.32	75.9305	25.324	25.7($\pm$ 0.25)
$^{238}_{94}$Pu	$^{30}_{12}$Mg	$^{208}_{82}$Pb	67.00	77.0323	25.053	25.7($\pm$ 0.25)
$^{238}_{94}$Pu	$^{32}_{14}$Si	$^{206}_{80}$Hg	78.95	91.2094	23.760	25.3($\pm$ 0.16)
$^{242}_{96}$Cm	$^{34}_{14}$Si	$^{208}_{82}$Pb	82.88	96.4315	21.963	>21.5

Table 9.5. The same as that of Table 9.4 but $r_0 = 1.015$ fm. Calculations have been done using observed kinetic energies and not Q-values

Parent Nuclei	Lighter Product	Heavier Product	E_k (MeV)	Q-value (Cal.)	log (T) Cal.	log (T) Expt.
$^{230}_{90}$Th	$^{24}_{10}$Ne	$^{206}_{80}$Hg	51.75	57.7767	24.941	24.6(± 0.07)
$^{236}_{94}$Pu	$^{28}_{12}$Mg	$^{208}_{82}$Pb	70.22	79.6690	21.020	21.7(± 0.3)
$^{238}_{94}$Pu	$^{32}_{14}$Si	$^{206}_{80}$Hg	78.95	91.2094	25.412	25.3(± 0.16)

For parent nuclei with odd number of nucleons, the data are not as good as the ones with the even-even parent nuclei. Nevertheless, the calculated results presented in Table 9.6 using a pre-formation probability of 10^{-4}, $C_0 = 1.03\,\text{fm}$, $\Delta R = 1.1$ and $V_0 = (-50)\,\text{MeV}$, i.e., the same values of parameters used in the calculations presented in Table 9.4, are in reasonable agreement with the data, except for the case of the emission of ^{24}Ne from ^{233}U, where the discrepancy is of about three orders of magnitude. However, changing C_0, slightly to 1.01 fm, one can improve the agreement considerably. The calculated logarithm of half-lives along with the data are presented in Table 9.7. In all cases E_{kin} has been used.

The half-lives calculated in the surface-cluster model [9.40] are noted in the last column of Table 9.3. These half-lives, calculated using asymptotic kinetic energies, E_k, noted in column 2, compare favorably with the data and

Table 9.6. The same as that of Table 9.4 but the pre-formation is taken to be 10^{-4}

Parent Nuclei	Lighter Product	Heavier Product	E_k (MeV)	Q-value (Cal.)	log (T) Cal.(sec)	log (T) Expt.(sec)
$^{221}_{87}$Fr	$^{14}_{6}$C	$^{207}_{81}$ Tl	29.28	31.2833	15.822	>15.77
$^{221}_{88}$Ra	$^{14}_{6}$C	$^{207}_{82}$Pb	30.34	32.3927	14.379	14.35
$^{223}_{88}$Ra	$^{14}_{6}$C	$^{209}_{82}$Pb	29.85	31.8515	15.343	15.2(± 0.05)
$^{225}_{89}$Ac	$^{14}_{6}$C	$^{211}_{83}$Bi	28.57	30.4673	19.161	>18.34
$^{231}_{91}$Pa	$^{23}_{9}$F	$^{208}_{82}$Pb	46.68	51.8404	24.992	>25.4
$^{231}_{91}$Pa	$^{24}_{10}$Ne	$^{207}_{81}$Tl	54.14	60.4195	22.038	23.4(± 0.08)
$^{233}_{92}$U	$^{24}_{10}$Ne	$^{209}_{82}$Pb	54.27	60.5005	21.846	24.8(± 0.06)
$^{233}_{92}$U	$^{25}_{10}$Ne	$^{208}_{82}$Pb	54.32	60.8368	24.107	24.8(± 0.06)
$^{233}_{92}$U	$^{28}_{12}$Mg	$^{205}_{80}$Hg	65.32	74.2440	26.556	>27.8
$^{235}_{92}$U	$^{24}_{10}$Ne	$^{211}_{82}$Pb	51.50	57.3579	28.331	>27.4
$^{235}_{92}$U	$^{25}_{10}$Ne	$^{210}_{82}$Pb	51.68	57.8189	28.322	>27.4
$^{237}_{93}$Np	$^{30}_{12}$Mg	$^{207}_{81}$Tl	65.52	75.0167	27.093	>27.4
$^{241}_{95}$Am	$^{34}_{14}$Si	$^{207}_{81}$Tl	80.60	93.8382	24.584	>25.3

Table 9.7. The same as that of Table 9.6 but $r_0 = 1.01$ fm

Parent Nuclei	Lighter Product	Heavier Product	E_k (MeV)	Q-value (Cal.)	log (T) Cal.(sec)	log (T) Expt.(sec)
$^{221}_{87}$Fr	$^{14}_{6}$C	$^{207}_{81}$Tl	29.28	31.2833	16.36	>15.77
$^{221}_{88}$Ra	$^{14}_{6}$C	$^{207}_{82}$Pb	30.34	32.3927	14.26	14.35
$^{223}_{88}$Ra	$^{14}_{6}$C	$^{209}_{82}$Pb	29.85	31.8515	15.39	15.2(± 0.05)
$^{225}_{89}$Ac	$^{14}_{6}$C	$^{211}_{83}$Bi	28.57	30.4673	19.69	>18.34
$^{231}_{91}$Pa	$^{23}_{9}$F	$^{208}_{82}$Pb	46.68	51.8404	25.81	>25.4
$^{231}_{91}$Pa	$^{24}_{10}$Ne	$^{207}_{81}$Tl	54.14	60.4195	23.80	23.4(± 0.08)
$^{233}_{92}$U	$^{24}_{10}$Ne	$^{209}_{82}$Pb	54.27	60.5005	23.99	24.8(± 0.06)
$^{233}_{92}$U	$^{25}_{10}$Ne	$^{208}_{82}$Pb	54.32	60.8368	24.90	24.8(± 0.06)
$^{233}_{92}$U	$^{28}_{12}$Mg	$^{205}_{80}$Hg	65.32	74.2440	27.35	>27.8
$^{235}_{92}$U	$^{24}_{10}$Ne	$^{211}_{82}$Pb	51.50	57.3579	28.86	>27.4
$^{235}_{92}$U	$^{25}_{10}$Ne	$^{210}_{82}$Pb	51.68	57.8189	29.98	>27.4
$^{237}_{93}$Np	$^{30}_{12}$Mg	$^{207}_{81}$Tl	65.52	75.0167	28.62	>27.4
$^{241}_{95}$Am	$^{34}_{14}$Si	$^{207}_{81}$Tl	80.60	93.8382	26.07	>25.3

half-lives computed in other models, which however, used Q-values in determining barrier penetration probabilities thereby neglecting the substantial recoil effect.

Thus, the surface-cluster model which has its root in the potential energy-surface calculated using energy-density functional theory, can account for the observed half-lives with observed kinetic energies. The identities of the clusters are established in the neck of low-density nuclear matter just prior to emission and they do not have to exist in cluster forms inside a nucleus.

9.6 Conclusion

In Chap. 5, the half-lives of the spontaneous fission of a number of even-even nuclei, their mass and charge distributions have been well accounted for with a potential energy surface having a finite repulsive core followed by an attractive part and a Coulomb potential and using observed asymptotic kinetic energies and not Q-values, to compute decay constants. Similar potential barriers can also explain the mass distributions and their variation with incident projectile energies in induced fission as discussed in Chap. 6.

The potential barriers used in Chaps. 5 and 6 are akin to the ones used in the surface cluster model of Sect. 9.5 in this chapter to describe cluster radioactivity. The use of an infinite repulsive barrier in the latter case, instead of a finite one used for the study of fission, is not significant, since the use of an infinite repulsive core would not have changed the results of Chaps. 5 and 6 in a significant way.

Table 9.8. Calculated half-lives in years, for alpha decay of a number of even-even nuclei noted in column 2 in surface cluster model (Column 4) are compared to the data [9.42] tabulated in the last column. Column 3 denotes observed Q-values [9.42]

Z	A	Q(exp) MeV	$T_{1/2}$ (Winslow with Q (exp)	Measured $T_{1/2}$ (years)
$_{92}$U	228	6.68	0.2×10^{-6}	2.0×10^{-6}
	230	5.89	7.8×10^{-2}	5.7×10^{-2}
	232	5.32	10.1×10^{-1}	7.2×10^{1}
	234	4.77	3.6×10^{5}	2.5×10^{5}
	236	4.49	4.0×10^{7}	2.4×10^{7}
	238	4.20	9.1×10^{9}	4.5×10^{9}
$_{94}$Pu	232	6.59	30.5×10^{-5}	6.9×10^{-3}
	234	6.20	17.3×10^{-3}	1.0×10^{-3}
	236	5.77	2.5×10^{0}	2.9×10^{0}
	238	5.50	7.5×10^{1}	8.7×10^{1}
	240	5.17	7.3×10^{3}	6.6×10^{3}
	242	4.90	4.3×10^{5}	3.9×10^{5}
	244	4.58	9.0×10^{7}	8.3×10^{7}
$_{96}$Cm	240	6.29	4.4×10^{-3}	7.4×10^{-2}
	242	6.12	2.8×10^{-1}	4.5×10^{-1}
	244	5.81	1.1×10^{1}	1.8×10^{1}
	246	5.39	2.8×10^{3}	4.7×10^{3}
	248	5.08	2.5×10^{5}	3.5×10^{3}
$_{98}$Cf	244	7.18	2.6×10^{-5}	3.8×10^{-5}
	246	6.79	2.0×10^{-3}	4.1×10^{-3}
	248	6.27	3.5×10^{-1}	9.6×10^{-1}
	250	6.03	0.6×10^{1}	1.3×10^{1}
	252	6.12	1.8×10^{9}	2.6×10^{0}
$_{100}$Fm	248	7.85	0.6×10^{-6}	1.2×10^{-6}
	250	7.44	2.0×10^{-5}	5.7×10^{-5}
	252	7.05	0.7×10^{-3}	2.6×10^{-3}
	254	7.16	2.3×10^{-4}	3.7×10^{-4}

High, Malmin and Malik [9.41] have also investigated alpha-decay of a number of even-even nuclei using the surface-cluster model with a finite repulsive barrier at $r < R_0$. Their results are shown in Table 9.8 for $C_0 = 1.1$ fm, $V_0 = (\text{Q–}60)$ MeV, $\Delta R = 1.2$ fm. The calculations are done with observed Q-values which, in this case, are equal to asymptotic energies. The agreement between the calculated and the observed half-lives are very good. As noted

in [9.41], the calculated results would not have been changed in any significant way by replacing the finite core by an infinite one. We can, therefore, conclude that the fission phenomena, and cluster-radioactivities as well as alpha- radioactivities could be described by a single model, having its root in the energy-density functional approach to calculate the potential energy surface.

References

1. H.J. Rose and G.A. Jones, Nature **307**, 245 (1984).
2. S. Gales, E. Hourani, M. Hussonnois, H.P. Shapira and M. Vergnes, Phys. Rev. Lett. **53**, 759 (1984).
3. D.V. Alexandrov, A.F. Belyatsky, Yu. A. Glukov, F.Yu. Nikolsky, B.G. Novatsky, A.A. Oglobin and D.M Stephanov, Pis'ma JETP **40**, 152 (1984).
4. P.B. Price, J.D. Stevenson, S.W. Barwick and H.L. Ravn, Phys. Rev. Lett. **54**, 297 (1985).
5. W. Kutschera, I. Ahmad, S.G. Armato III, A.M. Friedman, J.E. Gindler, J.E. Hennig, T. Issit, P. Paul and K.E. Rehm, Phys. Rev. C **32**, 2036 (1985).
6. A. Sandelescu and W. Greiner, J. Phys. G: Nucl. Phys. **3**, L189 (1977).
7. A.A. Oglobin, G. Pik-Pichak and S.P. Tretyakova, *Fission Dynamics of Atomic Clusters and Nuclei* eds. J. da Providencia, D.M. Brink, F. Karpechine and F.B. Malik (World Scientific, 2001) p. 143.
8. M. Hussonnois and G. Ardisson, Zeit. f. Physik, A **349**, 311(1994).
9. S. Rosenblum, J. de Physique et Rad. **1**, 438 (1930).
10. S.W. Barwick, P.B. Price, H.L. Ravn, E. Hourani and M. Hussonnois, Phys. Rev. C **34**, 362 (1986).
11. I. Reichstein and F.B. Malik, Cond. Matter Theories, **8**, 243 (1993).
12. B. Block and F.B. Malik, Phys. Rev. Lett. **19**, 239 (1967).
13. K.A. Brueckner, J.R. Buchler, R.C. Clark and R.J. Lombard, Phys. Rev. **181**, 1534 (1969).
14. Y.-J. Shi and W.J. Swiatecki, Nucl. Phys. A **438**, 450 (1985).
15. Y.-J. Shi and W.J. Swiatecki, Nucl. Phys. A **464**, 205 (1987).
16. A. Sandulescu and W. Greiner, Rep. Prog. Phys. **55**, 1423 (1992).
17. G.H. Winslow, Phys. Rev. **96**, 1032 (1954).
18. G. Gamow, Zeit. f. Physik, **51**, 204 (1928).
19. E.U. Condon and R.W. Gurney, Nature **122**, 439 (1928) and Phys. Rev. **33**, 127 (1929).
20. P.B. Price, *Clustering Phenomena in Atoms and Nuclei* eds, M. Brenner, T. Lőnnroth and F.B. Malik (Springer Verlag, 1993) p. 273.
21. P.B. Price, Ann. Rev. Nucl. Part Sci **39**, 19 (1989).
22. D.N. Poenaru, W. Greiner, K. Depta, M. Ivascu, D. Mazilu and A. Sandulescu, At. Data Nucl. Data Tables **34**, 423 (1986).
23. M. Ivascu and I. Silisteanu, Nucl. Phys. A **485**, 93 (1988).
24. I. Silisteanu and M. Ivascu, J. Phys. G: Nucl. Part. Phys. **15**, 1405 (1989).
25. R. Blendowske and H. Walliser, Phys. Rev. Lett. **61**, 1930 (1988).
26. B. Buck and A.C. Merchant, Phys. Rev. C **39**, 2097 (1989); J. Phys G: Nucl. Part. Phys. **16**, L85 (1990); *ibid* **15**, 615 (1989).

27. B. Buck, A.C. Merchant, S.M. Perez and P. Tripe, J. Phys. G: Nucl. Part Phys. **20**, 351 (1994); Phys. Rev. C **47**, 1307 (1993).
28. B. Buck, A.C. Merchant and S.M. Perez Nucl. Phys. A **617**. 195 (1997); *ibid* **59**, 750 (1999).
29. B. Buck, A.C. Merchant and S.M. Perez Nucl. Phys. A **617**. 195 (1997); *ibid* **634**, 15 (1998).
30. S.A. Gurvitz and G. Kalbermann, Phys. Rev. Lett. **59**, 262 (1987).
31. E. Hourany, G. Berrier-Rousin, A. Elayi, P. Hoffmann-Rothe, A.C. Mueller, L. Rosier, G. Rotbard, G. Renou, A. Liebe, D.N. Poenaru and H.L. Ravn, Phys. Rev. C **52**, 267 (1995).
32. H.A. Bethe, Rev. Mod. Phys. **9**, 69, 161 (1937); Phys. Rev. **50**, 977 (1936).
33. G.P. Mueller and J.W. Clark, Nucl. Phys. A **155**, 561 (1970).
34. D.M. Brink and J.J. Castro, Nucl. Phys. A **216**, 109 (1973).
35. G. Röpke, Cond. Matter Theories **16**, 416 (2001).
36. H.J. Mang, Phys. Rev. **119**, 1069 (1960); Zeit f. Physik, **148**, 572 (1957).
37. M.A. Preston, Phys. Rev. **82**, 515 (1951).
38. J.J Devaney, Phys. Rev. **91**, 587 (1953).
39. B. Block, J.W. Clark, M.D. High, R. Malmin and F.B. Malik, Ann. Phys. (N.Y.) **62**, 464 (1971).
40. M. Haque and F.B. Malik (Private Communication, 2004); M. Haque, Master Thesis, Southern Illinois University at Carbondale (2004)
41. M.D. High, R. Malmin and F.B. Malik, Helv. Physica Acta **45**, 738 (1972).
42. M. Lederer and V. Shirley, Table of Isotopes, 7th edition (John Wiley and Sons, Inc., New York 1998).
43. E. Hourani, M. Hussonnois, L. Stab, L. Brillard, S. Gales and J.P. Schapira, Phys. Lett. B **160**, 375 (1985).

A The Relation Between the Asymptotic Kinetic Energy, and the Condition for the Existence of a Meta-Stable State

In binary fission, a parent nucleus of mass M, with mass and charge numbers A and Z, respectively, is in a meta-stable state and decays into a daughter pair of masses $M(A_1Z_1)$ and $M(A_2Z_2)$, A_1 and A_2 being their mass numbers and Z_1 and Z_2 being their atomic mass number yielding an energy Q. The conservation of energy for the process is given by

$$M(AZ)c^2 = M(A_1Z_1)c^2 + M(A_2Z_2)c^2 + Q\ . \tag{A.1}$$

In case all three nuclei involved in (A.1) are in their ground states, Q is called the Q-value of the reaction.

In case of fission, $M(A_1Z_1)$ and $M(A_2Z_2)$ have been experimentally determined to be in excited states, having masses $M^*(A_1Z_1)$ and $M^*(A_2Z_2)$, respectively, and hence, the energy-balance equation reduces to

$$M(AZ)c^2 = M^*(A_1Z_1)c^2 + M^*(A_2Z_2)c^2 + Q^* \tag{A.2}$$

where Q^* is now less than Q. A decay process is determined by the asymptotic kinetic energy in the center of mass system, T. Thus, if the daughter pair is in excited states at the time of decay

$$T = Q^* < Q\ . \tag{A.3}$$

A typical experimentally determined pre-gamma ray and pre-neutron-emission Q^*-value is shown in Fig. A.1 indicating that Q is typically larger than Q^* by about 20 to 40 MeV. In the figure, the two solid lines are calculated Q-values using Greens [A.1] and Myers-Swiatecki's [A.2] mass formulas. The use of the most recent mass formulas [A.3] does not change the basic picture significantly.

In Bohr-Wheeler type of theories [A.4, A.5] (noted hereafter as B-W) and its modified version to incorporate a Strutinski [A.6] type of barriers, (noted hereafter as B-W-S) the penetration problem through a barrier is calculated using Schrödinger equation with deformation parameter β being the variable. Theories using barriers calculated from energy-density functional formalism use the separation distance R as the variable in Schrödinger equation [A.7]. Thus, the tunneling stage in either formalism is governed by the Schrödinger equation of the following type for $u_{n\ell}(x) = x\phi_{n\ell}(x)$, where $\phi_{n\ell}(x)$ is the radial

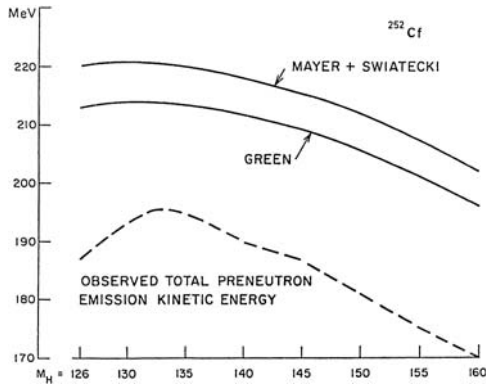

Fig. A.1. Calculated Q-values shown by *solid* lines in the spontaneous fission of ^{252}Cf to daughter pairs noted in the ordinate using the mass formulae of [A.1] and [A.2] are compared to the corresponding pre-neutron emission kinetic energies, shown as *broken* line [A.9]

wave function and x being either the characteristic deformation or separation distance:

$$\left[d^2/dx^2 - q^2(x) - \frac{l(l+1)}{x^2}\right] u_\ell(x) = 0 \tag{A.4}$$

with

$$q^2(x) = (2\mu/\hbar^2)(\text{Potential } V(x) - \text{asymptotic kinetic energy } T) \tag{A.5}$$

μ in (A.5) is the reduced mass.

The solution, that is regular at the origin, is given by the Volterra equation [A.8]

$$u_\ell(x) = x^{\ell+1} + (2\ell+1)^{-1} \int_0^x \left[(x/t)^{\ell+1/2} - (t/x)^{\ell+1/2}\right](xt)^{1/2} u_\ell(t) q^2(t) dt \,. \tag{A.6}$$

Then the derivative of $u_\ell(x)$, $du_\ell(x)/dx$ is given by

$$du_\ell(x)/dx = (\ell+1)x^\ell + (2\ell+1)^{-1}x^{-1} \times \int_0^x \left[(\ell+1)(x/t)^{\ell+1/2} + \ell(t/x)^{\ell+1/2}\right](xt)^{1/2} u_\ell(t) q^2(t) dt \tag{A.7}$$

$u_\ell(x)$ and $du_\ell(x)/dx$ are known up to an arbitrary constant but $u_\ell(x)$, being regular at the origin is proportional to $x^{\ell+1}$ near the origin. In this work, the proportionality constant is taken to be unity.

In particular for s-wave, we have the following equations

$$u_0(x) = x + \int_0^x (x-t)u_0(t)q^2(t)dt \tag{A.8}$$

and

$$du_0(x)/dx = 1 + \int_0^x u_0(t)q^2(t)dt \tag{A.9}$$

In case $q^2(t) > 0$ from the origin to the only turning point at $x = x_0$, as is the case in B-W or B-W-S type of theories, all iterated values of $u_\ell(x)$ in (A.6) and (A.8) are positive and when they are inserted in (A.7) and (A.9) yield a positive $du_\ell(x)/dx$ everywhere. Hence, the wave function *cannot* bend over from a positive slope to a negative one as required for a resonant-state *Hence, if* $q^2 > 0$ *everywhere, in the domain* $(0, x_0)$*, a resonant state characteristic of a decaying meta-stable state cannot be formed.*

In fact, $|\varphi_\ell(x)|^2$ where $\varphi_\ell(x) = u_\ell(x)/x$, the wave function, grows steadily from $x = 0$ to $x = x_0$ and decays almost instantaneously.

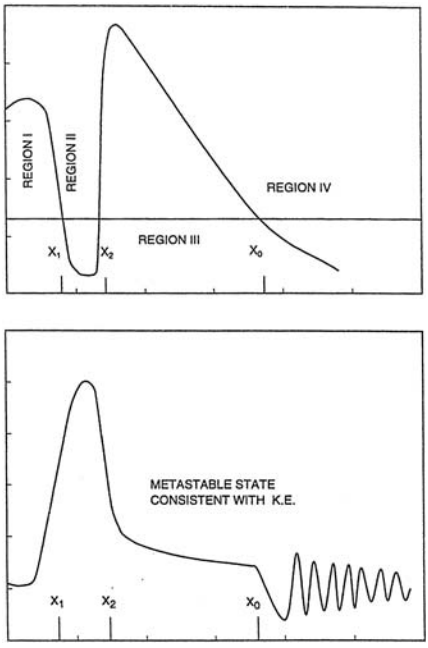

Fig. A.2. The ordinate for both inserts is x. The abscissa in the upper and lower inserts represents, respectively, the barriers potential and the decay function through the barrier

On the other hand if $q^2 \leq 0$ at least in one region in the interval $(0, x_0)$ as is the case for barriers derived from energy-density functional formalism in Chap. 3, $u_\ell(x)$ and $du_\ell(x)/dx$ could change from a positive to a negative value causing a change in its slope and $u_\ell(x)$ experiences a sudden increase in its amplitude generating a meta-stable state.

This is illustrated schematically in Fig. A.2. The wave function of a particle tunneling through a barrier depicted in the upper insert, is shown, schematically, in the lower insert of Fig. A.2. The amplitude of the wave function in the region $x_1 < x < x_2$, where $q_2 < 0$, suddenly increases in magnitude and changes its slope that is characteristic of the formation of a meta-stable state. In the upper insert, the barrier is the Q-value of the process at $x = 0$ and the solid line represents asymptotic kinetic energy, T, which is equal to Q^*, of the daughter pair. In case q^2 were positive in the entire domain $(0, x_0)$, the wave function would not have exhibited the resonant behavior. *Thus, the necessary and sufficient condition for the formation of a meta-stable state is that $q^2(x)$ must be zero or negative at least in one region in the interval* $(0, x_0)$. In the Gamow-Condon-Gurney theory of alpha-decay, $q^2(x) = 0$ near $x = 0$ and the condition is fulfilled.

The above theorem is derived for the one-dimensional single-channel case. This can be generalized to multi-channel case. In that case, $V(x)$ is to be identified as an effective potential generated by diagonalizing the set of coupled equation describing the decay process, an example of which is presented in Chap. 8 and Appendix C.

The above conclusion can also be derived in the JWKB approximation but no approximation has been done in our analysis here.

References

1. A.E.S. Green, Phys. Rev. **95**, 1006 (1954).
2. W.D. Myers and W.J. Swiatecki, Nucl. Phys. **81**, 1 (1966).
3. P. Möller, J.R. Nix, W.D. Myers and W.J. Swiatecki, At. Data Nucl. Data **59**, 185 (1995) *ibid.* **66**, 131 (1997).
4. N. Bohr and J.A. Wheeler, Phys. Rev. **56**, 426 (1939).
5. D.L. Hill and J.A. Wheeler, Phys. Rev. **89**, 1102 (1953).
6. V.M. Strutinsky, Nucl. Phys. **A95**, 420 (1967).
7. I. Reichstein and F.B. Malik, Ann. Phys. (N.Y.), **98**, 322 (1976).
8. F.B. Malik and P.C. Sabatier, Helv. Phys. Acta **46**, 303 (1973).
9. H.W. Schmitt, J.H. Neiler and F.J. Walter, Phys. Rev. **114**, 1146 (1966).

B The Expression for Half-Lives of Particles Tunneling Through the Barrier Shown in Fig. A.2

B.1 Exact Expression

We present here expressions for calculating half-lives pertinent to the penetration through a barrier shown in Fig. A.2. As noted in [B.1], one may obtain an exact expression for calculating half-lives, T, following Wigner [B.2] and Smith [B.3, B.4] who related T to the derivative of the phase shift, λ, of the scattered outgoing wave packet as follows

$$T = 2\hbar d\lambda(E)/dE = \sqrt{2\mu/E}d\lambda(k)/dk \tag{B.1}$$

In the above, E and k are, respectively, the energy and wave number of outgoing wave packet and μ is the reduced mass.

In this formalism, the half-life T of a meta-stable state is the probability of finding the system in the region of interaction minus the probability of finding a non-interacting wave packet in the same region. $u_{n\ell}(x) = x\phi_{n\ell}(x)$, where $\phi_{n\ell}(x)$ is the radial wave function, describes a particle in the region of interaction satisfying the following equation

$$\left[d^2/dx^2 - q^2(x) - \ell(\ell+1)/x^2\right] u_{n\ell}(x) = 0 \tag{B.2}$$

where

$$q^2(x) = \left(2\mu/\hbar^2\right) [\text{Potential}, V(x) - \text{Energy}, E] \; . \tag{B.3}$$

To obtain an explicit expression for $d\lambda(k)/dk$, we consider only s-wave (generalization to any other partial wave function is straight forward). In the presence of Coulomb interaction, the asymptotic form of $u(x)$ [dropping the suffix $(n\ell)$] is

$$u(x) \underset{x\to\infty}{\to} A(k)\sin(\varphi(k,x) + \lambda) + O(\eta/kR) \; . \tag{B.4}$$

where

$$\varphi(k,x) = kx - \eta\log 2kx + \sigma \tag{B.5}$$

In (B.5), η, the Coulomb parameter $= Z_1 Z_2 e^2/\hbar v$, Z_1 and Z_2 are the charges of the two decayed particles and v, their relative velocity and σ, the Coulomb phase shift $= \arg\Gamma(1+i\eta)$. In general, the second term in (B.4) is small and neglected henceforth.

Let us now consider wave functions, $u(k_1, x)$ and $u(k_2, x)$, having wave number k_1 and k_2, respectively, satisfying (B.2). Multiplying the equation for $u(k_1, x)$ with $u^*(k_2, x)$ and that for $u(k_2, x)$ with $u^*(k_1, x)$ and integrating over dx, we obtain the following equation after a substraction

$$\int_0^\infty dx\big[u^*(k_2,x)d^2u(k_1,x)/dx^2 - u^*(k_1,x)d^2u(k_2,x)/dx^2\big] + \int_0^\infty [u^*(k_2,x)k_1^2u(k_1,x) - u^*(k_1,x)k_2^2u(k_2,x)]dx = 0\,. \tag{B.6}$$

In case the non-Coulomb part of the potential is negligible for $r > R$, the above equation, after a partial integration (B.6) reduces to

$$u^*(k_2,x)du(k_1,x)/dx - u^*(k_1,x)du(k_2,x)/dx|_0^R + k_1^2\int_0^R u^*(k_2,x)u(k_1,x)dx - k_2^2\int_0^R u^*(k_1,x)u(k_2,x)dx = 0\,.$$

Substituting the behavior of $u^*(k_2, x)$ and $u(k_1, x)$ near the origin and their asymptotic forms (B.5), we get

$$(1/2)A(k_1)A(k_2)\,[(k_1+k_2)\sin(\varphi(k_2,R) - \varphi(k_1,R) + \lambda_2 - \lambda_1) + (k_1-k_2)\sin(\varphi(k_2,R) + \varphi(k_1,R) + \lambda_2 + \lambda_1)] = k_2^2\int_0^R u^*(k_1,x)u(k_2,x)dx - k_1^2\int_0^R u^*(k_2,x)u(k_1,x)dx\,. \tag{B.7}$$

Taking the limit $k_1 \to k_2$ and dropping the subscripts, we obtain

$$A^2(k)\,\{[(1/2)d\varphi(k,R)/dk + (1/2)d\lambda/dk] [1-\eta/2kR] - (1/4k)\sin(2\varphi(k,R) + 2\lambda)\} = \int_0^R |u(k,x)|^2dx\,. \tag{B.8}$$

Similarly for the case of a pure Coulomb potential only with a cut-off radius R, we get the following

$$A^2(k)\,[(1/2)(d\varphi(k,R)/dk)(1-\eta/2kR) - (1/4k)\sin(2\varphi(k,R)] = \int_0^R |u_c(k,x)|^2dx\,. \tag{B.9}$$

where u_c is the Coulomb function that is regular at the origin. The subtraction of (B.9) from (B.8) leads to the equation determining $d\lambda/dk$

$$A^2(k)\left[(1/2)(d\lambda/dk)(1-\eta/2kR)-(1/4k)\sin 2(\varphi(k,R)+\lambda)-\sin 2\varphi(k,R)\right]$$
$$=\int_0^R \left[|u(k,x)|^2-|u_c(k,x)|^2\right]dx\ . \tag{B.10}$$

Equation (B.10) may be used to get $d\lambda/dk$ since λ is obtained by solving (B.2) for a given potential using an appropriate numerical method. The half-life is, then, obtained from (B.1). This is exact.

Quite often, terms involving $(1/k)$ can be neglected. Then

$$d\lambda/dk=\left[2/A^2(k)\right]\int_0^R \left[u^2(k,x)-u_c^2(k,x)\right]dx \tag{B.11}$$

since both $u(k,x)$ and $u_c(k,x)$ are real.

B.2 JWKB Approximation

The kinetic energies of a daughter pair in the fission process is about 150 to 200 MeV and the energy equivalence of the masses of a daughter pair is large. In that case, wave number k is large and terms of the order of k^{-1} in (B.10) can be neglected, as long as one is interested in the half-lives of resonant states. As to the integrals on the right-hand-side of (B.10), its contribution in the region of $x_0 < x < R$, i.e. from the outer turning point to R, referring to Fig. A.2, contributes only of the order of A^2k^{-1} because of the oscillatory nature of both u and u_c. In fact, in the JWKB approximation the envelopes of u and u_c are equal.

Noting the absence of Coulomb potential in the interval region $0 < x < x_0$, we get the following expression for the derivative of λ with respect to k:

$$d\lambda/dk \cong 2/A^2\int_0^{x_0} u^2(k,x)dx\ . \tag{B.12}$$

Equations (B.10) and (B.12) are equivalent to the ones derived by F.T. Smith [B.3]. The formal difference between his formulas and ours is a consequence of his ansatz of averaging the wave function outside the range of interaction, which we have avoided here and constitutes a negligible difference towards half-lives between ours' and his formalism. It is also to be noted that the definition used for the half-life could differ from the definition used in the decay analysis by a factor of two. Our definition corresponds to the delay time introduced by Wigner in [B.2].

In the region I, i.e., in the interval $0 \le x < x_1,\ u(k,x)$ grows very slowly and its amplitude is small because $q_I^2(x)$, i.e. the value of $q(x)$ in the region is very large. Hence, (B.12) can further be approximated as

$$d\lambda/dk \cong \left(2/A^2\right) \int_{x_1}^{x_0} u^2(kx)dx \ . \tag{B.13}$$

In region II i.e., in the interval $x_1 < x < x_2$, the magnitude of q i.e., q_{II} is given by

$$q_{II}^2 = (2\mu/\hbar^2)(E - V(x)) \ . \tag{B.14}$$

It is no longer very large. The wave function, $u_{II}(k, x)$ in this region may be obtained by matching the wave function to the wave function in the region I at $x = x_1$ and is given by [B.4]

$$u_{II}(k, x) = 2\sqrt{2/\pi q_{II}} A_2 \cos(\pi/6) \cos\left[\int_{x_1}^{x} q_{II}(x)dx - \pi/4\right] \ . \tag{B.15}$$

Extending the limit of integration from x to x_2 and noting that

$$\int_{x_1}^{x_2} q_{II}(x)dx \cong \left(n + \frac{1}{2}\right)\pi \tag{B.16}$$

we get the following

$$u_{II}(k, x) = 2\left(\sqrt{2/\pi q_{II}}\right) A_2 \ \cos(\pi/6) \cos\left(n + \frac{1}{4}\right)\pi \ . \tag{B.17}$$

We note that (B.16) reflects the condition for the formation of a meta-stable state in this region. Noting that $\pi \cong 3$, we get

$$|u_{II}(k, x)|^2 = A_2/q_{II} \ . \tag{B.18}$$

Hence,

$$\int_{x_1}^{x_2} u_{II}^2(k_1, x)dx = A_2^2 \int_{x_1}^{x_2} dx/q_{II} \ . \tag{B.19}$$

In the region III, the penetration region where $x_2 < x < x_0$, the form of the wave function $u_{III}(k, x)$ is obtained from the matching condition at $x = x_2$ and is given

$$u_{III}(k, x) = A_2 \cos(\pi/6)\sqrt{2/\pi q_{III}} \exp\left(-\int_{x_2}^{x} q_{III}dx\right) \ . \tag{B.20}$$

This solution must match onto (B.4), i.e. onto the wave function in the region IV, where $x < x_0$. This leads to

$$A = A_2 k^{-1/2} \exp\left[-\int_{x_2}^{x_0} q_{III} dx\right] . \tag{B.21}$$

Substituting the ratio of A_2/A from (B.21), the expression for half-life is given by

$$T = \sqrt{2\mu/E}.k \left[\exp\left(2\int_{x_2}^{x_0} q_{III} dx\right) \int_{x_1}^{x_2} dx/q_{II} + (2/\pi)\cos^2(\pi/6) \int_{x_2}^{x_0} dx/q_{III}\right] . \tag{B.22}$$

The contribution of the second term in (B.22) to half-life is of the order of 10^{-22} sec, since it is basically the time taken to traverse the distance $(x_0 - x_2)$. Hence, it is appropriate to neglect it leading to the following expression

$$T = \sqrt{2\mu/E} \exp\left(2\int_{x_2}^{x_0} q_{III} dx\right) \int_{x_1}^{x_2} dx/(1 - V(x)/E) . \tag{B.23}$$

In case average value of $V(x)/E$ in region II is small,

$$T = \sqrt{2\mu/E} \exp\left(2\int_{x_2}^{x_0} q_{III} dx\right) . (x_2 - x_1) . \tag{B.24}$$

Thus, the critical parameter controlling the half-life for the decay through a barrier shown in Fig. A.2 is the difference $(V - E)$ in region III.

The actual shape of the potential in region II and its width $(x_2 - x_1)$ do not appreciably influence the numerical value in the calculation of half-life. The critical point is that there should be an interval like region II characterized by $E > V(x)$, so that a meta-stable state could form. In the absence of region II, the potential surface is essentially repulsive since $V(x) > E$ everywhere and the decay half-life is always of the order of 10^{-22} sec, the time taken for a projectile to traverse the potential.

References

1. F.B. Malik and P.C. Sabatier, Helv. Phy. Acta **46**, 303 (1973).
2. E.P. Wigner, Phys. Rev. **98**, 145 (1955).
3. F.T. Smith, Phys. Rev. **118**, 349 (1960).
4. M.L. Goldberger and K.M. Watson, *Collision Theory* (John Wiley and Sons, New York, 1964).
5. P.M. Morse and H. Feshbach, *Methods of Theoretical Physics Vol. 2* (McGraw Hill, New York, 1963).

C Diagonalization of the Coupled Set of Equations Describing Fission

In this appendix the decoupling of differential equation (8.20) is demonstrated for approximations (8.21). In order to achieve this, let us rewrite (8.16) with these approximations in the following form

$$\left[-\frac{\hbar^2}{2\mu}\nabla_R^2 - (E_n + V_{nD}(R))I - V_{nC}(R)C_{nN}\right] F_{nN}(R) = 0\,. \tag{C.1}$$

Where F_{nN} is a vector with elements $f_{n\beta}$, I is the $N \times N$ identity matrix and C_{nN} is the following constant matrix

$$C_{nN} = \begin{pmatrix} 0 & \gamma_{n2} & \gamma_{n3} & \cdots\cdots\cdots & \gamma_{nN} \\ \gamma_{n2} & 0 & 0 & \cdots\cdots\cdots & 0 \\ \gamma_{n3} & 0 & 0 & \cdots\cdots\cdots & 0 \\ . & & & & \\ . & & & & \\ \gamma_{nN} & 0 & 0 & \cdots\cdots\cdots & 0 \end{pmatrix}. \tag{C.2}$$

In order to diagonalize C_{nN}, let us define an $N \times N$ matrix

$$G_{nN} = C_{nN} - \lambda I = \begin{pmatrix} -\lambda & \gamma_{n2} & \gamma_{n3} & \cdots\cdots\cdots & \gamma_{nN} \\ \gamma_{n2} & -\lambda & 0 & \cdots\cdots\cdots & 0 \\ \gamma_{n3} & 0 & -\lambda & \cdots\cdots\cdots & 0 \\ . & & & & \\ . & & & & \\ \gamma_{nN} & 0 & 0 & \cdots\cdots\cdots & -\lambda \end{pmatrix}. \tag{C.3}$$

and claim that its determinant is given by the equation

$$Det[G_{nN}] = (-1)^N \left[\lambda^N - \lambda^{N-2}\sum_{j=2}^{N}\gamma_{nj}^2\right]. \tag{C.4}$$

In order to prove the above equation, let us note that (C.4) is valid for $N = 2$.

Thus, appealing to proof by induction, let us assume that (C.4) is true for N and make use of this assumption to prove that (C.4) is also valid for $N+1$. To prove this, let us use the $(N+1)$ th element of G_{nN+1} as the pivot, and find

$$Det[G_{nN+1}] = -\lambda Det[G_{nN}] - (-1)^{N+1}\gamma_{n(N+1)}Det(L_{nN})\ . \tag{C.5}$$

Where

$$L_{nN} = \begin{pmatrix} \gamma_{n2} & \gamma_{n3} & \cdots\cdots\cdots & \gamma_{nN+1} \\ -\lambda & 0 & \cdots\cdots\cdots & 0 \\ 0 & -\lambda & \cdots\cdots\cdots & 0 \\ . & & & \\ . & & & \\ 0 & 0 & \cdots\cdots\cdots -\lambda & 0 \end{pmatrix}\ , \tag{C.6}$$

with $Det(L_{nN}) = -(-1)^N(-\lambda)^{N-1}\gamma_{nN+1}$. Substitution of (C.4) and (C.6) in (C.5) lead to

$$\begin{aligned} Det[G_{nN+1}] &= (-1)^{N+1}\left[\lambda^{N+1} - \lambda^{N-1}\sum_{j=2}^{N}\gamma_{nj}^2\right] - (-1)^{N+1}\lambda^{N-1}\gamma_{nN+1}^2 \\ &= (-1)^{N+1}\left[\lambda^{N+1} - \lambda^{N-1}\sum_{j=2}^{N+1}\gamma_{nj}^2\right]\ . \end{aligned} \tag{C.7}$$

Equation (C.7) being identical to (C.4), except for N being changed to $N+1$, completes the induction proof and allows us to conclude that the $N \times N$ matrix C_{nN} has three distinct eigenvalues

$$\lambda = \left[\sum_{j=2}^{N}\gamma_{nj}^2\right]^{1/2},\quad 0,\quad -\left[\sum_{j=2}^{N}\gamma_{nj}^2\right]^{1/2}\ . \tag{C.8}$$

With eignenvalue $\lambda = 0$ having a multiplicity of $N-2$ the matrix CnN being symmetric, therefore is diagonalizable [C.2] and a constant $N \times N$ matrix P_{nN} exists such that

$$\Lambda_{nN} = {P^{-1}}_{nN}C_{nN}P_{nN} = \begin{pmatrix} \lambda & 0 & 0 & \cdots\cdots\cdots & 0 \\ 0 & -\lambda & 0 & \cdots\cdots\cdots & 0 \\ 0 & 0 & 0 & \cdots\cdots\cdots & 0 \\ . & & & & \\ . & & & & \\ 0 & 0 & 0 & \cdots\cdots\cdots & 0 \end{pmatrix} \tag{C.9}$$

where $\lambda \equiv [\sum_{j=2}^{N}\gamma_{nj}^2]^{1/2}$ and P_{nN} is the transformation matrix whose columns are the eigenvectors of C_{nN}. For example, it can be written as

$$P_{nN} = \begin{pmatrix} 1 & -1 & 0 & 0 & \cdots\cdots\cdots & 0 \\ \xi_{n2} & \xi_{n2} & -1 & 0 & \cdots\cdots\cdots & 0 \\ \xi_{n3} & \xi_{n3} & \zeta_{n3} & -1 & \cdots\cdots\cdots & 0 \\ \xi_{n4} & \xi_{n4} & 0 & \zeta_{n4} & \cdots\cdots\cdots & 0 \\ . & & & & & \\ . & & & & & \\ \xi_{nN-1} & \xi_{nN-1} & 0 & 0 & \cdots\cdots\cdots & -1 \\ \xi_{nN} & \xi_{nN} & 0 & 0 & \cdots\cdots\cdots & \zeta_{nN} \end{pmatrix} \tag{C.10}$$

where $\xi_{nj} = \gamma_{nj}/\lambda$ and $\zeta_{nj} = \gamma_{n(j-1)}/\gamma_{nj}$. Of course, due to our assumption that we have N coupled channels, γ_{nj} is all nonzero and therefore, ζ_{nj} is all well defined.

The application of above transformation matrix to (C.1) yields the desired result.

$$\left[-\frac{\hbar^2}{2\mu}\nabla_R^2 - (E_n + V_{nD}(R))I - V_{nC}(R)\Lambda_{nN}\right]\tilde{F}_{nN}(R) = 0\ . \qquad \text{(C.11)}$$

Where $\tilde{F}_{nN}(R) = {P^{-1}}_{nN}\ F_{nN}(R)$. As it can be seen, (C.11) is a set of N decoupled ordinary differential equations, containing only three distinct decoupled equations which are identical to equations (8.22a), (8.22b) and (8.22c), appearing in Chap. 8.

References

1. M.A. Hooshyar and F.B. Malik, Helv. Acta. Phys. **45**, 567 (1972).
2. D.B. Damiano and J.B. Little, *A course in Linear Algebra* (Academic Press, New York, 1988).

Author Index

Index

Copyright Permission

The permission to use or reprint from the following holders of copyright for the articles listed under them are hereby acknowledged.

1. 50 Years with Nuclear Fission eds. J. W. Behrens and A. D. Carlson (**American Nuclear Society**, La Grange Park, Illinois 60525, USA, 1989).

(a) From the article by N. E. Holden (starting p. 465)

Figures 1, 3, and 4.
Table III.

(b) From the article by A. C. Wahl (starting p. 525).

Figure 1.

(c) From the article by J. Throchon, G. Simon and C. Signarbieux (starting p. 313).

Figure III.

2. McGraw Hill

From the article by S. Katcoff, published in *Nucleonics,* vol. **18** (1960)

Figures on p. 201 and p. 202.

3. Academic Press (New York)

(a) Nuclear Fission by R. Vandenbosch and J. R. Huizenga (1973).

Figures XII-2, XIII-4, XIII-5, and XII-6,

(b) B. Block et al. Annals of Physics (N. Y.) Vol. 62, p. 464 (1971).

Figure 3

(c) I. Reichstein and F. B. Malik, Annals of Physics (N. Y.) Vol. 98, p. 322 (1976).

Figures 1, 2, 4, 6, 7, and 9.

4. Plenum Press

(a) I. Reichstein and F. B. Malik, Condensed Matter Theories, Vol. 8 p. 243 (1993).

Figure 5.

(b) Proc. Int'l. Symp. Om Superheavy Elements Ed. M. A. K. Lodhi. Article by I. Reichstein and F. B. Malik.

Figures 4 and 6.

(c) Frontier Topics in Nuclear Physics. Eds. W. Scheid and A. Sandulescu. Article by F. Gönnenwein.

Figure 1.

5. Springer Verlag

(a) M. Montoya, Zeit. Physik A. Vol. 319, p. 219 (1984).

Figure 1.

(b) J. Kaufman et al., Zeit. Physik A. Vol. 341, p. 319 (1992).

Figure 6.

6. Institute of Physics (U. K.)

(a) W. Mollenkopf et al., Journal of Physics G: Nucl. Part., Vol. 18, p. L203 (1992).

Figures 1 and 2

(b) A. Florescu et al., Journal of Physics G: Nucl. Part., Vol. 19, p. 669 (1993).

Figures 5 and 6.

7. American Institute of Physics

(a) H. W. Schmitt et al. Physical Review, Vol. 141, p. 1146 (1966).

Figure 8.

(b) J. Terrell, Physical Review, Vol. 127, p. 880 (1962).

Figure 11.

(c) K. A. Brueckner et al., Physical Review, Vol. 168, p. 1184 (1968).

Figure 1.

(d) F. J. Shore and V. L. Sailor, Physical Review, Vol. **112**, p. 191 (1958).

Figure 1.

(e) A. C. Wahl, R. L. Ferguson, D. R. Nethaway, D. E. Trouter, and K. Wolfsburg, Physical Review, Vol. **126**, p. 1112 (1962).

Figure 8.

8. **Helvetica Physica Acta**

(a) F. B. Malik and P. Sabatier, Vol. 46, p. 303 (1973).

Figure 1.

(b) M. A. Hooshyar and F. B. Malik, Vol. 46. p. 720 (1973).

Figure 1.

(c) M. A. Hooshyar and F. B. Malik, Vol. 46, p. 724 (1973).

Figure 1

9. **Elvesier**

(a) M. A. Hooshyar and F. B. Malik, Physics Letters B, Vol. 38. p. 495 (1972).

Figures 1, 2, and 3.

(b) M. A. Hooshyar and F. B. Malik, Physics Letters B

Tables 1, 2, and 3.

10. **Prof. Dr. F. Gönnenwein**

Private communication of fig. 7.4 of this book